# Muon-spin spectroscopy studies of materials hosting topological magnetic states

**Thomas James Hicken**

A thesis presented for the degree of
Doctor of Philosophy


Department of Physics
Durham University
United Kingdom

July 2021

# Contents

# Muon-spin spectroscopy studies of materials hosting topological magnetic states

**Thomas James Hicken**

## Abstract

This thesis applies muon-spin spectroscopy ($\mu$SR) to materials hosting topological magnetic states. Each study focuses on a different material family that hosts either a skyrmion lattice (SkL), or chiral soliton lattice (CSL) state. We study the static and/or dynamic magnetism of each material, distinguishing the behaviour of the topological magnetic states from those of the materials.

Longitudinal-field (LF) $\mu$SR measurements of $Cu_2OSeO_3$, $Co_xZn_yMn_{20-x-y}$, and $GaV_4S_{8-y}Se_y$ reveal that the SkL phase exhibits emergent dynamic behaviour at megahertz frequencies. These dynamics in $Co_xZn_yMn_{20-x-y}$ and $GaV_4S_{8-y}Se_y$ are well described by gigahertz excitations that reduce in frequency near the critical temperature. We find that as crystallographic site disorder increases, so too does the complexity of the dynamic response on the muon timescale, suggesting that site disorder plays a role in stabilising complex excitations. The temperature-evolution of the magnetic ground state of $GaV_4S_{8-y}Se_y$ is revealed through zero-field $\mu$SR measurements, whilst LF measurements show that the SkL exists under low-levels of substitution at both ends of the series. $\mu$SR measurements of polycrystalline Zn-substituted $Cu_2OSeO_3$ show that the reported splitting of the SkL phase in the $B$–$T$ phase diagrams of these materials occurs due to different levels of Zn-substitution in different grains of the sample.

Finally, in $Cr_{1/3}MS_2$ ($M$ = Nb or Ta) the presence of a gap-like feature (width in range 40–100 meV) in the density of states is confirmed by magnetometry measurements. Dynamic spin fluctuations driven by excitations across this gap are seen over a wide range of frequencies (0.1 Hz to MHz) with AC susceptibility and $\mu$SR measurements. Effects due to the CSL in $Cr_{1/3}NbS_2$, as detected with $\mu$SR, dominate over the gap-driven magnetism when the CSL is stabilised as the majority phase.

# Declaration

The work in this thesis is based on research carried out in the Department of Physics, Durham University, UK, with some experimental work carried out at the STFC ISIS Neutron and Muon Source, UK and the Swiss Muon Source, Paul Scherrer Institut, Switzerland; I am very grateful for the provision of beamtime. No part of this thesis has been submitted elsewhere for any other degree or qualification and it is all my own work unless referenced to the contrary in the text.

# List of publications

K. J. A. Franke, B. M. Huddart, **T. J. Hicken**, F. Xiao, S. J. Blundell, F. L. Pratt, M. Crisanti, J. A. T. Barker, S. J. Clark, A. Štefančič, M. Ciomaga Hatnean, G. Balakrishnan, and T. Lancaster. "Magnetic phases of skyrmion-hosting $GaV_4S_{8-y}Se_y$ $(y = 0, 2, 4, 8)$ probed with muon spectroscopy". Physical Review B **98**, 054428, 2018.

A. Štefančič, S. H. Moody, **T. J. Hicken**, M. T. Birch, G. Balakrishnan, S. A. Barnett, M. Crisanti, J. S. O. Evans, S. J. R. Holt, K. J. A. Franke, P. D. Hatton, B. M. Huddart, M. R. Lees, F. L. Pratt, C. C. Tang, M. N. Wilson, F. Xiao, and T. Lancaster. "Origin of skyrmion lattice phase splitting in Zn-substituted $Cu_2OSeO_3$". Physical Review Materials **2**, 111402(R), 2018.

R. C. Williams, W. J. A. Blackmore, S. P. M. Curley, M. R. Lees, S. M. Birnbaum, J. Singleton, B. M. Huddart, **T. J. Hicken**, T. Lancaster, S. J. Blundell, F. Xiao, A. Ozarowski, F. L. Pratt, D, J. Voneshen, Z. Guguchia, C. Baines, J. A. Schlueter, D. Y. Villa, J. L. Manson, and P. A. Goddard. "Near-ideal molecule-based Haldane spin chain". Physical Review Research **2**, 013082, 2020.

M. N. Wilson, M. T. Birch, A. Štefančič, A. C. Twitchett-Harrison, G. Balakrishnan, **T. J. Hicken**, R. Fan, P. Steadman, and P. D. Hatton. "Stability and metastability of skyrmions in thin lamellae of $Cu_2OSeO_3$". Physical Review Research **2**, 013096, 2020.

**T. J. Hicken**, S. J. R. Holt, K. J. A. Franke, Z. Hawkhead, A. Štefančič, M. N. Wilson, M. Gomilšek, B. M. Huddart, S. J. Clark, M. R. Lees, F. L. Pratt, S. J. Blundell, G. Balakrishnan, and T. Lancaster. "Magnetism and Néel skyrmion dynamics in $GaV_4S_{8-y}Se_y$". Physical Review Research **2**, 032001(R), 2020.

F. Xiao, W. J. A. Blackmore, B. M. Huddart, M. Gomilšek, **T. J. Hicken**, C. Baines, P. J. Baker, F. L. Pratt, S. J. Blundell, H. Lu, J. Singleton, D. Gawryluk, M. M. Turnbull, K. W. Krämer, P. A. Goddard, and T. Lancaster. "Magnetic order and disorder in a quasi-two-dimensional quantum Heisenberg antiferromagnet with randomized exchange". Physical Review B **102**, 174429, 2020.

**T. J. Hicken**, M. N. Wilson, K. J. A. Franke, B. M. Huddart, Z. Hawkhead, M. Gomilšek, S. J. Clark, F. L. Pratt, A. Štefančič, A. E. Hall, M. Ciomaga Hatnean, G. Balakrishnan, and T. Lancaster. "Megahertz dynamics in skyrmion systems probed with muon-spin relaxation". Physical Review B **103**, 024428, 2021.

B. M. Huddart, M. Gomilšek, **T. J. Hicken**, F. L. Pratt, S. J. Blundell, P. A. Goddard, S. J. Kaech, J. L. Manson, and T. Lancaster. "Magnetic order and ballistic spin transport in a sine-Gordon spin chain". Physical Review B **103**, L060405, 2021.

S. P. M. Curley, R. Scatena, R. C. Williams, P. A. Goddard, P. Macchi, **T. J. Hicken**, T. Lancaster, F. Xiao, S. J. Blundell, V. Zapf, J. C. Eckert, E. H. Krenkel, J. A. Villa, M. L. Rhodehouse, and J. L. Manson. "Magnetic ground state of the one-dimensional ferromagnetic chain compounds $M(\mathrm{NCS})_2(\mathrm{thiourea})_2$ $(M = \mathrm{Ni}, \mathrm{Co})$". Physical Review Materials **5**, 034401, 2021.

# Acknowledgements

I have had the privilege to work alongside a huge number of people who have been incredibly supportive, all of whom I am proud to say have made me into the scientist I am today. I have greatly enjoyed working with them, and they have taught me so much. I am exceptionally grateful to Tom Lancaster, who epitomises the perfect supervisor: kind, supportive, insightful, and perpetually generous with his time. A particular note must go to Murray Wilson, Zachary Hawkhead, and Samuel Holt, all of whom have contributed immeasurably both to my work, and to my PhD experience. I also want to thank: Geetha Balakrishnan, Marijan Beg, Steve Blundell, Stewart Clark, Kévin Franke, Matjaž Gomilšek, Amelia Hall, Peter Hatton, Ben Huddart, Martin Lees, Duncan McCallum, Sam Moody, Ben Nicholson, Francis Pratt, Mark Raine, Aleš Stefančič, Reece Stockport, Luke Turnbull, and Kristian Whatcott. Being part of the Skyrmion Project was a wonderful experience, and I am grateful to all of those who have been involved in it. I would like to thank Durham University for funding my studentship; the Institute of Physics and Ustinov College for financial support; Durham Hamilton HPC for computational support; and ISIS Neutron and Muon Source and the Paul Scherrer Institut for the provision of beamtime, my thanks in particular goes to the fantastic beamline scientists who have supported my experiments. None of this would have been possible without my parents and my brother, who have been endlessly supportive, and I will always support.

*For my grandparents: Nanna and Grandad, Nan and Grandin. I wish they were still here to see this.*

# Chapter 1

# Introduction

The 2016 Nobel Prize in Physics was awarded "for theoretical discoveries of topological phase transitions and topological phases of matter". The timing of this prize seems very apt, with a huge amount of experimental condensed matter physics research into topological properties of materials being pursued in the years since. Prime examples include topological insulators [1] and topological superconductors [2]. In this thesis we are interested in the application of topology to magnetism.

The skyrmion has been the poster-child of topological magnetic states since the discovery of the skyrmion lattice (SkL) phase in MnSi in 2009 [3]. Since then, there has been an explosion of interest in the area, with there now being myriad materials which host some form of topological magnetic state [4, 5]. There are at least two reasons for this interest in these states; (i) they provide a playground for testing new physics, and (ii) they have desirable properties that may lead to technological applications in wider society. In the case of (i), many simple models of magnetism have differing properties due to topological features [6]. A good example is the topological Hall effect, where electron transport through a material is affected by the geometry of the path it takes through space [7]. This has ramifications not just in condensed matter physics, but also in other areas of research. The technological applications of (ii) generally focus on the low current densities required to move these topological objects around [8, 9, 10], making

them ideal information carriers for a low-energy consumption world. In addition, there is great interest in possible use of these materials for different applications such as novel computing techniques [11].

Commensurate with the desire to research these topological magnetic states is the need to apply many different experimental techniques. In this thesis we apply a technique which has thus far been less commonly applied to the study of these systems, muon-spin spectroscopy ($\mu$SR). By implanting muons in the materials, we can study the static and dynamic magnetism of these topological states, and gain unique understanding of their behaviours. Historically, $\mu$SR has been applied to many problems in condensed matter physics, particularly to study subtle changes in magnetism [12]. $\mu$SR has also been very successful in elucidating the details of the superconducting vortex state of superconductors [13]; the parallel between this state and the SkL was one of the first reasons that $\mu$SR was investigated as a tool for studying topological magnetic states. In this thesis we show that $\mu$SR is also uniquely sensitive to dynamics of the topological magnetic states that are inaccessible with other experimental techniques. This provides a great number of insights into both the behaviour of the materials that host these states, and the topological magnetic states themselves. The study of the dynamics is particularly important in the case of the SkL, where despite there being a great deal of research into the high (GHz) frequency response, and using the low (Hz to kHz) frequency AC susceptibility response to identify materials as SkL-hosting candidates, very little is known about the intermediate (MHz) frequencies. It is these frequencies to which $\mu$SR is uniquely sensitive.

This thesis, after introducing the relevant concepts and techniques, discusses four different classes of material that host topological magnetic states, often looking at how small amounts of chemical substitution affects the magnetism. The high sensitivity of $\mu$SR to small changes in magnetism makes it an indispensable tool in this area of research. Three of the four materials host a SkL, with the results building on each other to form a consistent story of the behaviour of the SkL, irrespective of the material in which they are stabilised. The focus of the

thesis is slightly different for the fourth class of material, which hosts a magnetic chiral soliton lattice. Here $\mu$SR, in combination with other techniques, reveals details of the electronic structure, and how this influences the magnetism in these materials.

## 1.1 Layout of thesis

This thesis is organised as follows:

**Chapter 2:** I introduce the main concepts needed to understand the material in this thesis. I start by discussing the origin of magnetic moments, before going on to the possible arrangements of these moments in topologically non-trivial structures.

**Chapter 3:** I introduce the main techniques used in this thesis. Most of the chapter focuses on the muon-spin spectrscopy technique, and includes an example of its application to a topological magnetic state, the Haldane Chain. I also briefly introduce magnetometry techniques, and density functional theory.

**Chapter 4:** I report the results of muon-spin spectroscopy ($\mu$SR) experiments of skyrmion lattice (SkL) host, $Cu_2OSeO_3$. I show evidence for previously unreported megahertz spin dynamics that are associated with the skyrmion phase. I also study the $\mu$SR response to the SkL when the SkL is not the majority phase, showing that it is unlikely the SkL exists throughout the bulk of the sample when it is a metastable state.

**Chapter 5:** I report the results of $\mu$SR experiments of Zn-substituted $Cu_2OSeO_3$. The measurements demonstrate that the splitting of the SkL phase into two distinct pockets in the $B$–$T$ phase diagram that was previously reported in polycrystalline Zn-substituted $Cu_2OSeO_3$ occurs due to the coexistence of different grains of the sample with different Zn-substitution. I demonstrate that $\mu$SR is

sensitive to the volume fraction of each level of Zn-substitution in the samples.

**Chapter 6:** I report the results of $\mu$SR experiments of $Co_xZn_yMn_{20-x-y}$, once again observing megahertz dynamics associated with the SkL. In $Co_8Zn_9Mn_3$ I demonstrate that these dynamics are consistent with the reduction in frequency of the characteristic excitations of the skyrmion, with the first report of this frequency in $Co_xZn_yMn_{20-x-y}$. By studying the metastable SkL I am able to demonstrate that there is likely to be a second source of megahertz dynamics occurring due to decay of skyrmions. The measurements suggest that complex spin structures are more easily stabilised in materials with high chemical substitutional disorder.

**Chapter 7:** I report the results of $\mu$SR experiments of $GaV_4S_{8-y}Se_y$, which hosts a Néel SkL at the ends of the series. I find dynamics consistent with those reported in previous chapters. The measurements reveal that $GaV_4S_8$ has a complex magnetic groundstate of microscopically coexisting cycloidal and ferromagnetic environments, whilst chemical substitution leads to the growth of localised regions of spin density. At both ends of the series chemical substitution leads to an extended region of emergent dynamics, suggesting skyrmionic precursors. Low-temperature dynamics suggest the onset of glass-like dynamics that are observed at higher substitution levels.

**Chapter 8:** I report an experimental and theoretical investigation of $Cr_{1/3}MS_2$ ($M$ = Nb or Ta). $Cr_{1/3}NbS_2$ is of particular interest due to magnetic chiral soliton lattice (CSL) it exhibits at certain points in the $B$–$T$ phase diagram. I focus on unusual low-temperature magnetic and transport properties, which are demonstrated to occur due to a small gap-like feature at the Fermi energy in the density of states. Magnetometry measurements confirm the existence of this gap, and $\mu$SR studies the dynamic properties of excitations across it. We find that effects due the CSL dominate over gap-driven magnetism when it is stabilised as

the majority phase.

**Chapter 9:** I conclude the thesis with a summary of the main results, and discuss future avenues for research into materials hosting topological magnetic states.

**Appendix A:** I present a derivation of a model regularly used throughout the thesis, the contribution to the muon-spin polarisation decay rate in a longitudinal-field $\mu$SR experiment due to the reduction in frequency of the characteristic excitations of skyrmions as the temperature approaches the magnetic ordering temperature.

# Chapter 2

# Magnetism

This thesis discusses materials that host topological magnetic states, that is systems where, under the correct conditions, the magnetic moments arrange in a configuration whose properties are affected by the topology. To understand this, we must consider what we mean by (i) magnetic moments, and (ii) topology. This chapter serves as an introduction to these topics, before going on to discuss different types of topological magnetism, and experimental realisations of them in real systems.

## 2.1 Magnetic moments

Central to the understanding of magnetism is angular momentum; through direct or indirect analogy, magnetic moments can be defined in terms of their orbital and/or spin angular momentum. We will first discuss the classical picture of the angular momentum of a current loop, before extending this into real systems, which requires a quantum mechanical description. In absence of an alternative reference, the material in the following can be found in Ref. [14].

### 2.1.1 Orbital angular momentum

Consider a classical electron travelling around a loop of infinitesimal area $|\mathrm{d}\boldsymbol{S}|$. This defines a current $I$, and hence has a magnetic moment $\mathrm{d}\boldsymbol{\mu} = I\,\mathrm{d}\boldsymbol{S}$, where

d$\boldsymbol{S}$ points normal to the loop. If this electron instead travels around a loop of finite area, one can integrate over the area of the loop, finding

$$\boldsymbol{\mu} = \int \mathrm{d}\boldsymbol{\mu} = I \int \mathrm{d}\boldsymbol{S}. \tag{2.1}$$

Assuming the loop is circular with radius $r$, one can write the current as $I = e/T = ev/(2\pi r)$, where $e$ is the charge on an electron, and $T$ is the time period for one orbit. One can thus write Eqn. 2.1 as

$$\boldsymbol{\mu} = I \int \mathrm{d}\boldsymbol{S} = \left(\frac{ev}{2\pi r}\right) \pi r^2 \, \mathrm{d}\hat{\boldsymbol{S}} = \left(\frac{e}{2m_\mathrm{e}}\right) m_\mathrm{e} v r \, \mathrm{d}\hat{\boldsymbol{S}}, \tag{2.2}$$

where we have added in factors of the electron mass $m_\mathrm{e}$, and $d\hat{\boldsymbol{S}}$ is the unit vector pointing in the same direction as $d\boldsymbol{S}$. By identifying the angular momentum as $\boldsymbol{L} = m_\mathrm{e} v r d\hat{\boldsymbol{S}}$, one finds that

$$\boldsymbol{\mu} = \left(\frac{e}{2m_\mathrm{e}}\right) \boldsymbol{L} = \gamma_\mathrm{e} \boldsymbol{L}, \tag{2.3}$$

where we have defined the gyromagnetic ratio of the electron $\gamma_\mathrm{e} = e/(2m_\mathrm{e})$. Therefore, we can see that the magnetic moment of a charged object is directly proportional to its angular momentum.

In reality, electrons are not classical objects, and we therefore need a quantum mechanical description of angular momentum. The angular momentum operator is given by $\hbar\hat{\boldsymbol{L}} = \hat{\boldsymbol{r}} \times \hat{\boldsymbol{p}} = i\hbar\hat{\boldsymbol{r}} \times \nabla$, where $\hat{\boldsymbol{r}}$ and $\hat{\boldsymbol{p}}$ are the position and momentum operators respectively. Each of the three components of the angular momentum can be trivially derived from this equation, however it is not possible to simultaneously know them all. Fortunately, the square of the magnitude of the angular momentum, and one component (by convention, $L_z$), can be simultaneously known. The eigenfunctions of these operators are the spherical harmonics, and two quantum numbers are required to describe the state of the system: $l$, the angular momentum quantum number, and $m_l$, the magnetic quantum number. These quantum numbers can take the integer values $0 \leq l \leq n-1$ and $-l \leq m_l \leq l$, where $n$ is the principal quantum number, which describes the energy of the electron for hydrogenic atoms. (For completeness, we note that

in more complicated atoms electron-electron interactions are important, and the total energy depends on both $n$ and $l$.)

Within this quantum mechanical description, one finds that the magnitude of orbital angular momentum is $\sqrt{l\,(l+1)}\hbar$, with $z$-component $m_l\hbar$. By using Eqn. 2.3, we find that

$$\begin{aligned} |\boldsymbol{\mu}| &= \left(\frac{e\hbar}{2m_\mathrm{e}}\right)\sqrt{l\,(l+1)} = \mu_\mathrm{B}\sqrt{l\,(l+1)}, \\ \mu_z &= -m_l\mu_\mathrm{B}, \end{aligned} \tag{2.4}$$

where we have defined the Bohr magneton $\mu_\mathrm{B} = e\hbar/\,(2m_\mathrm{e})$, a common unit in magnetism. This gives expressions for the magnetic moment of a single electron that arises from the orbital angular momentum, however, this is not the only contribution.

### 2.1.2 Spin angular momentum

Much in the same way that particles have fundamental properties of mass and electrical charge, they also have a magnetic equivalent: spin. The spin of a particle acts in a mathematically equivalent sense to the orbital angular momentum already discussed, so we can therefore use many of the same equations to understand it. We correspondingly introduce two more quantum numbers to describe the spin state of a particle, $s$ and $m_s$. The fundamental difference between the spin and orbital momentum is that, whilst $l$ depends on the energy of the particle, $s$, being related to the intrinsic property of the particle, is a constant. For electrons, $s = 1/2$. Once again analogously, $m_s$ has $2s+1$ possible values, $s\hbar, (s-1)\,\hbar, ..., -s\hbar$. Thus, the magnitude of the spin angular momentum is $\sqrt{s\,(s+1)}\hbar$, with $z$-component $m_s\hbar$.

From these results we can calculate the magnetic moment arising from the spin of the electron,

$$\begin{aligned} |\boldsymbol{\mu}| &= \mu_\mathrm{B} g_s\sqrt{s\,(s+1)}, \\ \mu_z &= -m_s g_s \mu_\mathrm{B}. \end{aligned} \tag{2.5}$$

Note that both equations are now multiplied by a factor $g_s$; a similar factor $g_L$ actually appears in Eqn. 2.4, however in that case it is equal to 1, so is typically

omitted for clarity. In the case of the spin quantum numbers and an electron, $g_s$ is very close to 2, which means that, due to their intrinsic spin, electrons have a magnitude of magnetic moment of approximately $\sqrt{3}\mu_B$. As all the components of the spin are not able to be known simultaneously, rather than the magnitude, we normally just consider the component along the $z$-axis, approximately $\mp\mu_B$. We often refer to these two options as "down" and "up" spin.

### 2.1.3 Magnetic moments of atoms

Having considered the contribution to the magnetic moment of individual electrons, we now need to ask what happens when these electrons are put together to build an atom or ion. We describe the electrons in an atom as being in a shell (corresponding to $n$), and subshell (corresponding to $l$, such that $l = 0$ is denoted s, $l = 1$ is denoted p, $l = 2$ is denoted d, $l = 3$ is denoted f and so on). Electrons within these subshells are then distinguished by their $m_l$ and $m_s$ quantum numbers. Electrons will minimise their total energy, which means filling the lowest energy shells first. Working out the order the shells are filled is not completely trivial as there are other contributions to the energy of the electrons which we will not consider here. However, to understand the origin of the magnetic moment, we can restrict ourselves to considering how the subshells fill, and not concern ourselves with the order in which they are picked. We can split the subshells into two categories: filled and partially filled.

In a filled subshell, all electrons have the same $l$ (and $s$) quantum numbers, so all have the same magnitude magnetic moment. However, the orientation of these moments is not the same, due to the different $m_l$ and $m_s$ quantum numbers. As fermions, all possible values of $m_l$ and $m_s$ will exist in a filled subshell. That means, to work out the total magnetic moment of the filled subshell due to the orbital angular moment, we can work out the total moment in the $z$-direction through

$$\mu_z = -2\mu_B \sum_{m_l=-l}^{l} m_l = 0, \tag{2.6}$$

where the factor of 2 accounts for the two different spin species. Clearly, there

is no total magnetic moment arising from the orbital angular momentum, with a similar result from the spin angular momentum.

The highest energy electrons may only partially fill a subshell, where there are more states available to the electrons than will be occupied. We must consider which states are occupied. The answer is given by Hund's first rule, stating that the spin of the subshell in maximised. This can be understood with a classical argument, with this arrangement maximising the distance between the electrons, and hence minimising the contribution to the Coulomb energy. As an example, we will consider the situation where we have 7 electrons in the $3d$-orbital (as is the case for $Co^{2+}$). We have $n = 3$ and $l = 2$, with $-2 \leq m_l \leq 2$. This means we have 5 options for the orbital angular momentum, each of which can have either a spin-up or spin-down electron in. In total, there are 10 different states available. As we wish to maximise spin, we place our first 5 electrons such that they are all spin-up, each with different $m_l$. For electrons 6 and 7, we have no more unoccupied values of $m_l$, so we must start pairing them up, going in as spin-down. This leads to, in total, 2 pairs of electrons, and 3 unpaired electrons, resulting in a total orbital and spin angular momentum. This contribution means that the partially filled subshell will contribute to the total magnetic moment of the system.

To work out the magnetic moment from a partially filled subshell, one has to calculate the total angular momentum $\boldsymbol{J} = \boldsymbol{L} + \boldsymbol{S}$. As this is a vector sum, and the alignment of $\boldsymbol{L}$ and $\boldsymbol{S}$ can change, it is not immediately clear how one would calculate the magnitude $J = |\boldsymbol{J}|$ having applied Hund's rules. Given the magnitude of the orbital and spin angular momenta, $L = |\boldsymbol{L}|$ and $S = |\boldsymbol{S}|$ respectively, one can calculate $J = |L - S|$ if the subshell is less than half full, or $J = |L + S|$ if the subshell is more than half full. This total angular momentum has the same form as the orbital and spin angular momentum, with corresponding quantum numbers. We define the magnetic moment to be

$$\begin{aligned} \boldsymbol{\mu} &= \mu_{\mathrm{B}} \left( g_L \boldsymbol{L} + g_s \boldsymbol{S} \right) \\ &= \mu_{\mathrm{B}} g_J \boldsymbol{J}, \end{aligned} \tag{2.7}$$

where it can be determined from these definitions that $g_J$ is a constant,

$$\begin{aligned} g_J = \; & g_L \left[ \frac{J\left(J+1\right) + L\left(L+1\right) - S\left(S+1\right)}{2J\left(J+1\right)} \right] \\ & + g_s \left[ \frac{J\left(J+1\right) - L\left(L+1\right) + S\left(S+1\right)}{2J\left(J+1\right)} \right]. \end{aligned} \tag{2.8}$$

It is worth noting that the above argument only holds for a free ion; inserting the ion into a crystal structure changes the energies of different $n$, $l$, $m_l$ combinations due to different local symmetries and the shape of the different orbitals. This can remove some degeneracy and hence change the occupation of different states. Continuing the example of $Co^{2+}$, one finds that in a tetrahedral environment, orbital quenching (where $L = 0$ is the lowest energy state) is observed, however it is not observed in octahedral environments. Despite these complications, and with many details which have not been covered here, we have reached the main result of this section of the thesis: the magnetic moment of a system arises from the angular momentum (both intrinsic and actual) of the electrons, with contributions only occurring from partially filled subshells. The details of accurately predicting the expected orbital and spin angular momenta is somewhat complicated; fortunately we do not need those details for this thesis.

Before moving on, it is worth making a couple of short observations. Firstly, whilst we have predominantly restricted our discussion to electrons in a material, similar arguments exist for the nucleons in an atom, and indeed the nucleus can have a magnetic moment. These moments are typically much smaller than those arising from electrons, and in the experiments discussed in this thesis, a small external magnetic field is sometimes applied to overcome any effects from these nuclear moments. Secondly, we have considered a very basic picture of an atom in isolation, hardly considering any interaction between different electrons. Of course, that is not the situation that occurs in reality. One particularly acute example of this is in metallic systems, where we have free electrons that are not well bound to a single nucleus; the magnetism in these materials is often harder to understand intuitively, however the same result holds, and unpaired electrons are the dominant contribution to the magnetism.

## 2.2 Magnetic interactions

Having considered the origin of the magnetic moment, we now turn to the interaction between this moment and either an external magnetic field, or other magnetic moments. To do so, we will look at the contribution to the Hamiltonian of different interactions.

### 2.2.1 Interaction with a magnetic field

We start by considering the energy of an atom in a magnetic field. One can show that the contribution to the Hamiltonian because of the interaction between the electrons and the external magnetic field $\boldsymbol{B}$ (neglecting interaction between the orbital and spin angular momenta, which is covered later) is given by

$$\begin{aligned}\hat{\mathcal{H}}_{\boldsymbol{B}} &= \frac{\mu_{\mathrm{B}}}{\hbar}\left(\boldsymbol{L} + g\boldsymbol{S}\right)\cdot\boldsymbol{B} + \frac{e^2}{8m_{\mathrm{e}}}\sum_i \left(\boldsymbol{B}\times\boldsymbol{r}_i\right)^2, \\ &= \hat{\mathcal{H}}_{\mathrm{para}} + \hat{\mathcal{H}}_{\mathrm{dia}},\end{aligned} \tag{2.9}$$

where we sum over all the electrons in the atom. We can identify these two terms as leading to either paramagnetic or diamagnetic behaviour. The diamagnetic contribution occurs in all atoms, regardless of electron state occupation, and leads to a situation where the induced magnetisation aligns antiparallel to the applied magnetic field. However, if there is a paramagnetic contribution, as in all materials studied in this thesis, the diamagnetic effect can be typically neglected.

The paramagnetic contribution is often known as the Zeeman effect, and the energy contribution can be written as $E = -\boldsymbol{\mu}\cdot\boldsymbol{B}$. If this is the dominant contribution to the Hamiltonian, the material will be described as paramagnetic, and, in the absence of an applied field, will exhibit disordered moments with no correlation between neighbours, and no net magnetisation. As the magnitude of the applied field is increased, the moments will start to align with the applied field, until at a sufficiently high field all the moments have aligned and we describe the system as having reached saturation.

An analogous situation where paramagnetism is the most relevant description of the system is at sufficiently high temperatures (above a critical temperature

$T_c$) such that the thermal energy dominates over any energy terms arising due to interactions between magnetic moments. In this regime the thermal fluctuations will prevent any long-range magnetic ordering due to interaction between the magnetic moments, with no net magnetisation. There are differences to the susceptibility (that is, the change in magnetisation with applied field) that depend on the terms appearing in the Hamiltonian.

### 2.2.2 Exchange interaction

The long-range ordered state of a magnet normally occurs due to the presence of an exchange interaction between electrons. The most common example of this is direct exchange interaction, and it is this which we explore in the following. This interaction exists because electrons are fermions, and hence the wavefunction describing a collection of electrons must be antisymmetric under the exchange of two of them. Considering a 2-electron system, we can write the total wavefunction as a product of single electron states. If we take the first electron to be in state $\psi_a(\boldsymbol{r}_1)$ and the second to be in state $\psi_b(\boldsymbol{r}_2)$, then we have two possible options for the total wavefuction,

$$\begin{aligned} \Psi_{\mathrm{S}} &= \frac{1}{\sqrt{2}} \left[\psi_a(\boldsymbol{r}_1)\psi_b(\boldsymbol{r}_2) + \psi_a(\boldsymbol{r}_2)\psi_b(\boldsymbol{r}_1)\right] \chi_{\mathrm{S}}, \\ \Psi_{\mathrm{T}} &= \frac{1}{\sqrt{2}} \left[\psi_a(\boldsymbol{r}_1)\psi_b(\boldsymbol{r}_2) - \psi_a(\boldsymbol{r}_2)\psi_b(\boldsymbol{r}_1)\right] \chi_{\mathrm{T}}, \end{aligned} \tag{2.10}$$

where the spin state is given by $\chi_{\mathrm{S,T}}$ in each case. These two states are either singlet ($S = 0$, antisymmetric spin state), or triplet ($S = 1$, symmetric spin state).

As these cases have different spin configurations, it is informative to consider the energy difference between them to discover if there is any preference for the spin alignment. The energy of the singlet state is $E_{\mathrm{S}} = \int \Psi_{\mathrm{S}}^* \hat{\mathcal{H}} \Psi_{\mathrm{S}} \, \mathrm{d}\boldsymbol{r}_1 \, \mathrm{d}\boldsymbol{r}_2$, with a similar expression for the triplet state. The energy difference (assuming correct normalisation of the spin states) is therefore

$$E_{\mathrm{S}} - E_{\mathrm{T}} = 2 \int \psi_a^*(\boldsymbol{r}_1)\psi_b^*(\boldsymbol{r}_2)\hat{\mathcal{H}}\psi_a(\boldsymbol{r}_2)\psi_b(\boldsymbol{r}_1) \, \mathrm{d}\boldsymbol{r}_1 \, \mathrm{d}\boldsymbol{r}_2. \tag{2.11}$$

With this result we have related the electronic structure to the energy difference between the two different states, which in principle means the exchange interaction is known, as long as the Hamiltonian is known. We can make progress by assuming the Hamiltonian can be described by the dot product of the spin of the two particles, and that terms in $\boldsymbol{S}_1 \cdot \boldsymbol{S}_2$ are all one needs to describe the total energy change of the system. By considering the eigenvalues of the combination of these two moments, one finds that for the singlet state $\boldsymbol{S}_1 \cdot \boldsymbol{S}_2 = -3/4$, whereas for the triplet state $\boldsymbol{S}_1 \cdot \boldsymbol{S}_2 = 1/4$. One can therefore write $\hat{\mathcal{H}} = \frac{1}{4}(E_\mathrm{S} + 3E_\mathrm{T}) - (E_\mathrm{S} - E_\mathrm{T})\boldsymbol{S}_1 \cdot \boldsymbol{S}_2$, which reduces to give the relevant energy for the appropriate value of $\boldsymbol{S}_1 \cdot \boldsymbol{S}_2$. Using the result of Eqn. 2.11, one can write the spin-dependent part of the Hamiltonian as

$$\begin{aligned} \hat{\mathcal{H}}^{\mathrm{spin}} &= -2 \int \psi_a^*(\boldsymbol{r}_1)\psi_b^*(\boldsymbol{r}_2)\hat{\mathcal{H}}\psi_a(\boldsymbol{r}_2)\psi_b(\boldsymbol{r}_1)\,\mathrm{d}\boldsymbol{r}_1\,\mathrm{d}\boldsymbol{r}_2 \boldsymbol{S}_1 \cdot \boldsymbol{S}_2 \\ &= -2J\boldsymbol{S}_1 \cdot \boldsymbol{S}_2, \end{aligned} \tag{2.12}$$

where we have defined the exchange constant $J$ in terms of the electronic structure. From this result it is trivial to see that if $J > 0$, the triplet state (i.e. aligned spins) is preferred, whereas if $J < 0$, the singlet state (i.e. anti-aligned spins) is preferred.

This result is generalisable to systems of arbitrarily many moments such that

$$\hat{\mathcal{H}} = -\sum_{ij} J_{ij}\boldsymbol{S}_i \cdot \boldsymbol{S}_j, \tag{2.13}$$

where the factor of two has disappeared to account for the double counting of each spin-pair. We can see from Eqn. 2.12 that the magnitude of $J_{ij}$ will depend on the overlap of the single-particle wavefunctions for moments $i$ and $j$. This means that moments that are further spatially separated will interact less. Thus, it is often sufficient to consider only the nearest neighbour moments, and take them all to have a single exchange parameter $J$.

The exchange parameter $J$ sets the energy scale of interactions in the system, and therefore has important consequences. (1) The sign of $J$ determines the ordering of the system, as already discussed. A positive $J$ leads to ferromagnetic

order (where all the moments align), whereas a negative $J$ leads to antiferromagnetic order (where neighbouring moments anti-align). (2) We discussed in the previous section a critical temperature $T_\mathrm{c}$, above which the thermal energy dominates over interactions between the moments. Typically being the dominant energy term in the Hamiltonian of a magnetic system, it is often the case that $k_\mathrm{B}T_\mathrm{c} \sim J$.

There are various different mechanisms that can mediate the exchange interaction, all requiring the overlap of various single-particle wavefunctions, whether that is directly between two moments, or through intermediary particles. A good example of this is superexchange, where despite there being no overlap of the magnetic ion orbitals, there is still an exchange interaction mediated through a non-magnetic ion. The details of these are beyond the scope of this thesis, however it is useful to know that the details of which mechanism leads to the exchange interaction can change the properties of the system.

### 2.2.3 Spin-orbit interaction

Up to this point, we have assumed that the orbital and spin angular momentum are effectively independent of each other, however in reality they do interact, and this has effects on the energy levels of the system. To see why these two angular momentums interact, we will consider an electron orbiting a nucleus from the rest frame of the electron, where the nucleus is orbiting the electron. The nucleus gives rise to a magnetic field at the electron, $\boldsymbol{B} = \boldsymbol{\mathcal{E}} \times \boldsymbol{v}/c^2$, where the electric field $\boldsymbol{\mathcal{E}} = -(\boldsymbol{r}/r)\,\mathrm{d}V(r)/\,\mathrm{d}r$. We have already seen that a magnetic moment, such as that on the electron, interacts with a magnetic field, so we can write that the spin-orbit interaction contribution to the Hamiltonian is

$$\begin{aligned}\hat{\mathcal{H}}^{\mathrm{SO}} &= -\frac{1}{2}\boldsymbol{\mu}\cdot\boldsymbol{B} \\ &= -\frac{1}{2}\left(\frac{g_s e\hbar\boldsymbol{S}}{2m_\mathrm{e}}\right)\cdot\left(-\frac{\boldsymbol{r}\times\boldsymbol{v}}{c^2 r}\frac{\mathrm{d}V(r)}{\mathrm{d}r}\right).\end{aligned} \tag{2.14}$$

In this, we have used the fact that there is no orbital angular momentum of the electron (as it is stationary in this rest frame), hence the magnetic moment arises

purely from the spin. The prefactor of 1/2 is a relativistic correction that appears when one does the full calculation using Dirac's equation. As $\hbar \boldsymbol{L} = m_\mathrm{e} \boldsymbol{r} \times \boldsymbol{v}$,

$$\hat{\mathcal{H}}^{\mathrm{SO}} = \frac{g_s e \hbar^2}{2 m_\mathrm{e}^2 c^2 r} \frac{\mathrm{d}V(r)}{\mathrm{d}r} \boldsymbol{S} \cdot \boldsymbol{L}, \tag{2.15}$$

which demonstrates that there is an interaction between the spin and orbital angular momentum. This result generalises to many-particle systems. This interaction is often small compared to other interactions in the system, however has some important consequences. One of these is single-ion anisotropy, which sets a preference for a material to be magnetised in a certain direction due to both coupling between the orbital motion of the electrons and the electric field arising from nearby ions (the crystal electric field), and due to interaction between magnetic dipoles. Another effect of spin-orbit coupling is the Dzyaloshinskii-Moriya interaction.

### 2.2.4 Dzyaloshinskii-Moriya interaction

An interesting consequence of the spin-orbit interaction is revealed when second-order perturbation theory is applied [15]; the appearance of another interaction termed the Dzyaloshinskii-Moriya (DM) interaction, or antisymmetric exchange. This physical origin of this interaction can be understood by considering either the spin-orbit or exchange interaction raising a particular magnetic moment out of its ground state, before the other interaction returning it. We will not present a derivation here, merely state that the contribution to the Hamiltonian is

$$\hat{\mathcal{H}}^{\mathrm{DM}} = \sum_{ij} \boldsymbol{D}_{ij} \cdot (\boldsymbol{S}_i \times \boldsymbol{S}_j), \tag{2.16}$$

where the interaction strength is given by $\boldsymbol{D}_{ij}$. Similar arguments as for the exchange interaction can be applied here, replacing $\boldsymbol{D}_{ij}$ with $\boldsymbol{D}$ for nearest neighbours only.

The result of the cross product between moments means that this contribution to the Hamiltonian is minimised when adjacent moments align perpendicularly, in contrast to the parallel or antiparallel alignment that minises the exchange

interaction contribution. This will set up a competition between energy terms which is key to the existence of the complex magnetic textures we explore in this thesis. The parameter $\boldsymbol{D}$ is zero for a large number of crystal symmetries, only being non-zero when the crystal structure lacks a centre of inversion symmetry. This symmetry can be achieved in two different ways, either at an interface between two different materials (which is clearly not inversion symmetric), or in certain crystal classes. The former of these is the mechanism behind the stabilisation of topological magnetism such as skyrmions in thin film systems which is the focus of much current work, but will not be focused on in this thesis. We will instead concentrate on materials where the crystal symmetry gives rise to a DM interaction throughout the bulk of the material; different crystal symmetries give rise to different orientations of the $\boldsymbol{D}$ vector, which changes the nature of the topological object that is formed and will be discussed later.

In many of the materials studied in this thesis the static magnetic structure can be understood by restricting the Hamiltonian to have purely exchange and DM interaction terms. To start, we will explore a test system of a one-dimensional chain of Heisenberg moments (that is, they can point in any direction) of unit magnitude with the Hamiltonian

$$\hat{\mathcal{H}} = -J \sum_{ij} \boldsymbol{S}_i \cdot \boldsymbol{S}_j + \boldsymbol{D} \cdot \sum_{ij} \boldsymbol{S}_i \times \boldsymbol{S}_j, \tag{2.17}$$

where we set $J > 0, D > 0$ for nearest neighbour moments, and $J = D = 0$ otherwise. Without loss of generality, we fix $\boldsymbol{S}_0 = \hat{\mathbf{k}}$ to lie along the $z$-direction, and assign the other moments to be positioned along the $x$-axis. We will pick $\boldsymbol{D} = D\,\hat{\mathbf{i}}$. The second moment will point in a direction defined in spherical polars, i.e. $\boldsymbol{S}_1 = \sin\theta\cos\phi\,\hat{\mathbf{i}} + \sin\theta\sin\phi\,\hat{\mathbf{j}} + \cos\theta\,\hat{\mathbf{k}}$. Considering the energy of the first two moments, we have

$$E = -J\cos\theta - D\sin\theta\sin\phi. \tag{2.18}$$

Minimising with respect to $\phi$ tells us that $\phi = \pi/2$, whereas minimising with respect to $\theta$ gives $\theta = \arctan(D/J)$. Generalising to the rest of the moments, we can see that we have a system of moments that rotate in the $yz$-plane as you

travel along the $x$-direction, with the rotation between each moment depending on the relative size of $J$ and $D$; a bigger relative $D$ interaction will lead to a more dramatic rotation, as one would expect. What we have found is helical ground state, which looks like a continuous Bloch domain wall. If each moment is separated by $a$ (and assuming the angle between each moment is small), the total period of this helix will be $2\pi aJ/D$. All of the materials studied in detail in this thesis have a helical ground state that occurs due to competition between the exchange and DM interaction.

It is worth noting that there are other possible interactions between magnetic moments that have not been discussed here, many of which are important in certain systems. In all the materials studied in this thesis the behaviour can be well understood from consideration of the interactions discussed above alone.

## 2.3 Topological magnetism

So far we have discussed the origin of magnetic moments, and by exploring the different magnetic interactions, have seen some possible arrangements of them. This thesis focuses on materials with complex arrangements, which fall into the broad class of topological magnetic states, that is configurations of the magnetic moments which have some form of topological property. In absence of an alternative reference, the material in the following can be found in Ref. [6]. It incorporates some material published in Ref. [16].

Topology is the study of objects under continuous deformations such as stretching, excluding actions that would break the material in some way (opening/closing holes, tearing/glueing together etc.). In general, this means that those who study topology are interested in the overall shape of an object, rather than worrying about the precise details such as distances or angles between points (which would be the geometry). We can therefore define objects that are homeomorphic to each other as those which are topologically equivalent, even if they are geometrically very different. The classic example of this is the mug and donut; both of these objects have a single hole (the handle in the case of the mug), hence are

homeomorphic to each other. If one made a mug out of a stretchable clay, one could continuously mould it into the donut without adding or removing any new holes, therefore following the rules above.

Returning to magnetic moments, a topological magnetic state would be some configuration of magnetic moments that is defined in terms of some countable topological feature equivalent to the number of holes in the mug/donut example above, whilst not concerning itself with the distance between the topological features. What this topological feature is will depend on two things: the dimensionality of the system ($D$), and the dimensionality of the magnetic moments ($d$).

### 2.3.1 Kinks ($D = 1$, $d = 1$)

We will start by considering the simplest case, an infinite one dimensional chain ($D = 1$) of Ising moments ($d = 1$), that is moments that can point either up or down. We will assume a Hamiltonian that only has an exchange interaction $\hat{\mathcal{H}} = -J \sum_{ij} \boldsymbol{S}_i \cdot \boldsymbol{S}_j$, $J > 0$. The most energetically favourable configuration would be all moments pointing up, or all moments pointing down; these ground states are degenerate. Only slightly higher in energy would be the configuration where we introduce a kink, say all the moments on the left pointing down, and all the moments on the right pointing up, as shown in Fig. 2.1(a). This number of kinks is the countable topological feature in this situation, as no continuous deformation of the one-kink texture can transform the system to one where there is no kink. We could therefore classify this state by a topological charge, $N = 1$. Compared to the ground state, this configuration will only be slightly higher in energy, however removing the kink takes a semi-infinite amount of energy (requiring a half-infinite number of moments to be flipped). This is often referred to as topological protection, as (in an infinite system) it would take an unfeasibly large amount of energy to remove this kink. This simple picture demonstrates why the topology of the magnetic configuration is so important; very subtle changes to the configuration can have dramatic energy costs.

The kink we have introduced can be thought of as an excitation or particle, as it behaves like a single object. Consider the kink as the two moments that are anti-aligned; if we flip both the right-hand moment in the kink, and the next moment along in the chain, the kink has effectively moved to the right, but the total energy of the system remains unchanged. The kink can be moved along the chain for no (or in reality, very little) energy cost, acting as an object. (This property is a reason that topological magnetism is of great interest for low-energy magnetic memory applications.) In real systems, the movement of these topological objects is how one avoids the semi-infinite energy cost to destroy them. If the chain is finite, one can simply move the kink off the end of the chain for the small energy difference between the states. It is therefore important to realise that despite the theoretical property of topological protection, this may not manifest in real systems.

### 2.3.2 Vortices ($D = 2$, $d = 2$)

If we increase the dimension of both the space and the moments, we get a plane of moments that can point in any direction in that plane. Assuming the same Hamiltonian as before, the ground state will see all moments pointing in the same direction, with no preference for in-plane angle. Once again we can identify a topological feature similar to the kink in the previous example; in this case a vortex. This vortex is a point where all moments point radially from the centre [Fig. 2.1(b)]. As all the moments are roughly aligned, this is close to minimising the energy, with the largest energy cost being at the vortex core. Similar to the previous example, this vortex can be thought of as an excitation in its own right.

If we were to rotate all the moments in the vortex by a fixed angle, we would not have change the topological properties (as this is a continuous deformation). We can therefore again classify this vortex by a topological, or winding, number $N = 1$, which defines the number of times the moments wind round in one complete path around the core. We can further create objects with different $N$, for example, if the moments underwent two complete rotations on the path around

the core, this would be $N = 2$. If the moments rotate once in the opposite sense to the path around the core, we would define this as an anti-vortex with $N = -1$. We see that one can define a variety of different topological objects, none of these can be continuously transformed into another, and may have different properties.

There is a key difference to the $D = 1$, $d = 1$ case here, and that is the energy cost. Whilst the cost goes down as you get further from the vortex core, the moments infinitely far away from the core are still affected by the existence of the vortex, meaning that there is an infinite energy cost associated with the existence of the vortex. Consequently, this object will not exist in an infinite system in the absence of other interactions. In reality, there are a few reasons these objects can exist: (1) samples are finite in size, (2) two objects with opposite topological charge could exist in the same sample (the Berezinskii-Kosterlitz-Thouless transition), or (3) other interactions change the energetics of the system.

### 2.3.3 Hedgehogs ($D = 3$, $d = 3$)

Let us once again increase the dimension of both the space and the moments, leading to moments that can point in any direction at any point in space. The topological objects here are once again points where the moments point out from the core, but this time in three-dimensions. This configuration is shown in Fig. 2.1(c). They are often called hedgehogs owing to their similarity to the creature when it is rolled up into a ball. This situation is very similar as for the vortex in $D = 2$, $d = 2$, including the argument that the object is unlikely to exist due to the infinite energy cost.

It is useful to introduce a formal definition of the winding number at this stage, as it has become more difficult to identify the correct value by eye. For a set of moments whose direction is given by $\boldsymbol{m}$, we define the winding number to be

$$N = \frac{1}{4\pi} \int \int \boldsymbol{m} \cdot \left( \frac{\partial \boldsymbol{m}}{\partial \theta} \times \frac{\partial \boldsymbol{m}}{\partial \phi} \right) \mathrm{d}\theta \, \mathrm{d}\phi, \tag{2.19}$$

where $\theta$ and $\phi$ are the normal angles in spherical polar coordinates. Note that other choices of coordinate system are acceptable, however this is the convention.

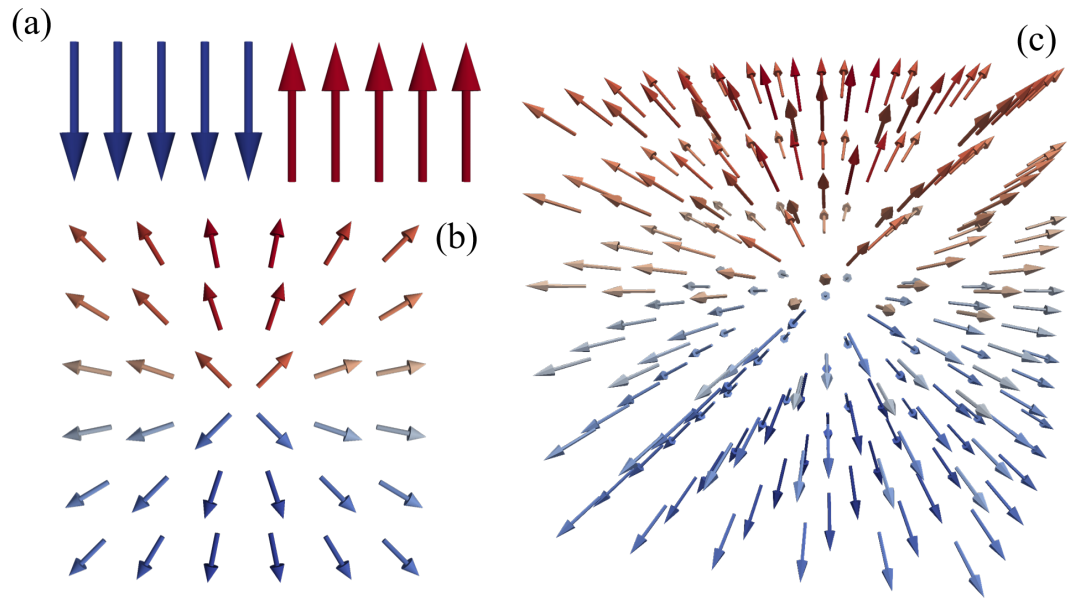


**Figure 2.1:** Different topological objects for the case where $D = d$. Objects shown are a (a) kink, (b) vortex, or (c) hedgehog.

### 2.3.4 Skyrmions ($D = 2$, $d = 3$)

Having so far explored situations where $D = d$ we have found that, excluding $D = d = 1$, these topological objects are very unlikely to exist. It would be reasonable to ask whether these topological objects are ever likely to be found in real materials. The answer is yes: we will discuss the first of these objects, and the one which a large proportion of this thesis is concerned with, now.

In $D = 2$, $d = 3$ we constrain the moments to lie on a 2D plane, but allow them to point in any direction. The topological object is called a skyrmion, and can be seen to be a lower-dimensional analogue of the hedgehog; a mathematical operation known as a stereographic projection converts the hedgehog into a skrymion. To visualise this operation, take the moment vertically above the centre of the hedgehog, and put it in the centre of your skyrmion; as you increase your angle away from the top position (i.e. change the latitude on the sphere), the moments you find are placed in the skyrmion at an ever increasing radial distance. The bottom of your sphere defines a set moment pointing in the opposite direction to the moment at the top, and these wrap around the outside of the

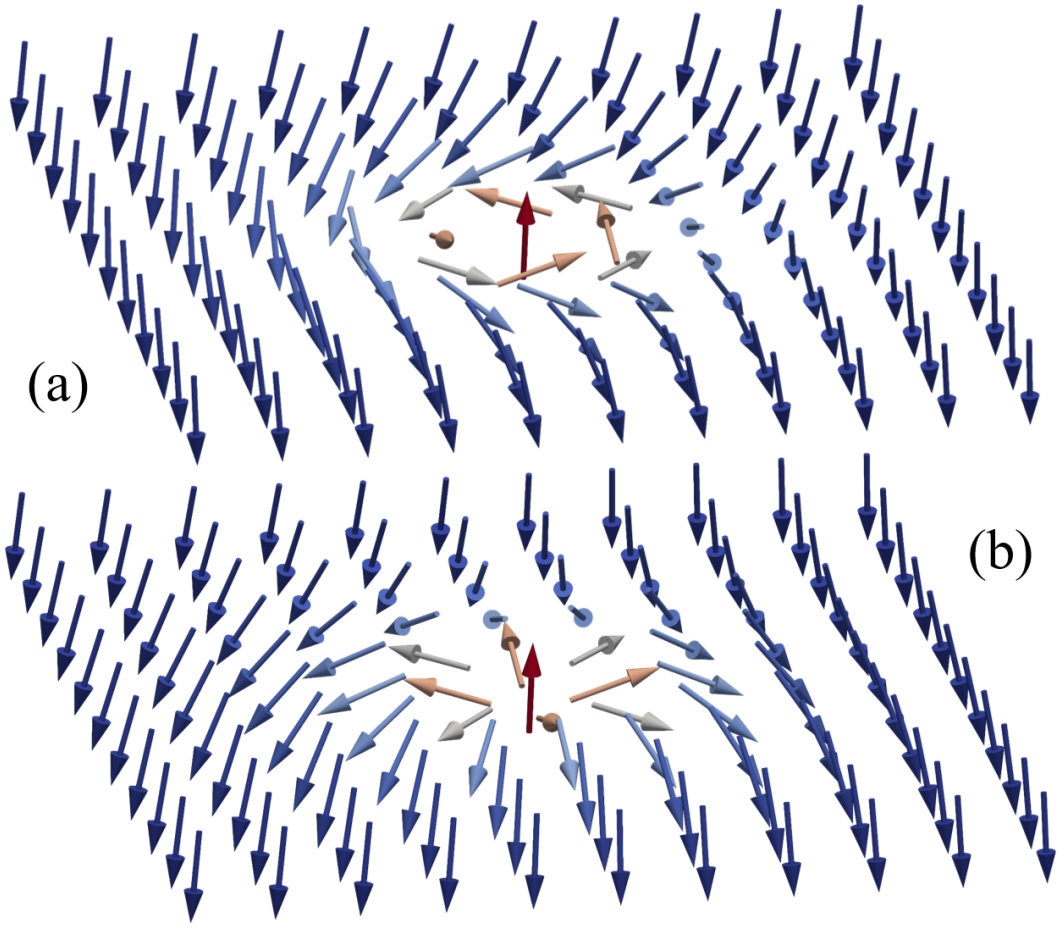


**Figure 2.2:** The topological object with winding number $N = 1$ for $D = 2$, $d = 3$: the skyrmion. Two topologically equivalent alternatives are shown, commonly referred to as the (a) Bloch or (b) Néel skyrmion.

skyrmion, defining the edge of the skyrmion. This highlights a key point; given the skyrmion object has a finite size, it also has a finite energy cost, and therefore can be expected to be stabilised in nature. Two different forms of an isolated skyrmion texture with $N = 1$ are shown in Fig. 2.2.

As in the case of the hedgehog, to understand the topological properties of the skyrmion it is helpful to define the winding number. The equation is almost identical to Eqn. 2.19, just with a coordinate transformation relevant for the reduction in dimension,

$$N = \frac{1}{4\pi} \int \int \boldsymbol{m} \cdot \left( \frac{\partial \boldsymbol{m}}{\partial x} \times \frac{\partial \boldsymbol{m}}{\partial y} \right) \mathrm{d}x \, \mathrm{d}y. \tag{2.20}$$

It is possible to have $N \neq 1$ configurations, the most commonly discussed ones are the antiskyrmion ($N = -1$), and biskyrmion ($N = 2$), however this thesis focuses on $N = 1$ objects. Although topologically equivalent, there are two different common forms of $N = 1$ skyrmion, both of which are shown in Fig. 2.2. The first is the Bloch skyrmion, where as you cross the skyrmion radially the moments form a Bloch domain wall, and the second is the Néel skyrmion, named for equivalent reasons. These two configurations are related by a global change of $\pi/2$ in the phase of the moments.

Skyrmions can be found in real materials due to the competition of two different interactions, most commonly exchange and DM. The competition leads to complex magnetic textures, particularly under the application of an external magnetic field. Materials that host skyrmions can be broadly split into two categories: (1) materials with interfacial DM interaction, typically thin-film or similar systems, and (2) materials with interactions throughout their bulk that give rise to skyrmions.

We will first discuss (1). In magnetic thin films that already possess an exchange interaction, it is possible to manufacture the system to stabilise skyrmions by introducing an interfacial DM interaction. The origin of this interaction is clear; the DM interaction occurs when there is a lack of inversion symmetry, a condition which is automatically satisfied at the boundary between two different layers. This DM interaction, which only occurs near the surface, leads to the stabilisation of individual skyrmions, typically in a seemingly random pattern. These skyrmions can be moved around for very little energy cost, making them potentially exciting for computer memory applications [8, 9, 10]. Further, the way they respond to changes in current and magnetic field leads to potential usage in unconventional computing [11]. Lots of research is ongoing in this area [4, 17], however this class of skyrmion will not be the focus of this thesis.

In case (2), the crystal symmetry gives rise to competing interactions throughout the bulk of the material, which stabilises skyrmions throughout the system. There are multiple different possibilities for interactions, each of which gives rise

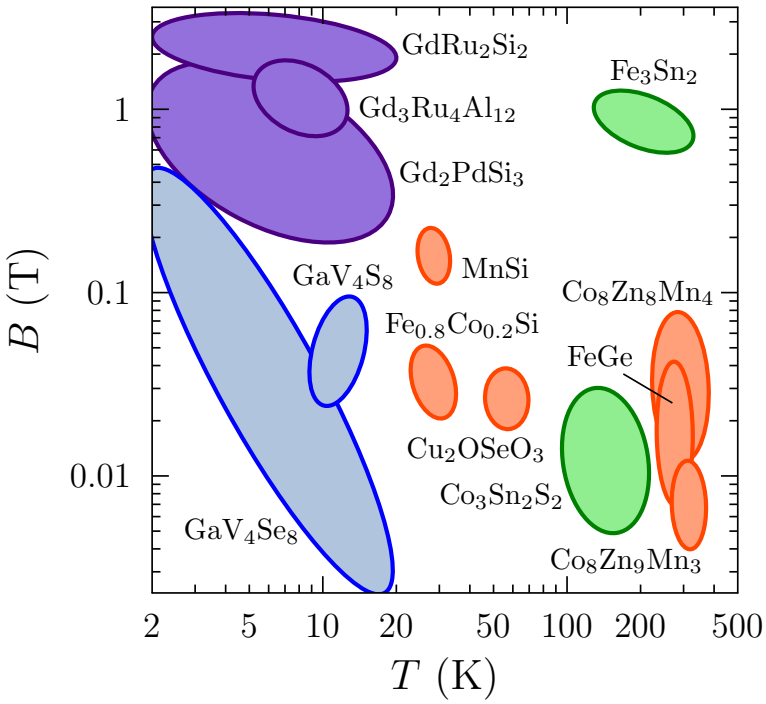


**Figure 2.3:** Location of the skyrmion phase in the $B$-$T$ phase diagram of bulk materials. Stabilisation of the skyrmion phase occurs through various mechanisms: (i) competition between the exchange and Dzyaloshinskii–Moriya interactions, leading to a Bloch (orange) or Néel (blue) skyrmion lattice, (ii) competition between exchange and uniaxial anisotropy (green), (iii) geometric frustration from the interplay of RKKY and four-spin interactions (purple). Phase boundaries taken from Refs. [3, 18, 19, 20, 21, 22, 23, 24, 25, 26, 27, 28, 29].

to different behaviours. The location of the skyrmion phase in the $B$–$T$ phase diagram of various materials, with the stabilisation mechanism associated with each, is shown in Fig. 2.3.

In this thesis we restrict our discussion to materials where there is competition between exchange and bulk DM interaction. To understand the magnetic textures this leads to, it is helpful to introduce a description of $q$-vectors, which are vectors in reciprocal space that point in the direction of change of the magnetic moment. This is a continuum approach, where we think about the field that represents the moment at a specific location in space, rather than individuals magnetic moments as we have discussed so far. We write a general magnetic structure as

$\boldsymbol{m}(\boldsymbol{r}) = \sum_{\boldsymbol{q}} \boldsymbol{m}_{\boldsymbol{q}} \exp(i\boldsymbol{q}\cdot\boldsymbol{r})$, where there can be as many $q$-vectors as needed. For the helical state already shown to be the ground state in a system containing just exchange and DM interactions, one $q$-vector is required (which makes sense, as the orientation of the magnets moments changes in one-dimension only). The magnitude of this $q$ vector $|\boldsymbol{q}| = 2\pi/L$, where $L$ is the periodicity of the helical state. For magnetic moments of magnitude $m$ the helical state can be defined in terms of two unit vectors, $\hat{\boldsymbol{a}}$ and $\hat{\boldsymbol{b}}$, which form an orthonormal set with $\boldsymbol{q}/|\boldsymbol{q}|$. We find that

$$\boldsymbol{m}_{\mathrm{H}}(\boldsymbol{r}) = m\left[\cos(\boldsymbol{q}\cdot\boldsymbol{r})\,\hat{\boldsymbol{a}} - \sin(\boldsymbol{q}\cdot\boldsymbol{r})\,\hat{\boldsymbol{b}}\right], \tag{2.21}$$

where $\boldsymbol{q}/|\boldsymbol{q}| = \hat{\boldsymbol{a}} \times \hat{\boldsymbol{b}}$ [30].

Returning to skyrmions, it is immediately obvious that a single $q$-vector is going to be insufficient to describe the magnetic texture (as the magnetic moments change orientation in two-dimensions). It turns out that the so called "triple-$q$" model well captures the topology of a skyrmion. (Although the triple-$q$ model does not minimise the free energy of the system, it is a very good approximation in many situations, and is the description employed in this thesis.) In this model, three $q$-vectors are needed such that $\boldsymbol{q}_1 + \boldsymbol{q}_2 + \boldsymbol{q}_3 = 0$. The triple-$q$ model is therefore defined as $\boldsymbol{m}(\boldsymbol{r}) = \boldsymbol{m}_{\mathrm{Sk}}(\boldsymbol{r})/|\boldsymbol{m}_{\mathrm{Sk}}(\boldsymbol{r})|$, where $\boldsymbol{m}_{\mathrm{Sk}}(\boldsymbol{r}) = \sum_{i=1}^{3} \boldsymbol{m}_{\mathrm{H}}(\boldsymbol{r}, q_i)$. Unlike the isolated, singular skyrmions shown in Fig. 2.2, this equation defines a skyrmion lattice of hexagonally packed (i.e. space filling) skyrmions. In bulk DM interaction systems, these skyrmions are typically 5–100 nm in size [31]. In the third dimension, the two-dimensional skyrmions sit on top of each other, defining skyrmion tubes throughout the material [32, 33]. These tubes can be considered the analogy of many similar structures in condensed matter physics [34], perhaps most obviously the vortex lines in type-II superconductors [35]. This configuration of skyrmion tubes is the energetically favourable skyrmion state in these systems.

Other magnetic states observed in these materials can be similarly defined in terms of relevant $\boldsymbol{q}$-vectors. The most common variant is the conical phase, which is very similar to the helical phase, but with a component of the magnetic

moments in the direction of the applied field.

With a mathematical description of the states in these materials, we return to the question of stability. It is possible to show, using Derrick's theorem [36], that the energy of the DM interaction term for the skyrmion state grows as $L^2$; as this is a positive energy term it would imply that skyrmions are not stable (much as vortices and hedgehogs). This also matches our understanding that the helical state (not skyrmions) is the magnetic ground state. The picture changes, however, when an external magnetic field is applied. The Zeeman contribution to the Hamiltonian also scales as $L^2$, but this time the energy term is negative. Energetically it is therefore only possible to stabilise skyrmions as the equilibrium state in an applied field; in fact, in systems where exchange and DM interactions dominate, this is found to be true experimentally [3, 18, 19, 20, 21, 22, 23]. Typically, the skyrmion lattice state is found to be in equilibrium in a small pocket of the $B$–$T$ phase diagram just below $T_c$ under application of an external magnetic field.

An important distinction at this point is the difference between the Bloch and Néel skyrmion. Why is the skyrmion that is stabilised different in different systems, even though the dominant energy terms are the same? The answer is due to the vectorial nature of $\boldsymbol{D}$; different orientations favour the twists in the skyrmion to be oriented differently. As we have already discussed, the direction of $\boldsymbol{D}$ depends on the crystal symmetry, and therefore sets the type of skyrmion one can expect to find in a particular material. In chiral magnets one finds Bloch skyrmions, whereas in polar magnets Néel skyrmions are preferred.

There are multiple experimental techniques that can observe skyrmions [31, 37]. In real space Lorentz Transmission Electron Microscopy is the most common technique [38], with x-ray holography being more recently employed [39, 40]. In reciprocal space, the skyrmion lattice forms a hexagonal pattern of diffraction peaks which are commonly observed with small angle neutron scattering [3] or x-ray techniques [41, 42].

So far we have restricted our discussion to the static structure of magnetic

moments. Of course, there are myriad dynamic effects at play as well, some of which are specific to the topological object formed. Much of the research into the dynamics of skyrmions is concerned with their translation through the material, primarily due to the possibility of application to computer memory technologies [31, 37], however for this thesis it is beneficial to be aware of the lowest-energy excitations of the skyrmion that occur without an overall translation. These single skyrmion dynamics are modes of the object, and in real materials typically have frequencies in the gigahertz regime [43]. All of these modes involve motions of the core of the skyrmion. The lowest energy mode corresponds to a counter-clockwise rotation of the core of the skyrmion. At approximately twice this energy, a skyrmion breathing mode, where the core cyclically expands and shrinks, is found, with a clockwise rotation only slightly higher in energy. All of these modes are shown diagrammatically in Fig. 2.4. These collective motions of the magnetic moments are detectable with various different experimental techniques, most notably microwave resonance experiments [44]. The reduction in frequency of the skyrmion modes as the temperature approaches $T_c$ is a mechanism discussed in this thesis as a possible explanation for some of the observed behaviour, see App. A.

### 2.3.5 Solitons ($D = 1$, $d = 3$)

The final combination of dimensions we will consider in this chapter is $D = 1$, $d = 3$. In this situation we constrain the magnetic moments to a line, allowing them to point in any direction. If we consider the same Hamiltonian again, with just exchange and DM interactions, we can see that the ground state is still the helical configuration previously observed. As we saw with skyrmions however, there are however more interesting topological states that form upon application of an external magnetic field.

When adding a Zeeman term to the Hamiltonian there is a preference for the magnetic moments to align with the magnetic field. If this field is applied perpendicular to the chain of magnetic moments, regions of field-aligned moments

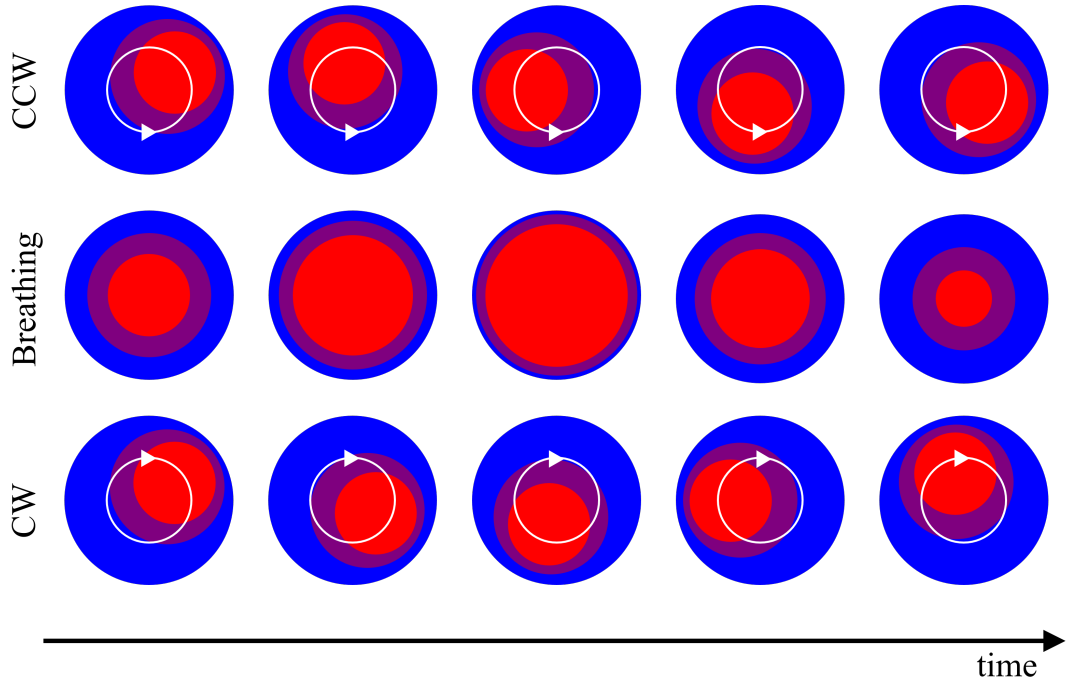


**Figure 2.4:** A diagrammatic representation of the lowest energy skyrmion modes, showing the motion of the core of the skyrmion (where the magnetic moments point out of the page) with respect to the overall skyrmion. The shown modes are the counter-clockwise (CCW) rotation, breathing mode, and clockwise (CW) rotation.

**Figure 2.5:** Two solitons, a topological object for $D = 1$, $d = 3$. A soliton is defined as the moments that are rotating, separated from other solitons by regions of aligned moments.

will appear in between the twists integral to the helical state, as seen in Fig. 2.5. We have effectively separated out these twists, which now become topological objects in their own right. We call these objects magnetic solitons. (It is worth noting that the term "soliton" is also used to refer to all topological objects, for example a skyrmion is a soliton in $D = 2$, $d = 3$. For the avoidance of confusion, when solitons are referred to in this thesis, we mean the $D = 1$, $d = 3$ topological object.)

Solitons are the reduced-dimensional analogue to skyrmions, and share many of the same properties. In particular, they form a lattice in bulk materials, however their periodicity is dependent on the magnitude of the external field. The way solitons manifest can be changed by tilting the magnetic field towards the chain of moments, leading to a tilted soliton lattice. If the field points along the chain of moments, no solitons will form.

Solitons, in comparison to skyrmions, are found to exist in very few materials. This is likely due to the additional requirements for their formation, in addition to the right crystal symmetry for appropriate exchange and DM interactions, one needs to find a system that has magnetic moments that are relatively well isolated into one-dimensional chains. So far the best studied example of a soliton-hosting material, and one that is studied in this thesis, is $Cr_{1/3}NbS_2$ [45]. In this material the solitons exist over a large region of the $B$–$T$ phase diagram below $T_c$.

# Chapter 3

# Techniques

In this thesis we apply various different techniques, be they experimental or theoretical, to the study of materials hosting topological magnetic states. This chapter serves as an introduction to those that are used most frequently. The chapter is dominated by the discussion of muon-spin spectroscopy ($\mu$SR), this being the technique that is most commonly used in this thesis to study the physics in the materials of interest.

## 3.1 Muon-spin spectroscopy

Muon-spin spectroscopy (otherwise commonly referred to as muon-spin rotation or relaxation, hence the $\mu$SR acronym) is a technique which employs the implantation of muons within a sample to obtain information about the internal magnetic field. As such, it is a rare example of a technique that gives microscopic magnetic information, rather than an average over all the behaviour in a system. $\mu$SR often picks up magnetic effects that are missed by macroscopic techniques, being uniquely sensitive to small changes in the magnetism. It can be used to understand both the static and dynamic processes in magnets. We will discuss both the theory behind the technique, and practical considerations, below. We conclude with an example application to a topological magnetic state. In the absence of other references, the material presented here can be found in

**Table 3.1:** The properties of the muon ($\mu$), with comparisons to the electron (e) and proton (p). Data from Ref. [49].

| | $q$ | spin | $m$ (MeV) | moment ($\mu_B$) | $\gamma/2\pi$ (MHzT$^{-1}$) | $\tau$ ($\mu$s) |
|---|---|---|---|---|---|---|
| e | $\pm e$ | 1/2 | 0.51 | 1 | 28000 | $> 10^{40}$ |
| $\mu$ | $\pm e$ | 1/2 | 105.7 | $4.84 \times 10^{-3}$ | 135.5 | 2.19 |
| p | $\pm e$ | 1/2 | 938 | $1.52 \times 10^{-3}$ | 42.6 | $> 10^{42}$ |

Refs. [12, 13].

### 3.1.1 The muon

The muon, a fundamental particle similar to, but heavier than, an electron has a history of being misunderstood. Despite the discovery of cosmic rays in 1912 (of which muons are the major constituent) winning Victor Hess the 1936 Nobel Prize in Physics [46], understanding the properties of the muon took time. Muons were originally thought to be the particle that mediated the strong force, and it was not until the 1940s [47, 48] that this was realised to be incorrect. The properties of the muon (compared to those of an electron and proton in Tab. 3.1) were explored over the following decades, and the potential applications of the positive muon ($\mu^+$) to condensed matter physics, particularly magnetism, were quickly realised.

The muon is a spin-1/2 particle, and therefore interacts with magnetic fields. This property of the muon makes it suitable for the study of magnetism, however it is not a unique property (both the electron and proton are also spin-1/2 particles, for example). Where the muon is unique is its lifetime, $\tau_\mu = 2.2$ $\mu$s. The muon decays via

$$\mu^+ \rightarrow e^+ + \nu_e + \bar{\nu}_\mu \tag{3.1}$$

into a positron and two neutrinos. This decay involves the weak interaction and therefore does not preserve parity [50], which leads to the emission of the positron preferentially in the direction of the muon-spin at the time of decay. This allows one to follow the spin of an ensemble of muons by detecting the direction of the

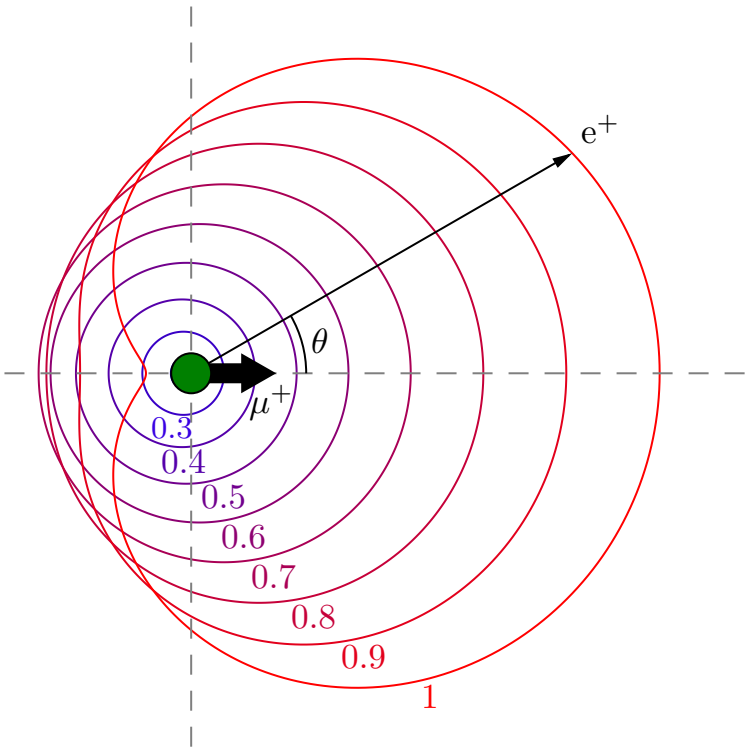


**Figure 3.1:** The probability of positron emission at an angle $\theta$ to the muon-spin. The distance of each line from the muon represents the probability of positron emission in that direction at that energy. Each line represents the total probability of emission from positrons of energy over a range of $(x-0.1)E_{\max}$ to $xE_{\max}$, with $E_{\max} = 52.8$ MeV, where $x$, the upper limit for each line, is indicated. As can be seen, there is a strong preference for the positrons to be emitted in the direction of the muon-spin.

decay positrons as a function of time, and it is this property which makes the muon ideally suited to condensed matter physics experiments.

The probability of muon decay at a particular angle $\theta$ with respect to the instantaneous muon spin direction is proportional to $2\epsilon^2(3-2\epsilon)[1+a(\epsilon)\cos\theta]$, where $\epsilon$ is the normalised kinetic energy of the positron ($\epsilon = 1$ corresponds to the maximum kinetic energy of $E_{\max} \simeq 52.8$ MeV, approximately half the muon rest energy as one would expect), and $a(\epsilon) = (2\epsilon-1)/(3-2\epsilon)$. By integrating this expression between energy limits, one can obtain the probability of a positron being emitted in each direction. This is shown, for bands of $0.1E_{\max}$, in Fig. 3.1.

In this figure, to obtain the total emission probability, one sums all the shown lines (equivalent to integrating between 0 and $E_{\max}$). As can be seen, there is a strong preference for emission in the direction of the muon-spin. (In reality, this effect is further enhanced by preferential absorption of low-energy positrons, which are more commonly emitted away from the muon-spin direction.) By implanting many muons in a sample, the decay to positrons (each of which occurs after a different length of time) allows one to track the average direction of the muon-spin.

Experimentally, the positrons emitted from muon-decay are detected by detectors surrounding the sample of interest. Most commonly we discuss the forward or backward detector (where the name refers to the direction with respect to the muon-momentum, not muon-spin), and we define a quantity known as the asymmetry $A(t)$ in terms of the number of counts $N_\alpha(t)$ detected in the $\alpha$ detector,

$$A(t) = \frac{N_{\mathrm{B}}(t) - \alpha_{\mathrm{exp}} N_{\mathrm{F}}(t)}{N_{\mathrm{B}}(t) + \alpha_{\mathrm{exp}} N_{\mathrm{F}}(t)}, \tag{3.2}$$

where $\alpha_{\mathrm{exp}}$ is an experimentally determined parameter relating to the detector efficiency. The asymmetry is proportional to the muon-spin polarisation $P(t)$, $A(t) = a_0 P(t)$. The maximum value of $a_0 = 1/3$ can be can obtained by averaging $a(\epsilon)$ over all positron energies, however this ideal case is never found in practise, with $a_0$ typically slightly lower. The experimental configuration is shown in Fig. 3.2.

Having shown that it is possible to detect the average direction of the muon-spin in an ensemble of muons as a function of time, we must now consider why this is beneficial. The answer lies in the gyromagnetic ratio of the muon. As previously defined for the electron in Chap. 2, the gyromagnetic ratio of the muon is $\gamma_\mu = ge/2m_\mu$, where in this case $g$ is very close to 2. This gives $\gamma_\mu = 135.5\ \mathrm{MHzT}^{-1}$. This value, for reasons we will see later, sets the timescale for muon interactions, and hence determines the range of dynamics to which the muon is sensitive. This can be summarised in Fig. 3.3, where we can see that the muon covers a frequency range that is not accessible with other techniques. The sensitivity to low frequencies makes $\mu$SR uniquely sensitive to low-moment

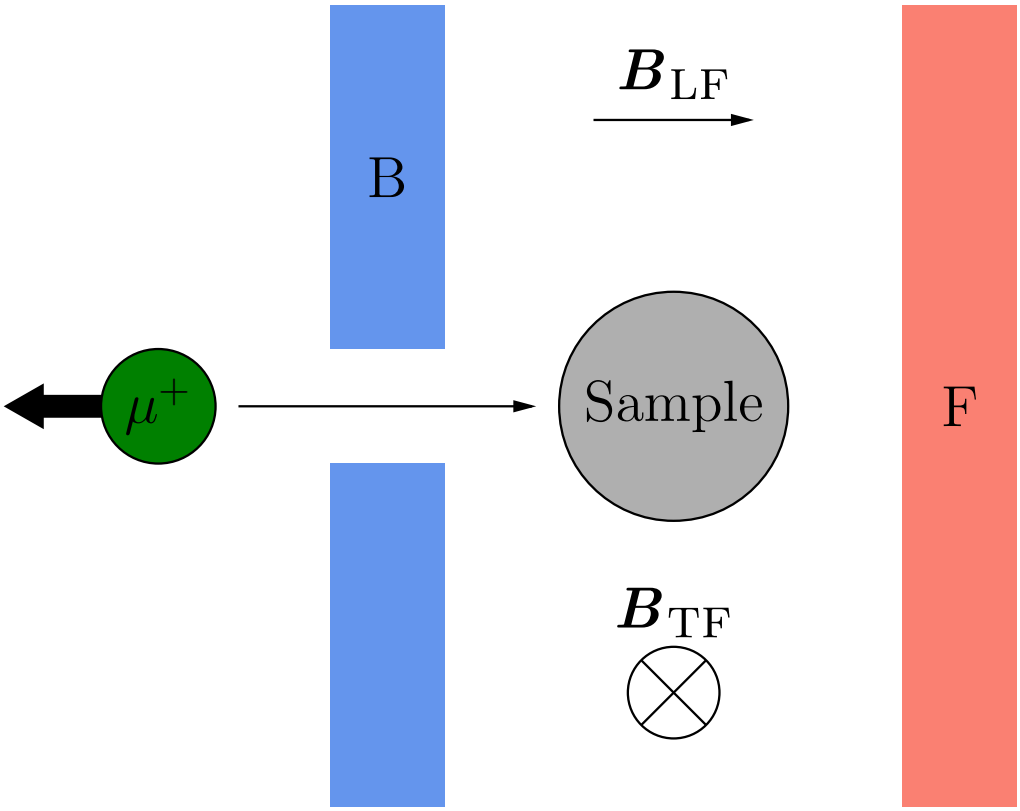


**Figure 3.2:** The experimental configuration for the muon-spin spectroscopy technique, showing the position of the detectors with respect to the sample. The muon is incident upon the sample with spin antiparallel to the momentum. The direction of the longitudinal field (LF) and transverse field (TF) are shown.

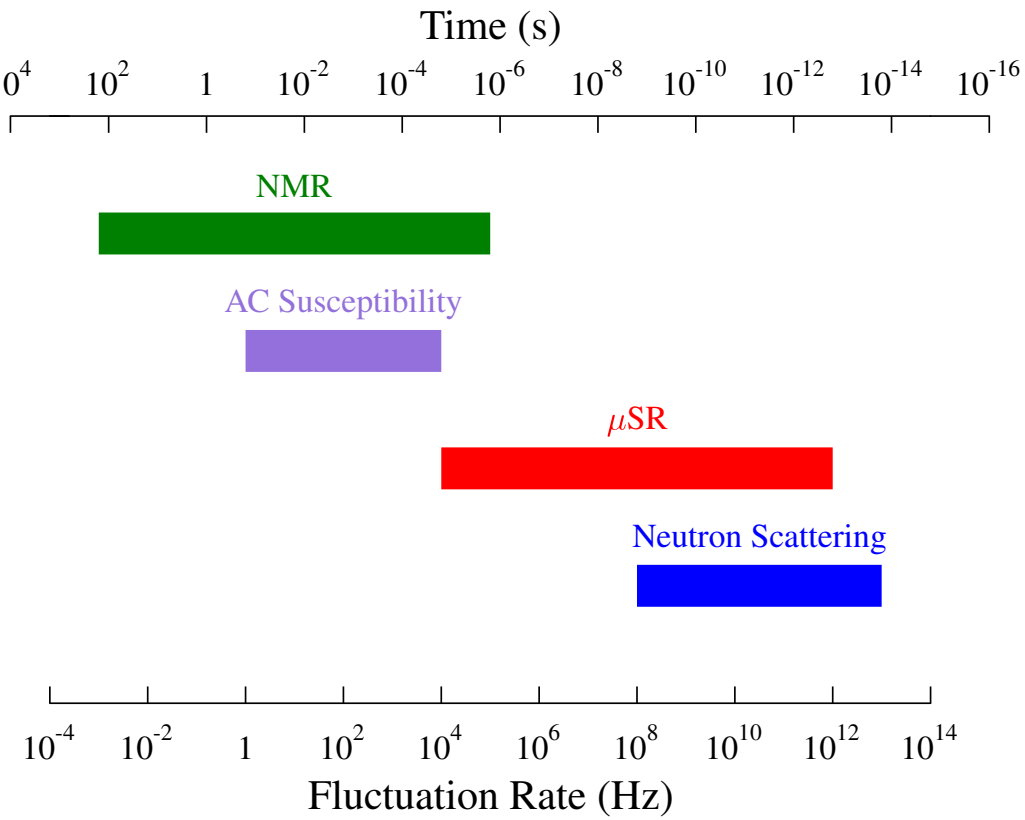


**Figure 3.3:** The frequency range over which the muon-spin spectroscopy technique is sensitive, compared to other experimental techniques. Frequency ranges based on those in Ref. [52].

samples (down to samples with a moment of around $10^{-3}\mu_B$), and small changes in the magnetism [51].

The entire dynamic range shown for $\mu$SR is not accessible in a single experiment, but rather represents the absolute limits of the technique. The range of frequencies to which a particular experiment is sensitive is determined by the experimental setup, choice of instrument/muon source, and sample properties. We will discuss these details later.

### 3.1.2 Time evolution of the muon-spin

We have seen that the properties of the muon make it a prime candidate for extracting information on the magnetism of a sample by detecting the time evo-

lution of the muon-spin. We now consider the interactions between the muon-spin and the sample that dictate the behaviour we hope to detect. We follow the description in Ref. [53]. We will assume that the muon is sat inside the sample, without any chemical bonds to any nearby ions/electrons, and the spin is free to evolve. This scenario turns out to be the one that is most appropriate in this thesis, and although different situations are possible, they are not discussed here.

We have seen that the quantity of interest in the experiment is the muon-spin polarisation, which we project along a particular axis. To make progress with this, we must introduce the Pauli spin operators $\boldsymbol{\sigma}$, which are a mathematically convenient way to express the spin of the system [54]. They are defined as $\boldsymbol{\sigma} = (\hat{\sigma}_x, \hat{\sigma}_y, \hat{\sigma}_z)$, with

$$\hat{\sigma}_x = \begin{pmatrix} 0 & 1 \\ 1 & 0 \end{pmatrix}, \quad \hat{\sigma}_y = \begin{pmatrix} 0 & -\mathrm{i} \\ \mathrm{i} & 0 \end{pmatrix}, \quad \hat{\sigma}_z = \begin{pmatrix} 1 & 0 \\ 0 & -1 \end{pmatrix}. \tag{3.3}$$

The spin operator is defined as $\hat{\boldsymbol{S}} = \hbar\boldsymbol{\sigma}/2$. It is therefore clear to see that (after normalisation) the time evolution of the average muon-spin polarisation along an axis $q$ is

$$P_q(t) = \langle \hat{\sigma}_q(t) \rangle . \tag{3.4}$$

Assuming a time-independent Hamiltonian, we can further write this in terms of the density operator $\hat{\rho} = |\psi\rangle\langle\psi|$, where $|\psi\rangle$ is the state of the system,

$$\langle \hat{\sigma}_q(t) \rangle = \mathrm{Tr}\left[\hat{\rho} \cdot \hat{\sigma}_q(t)\right], \tag{3.5}$$

where $\hat{\sigma}_q(t) = \exp\left(\mathrm{i}\hat{\mathcal{H}}t/\hbar\right)\hat{\sigma}_q \exp\left(-\mathrm{i}\hat{\mathcal{H}}t/\hbar\right)$ is expressed using the Heisenberg representation [55]. Taking the initial muon-spin direction to be along the $b$ direction (with this defining the basis), and assuming the muon ensemble is entirely spin-polarised (as it is in experiment), we can write

$$\hat{\rho} = \begin{pmatrix} 1 & 0 \\ 0 & 0 \end{pmatrix} = \frac{1}{2}\left(\hat{I} + \hat{\sigma}_b\right), \tag{3.6}$$

where $\hat{I}$ is the identity matrix. Combining all of these expressions, and using the fact that Pauli matrices are traceless, one finds

$$P_q(t) = \frac{1}{2}\,\mathrm{Tr}\left[\hat{\sigma}_b \exp\left(\mathrm{i}\hat{\mathcal{H}}t/\hbar\right)\hat{\sigma}_q \exp\left(-\mathrm{i}\hat{\mathcal{H}}t/\hbar\right)\right]. \tag{3.7}$$

This expression allows us to calculate the time-evolution of the muon-spin polarisation, given we know the Hamiltonian of the system.

Before proceeding any further, it is worth considering which axes we will wish to use in Eqn. 3.7 in the experiment. Typically we have two different geometries, longitudinal field (LF, where the initial muon-spin is parallel to the applied field), and transverse field (TF, where the initial-muon spin and applied field are perpendicular). In the absence of an applied field (ZF) we typically use the LF geometry. We are normally interested in the polarisation along the initial muon-spin axis. As typical, if we define the $z$-axis to be the direction of the applied field, we can therefore see that the two cases are: LF, $q = b = z$; and TF, $q = b = x$. These configurations are shown in Fig. 3.2. For the LF geometry (which dominates the work in this thesis), this therefore reduces Eqn. 3.7 to

$$P_z(t) = \frac{1}{2}\sum_{m,n} |\langle m|\sigma_z|n\rangle|^2 \exp\left[\frac{\mathrm{i}\,(E_m - E_n)\,t}{\hbar}\right], \tag{3.8}$$

where $|m\rangle$ and $|n\rangle$ are the eigenstates of $\hat{\mathcal{H}}$ with respective energies $E_m$ and $E_n$.

### 3.1.3 Muon-spin precession

We start with the simplest case, a muon sat in a static magnetic field $\boldsymbol{B}$. As the muon acts as a heavy electron, we know from Chap. 2 that the appropriate Hamiltonian is $\hat{\mathcal{H}} = -\boldsymbol{\mu}\cdot\boldsymbol{B} = -\hbar\gamma_\mu\hat{\boldsymbol{S}}\cdot\boldsymbol{B}$, where we have used Eqn. 2.7, and the knowledge that the stationary muon has no orbital angular momentum. This can be expressed in spherical polar coordinates, where $\boldsymbol{B} = B(\sin\theta\cos\phi, \sin\theta\sin\phi, \cos\theta)$, as

$$\begin{aligned}\hat{\mathcal{H}} &= \frac{-\hbar\gamma_\mu B}{2}\left(\sin\theta\cos\phi\hat{\sigma_x} + \sin\theta\sin\phi\hat{\sigma_y} + \cos\theta\hat{\sigma_z}\right) \\ &= \frac{-\hbar\gamma_\mu B}{2}\begin{pmatrix}\cos\theta & \sin\theta\exp(-\mathrm{i}\,\phi)\\ \sin\theta\exp(\mathrm{i}\,\phi) & -\cos\theta\end{pmatrix}.\end{aligned} \tag{3.9}$$

Diagonalisation finds the two eigenstates needed for Eqn. 3.8, which we denote using the basis of $|\uparrow\rangle$ and $|\downarrow\rangle$, corresponding to the muon-spin pointing parallel or antiparallel to the $z$-axis. The eigenstates, corresponding to alignment or

anti-alignment with the applied field respectively, are

$$\begin{aligned} |+\rangle &= \sin\left(\frac{\theta}{2}\right)\exp\left(\frac{-\,\mathrm{i}\,\phi}{2}\right)|\uparrow\rangle - \cos\left(\frac{\theta}{2}\right)\exp\left(\frac{\mathrm{i}\,\phi}{2}\right)|\downarrow\rangle\,, \\ |-\rangle &= \cos\left(\frac{\theta}{2}\right)\exp\left(\frac{-\,\mathrm{i}\,\phi}{2}\right)|\uparrow\rangle + \sin\left(\frac{\theta}{2}\right)\exp\left(\frac{\mathrm{i}\,\phi}{2}\right)|\downarrow\rangle\,, \end{aligned} \tag{3.10}$$

which have energies $E_{\pm} = \pm\hbar\gamma_\mu B/2$.

Substitution into Eqn. 3.8 gives the important result

$$P_z\left(t\right) = \cos^2\theta + \sin^2\theta\cos\left(\gamma_\mu B t\right), \tag{3.11}$$

which shows that the spin of the muon will precess in a static magnetic field. Alternatively, if one were to watch the time-evolution of the spin in the $x$-direction instead, with the spin initially pointing along $x$ (as is done in the TF geometry), one can see from symmetry that

$$P_x\left(t\right) = \cos^2\theta + \sin^2\theta\cos\left(\gamma_\mu B t\right). \tag{3.12}$$

Averaging uniformly over $\theta$ (for example, the situation one would expect for a polycrystalline sample where each grain is randomly oriented with respect to the initial muon-spin direction) gives, for example,

$$P_z\left(t\right) = \frac{1}{3} + \frac{2}{3}\cos\left(\gamma_\mu B t\right). \tag{3.13}$$

It is clear from these expressions why $\gamma_\mu$ sets the timescale over which $\mu$SR is sensitive. A situation that closely approximates this is a long-range ordered magnet, where the muons that stop in crystallographically equivalent sites will all show spin-precession at a similar rate, hence detecting these oscillations is a classic way to look for magnetic order.

### 3.1.4 Static field distributions

We now complicate the above situation by placing our ensemble of muons in a distribution of static magnetic fields with probability distribution function $p\left(\boldsymbol{B}\right)$. The polarisation can now be calculated by applying the appropriate weight from

the probability distribution to Eqn. 3.11 [51]. Here we show the result for the LF geometry,

$$P_z(t) = \int p(\boldsymbol{B}) \left[\cos^2\theta + \sin^2\theta \cos(\gamma_\mu B t)\right] \mathrm{d}^3\boldsymbol{B}. \tag{3.14}$$

The result for the TF geometry is similar.

Starting with the simplest example, let us consider the consequence of a distribution of magnetic fields centred on zero. This may occur, for example, above $T_c$ when the electronic moments are fluctuating too rapidly to be detected with $\mu$SR, leaving just nuclear moments to interact with the muon-spin. From the central limit theorem, assuming a Gaussian distribution is likely a good approximation in most cases. We define $\Delta = \gamma_\mu \left\langle (B - \langle B \rangle)^2 \right\rangle^{1/2}$ such that the width of the distribution is $\Delta/\gamma_\mu$, which means

$$p(\boldsymbol{B}) = \left(\frac{\gamma_\mu^2}{2\pi\Delta^2}\right)^{\frac{3}{2}} \exp\left(\frac{-\gamma_\mu^2 B^2}{2\Delta^2}\right). \tag{3.15}$$

Inserting this into Eqn. 3.14, and performing an angular average, gives the famous result

$$P_z(t) = \frac{1}{3} + \frac{2}{3}\left(1 - \Delta^2 t^2\right) \exp\left(\frac{-\Delta^2 t^2}{2}\right), \tag{3.16}$$

the Kubo-Toyabe function [56]. This is shown in Fig. 3.4 (when $\gamma_\mu B_0/\Delta = 0$), and shows Gaussian-like behaviour [$P_z(t) \propto \exp(-\Delta^2 t^2)$] at early times, and the '1/3-tail' at long times.

We can modify the above example by applying a magnetic field. Let us first consider a transverse magnetic field $\boldsymbol{B}_0$ that is much larger than any field produced by the material itself, such that $p(\boldsymbol{B}) = \delta^{(3)}(\boldsymbol{B} - \boldsymbol{B}_0)$. In this case, we can approximate $B_x = B_y = 0$, $B_z = B_0 + X$, where $X$ will be the shift away from $B_0$ (normally due to the internal field of the magnet). We assume $X$ is an even function (as is the case for a Gaussian) for mathematical simplicity. The triple integral of Eqn. 3.14 has reduced to a single integral, and with some manipulation, one can show that

$$P_x(t) = \left[\int_{-\infty}^{\infty} p(X) \cos(\gamma_\mu X t)\right] \cos(\gamma_\mu B_0 t). \tag{3.17}$$

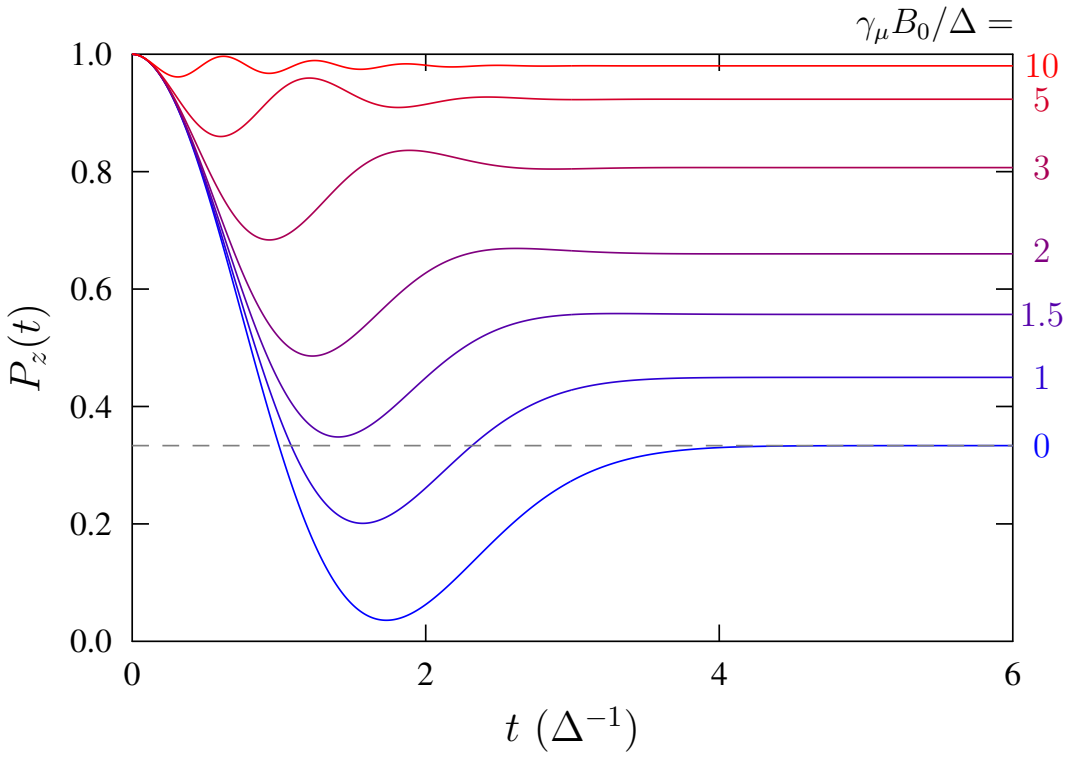


**Figure 3.4:** The Kubo-Toyabe function, both with and without application of a magnetic field $\boldsymbol{B}_0$ parallel to the initial muon-spin direction. The dashed line indicates $P_z(t) = 1/3$, the value of $P_z(t \to \infty)$ when $B_0 = 0$.

Assuming a Gaussian distribution of internal fields around the applied field, this reduces to

$$P_x(t) = \exp\left(\frac{-\Delta^2 t^2}{2}\right)\cos(\gamma_\mu B_0 t), \tag{3.18}$$

and we find a result that we use for TF experiments throughout the thesis: when the static precession of the muon-spin dominates, the expected observed behaviour is a damped cosine where the damping is proportional to the width of the field at the muon site, and the precession is at a rate set by the average internal field.

An alternative would be to apply the magnetic field $\boldsymbol{B}$ along the initial muon spin direction, as would be done in the LF geometry. This will again change the distribution of fields at the muon site, and similar analysis leads to the polarisation

$$\begin{aligned} P_z(t) = 1 - \frac{2\Delta^2}{\gamma_\mu^2 B_0^2}\left[1 - \exp\left(\frac{-\Delta^2 t^2}{2}\right)\cos(\gamma_\mu B_0 t)\right] \\ + \frac{2\Delta^4}{\gamma_\mu^3 B_0^3}\int_0^t \exp\left(\frac{-\Delta^2 \tau^2}{2}\right)\sin(\gamma_\mu B_0 \tau)\,\mathrm{d}\tau, \end{aligned} \tag{3.19}$$

which is known as the LF Kubo-Toyabe [57]. I have calculated an alternative form of this equation using MATHEMATICA [58] which is more computationally efficient. We employ the complex error function $\mathrm{erfi}(z) = -\mathrm{i}\,\mathrm{erf}(\mathrm{i}\,z)$ [59], such that

$$\begin{aligned} P_z(t) = 1 - \frac{2\Delta^2}{\gamma_\mu^2 B_0^2}\left[1 - \exp\left(\frac{-\Delta^2 t^2}{2}\right)\cos(\gamma_\mu B_0 t)\right] \\ + \frac{\Delta^3}{\gamma_\mu^3 B_0^3}\sqrt{\frac{\pi}{2}}\exp\left(\frac{-\gamma_\mu^2 B_0^2}{2\Delta^2}\right)\left[2\,\mathrm{erfi}\left(\frac{\gamma_\mu B_0}{\sqrt{2}\Delta}\right)\right. \\ \left. - \mathrm{erfi}\left(\frac{\gamma_\mu B_0 - \mathrm{i}\,\Delta^2 t}{\sqrt{2}\Delta}\right) - \mathrm{erfi}\left(\frac{\gamma_\mu B_0 + \mathrm{i}\,\Delta^2 t}{\sqrt{2}\Delta}\right)\right]. \end{aligned} \tag{3.20}$$

The LF Kubo-Toyabe is also shown in Fig. 3.4. An important feature of this function is the recovery of the '1/3-tail'; as a greater external field is applied, more of the muon-spins are locked along the field direction and cannot depolarise. This is a very important point for the study of dynamics with $\mu$SR, and it the effect of the dynamics on this tail which we will concentrate on.

### 3.1.5 Dynamic magnetism

Having so far assumed a static distribution of magnetic fields at the muon site, we now introduce dynamics. We first assume a situation where dynamics dominate, meaning the muon-spin must align either parallel, or anti-parallel to the initial muon-spin direction; we take this as the $z$-axis for simplicity. (This could happen, for example, if there is a large applied field along the muon-spin direction direction, as we saw at the end of the previous section.) Defining the number of muon-spins parallel/antiparallel to the $z$-axis as $n_\uparrow$ and $n_\downarrow$ respectively, and setting the transition rates between the two states to be $W_\pm$, we can write

$$\begin{aligned} \dot{n}_\uparrow &= W_+ n_\downarrow - W_- n_\uparrow, \\ \dot{n}_\downarrow &= W_- n_\uparrow - W_+ n_\downarrow. \end{aligned} \tag{3.21}$$

Subtracting these equations, and using the fact that $W_+ n_\uparrow = W_- n_\downarrow = 0$, we find

$$\frac{\mathrm{d}(n_\uparrow - n_\downarrow)}{\mathrm{d}t} = -\left(W_+ + W_-\right)\left(n_\uparrow - n_\downarrow\right). \tag{3.22}$$

The polarisation $P_z(t) = (n_\uparrow - n_\downarrow)/(n_\uparrow + n_\downarrow)$, so it is evident from Eqn. 3.22 that $P_z(t) = P_z(0)\exp(-\lambda t)$, where $\lambda = W_+ + W_-$. We have therefore shown that, when the system is dominated by dynamics, we would expect exponential decay of the muon-spin polarisation. The next challenge is to identify the relaxation rate $\lambda$ in terms of more useful quantities. There are a variety of different methods to do this [53], however we will employ the strong collision model.

The strong collision model allows the evolution of the muon-spin to go on undisturbed for an average period of time $\tau$, before suddenly changing evolution to be that of a different field distribution. The muon-spin then evolves as determined by the new configuration, with the polarisation starting from the previous value, until it is disturbed by another "collision", and so on. These changing field distributions occur in magnetic systems because of dynamic fluctuations changing the distribution of magnetic moments. We illustrate the situation in Fig. 3.5, where two regimes are shown, (a) the slow-fluctuation regime ($\gamma_\mu B\tau \gg 1$) where there is sufficient time for spin precession before the change in field distribution, leading predominantly to a relaxation of the '1/3-tail', and (b) the fast-fluctuation

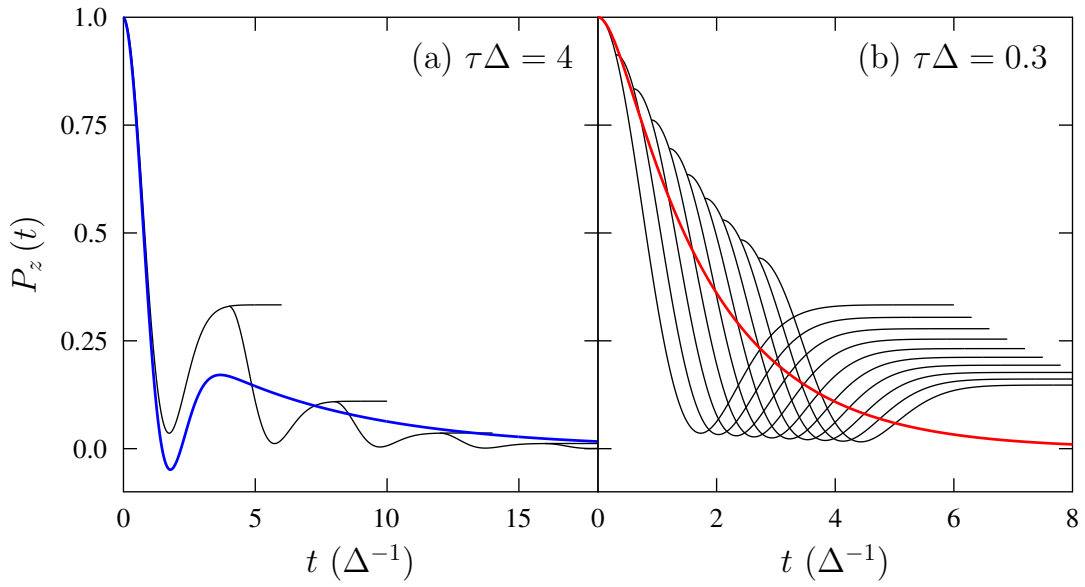


**Figure 3.5:** The principle behind the strong collision model approach to dynamicisation. Successive collisions reset the polarisation (black lines), with the overall polarisation shown in colour. The slow-fluctuation regime is shown in (a), where the overall polarisation is given by Eqn. 3.26, with the fast-fluctuation regime shown in (b), where Eqn. 3.27 gives the overall polarisation.

regime ($\gamma_\mu B\tau \ll 1$, typical for ordered magnets such as those studied in this thesis) where the rapid resetting of the polarisation leads to the exponential decay we have already shown we expect.

We will now perform the above steps mathematically, focusing on the LF geometry. The polarisation function can be written in terms of contributions from muons that have experienced $l$ field changes up to time $t$, i.e.

$$P_z(t) = \sum_{l=0}^{\infty} R_{z,l}(t)\,. \tag{3.23}$$

The probability of the field having not changed by time $t$ is $\exp(-\nu t)$, where $\nu = 1/\tau$ is the fluctuation rate. Hence $R_{z,0}(t) = P_z^{\mathrm{s}}(t)\exp(-\nu t)$, where $P_z^{\mathrm{s}}(t)$ is the static polarisation function that the muon-spin will follow between collisions. Subsequent collisions change the polarisation from previous collision, so we can write

$$R_{z,l+1}(t) = \nu \int_0^t R_{z,l}(t-t')\,R_{z,0}(t')\,\mathrm{d}t', \tag{3.24}$$

and hence

$$P_z(t) = P_z^{\mathrm{s}}(t)\exp(-\nu t) + \nu\int_0^t P_z(t-t')\,P_z^{\mathrm{s}}(t')\exp(-\nu t')\,\mathrm{d}t'. \tag{3.25}$$

From this equation one can calculate (numerically) the expected polarisation decay from any static polarisation function.

Progressing further analytically requires the use of Laplace transforms and is well documented [57, 60], however the process of doing these transformations provides no great physical insight. We shall instead present the results one obtains for various different scenarios and discuss the implications.

The first scenario we consider is that of the Gaussian distribution of fields around zero, which we have shown without dynamics leads to the Kubo-Toyabe function. In the slow-fluctuation limit ($\nu/\Delta \ll 1$) we find

$$P_z(t) = \frac{1}{3}\exp\left(\frac{-2\nu t}{3}\right) + \frac{2}{3}\left(1-\Delta^2 t^2\right)\exp\left(\frac{-\Delta^2 t^2}{2}\right), \tag{3.26}$$

showing the '1/3-tail' is relaxed, with the early precession unaffected, as we expected from Fig. 3.5. In the fast-fluctuation limit ($\nu/\Delta \gg 1$)

$$P_z(t) = \exp\left\{\frac{-2\Delta^2}{\nu^2}\left[\exp(-\nu t) - 1 + \nu t\right]\right\}, \tag{3.27}$$

which we can reduce further when $\nu t \gg 1$ to

$$P_z(t) = \exp(-\lambda t), \quad \lambda = \frac{2\Delta^2}{\nu}. \tag{3.28}$$

We have recovered the expected exponential decay, relating the relaxation rate to the width of the distribution of fields at the muon site, and the fluctuation rate. Both Eqns. 3.26 and 3.27 are shown in Fig. 3.5.

As discussed above, one way to ensure dynamics dominate is to apply a large magnetic field $\boldsymbol{B}_0$ parallel to the initial muon-spin direction. This is similar to the previous case, however with the $z$-component of the field boosted by $B_0$. In the static limit, this gave the LF Kubo-Toyabe. Introducing dynamics one can show (this time with a perturbation theory approach [61]) that the result is once again an exponential. In general, we find the Keren function $P_z(t) = \exp[-\lambda(t)\,t]$

where

$$\lambda(t)\,t = \frac{2\Delta^2}{\left(\gamma_\mu^2 B_0^2 + \nu^2\right)^2}\Big\{ \left[\gamma_\mu^2 B_0^2 + \nu^2\right]\nu t + \left[\gamma_\mu^2 B_0^2 - \nu^2\right]\left[1 - \exp(-\nu t)\cos(\gamma_\mu B_0 t)\right] - 2\nu\gamma_\mu B_0 \exp(-\nu t)\sin(\gamma_\mu B_0 t)\Big\}, \tag{3.29}$$

which is valid for $\nu > \Delta$. Once again, taking the fast-fluctuation limit, we find relaxation rate

$$\lambda = \frac{2\Delta^2\nu}{\nu^2 + \gamma_\mu^2 B_0^2}, \tag{3.30}$$

which is potentially the most important equation in this thesis.

We have seen that $\mu$SR is highly sensitive to the dynamics of a magnetic system, so the question of which dynamics we might hope to detect is worth considering. We can see from Eqn. 3.30 that the largest response will be for frequencies around $\gamma_\mu B_0$, and hence we need to look for processes in magnets around this timescale. The most obvious candidate is individual spin flips, which needs energy on the scale $J$, and hence (using $\Delta E \Delta t \simeq \hbar$) happens on a timescale $\hbar/J$. This is typically very short, and $\mu$SR is normally insensitive to these high-frequency dynamics. Instead, $\mu$SR is sensitive to collective dynamics that involve lots of magnetic moments. In this case, as the wavevector of the process $q \to 0$, the frequency $\omega \to 0$. These types of dynamics can be split into propagating and diffusive modes, and we typically find it is the diffusive modes to which $\mu$SR is most sensitive. A perfect example of these modes occurs around a second-order phase transition at $T_c$, where there is a dissipative mode from the order parameters with $\nu = c/\chi$, where $c$ is a constant and $\chi$ is the susceptibility. It is therefore often the case that near $T_c$ the relaxation rate $\lambda$ follows power law behaviour as $\nu \propto |T - T_c|^\gamma$ [14]. We term this critical slowing down, and is often discussed later in the thesis.

### 3.1.6 The field at the muon site

Having seen the effect on the muon-spin of a magnetic field, we must now consider the physical origin of these fields. There are seven terms that contribute to the

total field at the muon site,

$$\boldsymbol{B} = \boldsymbol{B}_0 + \boldsymbol{B}_{\text{dip}} + \boldsymbol{B}_{\text{Lor}} + \boldsymbol{B}_{\text{dem}} + \boldsymbol{B}_{\text{con}} + \boldsymbol{B}_{\text{trans}} + \boldsymbol{B}_{\text{dia}}. \tag{3.31}$$

We discuss each in turn.

The contribution from an externally applied field $\boldsymbol{H}_0$ is captured in $\boldsymbol{B}_0 = \mu_0 \boldsymbol{H}_0$. Note that, for clarity, in much of the work in this thesis we often use the notation $\boldsymbol{B}_{\text{ext}}$ to make the origin of this contribution clear.

The terms $\boldsymbol{B}_{\text{dip}}$, $\boldsymbol{B}_{\text{Lor}}$, and $\boldsymbol{B}_{\text{dem}}$ all arise due to the dipolar interaction between moments (only considering moments that are sufficiently far away from the muon such that there is no overlap between the muon and magnetic moments wavefunction). The dipolar field from a single magnetic moment $\boldsymbol{m}$ at a displacement $\boldsymbol{r}$ from the moment is given by

$$\boldsymbol{B}(\boldsymbol{r}) = \frac{\mu_0}{4\pi r^3}\left[\frac{3(\boldsymbol{m}\cdot\boldsymbol{r})\,\boldsymbol{r}}{r^2} - \boldsymbol{m}\right], \tag{3.32}$$

so for the field at the muon site $\boldsymbol{r}_\mu$, one needs to sum all of the contributions from all moments. This is clearly complicated, so we split the contribution up into (i) $\boldsymbol{B}_{\text{dip}}$ from moments close to the muon (within the so-called Lorentz sphere) that we consider precisely, (ii) $\boldsymbol{B}_{\text{Lor}}$, a background from the moments outside the Lorentz sphere, and (iii) $\boldsymbol{B}_{\text{dem}}$ from moments on the surface of the material. As such, these three contributions are

$$\boldsymbol{B}_{\text{dip}} = \frac{\mu_0}{4\pi}\sum_{r_i<R_{\text{sphere}}}\left(\frac{3(\boldsymbol{m}_i\cdot\boldsymbol{r}_i)\,\boldsymbol{r}_i}{r_i^5} - \frac{\boldsymbol{m}_i}{r_i^3}\right), \tag{3.33}$$

where we sum over the all $i$th moments within the Lorentz sphere which has radius $R_{\text{sphere}}$,

$$\boldsymbol{B}_{\text{Lor}} = \frac{\mu_0 \boldsymbol{M}_{\text{Lor}}}{3} = \frac{\mu_0}{4\pi R_{\text{sphere}}^3}\sum_{r_i<R_{\text{sphere}}}\boldsymbol{m}_i, \tag{3.34}$$

and

$$\boldsymbol{B}_{\text{dem}} = -\mu_0 \boldsymbol{N}\boldsymbol{M}_{\text{meas}}, \tag{3.35}$$

where $\boldsymbol{N}$ is the demagnetisation tensor that depends on the shape of the sample, and $\boldsymbol{M}_{\text{meas}}$ is the measured magnetisation.

Moments that are very close to the muon such that their wavefunction overlaps with that of the muon contribute to the field at the muon site via the hyperfine field $\boldsymbol{B}_{\text{hyp}} = \boldsymbol{B}_{\text{con}} + \boldsymbol{B}_{\text{trans}}$. This term is typically more significant in metals where there is a larger probability of electron-muon wavefunction overlap. Both of these terms are slightly complicated to calculate exactly, but fortunately they are not required for this thesis. The contact hyperfine field $\boldsymbol{B}_{\text{con}}$ is proportional to the electron spin-density at the muon site, whilst the transferred hyperfine field $\boldsymbol{B}_{\text{trans}}$ is from higher orbital momentum contributions to the diploar field, and in metals arises due to the Ruderman-Kittel-Kasuya-Yosida (RKKY) interaction.

The final contribution, $\boldsymbol{B}_{\text{dia}}$ arises due to screening currents in superconductors. It is not relevant in this thesis.

### 3.1.7 Muon sources

We have seen that by tracking the muon-spin polarisation one can tell a great many things about both the static and dynamic properties of the internal field at the muon site. Critically, there are two main types of experiment one can perform, either looking at static or dynamic information.

For an experiment focusing on static information, one wants the best time resolution possible, allowing detection of fast oscillations, and hence high magnetic fields. Most suited to this experiment is a cyclotron source of muons, where single protons are accelerated in a spiral path through the accelerator. These protons are then collided with a target, producing a single muon at a time. This is known as a continuous muon beam, and allows for excellent time resolution at the cost of a shorter interval between muons. The Paul Scherrer Institute, used in the work in this thesis, hosts a cyclotron accelerator.

Conversely, for better sensitivity to dynamic information a long measurement time is required, often at the cost of the high time resolution. In this case, a synchrotron is best, where two packets of ionised hydrogen orbits 180$^{\text{o}}$ out of phase. Once these packets are sufficiently tightly packed they are ejected into the graphite target, resulting in pulses of a large number of muons getting implanted

into the sample. The muon pulses have a finite width in time limiting the time resolution of the instrument. This constrains the maximum detectable frequency of oscillations (hence internal fields). As there are a large number of muons in each pulse the pulses can be well separated in time, allowing systems with slowly relaxing polarisation to be measured. The ISIS Neutron and Muon source, a synchrotron, has been used for measurements that are presented throughout this thesis. An important consequence of this type of measurement is the "lost asymmetry", where in materials that host long-range magnetic order have a fraction of the muons that are precessing too fast to be detected in these experiments, and hence a fraction of the asymmetry is lost. This asymmetry recovers as the temperature is increased through the ordering temperature, and can be used to identify the critical temperature of a system.

### 3.1.8 Example measurement: The Haldane Chain

I now present an example of the $\mu$SR technique applied to topological magnetism. This section is based on work published in Ref. [62], where the properties of a molecular magnet were explored, demonstrating that the $S = 1$ Haldane Chain model well describes the system. As part of this collaboration, I was responsible for the analysis of the zero-field $\mu$SR data analysis.

So far in this thesis we have looked at systems of differing dimensionality. We now return to the $D = 1$, $d = 3$ scenario, but this time with some subtle differences. The key difference is rather than the ferromagnetic ($J > 0$) coupling we have concentrated on, we will consider antiferromagnetic ($J < 0$) coupling, leading to a preference for adjacent spins to align anti-parallel. In the case of the magnetic moments being $S = 1/2$, this leads to a state known as the Tomonaga-Luttinger liquid (TLL), which has low-energy excitations (called spinons) which have fractional spin. Perhaps even more curious is the behaviour if the magnetic moments instead have $S = 1$, where the ground state is expected to remain disordered [63, 64]. This configuration is known as the Haldane Chain, and is topologically distinct from the TLL. The Haldane chain phase is protected by an

energy-gap, above which excitations propagate. Small changes in the Hamiltonian describing these systems lead to dramatic changes in the expected magnetic phase diagram [65, 66, 67], and hence finding materials that well match these models is an active area of research.

Measurements of $NiI_2(3,5\text{-lut})_4$ where $(3,5\text{-lut}) = (3,5\text{-lutidine}) = (C_7H_9N)$ reveal it to be an antiferromagnetically coupled spin-1 chain with single-ion anisotropy that makes it among the most isotropic candidate Haldane chain reported [62]. Further, the energy scales of the material make it well suited to experimental study (requiring attainable magnetic field strengths to saturate the system). It is therefore a promising candidate for a material in which the physics of the Haldane chain can be studied; it is important to verify whether the ground-state is disordered as expected. For this we employ ZF $\mu$SR.

ZF $\mu$SR measurements of $NiI_2(3,5\text{-lut})_4$ were made on the LTF and GPS instruments at the Swiss Muon Source (S$\mu$S), Paul Scherrer Institut, Switzerland. For the measurements, samples were packed in Ag foil envelopes (foil thickness 12.5 $\mu$m), attached to a silver fork and mounted in a cryostat. Data analysis was carried out using the WiMDA program [68]. Example asymmetry spectra are shown in Fig. 3.6(a). No oscillations are observed in the spectra, indicating a lack of long-range magnetic order, consistent with the realisation of a Haldane chain state.

The spectra in Fig. 3.6(a) are well described over the entire temperature regime by

$$A(t) = A_1 \exp(-\lambda_1 t) + A_2 \exp(-\lambda_2 t) + A_\mathrm{b}. \tag{3.36}$$

Each component of the fit accounts for muons that stop in different environments. The $A_\mathrm{b}$ component arises due to muons that stop outside of the sample, for example in the silver foil. The two exponential components can be classified as a slow ($\lambda_1$) and fast ($\lambda_2$) component, with their amplitudes $A_i$ reflecting the proportion of muons stopping in the two; we find $A_1 + A_2 = 11.1(7)\%$ and $A_2/(A_1 + A_2) = 0.61(7)$ to be temperature independent (the proportion of muons stopping in each site should not change over this temperature range, so this is as

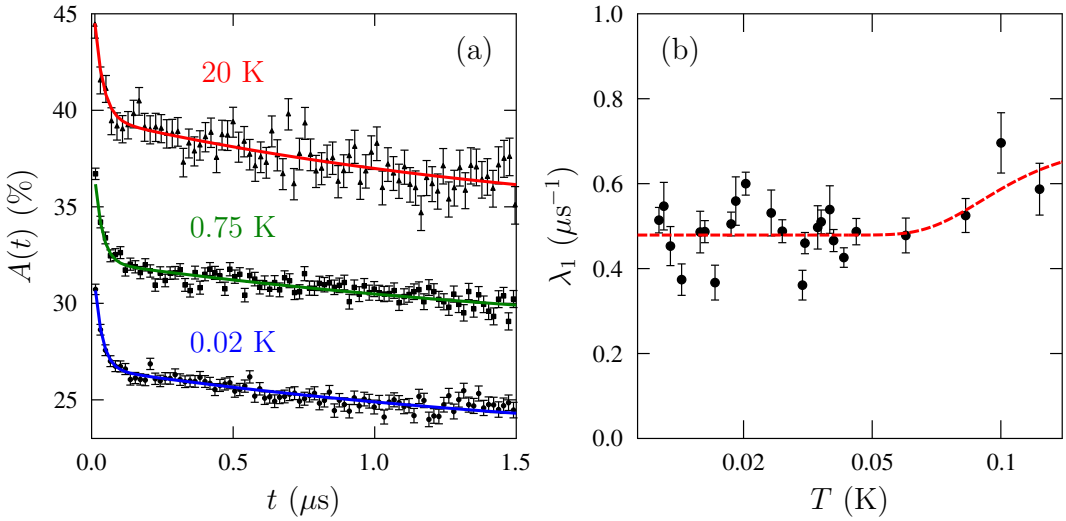


**Figure 3.6:** Zero-field muon-spin relaxation measurements of $NiI_2(3,5\text{-lut})_4$. Example asymmetry spectra $A(t)$ at various temperatures are shown in (a). In this figure data from multiple experiments on different instruments is shown, and hence the absolute value of asymmetry cannot be directly compared; here the data is shown with arbitrary vertical offsets for clarity. The slow relaxation rate $\lambda_1$, extracted from the asymmetry spectra, is shown in (b), with $\lambda_1 \propto \exp(-\Delta/k_B T)$, $\Delta = 7$ K, indicated by the red dashed line.

one would expect). The fast relaxing component typically arises from muons that stop and form bound states and therefore are insensitive to the magnetism of the system [69]. This is once again a temperature-independent effect in this regime, hence $\lambda_2 = 38\ \mu s^{-1}$ was held constant. Conversely, the slow relaxing component arises from muons that stop in the material and interact as previously discussed in this chapter. As such, the exponential form of the relaxation indicates that dynamically fluctuating magnetism dominates the muon response.

The value of $\lambda_1$ as a function of temperature is shown in Fig. 3.6(b). At a phase transition, one would expect a significant increase in the value of $\lambda_1$, indicating that there is a large variation in the values of internal magnetic fields, or a slowing of dynamics. As the value of $\lambda_1$ stays approximately constant throughout the whole temperature range this suggests there is no phase transition, again indicating that there is no transition to long-range order even down to the lowest measured temperatures.

Previous work [70] has shown that the relaxation rate $\lambda_1$ in a Haldane chain should vary as $\lambda_1 \propto \exp(-\gamma\Delta/k_B T)$, where $\Delta$ is the magnitude of the energy gap above the Haldane chain state, and the value of the constant $\gamma$ depends on the temperature regime and details of the model. Fig. 3.6(b) shows this scaling law for $\Delta = 7$ K (found for this material with other measurements [62]) and $\gamma = 1$ (expected for low temperatures), suggesting that the slight increase in $\lambda_1$ above the gap temperature is consistent with the predicted behaviour. Although there is insufficient data density to test which value of $\gamma$ best describes this system, the location of the upturn is supportive of the value $\Delta \simeq 7$ K found through other techniques.

There are several other possible causes of the occurrence of the relaxation parametrised by $\lambda_1$, all consistent with the realisation of a Haldane chain phase in this material. One possibility is that chain ends give rise to magnetic moments, which introduce some magnetic-field dynamics that cause the relaxation. Another possibility is that defects in the sample affect the local-field configuration, again leading to a small, fluctuating magnetic field. It is also possible that the muon

itself distorts the local environment at the implantation site inducing a small local moment. This has been observed previously in the magnetically disordered state of molecular spin-ladder systems [71], where it was shown that it did not prevent the muon from being a faithful probe of the intrinsic physics of the system.

With this example, we have seen how $\mu$SR can be applied to topological magnetism, revealing details of not only the static magnetism, but also the dynamics. Throughout this thesis we apply this technique to other systems hosting topological magnetism.

## 3.2 Magnetometry

Magnetometry techniques are those that are concerned with measuring the bulk magnetic properties of a sample, specifically those properties relating to either the magnetisation or magnetic susceptibility. In general, and in this thesis, we split the technique into two different areas, DC and AC magnetometry.

### 3.2.1 DC magnetometry

DC magnetometry determines the magnetisation of the sample. The magnetisation, defined as the total magnetic moment (normally per unit volume, although the measurements measure the total magnetic moment of the sample), is arguably the most important property of a magnet, and hence measuring it is considered a prerequisite for most other experimental techniques. We present a very brief overview of the technique here.

For the work in this thesis the magnetisation was measured using a Superconducting QUantum Interference Device (SQUID). A SQUID consists of a superconducting loop of wire, which has two non-superconducting regions in parallel at opposite sides of the loop [72]. Both of these regions are each a Josephson junction, a region which allows a small current to pass through. The superconducting ring only allows certain magnetic flux values through the centre. When the stray field from a sample with net magnetisation is passed through the loop,

the flux in the superconducting ring will change with time. Consequently, the current in the loop will also change (as one would expect from Faraday's Law of Induction) to ensure the total flux remains quantised, with an oscillatory period that is proportional to the change in flux in the loop. Typically SQUIDs are operated under a bias current, so measuring the oscillations in the voltage across the loop allows one to sensitively measure the change in flux, and hence infer the magnetisation of the sample being passed through the loop.

### 3.2.2 AC magnetometry

The quantity that is measured with AC magnetometry is the magnetic susceptibility $\chi = \partial M/\partial H$. In this technique [52] a sinusoidal time-varying magnetic field of amplitude $H_{\mathrm{AC}}$ and frequency $\omega$ is applied to the sample, potentially in addition to a constant magnetic field ($H_{\mathrm{DC}}$). The field of the time-dependent magnetisation induced can be picked up by the SQUID without moving the sample. The magnetisation detected by the SQUID is hence $M_{\mathrm{AC}}(t') = \chi(t' - t) H_{\mathrm{AC}} \sin(\omega t)$, allowing for measurement of the susceptibility. In general (particularly at higher frequencies), the response will not be in phase with the applied magnetic field, but there will be some phase lag $\phi$. We typically consider the susceptibility of the signal to be split into two parts, the real (or in-phase) component $\chi' = \chi \cos\phi$, and the imaginary (or out-of-phase) component $\chi'' = \chi \sin\phi$.

How well the system responds at $\omega$ is most clearly seen by the magnitude of $\chi'$, and hence this can be thought of as similar to the dynamic measurements already discussed for $\mu$SR. In the low frequency limit, $\chi''$ will be zero, and $\chi' = \chi$ will simply be the derivative of the $M$-$H$ curve that could be measured with DC magnetometry. If $\chi''$ is non-zero, this indicates dissipative processes in the sample where there are losses of energy [52]. Most commonly in the systems studied in this thesis, this will be due to the irreversible motion of domain walls (of which we have already seen the topological magnetic states are closely related to). These irreversible motions will be most prominent at thermodynamic phase transitions, and hence $\chi''$ is often used to detect phase boundaries.

## 3.3 Density functional theory

Another technique regularly employed throughout this thesis is density functional theory (DFT). Although we will not go into great detail on the technique, it is worth having a brief overview of DFT to aid understanding of the results it produces. We follow the approach of Ref. [73].

A quantum mechanical system can be described by a wavefunction that depends on the position of all $N$ electrons $\boldsymbol{r}_N$ and $I$ nuclei $\boldsymbol{R}_I$, i.e., omitting time-dependence, $\Psi\left(\boldsymbol{r}_1, \boldsymbol{r}_2, ..., \boldsymbol{r}_N, \boldsymbol{R}_1, \boldsymbol{R}_2, ..., \boldsymbol{R}_I\right)$. Here we have assumed that the nuclear degrees of freedom can be separated from the electronic ones, a statement that is justified if we make the assumption that, due to the much larger mass, the nuclei are stationary on the timescale of the electron motion. This is known as the Born-Oppenheimer approximation. We thus write the many-electron and nuclei wavefunctions as $\psi$ and $\phi$ respectively.

The Hamiltonian for the system can be split into five different parts: (i) the electronic kinetic energy, (ii) the nuclear kinetic energy, (iii) the electron-nuclear interactions, (iv) the electron-electron interactions, and (v) the nuclear-nuclear interactions. The Born-Oppenheimer approximation is very helpful for simplying the problem; the nuclear kinetic energy can be taken to be zero, and the nuclear-nuclear interactions can be taken as a constant. Despite these simplifications, we still have the challenge of finding a wavefuction to describe the system. It turns out that, apart from the most trivial systems, this is not possible to do analytically, and even numerically it becomes impossibly expensive. We therefore must make further simplifications, which is where DFT comes in.

DFT aims to calculate the electronic structure of a material given a fixed set of nuclei. To do this, one must solve the time-independent Schrödinger equation for the electrons

$$\hat{\mathcal{H}}\psi = E\psi. \tag{3.37}$$

DFT tackles this problem by recasting this equation in terms of the electron

density $n(\boldsymbol{r})$, which is related to the electronic wavefunction,

$$n(\boldsymbol{r}) = N \int \mathrm{d}\boldsymbol{r}_2 ... \int \mathrm{d}\boldsymbol{r}_N \psi^*(\boldsymbol{r}_1, \boldsymbol{r}_2, ..., \boldsymbol{r}_N)\, \psi(\boldsymbol{r}_1, \boldsymbol{r}_2, ..., \boldsymbol{r}_N)\,. \tag{3.38}$$

We will not go into great detail about exactly how this is done, however it is most common to use the Kohn-Sham formulation [74, 75], where the Schrödinger-like equations to be solved are

$$\hat{\mathcal{H}}_{\mathrm{KS}} \psi_i(\boldsymbol{r}) = \epsilon_i \psi_i(\boldsymbol{r})\,, \tag{3.39}$$

where $\epsilon_i$ is the eigenvalue of $\psi_i(\boldsymbol{r})$. This treats the electrons as non-interacting; this makes this problem solvable. The electron density is

$$n(\boldsymbol{r}) = \sum_i^N |\psi_i(\boldsymbol{r})|^2\,, \tag{3.40}$$

and the Hamiltonian is

$$\hat{\mathcal{H}}_{\mathrm{KS}} = -\frac{\hbar^2}{2m_{\mathrm{e}}}\nabla^2 + v_{\mathrm{ext}}(\boldsymbol{r}) + v_{\mathrm{H}}(\boldsymbol{r}) + v_{\mathrm{XC}}(\boldsymbol{r})\,, \tag{3.41}$$

with $v_{\mathrm{ext}}(\boldsymbol{r})$ accounting for external potentials, $v_{\mathrm{H}}(\boldsymbol{r})$, the Hartree potential, arising from electrostatic potential from the electrons, and $v_{\mathrm{XC}}(\boldsymbol{r})$, the exchange-correlation potential, which is a term required to make the non-interacting electrons behave as if they are interacting. The correct choice of these potentials will, in theory, give exact results that would be solutions to the Schrödinger equation, and developing the best potentials is an active area of research. The current best options are available in most implementations. In practice, when using DFT to tackle a problem, how one goes about solving these equations is decided by the implementation of DFT one uses. In this thesis, we employ CASTEP [76].

CASTEP is a plane-wave psuedopotential code that implements Kohn-Sham DFT. This approach writes $\psi_n(\boldsymbol{r})$ as the sum of plane waves up to a certain cut-off energy. This well approximates the infinite sum that would be needed to make this an exact representation. It then uses pseudopotentials (note that these are different to the potentials discussed before) to replace the nuclei and core electrons with a simpler function to reduce the computational complexity; this function exactly matches the behaviour far from the nucleus. Near the nucleus

the approximation is less good, however this does not change the physics of the system as the electrons are typically far from the Fermi energy, and therefore do not significantly contribute to the overall behaviour. By applying the CASTEP to problems in condensed matter physics one is able to get a very good approximation to the electronic structure of a material. The results from these calculations can be compared to experimental results to gain greater physical insight into the system of interest, a strategy which is employed regularly throughout this thesis.

# Chapter 4

# Megahertz dynamics in $Cu_2OSeO_3$

This chapter presents muon-spin spectroscopy ($\mu$SR) measurements on one of the most well-studied skyrmion-hosts, $Cu_2OSeO_3$. I present high-statistics, high-resolution measurements of the $\mu$SR asymmetry in the skyrmion lattice (SkL). We find that the SkL phase of $Cu_2OSeO_3$ exhibits emergent dynamic behaviour at megahertz frequencies, likely due to collective excitations, allowing the SkL to be unambiguously identified from the $\mu$SR response. These results are analysed, with support of density functional theory (DFT) calculations of the muon stopping site and simulations of the magnetic field at these muon sites. From this analysis, and additional measurements following different cooling protocols and under application of an electric field, we are able to study the nature of the SkL when it exists as a long-lived metastable state. Specifically, we show that it is highly unlikely that the SkL exists throughout the bulk of the sample in this metastable state at the fields and temperatures where it is often observed.

This chapter is based on work published in Ref. [16]. The samples were provided by collaborators at the University of Warwick. The phase diagram was measured using AC susceptibility by myself. The $\mu$SR data were measured by myself, alongside collaborators from Durham University and ISIS Neutron and Muon Source; sample preparation for these experiments was similar. The

analysis of the $\mu$SR data is my own and utilises muon site calculations performed by a collaborator, Zachary Hawkhead (Durham University), which I subsequently interpreted and used to calculate the field at the muon site for various different magnetic structures. The mathematical formulation of the SkL as a Fourier series was a combination of my work and that of a collaborator, Ben Huddart (Durham University). The overall discussion is my own.

## 4.1 Introduction

Of the Bloch SkL-hosting materials [20], there are perhaps none more studied in recent years than $Cu_2OSeO_3$. An insulating, multiferroic ferrimagnet which crystallises in the $P2_13$ structure [77], $Cu_2OSeO_3$ has a variety of properties that make it particularly intriguing; if it were not for the low magnetic ordering temperature of $T_c \simeq 57$ K it would be the prime candidate for applications in spintronic devices. The stability and extent of the skyrmion lattice in $Cu_2OSeO_3$ can be controlled both with an externally applied electric field ($E$-field) [78] and through chemical substitution of the magnetic Cu ions [79, 80].

The $P2_13$ space group is noncentrosymmetric and hence lacks a centre of inversion symmetry, meaning that $Cu_2OSeO_3$ can host a Dzyaloshinskii-Moriya interaction, as discussed in Chap. 2. (The structure of $Cu_2OSeO_3$ is discussed later with regards to the muon stopping sites, and can be seen in Fig. 4.5.) In the structure there are two inequivalent $Cu^{2+}$ sites, each with different coordination environments. The site we denote $Cu^{I}$ has trigonal bipyramidal cooridination geometry, whereas $Cu^{II}$ has a square pyramidal geometry; these sites are present in the ratio 1:3. Both sites have $S = 1/2$, however they antialign, creating a ferrimagnetic structure [81, 82, 83]. The exchange interaction between the ions is mediated through the oxygen atoms.

The magnetic phase diagram of pristine $Cu_2OSeO_3$ is shown in Fig. 4.1, here based on AC susceptibility measurements of the same crystal that is later discussed in this chapter. The SkL exists in a small pocket, spanning a few Kelvin just below $T_c$, when a field of around 20 mT is applied. Below $T_c$, at zero-field,

and under application of a small external field, a helical state is stabilised; once the external field is significantly large, this state deforms into a conical state. At high field the system becomes field-polarised. Above $T_c$ $Cu_2OSeO_3$ is paramagnetic. This phase diagram is typical for chiral magnetic systems which host a SkL phase.

The phase diagram of $Cu_2OSeO_3$ near the SkL changes only slightly when changing the angle between the applied magnetic field and the crystallographic axes; what is far more dramatic is changes under different field-protocols [84, 85]. The phase diagram shown in Fig. 4.1 is that obtained by cooling in zero applied field (typically denoted ZFC). When rapidly cooling through the SkL a metastable SkL is formed; this metastable state persists over a much wider range of temperature and magnetic field, and is affected dramatically by chemical substitution [79]. This non-equilibrium phase allows study of the SkL over a much wider range of conditions, and as such can be very useful for understanding the properties of the SkL. Other field-cooling protocols (for example, cooling in a large applied field) further stabilise different magnetic phases (for example, a tilted conical or second, distinct SkL phase) [84, 85]. Although these phases are beyond the scope of this thesis, it is important to be aware of the dramatic affect on the phase diagram relatively subtle changes can make.

Another way to change the stability, and hence extent, of the SkL in $Cu_2OSeO_3$ is through application of an electric-field [78]. Applying an electric-field parallel to the applied magnetic field enhances the extent of the SkL, whereas anti-parallel application inhibits it. This once again provides a way to probe both the static nature of the SkL, and the dynamics of the state; rapid removal of the $E$-field will change the equilibrium state and allow the effects of metastability to be studied [86].

Whilst the equilibrium, static magnetism of $Cu_2OSeO_3$ is relatively well understood, it is also important to study the spin dynamics of the SkL. Originally detected using microwave spectroscopy techniques, $Cu_2OSeO_3$ demonstrates the excitations typical for the Bloch skyrmion [87]; three modes in the gigahertz regime

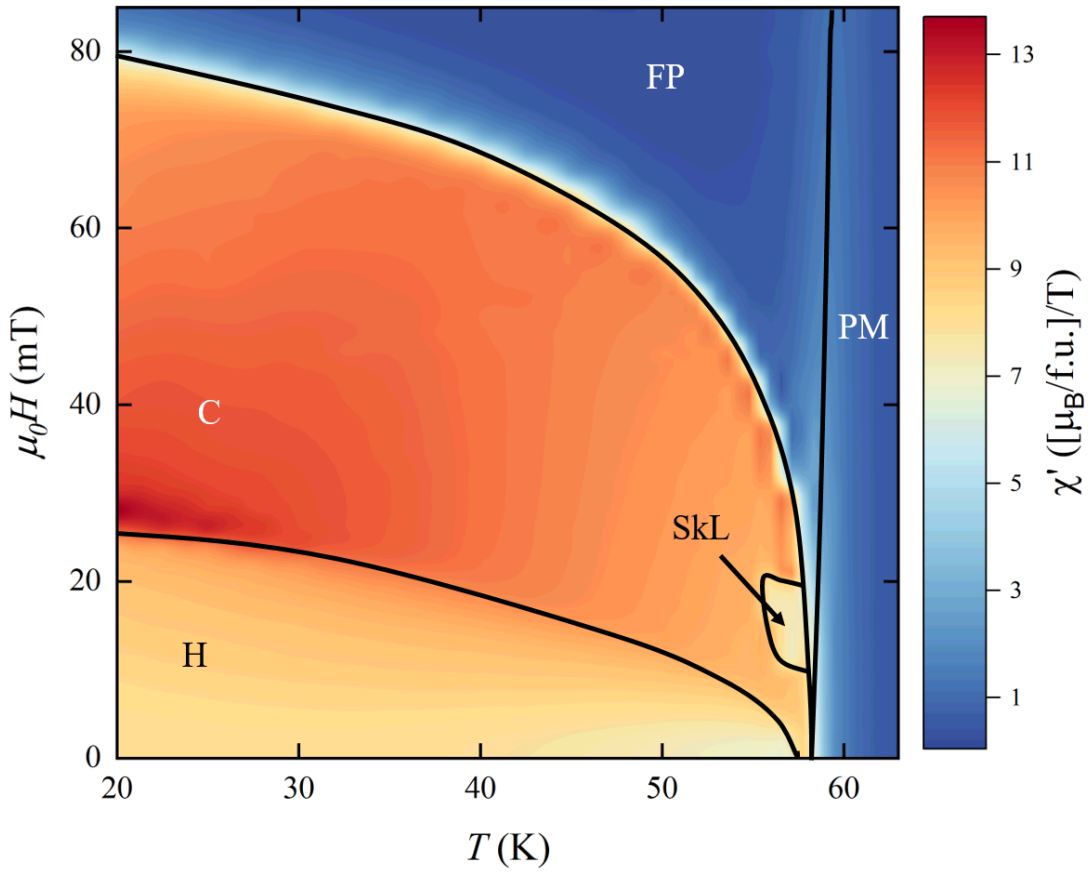


**Figure 4.1:** The magnetic phase diagram of a single crystal of $Cu_2OSeO_3$, as measured by AC susceptibility. For these measurements the external magnetic field was applied along the [100] crystallographic axis. In addition to the constant applied field, and a time varying magnetic field of amplitude 0.3 mT was also applied at a frequency of 111 Hz. Indicated phases are helical (H), conical (C), skyrmion-lattice (SkL), field-polarised (FP), and paramagnet (PM). The lines separating phases are guides to the eye.

are identified as excitations of the Bloch skyrmion: counterclockwise, breathing, and clockwise modes [44], see Chap. 2. In addition, $Cu_2OSeO_3$ also hosts terahertz excitations due to spin excitations in high-energy magnon bands [88, 89, 90, 91]. In general, ordered magnets host diffusive and propagating magnetic excitations; we therefore expect excitations over a wide range of frequencies. Despite this, there are few reports on the excitation spectra of SkL-hosting materials in the megahertz regime. In this chapter we will use muons to observe a dynamic response in $Cu_2OSeO_3$ on the megahertz timescale that is unique to fields which stabilise the SkL.

## 4.2 Experimental Methods

Single crystal and polycrystalline $Cu_2OSeO_3$ samples were synthesised and characterised by Geetha Balakrishnan, Ales Štefančič, and Samuel Holt at the University of Warwick, as described in Ref. [92].

Longitudinal-field (LF) $\mu$SR measurements were carried out at the STFC-ISIS facility, UK. Measurements on single-crystal samples of $Cu_2OSeO_3$ were performed using the MuSR instrument, with a mosaic of crystals aligned such that the external magnetic field $B_{\text{ext}}$ was applied along the [111] direction. The mosaic was arranged in a Ag foil packet and mounted in a $^4$He cryostat. Measurements on a polycrystalline pellet of $Cu_2OSeO_3$ under the application of an $E$-field applied parallel/antiparallel to $B_{\text{ext}}$ were made using the EMU instrument. The $Cu_2OSeO_3$ pellet had electrical contacts deposited by sputtering consisting of a base layer of 15 nm Al, topped with 500 nm Ag and was mounted in a PTFE frame on a grounded Al backing plate, with an electric connection made to the other side of the pellet. In all other cases the samples were packed in Ag foil envelopes (foil thickness 12.5 $\mu$m) and mounted on a silver plate. Transverse field (TF) $\mu$SR measurements of a single crystal of $Cu_2OSeO_3$ were performed at the Swiss Muon Source, Paul Scherrer Institut, Switzerland using the GPS instrument. Regardless of measurement orientation, unless otherwise stated, samples were cooled in the absence of an applied field. Data analysis was carried out

using the WiMDA program [68] and made use of the MINUIT algorithm [93] via the iminuit [94] Python interface for global refinement of parameters.

DFT calculations were performed to calculate the muon stopping sites in $Cu_2OSeO_3$ using the plane wave, pseudopotential code, CASTEP [76]. Calculations were carried out using the PBE exchange-correlation functional [95], with the experimentally obtained crystal structure relaxed with the lattice parameters held constant. Modeling the implanted muon as an ultrasoft hydrogen pseudopotential, various initial positions were used to randomly sample the crystal structure. Calculations are converged to 10 meV per cell. The structure and the implanted muon were allowed to relax until the calculated forces on the atoms were all $< 5\times10^{-2}$ eV Å$^{-1}$ and the total energy and atomic positions converged to within $2 \times 10^{-5}$ eV per atom and $1 \times 10^{-3}$ Å, respectively. These muon positions were subsequently used in the MUESR code [96] to calculate transverse-field (TF) $\mu$SR spectra for various magnetic structures in $Cu_2OSeO_3$. For these calculations, the temperature dependence of the saturated magnetic moment was taken from Ref. [82], and the magnetic structures used were as presented in Refs. [97, 98, 99]. As the sample shape was approximately cubic, we have used a demagnetisation factor of $N = 1/3$ in all our simulations.

## 4.3 Results & Discussion

### 4.3.1 The skyrmion lattice in equilibrium

We will first consider the $\mu$SR response to the equilibrium SkL, which is stabilised under application of an applied external field. This gives us access to information on the static magnetism through TF $\mu$SR, and on the dynamics of the system with LF $\mu$SR. TF $\mu$SR measurements of $Cu_2OSeO_3$ have previously been published [98], and show that the magnetic phase can be identified from the TF $\mu$SR response. Here we consider the dynamic response of the muon-spin to the SkL.

LF $\mu$SR measurements on a mosaic of single-crystals of $Cu_2OSeO_3$ were performed on warming, after cooling in zero applied magnetic field (ZFC). Temper-

ature scans were performed at $B_{\text{ext}} = 22$ mT, which stabilises the SkL state between $\approx$ 56 K and $\approx$ 58 K, and at $B = 40$ mT, which does not stabilise a SkL at any temperature [Fig. 4.2(a)]. Example spectra are shown in Fig. 4.2(b), where the asymmetry decays monotonically, with an exponential decay typical of relaxation due to the dynamics of a dense array of fluctuating local moments. Since the material is in an ordered phase, we expect the $\mu$SR spectra to have contributions from (i) muons with their spins initially oriented perpendicular to the local magnetic field at the muon site; (ii) those muons with spin components initially parallel to the local magnetic field. However, the width of the pulsed beam at the ISIS facility does not typically allow us to resolve the first of these contributions in many of our spectra, and so our signal is then due to the muon with spin aligned along the local field. The spectra are well described at all measured temperatures using a relaxation function

$$A(t) = a_{\text{r}} \exp(-\lambda t) + a_{\text{b}}, \tag{4.1}$$

where the component with amplitude $a_{\text{r}}$ captures the contribution from muons stopping in the sample with their spin initially aligned along the local magnetic field, and the baseline amplitude $a_{\text{b}}$ accounts for muons that stop outside of the sample or at positions in the material where a fluctuating field does not dephase them. The relaxing amplitude $a_{\text{r}}$ increases as the temperature is raised through the ordering temperature $T_{\text{c}}$. To model this, $a_{\text{r}}$ is constrained to

$$a_{\text{r}} = a_{\text{r0}} + \frac{L}{1 + \exp[-k(T - T_{\text{c}})]}, \tag{4.2}$$

where $a_{\text{r0}}$ is the relaxing amplitude for $T \ll T_{\text{c}}$, $L$ is difference between the maximum and minimum relaxing amplitude, and $k$ is a parameter which defines the rate of increase of $a_{\text{r}}$ around $T_{\text{c}}$. This allows one to extract $T_{\text{c}}$ independently of $\lambda$. (Extracted values of $T_{\text{c}}$ agree well with those from AC susceptibility, appearing to be sensitive to the top of the SkL where the transition from magnetic order to disorder commences.) There is no temperature dependence to $a_{\text{b}}$, leaving only $\lambda$ [Fig. 4.3(a)] varying in our fits. Other parameters refined globally at each applied field are shown in Tab. 4.1. (This method is particularly helpful for

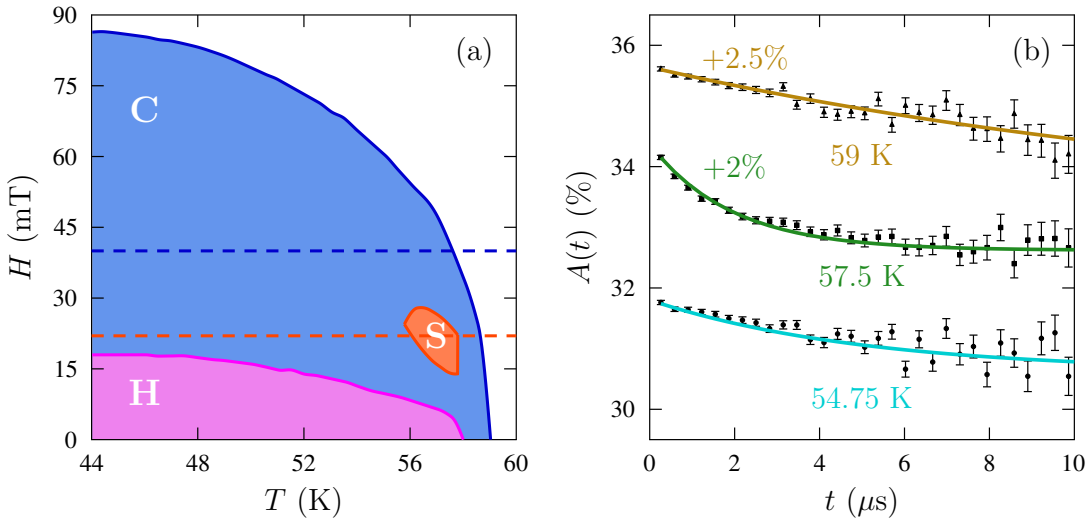


**Figure 4.2:** (a) Phase diagram of $Cu_2OSeO_3$, showing conical (C), helical (H) and skyrmion (S) phases, reproduced from Ref. [92]. Orange color: fields at which the SkL is stabilised, blue: fields which only stabilise C order below $T_c$, and pink: H order. Dashed lines indicate fields at which LF $\mu$SR measurements were performed. (b) Example LF $\mu$SR spectra for $Cu_2OSeO_3$ measured in $B = 22$ mT. Top two data sets are shown with indicated vertical offsets.

reliably extracting correlated parameters, such as $a_b$ and $\lambda$; by refining $a_b$ at all temperatures simultaneously, one is able to obtain the best estimated of $\lambda$.)

There are striking differences in the behaviour of $\lambda$ between the two temperature scans. On scanning through the fields in the $B$–$T$ phase diagram where the SkL is realised, $\lambda$ is significantly enhanced at those temperatures where the SkL phase is found, resulting in a broad shoulder above 56.5 K that terminates in a peak on the high temperature side. No such enhancement is observed at

**Table 4.1:** Parameters obtained from fitting LF $\mu$SR measurements of $Cu_2OSeO_3$ at a particular applied field to Eqns. 4.1 and 4.2.

| $\mu_0 H$ (mT) | $a_b$ (%) | $a_{r0}$ (%) | $k$ | $L$ (%) | $T_c$ (K) |
|---|---|---|---|---|---|
| 22 | 30.62(2) | 1.17(2) | 1.69(9) | 1.52(3) | 57.78(3) |
| 40 | 31.46(9) | 1.12(9) | 0.70(12) | 1.19(13) | 57.8(2) |

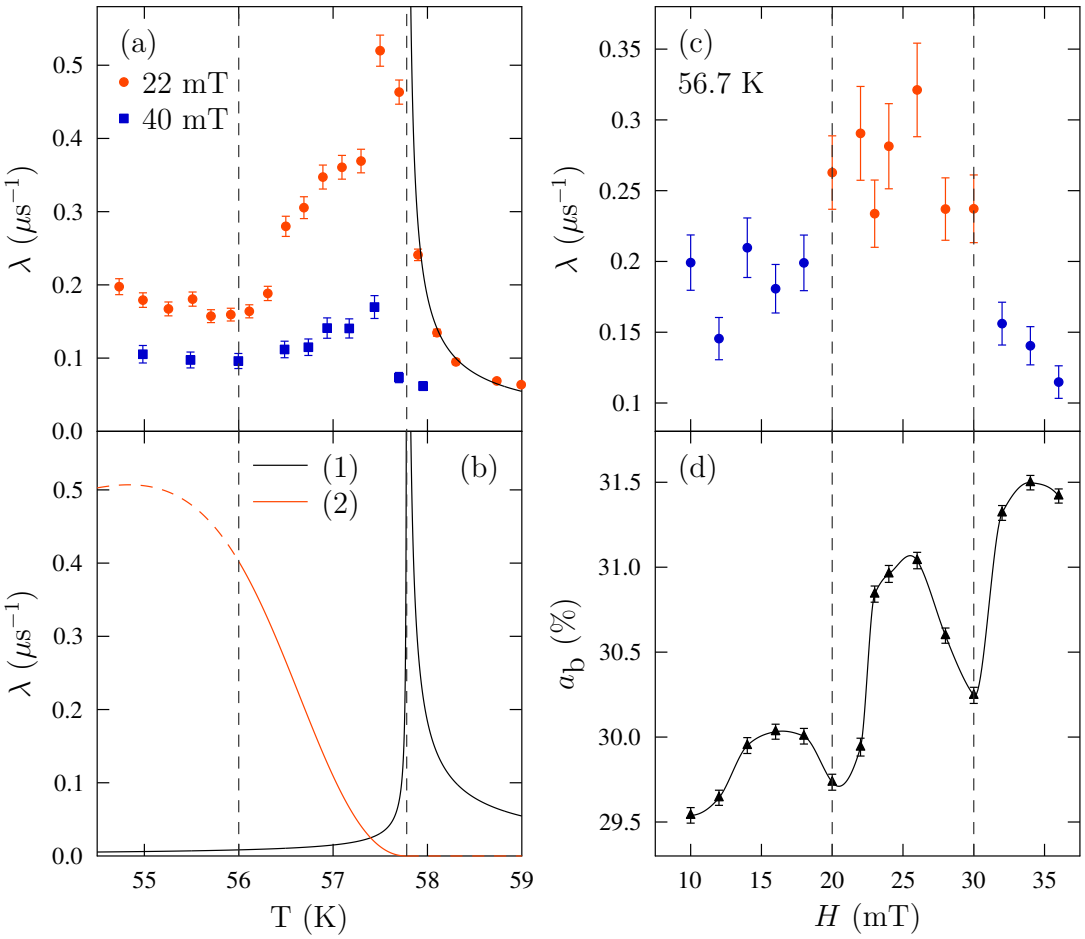


**Figure 4.3:** (a) Extracted values of $\lambda$ from LF $\mu$SR measurements of $Cu_2OSeO_3$. (b) Simulations of contributions to $\lambda$ due to: (1) critical slowing down of magnetic fluctuations near $T_c$ (black solid line); (2) reduction in frequency of gigahertz spectral density (orange solid line). Orange dashed line indicates the value of $\lambda$ one would obtain if the SkL was stabilised at those temperatures. Vertical dashed lines indicate the location of the SkL at 22 mT from AC susceptibility. (c) Extracted values of $\lambda$ from a field scan at $T = 56.7$ K, with (d) accompanying baseline amplitude (solid line is a guide to the eye). Dashed lines indicate the location of the SkL at 56.7 K.

higher fields. This indicates significantly enhanced spectral density $J(\omega)$ around $\omega_0 \simeq 3$ MHz in the SkL phase. Therefore, we conclude that LF $\mu$SR has a characteristic response to the SkL, specifically an increase in relaxation rate compared to the surrounding magnetic phases.

As variation in the amplitude of the fluctuating field $\Delta/\gamma_\mu$ is likely to follow the magnetisation, the observed variation in $\lambda$ likely results from the temperature dependence of $\nu$, and could reflect: (1) critical slowing down of the magnetic fluctuations near $T_c$, typical of a second-order phase transition; (2) reduction in frequency of the skyrmion excitation modes near $T_c$; (3) other collective dynamics of the system occurring on the megahertz timescale. We explore each of these effects in turn.

(1) Above $T_c$, the relaxation rate $\lambda$ is well described by power-law behaviour [100] typical of critical fluctuations in a 3D Heisenberg magnet [101, 102, 103, 104] with a fluctuation time $1/\nu \propto |T - T_c|^{-w'}$ with $w' = 0.709$, typical for a 3D Heisenberg magnet. Below $T_c$ the same critical parameters do not account for $\lambda$ which should show a sharp rise very close to $T_c$ [Fig. 4.3(b)].

(2) The skyrmion rotational and breathing modes are expected to broaden and decrease in frequency (or soften) as $T$ approaches $T_c$ from below (see, for example, Ref. [79]), contributing to the spectral weight $J(\omega)$ centred around $\omega_0 = \gamma_\mu B_{\text{ext}}$ ($2\pi \times 3$ MHz at our value $B_{\text{ext}}$). Assuming that the time-dependent magnetisation that results from skyrmion modes determines the relaxation, we can use typical exponents for a 3D Heisenberg model to predict

$$\lambda = \frac{2\Delta_0^2 \nu_0 \left[1 - (T/T_c)^{3/2}\right]^{0.73} (1 - T/T_c)^{1.43}}{\gamma_\mu^2 B_{\text{ext}}^2 + \nu_0^2 (1 - T/T_c)^{2.86}}. \tag{4.3}$$

The derivation of this result is discussed in more detail in App. A. $Cu_2OSeO_3$ exhibits its lowest frequency skyrmion mode (counter-clockwise rotational) at $\nu_0 = 2.3$ GHz [43], giving the behaviour shown in Fig. 4.3(b), which does not describe the measured data. Note that $\nu_0 = 10$–$20$ GHz would be a better match to the data, but this is at least a factor of 3–4 higher than the three lowest energy modes of the SkL in $Cu_2OSeO_3$ [43], but too low in frequency to be the THz excitations previously observed.

(3) Alternatively, $\lambda$ could reflect the occurrence of other low-energy, collective excitations emerging from the SkL involving individual skyrmions or from motion of the SkL (e.g. diffusive excitations resulting when the SkL undergoes collective motion, or where individual skyrmions are created or destroyed.) This is plausible given that diffusive dynamics for single skyrmions [105, 106] typically occur in the gigahertz regime, while the motion of Bloch points along skyrmion tubes are likely to occur at megahertz frequencies. It could also be that $\Delta$ increases near the transition owing to rapid changes in width of the local field distribution at the muon sites. In each of these cases a change in the distribution of skyrmions in the SkL is required.

To further investigate the response to the SkL, LF $\mu$SR measurements were also made as a function of increasing applied magnetic field $B$ at fixed temperature $T = 56.7$ K after ZFC. These data are also well described by Eq. 4.1, with a field-independent amplitude $a_\mathrm{r}$ and a baseline $a_\mathrm{b}$ that increases with $B$, as is often observed in LF $\mu$SR. We again observe enhanced values of $\lambda$ in the SkL phase, along with discontinuous behaviour in $a_\mathrm{b}$ marking the transitions in and out of the SkL phase [Fig. 4.3(c–d)], providing another method of identifying the SkL phase boundaries. A likely explanation of the observed behaviour comes from demagnetisation effects which are known to cause the magnetic transition in and out of the SkL state to occur at slightly different fields for different parts of the sample [107]. This leads to increased disorder in the field distribution at the muon sites, resulting in fewer muons stopping with their spin parallel to the local field, and hence dephasing too rapidly to be observed resulting in a loss of the total, and hence baseline, asymmetry. It is also possible that, as $a_\mathrm{b}$ is correlated with $\lambda$ in the fitting, that these changes actually represent changes in the dynamics. Unfortunately it is not possible to globally constraint $a_\mathrm{b}$ as is done for measurements that are taken as a function of $T$, however this would not change the conclusions drawn here: the field range that stabilises a SkL is clear from LF $\mu$SR.

### 4.3.2 Metastable skyrmion lattice

Having addressed the dynamic response of the equilibrium SkL, we now turn our attention to the metastable SkL, stabilised either through rapid cooling in an applied field (passing through the equilibrium SkL in the $B$–$T$ phase diagram), or via application of an electric field parallel/anti-parallel to the applied magnetic field. We will start by discussing the internal field distribution, for which we have employed calculations of the muon stopping sites. We performed TF $\mu$SR measurements on a single crystal of $Cu_2OSeO_3$ after ZFC and rapid cooling in applied field (FC) ($\approx$ 17 K/minute). This rapid FC is expected to stabilise metastable skyrmions at temperatures that host a conical phase for ZFC [79]. TF measurements are sensitive to the static internal magnetic field distribution of the sample at the muon sites, and have been shown to be sensitive to changes in the magnetic state in this material [98]. Internal field distributions derived from TF measurements measured after both ZFC and rapid FC are compared in Fig. 4.4 in an applied field of 22 mT. There is a characteristic change in distributions for the different magnetic states [98], which are observed after both field protocols, but no significant difference is observed between the two protocols, suggesting that the local field distribution is similar in both cases. (The peak observed at 22 mT at all temperatures occurs from muons stopping outside of the sample and precessing in the applied field.)

To model magnetic field distributions for the ordered states in $Cu_2OSeO_3$, muon stopping sites were determined using DFT methods to relax the structure with an implanted muon. We find different sites to those identified in Ref. [83], which were determined by finding the minima of the unperturbed electrostatic potential in the crystal with no muon present. In $Cu_2OSeO_3$ we find that the positions of the muons are clustered into 3 distinct sites shown in Fig. 4.5, with coordinates given in Tab. 4.2. Sites 1 and 2 are each located approximately 1 Å from the nearest O ion, which is common for muon stopping sites. All three sites have low relative energy differences, suggesting that they could all be occupied, however site 3 is notable in that it sits along the Cu–O bond inside the

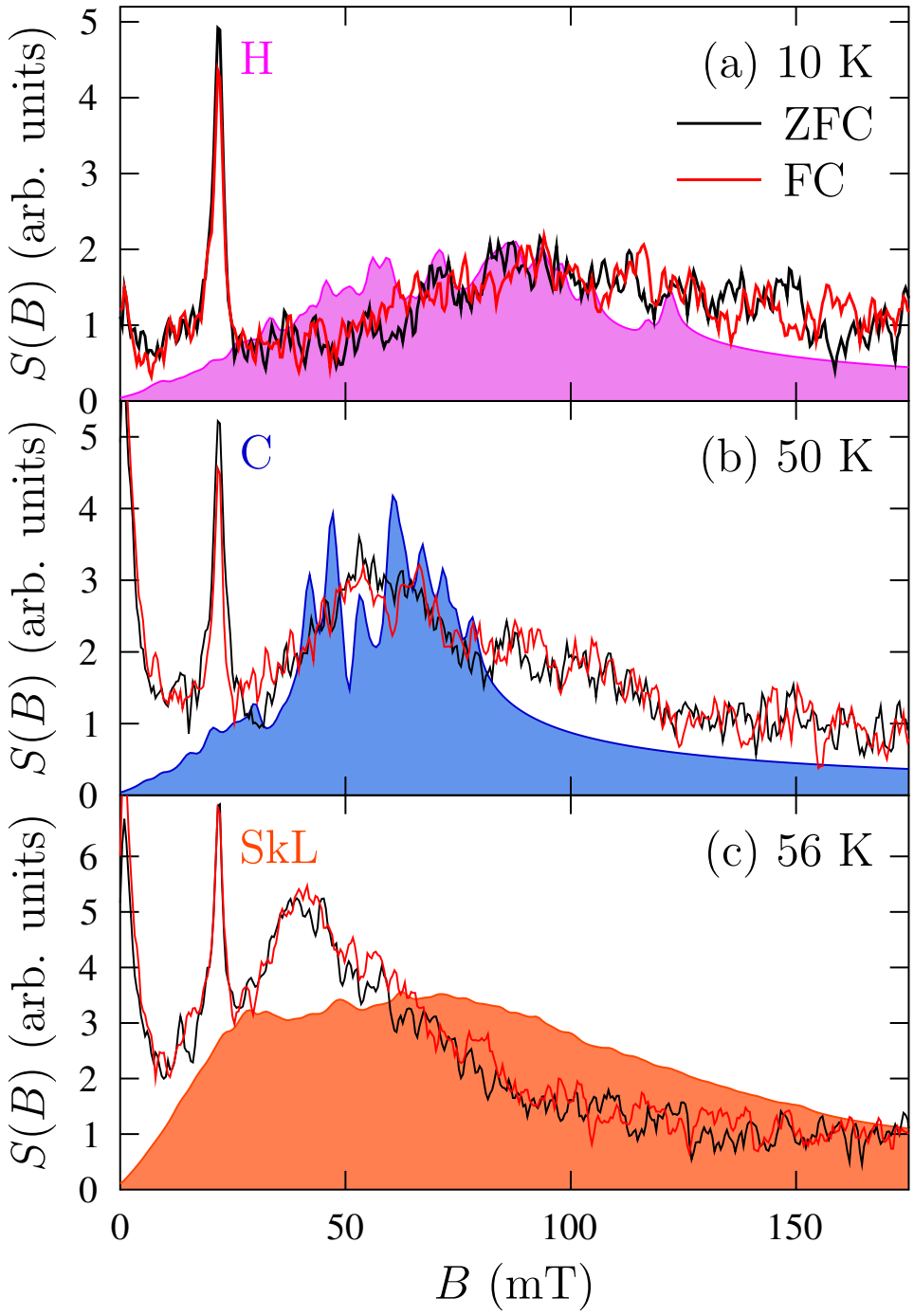


**Figure 4.4:** Internal magnetic field distributions $[S(B)]$ of $Cu_2OSeO_3$ at various $T$ measured by TF $\mu$SR for $B_{\text{ext}} = 22$ mT, with comparison to simulations. Black lines: measurements performed after ZFC; red lines: after rapid FC ($\approx$ 17 K/minute); solid color: simulated distributions for different spin structures.

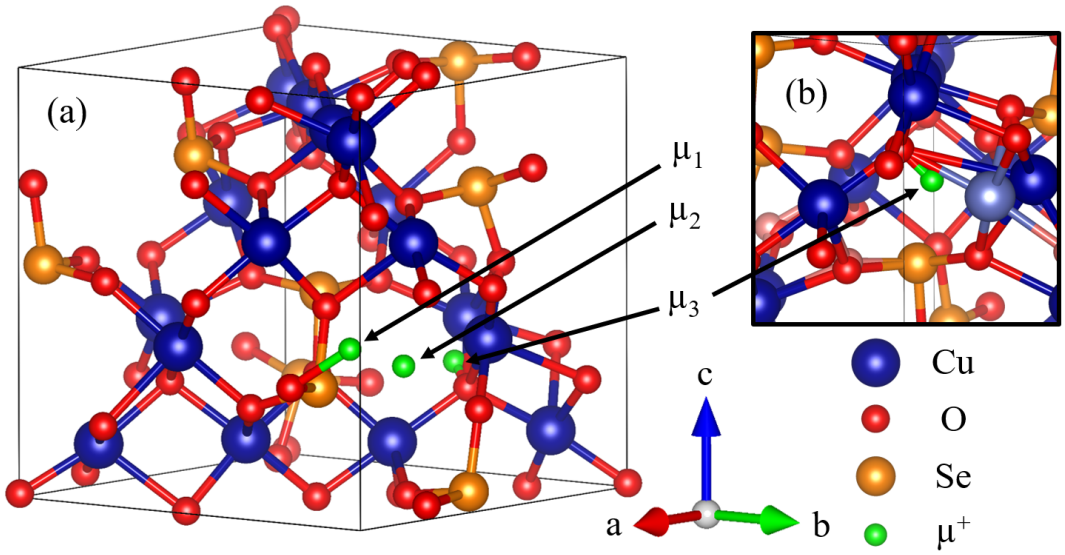


**Figure 4.5:** (a) Muon sites in $Cu_2OSeO_3$, with coordinates in Tab. 4.2. (b) The local environment around muon site 3, showing the Cu ion position in the absence of the muon (light translucent), and after implantation (full colour). Image produced with VESTA [108].

tetragonal cage of Cu ions and causes significant distortion of the crystal, with the nearest Cu ion being displaced by approximately 0.7 Å, approximately 35% of the undistorted bond length. The initial muon positions that relax to this final site are mostly initialised inside the Cu cage. Due to the large local distortions of the crystal, it is unlikely an external muon would have sufficient energy to occupy this site due to the significant energy barrier to entering the cage. It is also likely that such a distortion to the Cu–O bond length would cause a collapse of the local crystal structure. We, therefore, conclude that site 3 is unoccupied, leaving two sites which matches the experimental observations with zero-field $\mu$SR of two magnetic sites [83]. Muon sites 1 and 2 show no significant distortion of the Cu or Se ions, however the O ions local to the muon are commonly shifted so as to be closer to the muon, sometimes by up to 1 Å.

I have performed simulations of the magnetic field distribution as seen by the muon using MUESR [96], as discussed in Sec. 4.2. Despite identification of the stopping sites, DFT methods are not currently able to predict the proportion

**Table 4.2:** Calculated muon stopping sites in $Cu_2OSeO_3$. Energies are given relative to the lowest energy site.

| Muon site | Fractional coordinates | Energy (eV) |
|---|---|---|
| 1 | (0.906, 0.590, 0.100) | 0.00 |
| 2 | (0.172, 0.365, 0.319) | 0.09 |
| 3 | (0.224, 0.670, 0.289) | 0.15 |

of muons with will stop in each site; we therefore have to estimate this through comparison to experiment. In the helical state our calculations predict an average field in site 1 of 1.04 times the magnitude of that in site 2, close to the experimentally observed zero-field value of 1.07(2) [83]. Therefore, I have used the ratio of 1:4 for the occupancies of sites 1:2 for the simulations shown here, as found in Ref. [83]. It is worth noting that, should site 3 be included in the simulations, the magnetic field at this muon site is significantly higher than the field at sites 1 or 2 for all magnetic structures trialled, which is inconsistent with the measured spectra. This further supports the assertion that this site is not occupied in experiment.

To simulate the SkL configuration, a Fourier decomposition using the propagation vector formalism of the triple-$q$ model used in Ref. [98] and introduced in Chap. 2 was performed. (It is not possible to use MUESR to calculate the magnetic field at the muon site from the triple-$q$ model directly due to the complex normalisation required.) The triple-$q$ model is given by $\boldsymbol{m}(\boldsymbol{r}) = \boldsymbol{m}_{\rm sk}/|\boldsymbol{m}_{\rm sk}|$ where

$$\boldsymbol{m}_{\rm sk}(\boldsymbol{r}) \;=\; \mathrm{Re}\left[\sum_{j=1}^{3} \boldsymbol{S}_j \exp(-\mathrm{i}\boldsymbol{q}_j \cdot \boldsymbol{r})\right]. \tag{4.4}$$

This represents the sum of three helices with propagation vectors $\boldsymbol{q}_1 = F(1,0,0)$, $\boldsymbol{q}_2 = F(-\frac{1}{2}, \frac{\sqrt{3}}{2}, 0)$ and $\boldsymbol{q}_3 = F(-\frac{1}{2}, -\frac{\sqrt{3}}{2}, 0)$, where $F = 2\pi/L_{\rm sk}$. We take the skyrmion wavelength $L_{\rm sk} = 63$ nm, similar to the value reported in Ref. [20]. The Fourier components are $\boldsymbol{S}_j = \hat{\boldsymbol{e}}_z + i\hat{\boldsymbol{e}}_j$, where $\hat{\boldsymbol{e}}_z = (0,0,1)$, $\hat{\boldsymbol{e}}_1 = (0,1,0)$, $\hat{\boldsymbol{e}}_2 = (-\frac{\sqrt{3}}{2}, -\frac{1}{2}, 0)$ and $\hat{\boldsymbol{e}}_3 = (\frac{\sqrt{3}}{2}, -\frac{1}{2}, 0)$. Once normalised, $\boldsymbol{m}(\boldsymbol{r})$ no longer represents a sum of helices (as written) because $1/|\boldsymbol{m}_{\rm sk}|$ is a function of the propagation

vectors $\boldsymbol{q}_i$. However, $1/|\boldsymbol{m}_{\mathrm{sk}}|$ has the same periodicity as the skyrmion lattice and can therefore be expressed as a two-dimensional (2D) Fourier series, i.e.

$$\frac{1}{|\boldsymbol{m}_{\mathrm{sk}}|}(x_1, x_2) \;=\; \sum_{n,m} c_{nm} \exp\left[-\mathrm{i}(nx_1 + mx_2)\right], \tag{4.5}$$

where $x_i = \boldsymbol{q}_i \cdot \boldsymbol{r}$ and we have used that fact that $\boldsymbol{q}_1 + \boldsymbol{q}_2 + \boldsymbol{q}_3 = 0$ to eliminate $\boldsymbol{q}_3$. In this expansion $n$ and $m$ can take all positive and negative integer values. We obtain the coefficients $c_{nm}$ via a 2D discrete Fourier transform of

$$\begin{aligned}\frac{1}{|\boldsymbol{m}_{\mathrm{sk}}|}(x_1, x_2) \;=\; \big[3 &+ \tfrac{3}{2}\cos x_1 + \tfrac{1}{2}\cos(x_1 - x_2) + \tfrac{3}{2}\cos x_2 \\ &+ \tfrac{3}{2}\cos(x_1 + x_2) + \tfrac{1}{2}\cos(2x_1 + x_2) \\ &+ \tfrac{1}{2}\cos(x_1 + 2x_2)\big]^{-1/2}.\end{aligned} \tag{4.6}$$

We can then express $\boldsymbol{m}(\boldsymbol{r})$ as the propagation vector expansion

$$\boldsymbol{m}(\boldsymbol{r}) \;=\; \mathrm{Re}\left[\sum_{n,m}\sum_{j=1}^{3} c_{nm}\boldsymbol{S}_j \times \exp\left[-\mathrm{i}(n\boldsymbol{q}_1 + m\boldsymbol{q}_2 + \boldsymbol{q}_j)\cdot\boldsymbol{r}\right]\right], \tag{4.7}$$

which represents a weighted sum of all helices whose propagation vectors are linear combinations of $\boldsymbol{q}_1$ and $\boldsymbol{q}_2$ with integer coefficients.

The simulated field distributions at the muon sites for helical, conical, and SkL states are shown in Fig. 4.4. The simulations describe the experimental results reasonably well, with the worst match being for the SkL where, on increasing field, the rapid increase followed by slow decrease of spectral weight is captured. but the absolute values do not agree closely. The good match between simulation and experiment in the helical and conical state show that the static magnetism in these phases is sufficient to describe the response on the muon timescale. The greater discrepancy between simulation and experiment in the SkL state provides further evidence, independently from the LF $\mu$SR already presented, that there is a significant dynamic effect on the muon timescale which affects the internal magnetic field distribution of the sample.

When employing different field cooling procedures in $Cu_2OSeO_3$, one either stabilises the equilibrium helical/conical state (if cooling in zero-applied field [ZFC]), or a metastable skyrmion lattice (if cooling in an applied field [FC]) [79].

To explain the lack of difference in the distributions observed after ZFC and FC protocols, one must consider the skyrmion density in the sample, and hence the proportion of muons that are sensitive to the SkL. Assuming the muon is sensitive to a magnetic structure when the order is continuous over 10 unit cells [109], the nature of the domains in the sample will affect the measurement. There are two limiting cases: (i) where the SkL grows as a single domain, and (ii) where the SkL forms random domains. For (i), the proportion of muons sensitive to the SkL will be equal to the number density of skyrmions in the sample $N_{\mathrm{sk}}$. For (ii) only muons in sufficiently large domains see the the SkL. I have simulated this with a 2D hexagonal array of magnetic order and results are shown in Fig. 4.6. For the majority of muons to be sensitive to the SkL $N_{\mathrm{sk}}$ must approach 0.9. The real stabilisation mechanism of the SkL is likely to lead to a situation somewhere between these two cases, however, my model suggests that $N_{\mathrm{sk}}$ must be over 0.5 (and likely significantly higher) for $\mu$SR to be sensitive to the SkL. The lack of difference from TF $\mu$SR after different field protocols suggests that the metastable SkL does not exist over a sufficient proportion of the sample volume to be detectable with muons. We therefore suggest that the metastable SkL is not the majority phase through the entire sample. This could suggest that the metastable SkL is more likely to exist in particular parts of a sample, such as sample edges or defects. A propensity for skyrmions to form near surfaces would explain the lack of any muon signal up to an even higher volume fraction than that shown in Fig. 4.6; since the muons penetrate several microns into the sample in the measurements, changes to the magnetism at the surface of the sample are typically not observed.

To further investigate the effect of the SkL when it is not the majority phase in $Cu_2OSeO_3$, we have performed LF $\mu$SR measurements on a polycrystalline pellet of $Cu_2OSeO_3$ in the presence of an $E$-field coaligned with the $B$-field; this enhances the region of stability of the SkL in the $B$-$T$ phase diagram. An $E$-field of $\pm 3.6$ V/$\mu$m was applied across the sample, which is sufficient to cause significant changes to the magnetic phase diagram measured using other tech-

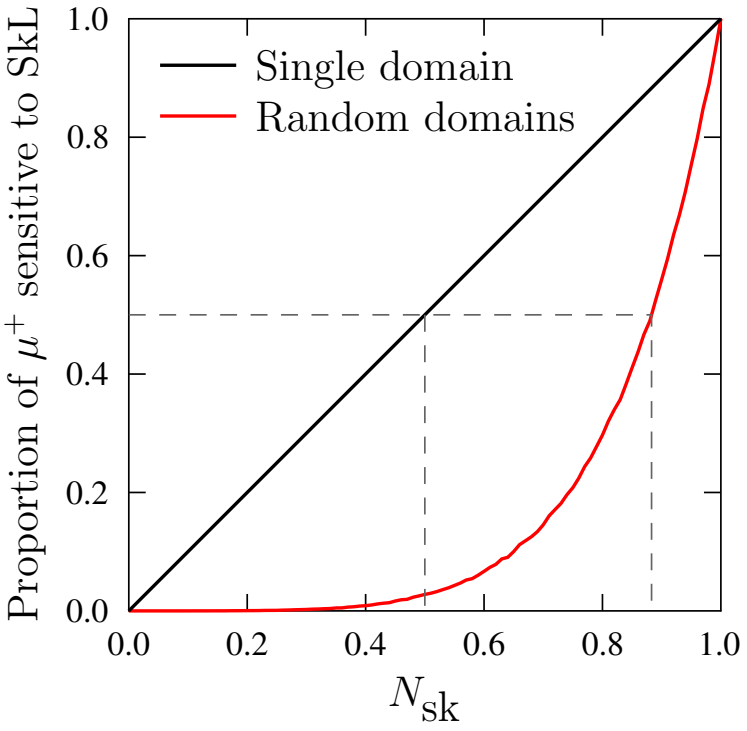


**Figure 4.6:** Estimated proportion of muons sensitive to the SkL for different types of domain growth. Dashed lines highlight a proportion of 50%, and the corresponding $N_{\mathrm{sk}}$ for each model.

niques [78, 86]. To prevent a build up of charge, the $E$-field was cycled, between on (positive polarity), off, on (negative polarity) and off, for 12.5 s periods at each value of $E$. All measured spectra were found to be similar to those for the mosaic of single crystals experiment, showing exponential decay. Different values of applied $E$-field within a cycle have little effect on $\lambda$; we show the region just below $T_c$ at 25 mT (cutting through the center of the SkL phase in this sample) in Fig. 4.7, as this is likely to have the most dramatic change in $\lambda$ due to the state changing between SkL and C. The lack of a difference in $\lambda$ can be explained given the specific $E$-field protocol employed. The application of an $E$-field can stabilise a SkL where it is not stable without one, so we might expect a difference. However, if we compare the cycle times and the $E$-field induced skyrmion lifetimes (using 40 s as found for $(Cu_{0.976}Zn_{0.024})_2OSeO_3$ [86]) we can estimate the changes in skyrmion number density during a cycle. For the protocol consisting of a skyrmion creation period (15 s) followed by an annihilation period (15 s) we find the number of skyrmions in both creation and annihilation periods make up around 5% of the volume fraction. The average number of $E$-field created skyrmions does not, therefore, change dramatically and is never the majority phase. Even if these lifetimes are shortened by an order of magnitude (as might be expected in a pristine material [79]), there is still significantly less than 50% skyrmion density at all times, which is likely to be too small to give a measurable difference using $\mu$SR. Whilst an effect may be detectable with longer $E$-field cycle times (leading to a higher proportion of the sample hosting the SkL), charge build-up prevents this being a viable experiment. In summary, we find that in those cases where the SkL is not the majority phase its dynamic signature is not resolved, making it likely that $\mu$SR is sensitive to the SkL in this system only when it is the majority volume phase.

Interestingly, when performing a temperature scan at 50 mT using the same $E$-field protocol, there is no peak in $\lambda$, which would be characteristic for a second-order phase transition. This suggests that at 50 mT, under the application of an $E$-field, the transition at $T_c$ is smeared out over a wider temperature range.

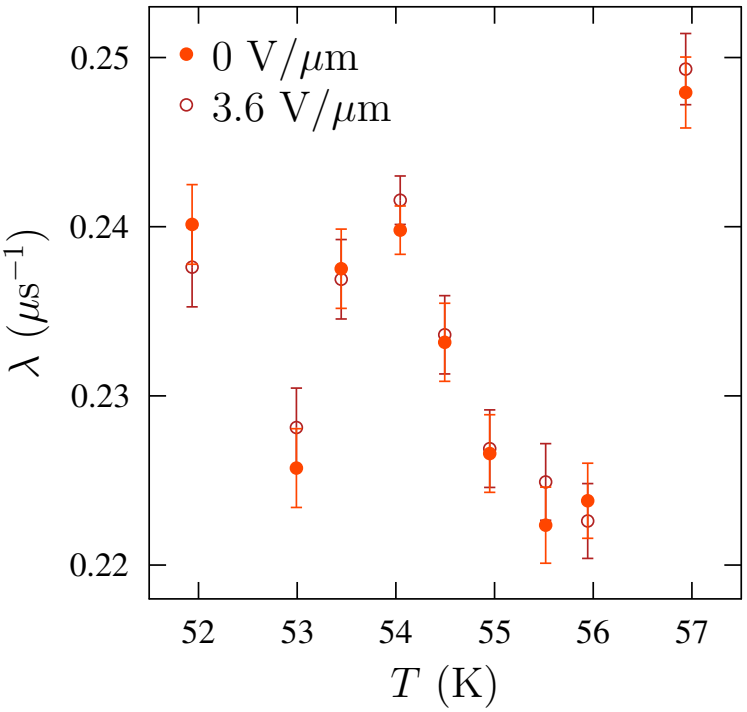


**Figure 4.7:** Relaxation rate $\lambda$ from fitting LF $\mu$SR measurements of $Cu_2OSeO_3$ under application of an $E$-field at 25 mT. Comparison shows the region where the greatest difference is expected between electric field on and off.

## 4.4 Conclusion

In $Cu_2OSeO_3$ high statistics LF $\mu$SR measurements reveal complex behaviour in the SkL phase, with clear evidence that there are enhanced dynamics on the megahertz timescale that are unique to the SkL. These dynamics appear both in measurements on warming in a fixed applied field, or at a fixed temperature on increasing magnetic field, and the location in the $B$–$T$ phase diagram of these dynamics corresponds well to the location of the SkL as measured with AC susceptibility. Above $T_c$ the dynamics of $Cu_2OSeO_3$ can be well described by critical slowing down of the magnetic fluctuations that one would expect at a second order phase transition. In the SkL of $Cu_2OSeO_3$ the source of the dynamics is unclear, but they cannot be well described by the reduction in frequency of characteristic excitations of individual skyrmions that one would expect near $T_c$. We suggest it is most likely that these dynamics reflect diffusive excitations of the skyrmion state, either through collective motion or the creation or decay of skyrmions.

Our TF $\mu$SR measurements and calculation of the muon stopping sites in $Cu_2OSeO_3$ allow theoretical models of the different magnetic states to be compared to experiment by calculating the local magnetic field at the muon stopping sites. We find good agreement for the helical and conical states, but show that, whilst the overall behaviour of the SkL is captured in our simulations, the distribution of fields is too broad compared to experiments. This likely reflects the importance of dynamics (which are known to narrow the spectra) when considering the structure of the SkL. We have performed TF $\mu$SR measurements under ZFC and FC protocols, as well as LF $\mu$SR measurements after application of an $E$-field for a brief period of time; both of these experiments should stabilise metastable skyrmions in $Cu_2OSeO_3$. The lack of difference when making these changes in both experiments indicates that the metastable SkL is unlikely to be found throughout the entire sample, and we suggest that it may be more stable at boundaries and surfaces.

# Chapter 5

# Phase separation in Zn-substituted $Cu_2OSeO_3$

In the previous chapter we studied the muon-spin spectroscopy ($\mu$SR) response to the skyrmion lattice (SkL) in $Cu_2OSeO_3$, finding that stabilisation of the SkL leads to enhanced dynamics on the megahertz timescale, most obviously seen by a sizeable increase in the rate of decay $\lambda$ of the muon-spin polarisation in longitudinal field (LF) $\mu$SR measurements. In this chapter we will extend our analysis to Zn-substituted $Cu_2OSeO_3$, where non-magnetic Zn ions replace magnetic Cu ions. Despite the initial observation in polycrystalline samples of Zn-substituted $Cu_2OSeO_3$ of multiple distinct SkL phases at different locations in the $B$–$T$ phase diagram, we are able to demonstrate with $\mu$SR that these pockets are in fact arising due to spatially separated magnetic domains. Our work, in combination with magnetometry and x-ray diffraction techniques, therefore concludes that the splitting of the SkL phase is simply due to a mixture of different Zn-substitution levels in different grains of the polycrystalline sample.

This chapter is based on work published in Ref. [92]. The samples were provided by collaborators at the University of Warwick. The $\mu$SR data were measured by myself, alongside collaborators from Durham University and ISIS Neutron and Muon Source. The analysis of the $\mu$SR data is my own, as is the overall discussion.

## 5.1 Introduction

There are relatively few distinct skyrmion systems that are currently known, and even fewer have desirable properties for applications. By chemically substituting these systems one can tailor the properties to attempt to match those required, and hence it seems probable that a material used for device applications may be a substituted system. It is therefore very important to understand the magnetism in chemically substituted skyrmion systems. To study these effects at the microscopic level, we employ LF $\mu$SR, where comparison to the results presented in the previous chapter allow us to gain a greater insight into the magnetism in related systems. We start by studying Zn-substituted $Cu_2OSeO_3$. The interest in substituted systems is particularly acute due to the observations of dramatic changes in magnetic properties at relatively low substitution levels; in $Cu_2OSeO_3$ these observations include the increased lifetime of metastable skyrmions at modest levels of Zn-substitution [79], and an expansion of the SkL phase upon Ni-substitution [80]. Perhaps most surprising of all these observations was the splitting of the SkL into two distinct phases in Zn-substituted $Cu_2OSeO_3$ [110]; it is this observation we will focus on here.

In Zn-substituted $Cu_2OSeO_3$, non-magnetic $Zn^{2+}$ ions are substituted into the crystal structure, replacing the $Cu^{2+}$ ions. The two inequivalent $Cu^{2+}$ sites in $Cu_2OSeO_3$, discussed in Chap. 4, are denoted as $Cu^{I}$ and $Cu^{II}$ and are present in the ratio 1:3, with the spin on each of these sites aligning antiparallel, forming a ferrimagnetic structure. As Zn is substituted into the system, the magnetic moment monotonically decreases [110], which is interpreted as the Zn preferentially substituting on the $Cu^{II}$ site. This reduction in magnetic moment is accompanied by a reduction in $T_c$ as the level of Zn-substitution is increased. Above approximately 2% Zn-substitution in polycrystalline samples, Ref. [110] observed that the SkL phase splits into two distinct regions in the $B$–$T$ phase diagram, and that upon further substitution the separation between these two SkL regions increases. This observation was repeated in our polycrystalline samples when measured with AC susceptibility [92]; here we employ $\mu$SR to understand the

microscopic magnetism.

## 5.2 Experimental Methods

Single crystal and polycrystalline $Cu_2OSeO_3$ samples were synthesised and characterised by Geetha Balakrishnan, Ales Štefančič, and Samuel Holt at the University of Warwick, as described in Ref. [92].

LF $\mu$SR measurements were carried out at the STFC-ISIS facility, UK. Measurements on powder samples of polycrystalline $Cu_2OSeO_3$ where the magnetic Cu ion is substituted for non-magnetic Zn ions at different concentrations (0%, 6.4% and 10.5%) were performed on the HiFi instrument. In all cases the samples were packed in Ag foil envelopes (foil thickness 12.5 $\mu$m) and mounted on a silver plate. Transverse field (TF) $\mu$SR measurements were performed at the Swiss Muon Source, Paul Scherrer Institut, Switzerland using the GPS instrument. Measurements of polycrystalline 6.4% Zn-substituted $Cu_2OSeO_3$ were performed. Regardless of measurement orientation samples were cooled in the absence of an applied field. Data analysis was carried out using the WiMDA program [68] and made use of the MINUIT algorithm [93] via the iminuit [94] Python interface for global refinement of parameters.

## 5.3 Results & Discussion

To enable direct comparison to LF $\mu$SR measurements of polycrystalline Zn-substituted $Cu_2OSeO_3$, we have measured the LF $\mu$SR response of polycrystalline pristine $Cu_2OSeO_3$. Measurements were performed at two different applied fields, 18 mT (which cuts through the SkL phase), and 35 mT (which does not, stabilising a conical state at most temperatures below $T_c$). The asymmetry spectra are very similar to those shown in Fig. 4.2(b), showing monotonic decay. As for the single crystal measurements, Eqn. 4.1 well describes the data, and once again the relaxing asymmetry is constrained to follow Eqn. 4.2. The extracted relaxation rate $\lambda$ is shown in Fig. 5.1 for both applied fields, with other fitted parameters

shown in Tab. 5.1.

Whilst the temperature resolution of the results presented in Fig. 5.1 is not sufficient to observe such fine structure as the shoulder shown in Fig. 4.3, $\lambda$ is still significantly enhanced when cutting through the SkL compared to measurements at 35 mT. Curiously, there is a more substantial peak at 35 mT than observed on single crystal measurements at 40 mT, suggesting that the nature of the transition at these fields changes. As $\mu_0 H_{\text{ext}}$ increases the transition becomes more gradual (reflected in the changing gradient of the conical to field-polarised boundary), explaining this observation.

Another notable feature of the data is the distance between $T_c$ and the peak in $\lambda$. As already discussed, for critical slowing down typical of a second order phase transition these two features should coincide. At 35 mT, Fig. 5.1 shows closer agreement between the extracted value of $T_c$ and the peak in $\lambda$ than at 18 mT. Whilst these features should again not be over-interpreted due to the limited temperature resolution, this suggests the model used to fit the data more closely matches one that would suggest critical slowing down, and hence a lack of complex dynamics due to the SkL phase, at 35 mT. It is also notable that the extracted value of $k$ in these fits decreases with increasing applied field, as was the case in the single crystal measurements in Chap. 4, once again suggesting that the magnetic transition is more gradual at higher $\mu_0 H_{\text{ext}}$.

LF $\mu$SR measurements were also performed on 6.4% and 10.5% Zn-substituted polycrystalline $Cu_2OSeO_3$, which AC susceptibility measurements reveal exhibit three and two distinct SkL phases respectively. Various external magnetic fields were applied such that both fields which stabilise the SkL at certain temperatures, and fields which do not, were measured. The spectra are visually very similar to those for the pristine material, once again showing monotonic decay (with the exception of measurements performed in a small applied field, discussed later). Despite this similarity, the combination of Eqns. 4.1 and 4.2 does not adequately describe these data. To investigate this observation, we can plot the natural logarithm of the background-subtracted data; examples of this manipulation for both

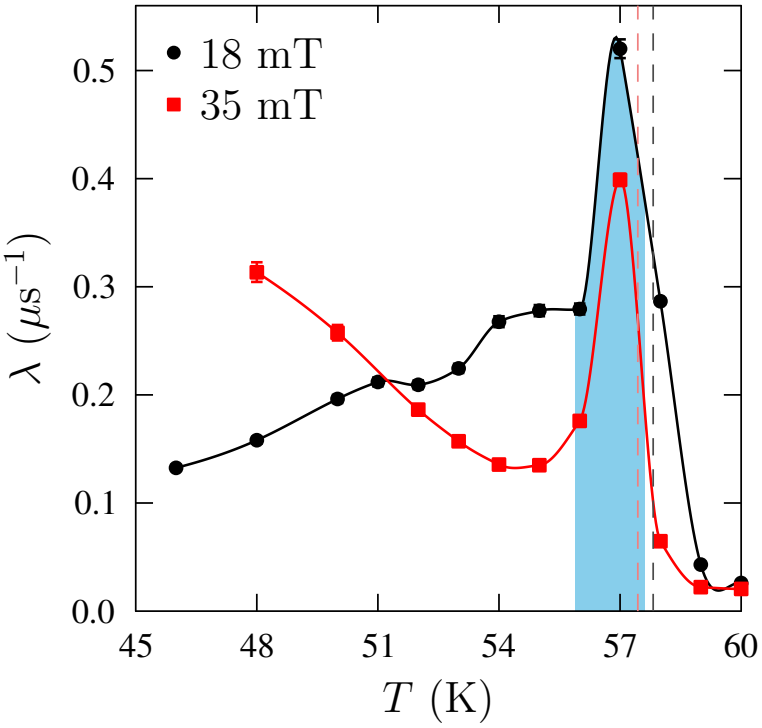


**Figure 5.1:** Relaxation rate $\lambda$ extracted from LF $\mu$SR measurements of pristine polycrystalline $Cu_2OSeO_3$. Measurements were performed under application of an appropriate external magnetic field to stabilise the SkL at certain temperatures (18 mT), and at a field which is too large to stabilise the SkL at any temperature (35 mT). The location of the SkL phase at 18 mT as identified by AC susceptibility measurements is indicated in light blue, with $T_c$ at each field as extracted with $\mu$SR shown as dashed lines (18 mT: grey, 35 mT: pink). The solid lines are a guide to the eye.

**Table 5.1:** Parameters refined by simultaneously fitting all LF $\mu$SR data at a particular applied field for polycrystalline Zn-substituted $Cu_2OSeO_3$. Additional parameters accounting for the oscillatory component in low-field measurements are seen in Tab. 5.2.

| Zn (%) | $\mu_0 H_{\mathrm{ext}}$ (mT) | $a_{\mathrm{b}}$ (%) | $a_{\mathrm{r0}}$ (%) | $k$ | $L_{(1)}$ (%) | $T_{\mathrm{c}(1)}$ (K) | $L_2$ (%) | $T_{\mathrm{c}2}$ (K) |
|---|---|---|---|---|---|---|---|---|
| 0 | 18 | 17.60(2) | 3.06(2) | 2.05(2) | 8.104(12) | 57.820(5) | - | - |
| | 35 | 19.12(3) | 2.57(3) | 1.043(9) | 7.27(2) | 57.440(9) | - | - |
| 6.4 | 5 | 13.8(2) | 9.8(2) | 2.34(5) | 2.15(2) | 51.50(2) | 2.32(2) | 54.60(2) |
| | 18 | 21.41(3) | 1.93(3) | 1.35(3) | 2.00(2) | 50.89(4) | 2.36(3) | 54.23(3) |
| | 35 | 22.01(6) | 1.38(7) | 0.81(2) | 1.32(7) | 48.1(3) | 3.12(10) | 52.66(8) |
| 10.5 | 4 | 18.84(4) | 3.3(2) | 2.15(4) | 6.2(3) | 47.55(2) | 4.3(2) | 54.040(14) |
| | 16 | 19.03(3) | 2.05(3) | 1.68(2) | 4.37(2) | 47.267(10) | 2.798(13) | 53.767(11) |

Zn-substitution levels are shown in Fig. 5.2. If these data are simple-exponential decays, as in the previous case, one should obtain a straight line. Irrespective of the choice of background, it is not possible to obtain a straight line at all temperatures for both of the Zn-substituted samples, instead finding two approximately linear regimes that crossover at 2–4 $\mu$s. (At some temperatures a visually linear result is obtained, suggesting that there are minimal differences in behaviour between the two regimes identified by the two straight lines. This behaviour would be expected far from $T_c$ where the relaxation rate should not have significant temperature dependence.) This demonstrates that a more complex model to fit these data is required. Note that if the same analysis is carried out on the asymmetry spectra measured on pristine $Cu_2OSeO_3$ then a straight line is obtained at all temperatures.

The two approximately linear regimes observed suggests that the asymmetry spectra of the Zn-substituted $Cu_2OSeO_3$ samples needs at least two distinct exponential relaxation rates to describe the behaviour. To observe such relaxation, at least two, spatially distinct classes of muon site must be realised in these samples, and these sites must have different correlation times [111]. If there were only one muon site subject to fluctuations with multiple distinct correlation times, the slowest one would dominate, leading to a single relaxation rate. Given that there is significant amplitude in each signal, these classes of muon site must occur within the bulk of the material (muons stopping near edges, for example, would not contribute significant amplitude, as discussed previously). Muons stopping outside of the sample (in the Ag foil or similar) can also be ruled out due to significant temperature dependence observed in the signal. The most obvious explanation for these sites is the different muon stopping sites already reported (see Fig. 4.5 and Tab. 4.2), however the lack of a similar observation of a complex spectra in the pristine material makes this impossible. We therefore conclude that there are at least two, spatially distinct classes of muon stopping site in the bulk of the polycrystalline Zn-substituted $Cu_2OSeO_3$ samples.

The most likely explanation for distinct muon sites, each of which is sensitive

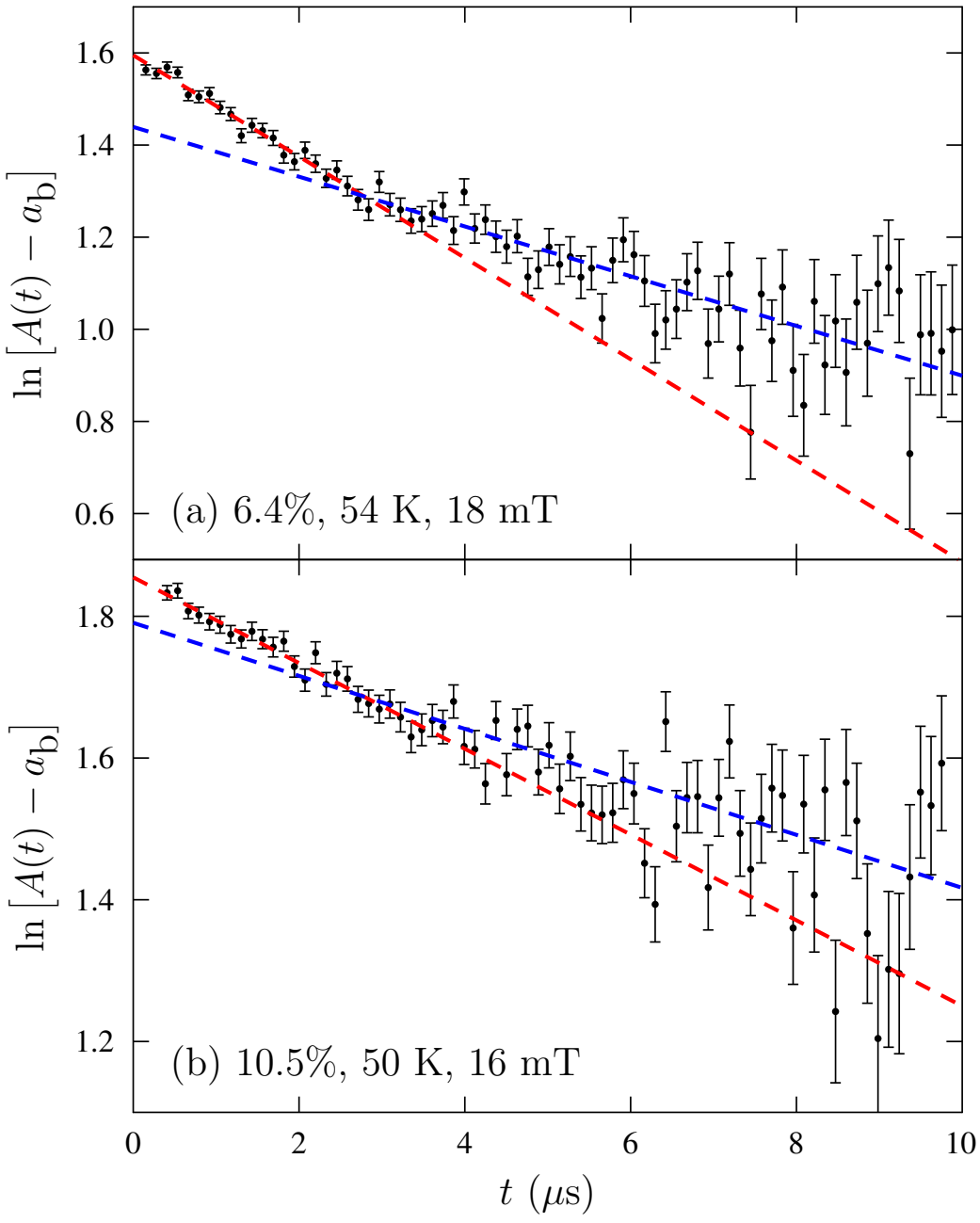


**Figure 5.2:** Manipulated $\mu$SR asymmetry spectra of (a) 6.4% and (b) 10.5% Zn-substituted polycrystalline $Cu_2OSeO_3$, as measured at the indicated temperature and applied magnetic field. Straight lines are shown as guides to the eye and indicate that these spectra are not simple exponential decay. This result is robust under any choice of $a_b$.

to different magnetic behaviour, is that the different muon sites are in different regions of the sample which host different Zn-concentrations. As $T_c$ is highly sensitive to the level of Zn-substitution in the sample, a mixture of different Zn-concentrations in a single powder sample would explain the observed AC susceptibility phase diagrams, which can be viewed as the superposition of multiple phase diagrams, each of which has a different $T_c$. This also explains why only one exponential is observed in the pristine sample, where there is only one composition, and why the spectra far from any value of $T_c$ in the sample show linear behaviour when the same analysis as that presented in Fig. 5.2 is employed (as $\lambda$ in each composition will be about the same). High-resolution x-ray measurements confirm that the polycrystalline samples are in fact composed of multiple different Zn-substitution crystallites [92]. This therefore explains the reported SkL-phase splitting.

With an understanding of the composition of these materials, we can now establish an appropriate model to fit the LF $\mu$SR data with. As the AC susceptibility measurements can be viewed as a superposition of multiple different phase diagrams, the $\mu$SR data should also be a superposition of distinct contributions from each Zn-substitution level (the advantage of $\mu$SR being that, as a microscopic probe, the effects should be separable). The model that one should therefore expect to fit the data is

$$A(t) = \sum_{i=1}^{n} a_{ri} \exp(-\lambda_i t) + a_b, \tag{5.1}$$

where $a_{ri}$ are all given by Eqn. 4.2 with independent parameters. Unfortunately, due to the very similar values of $\lambda_i$ often observed at a particular temperature, it was not possible to unambiguously fit this model to the data at all temperatures. Instead, for both 6.4% and 10.5% Zn-substituted $Cu_2OSeO_3$ measurements, a model was used that replaced $\lambda_i$ with a single $\lambda$, which can be viewed as an average value. This model provides consistent fits that work well for all measurements, allowing comparison between different regimes at the cost of making the absolute value of $\lambda$ difficult to interpret. The model used was

$$A(t) = a_r \exp(-\lambda t) + a_b, \tag{5.2}$$

where

$$a_{\mathrm{r}} \;=\; a_{\mathrm{r}}0 + \frac{L_1}{1+\exp\left[-k\left(T-T_{\mathrm{c}1}\right)\right]} + \frac{L_2}{1+\exp\left[-k\left(T-T_{\mathrm{c}2}\right)\right]}, \tag{5.3}$$

where parameters have the same meaning as for Eqn. 4.2. Here there are two independent critical temperatures, and the fractional composition of each Zn-substitution in the sample can be estimated from $L_i/(L_1+L_2)$ (discussed later). In this model it is assumed that the behaviour of the amplitude of the asymmetry around $T_{\mathrm{c}}$ is similar between different compositions by sharing a single $k$. Analysis of the data without this assumption finds values of $k$ that are very similar, justifying this approximation. This model is appropriate for measurements made at applied fields that will stabilise the SkL at certain temperatures, and for fields above that; lower fields were also measured, but need a modification to the model and are discussed later. Fitted values of $\lambda$ from 6.4% and 10.5% Zn-substituted $Cu_2OSeO_3$ measurements are shown in Fig. 5.3, with fitted parameters shown in Tab. 5.1.

The relaxation rates seen in Fig. 5.3 show clear evidence for multiple phase transitions, consistent with the picture of multiple different Zn-compositions coexisting within the samples. Considering the 6.4% Zn-substituted sample [Fig. 5.3(a)], there are clearly enhanced peaks at 18 mT (cutting through the SkL phases) compared to 35 mT, as one would expect. At 35 mT, rather than the peaks one would expect from critical slowing down of the magnetic fluctuations, we instead observe step-like features. This may suggest subtly different transition temperatures at this applied field, leading to a smearing out of the transition such that a peak cannot be resolved. This could occur if the demagnetisation effects significantly change the effective field in different grains of the polycrystalline sample, which leads to the transition from the conical to field-polarised state to occur at different temperatures. As the demagnetisation field is proportional to the magnetisation, which is in turn proportional to the applied field ($B_{\mathrm{demag}} \propto M \propto H_{\mathrm{ext}}$), this effect will be greater at 35 mT than at 18 mT. The smearing out is also seen in the value of $k$ extracted from the fitting, which decreases with increasing applied field. As this also occurs in the single

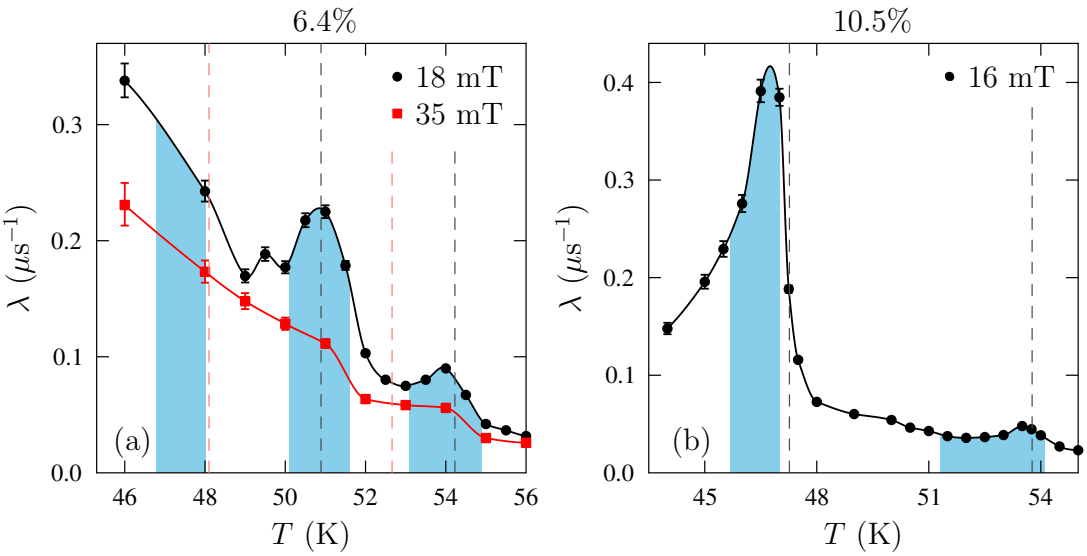


**Figure 5.3:** Relaxation rate $\lambda$ extracted from LF $\mu$SR measurements of polycrystalline (a) 6.4% or (b) 10.5% Zn-substituted $Cu_2OSeO_3$. Measurements were performed under application of an appropriate external magnetic field to stabilise the SkL at certain temperatures [(a)18 mT, (b) 16 mT], and at a field which is too large to stabilise the SkL at any temperature (35 mT). The location of the SkL phase at 18 mT/16 mT as identified by AC susceptibility measurements is indicated in light blue, with $T_c$ at each field as extracted with $\mu$SR shown as dashed lines (18 mT/16 mT: grey, 35 mT: pink). The solid lines are a guide to the eye.

crystal measurements already presented, some of this smearing out is likely an intrinsic effect (which may be expected due to the decreasing gradient with increasing applied of the conical/field polarised transition line in the $B$–$T$ phase diagram). After these measurements were performed, AC susceptibility measurements detected a possible third, lower $T$ SkL phase in these samples [marked in Fig. 5.3(a)], however these $\mu$SR data do not have sufficient $T$ resolution to study this phase.

In the 10.5% Zn-substituted sample [Fig. 5.3(b)] there are also two clear transitions that coincide well the location of the SkL according to AC susceptibility measurements. The most striking feature of these data is the difference in peak amplitude at the two transitions. This is most likely an artefact of the fitting model where the extracted $\lambda$ can be thought of as an "average" of the different relaxation rates in different compositions. At low $T$, as some of the sample goes through $T_c$, the relaxation rate of the muon-spin-polarisation in the parts of the sample well below $T_c$ is still substantial, leading to a significant overall peak. At high $T$, much of the sample is well above $T_c$ and will lead to very little relaxation, leading to a reduced overall peak in $\lambda$. This can be seen, to a lesser extent, in Fig. 5.3(a), where each subsequent peak in $\lambda$ has a lower peak amplitude.

The other notable feature in Fig. 5.3 is the extracted location of $T_c$. These values all agree with values extracted through AC susceptibility, appearing to best correlate with either the top of the SkL (when a SkL is stabilised), which marks the onset of the transition from magnetic order to disorder, or the transition between the conical and field-polarised state. Unlike in previous measurements, particularly in the 6.4% Zn-substituted $Cu_2OSeO_3$ measurements, there is not a clear separation between the peak in $\lambda$ and the location of $T_c$. Given the enhanced relaxation rate consistent with measurements through the SkL, it is possible this is an artefact of limited $T$ resolution which leads to systematic errors in these values.

Further LF $\mu$SR measurements of Zn-substituted $Cu_2OSeO_3$ were performed in a small applied field (5 mT for 6.4%, 4 mT for 10.5%). In these measurements

**Table 5.2:** Additional fitting parameters that are required at for low-applied field LF $\mu$SR measurements. Refined by simultaneously fitting all data for polycrystalline Zn-substituted $Cu_2OSeO_3$ at a particular applied field.

| Zn conc. (%) | $\mu_0 H_{\text{ext}}$ (mT) | $a_2/(a_1+a_2)$ (%) | $B$ (mT) | $\phi$ (°) |
|---|---|---|---|---|
| 6.4 | 5 | 0.041(2) | 4.6(2) | −15(7) |
| 10.5 | 4 | 0.33(3) | 4.5(2) | −89(8) |

there was still a small oscillatory component resolvable in the data, therefore the model was adjusted to

$$A(t) = a_{\text{r}}\left[a_1 \exp(-\lambda t) + a_2 \exp(-\Lambda t)\cos(\gamma_\mu B + \phi)\right] + a_{\text{b}}, \tag{5.4}$$

where $a_1 + a_2 = 1$. The relaxation rate $\Lambda$ additionally accounts for a distribution of fields at the muon site centred on $B$, and $\phi$ is a phase offset. Temperature-dependent extracted parameters are seen in Fig. 5.4, with globally refined temperature independent parameters given in Tabs. 5.1 and 5.2. In both cases, the oscillatory component is only a small part of the total amplitude, suggesting this component only accounts for a small fraction of the muons.

The dynamic relaxation rate $\lambda$ [Fig. 5.4(a–b)] shows similar behaviour to measurements at higher applied field for both Zn-substitutions. For the 6.4% Zn-substituted $Cu_2OSeO_3$ sample, $\lambda$ is significantly suppressed compared to measurements at other fields. However, this is not the case in the 10.5% Zn-substituted $Cu_2OSeO_3$ measurements. This may suggest that, whilst the SkL still has dramatic effects on the magnetism at 6.4% Zn-substitution (only enhancing $\lambda$ when the SkL is stabilised), by 10.5% Zn-substitution the dominant relaxation channels for the muon-spin are more likely to be occurring due to other magnetism in the sample. The relevant timescales for dynamic processes in these systems change with Zn-substitution, as evidenced by the dramatic change in lifetimes of the metastable SkL in Zn-substituted $Cu_2OSeO_3$ [79]. It is therefore possible that the relaxation channels in the muon time-window change with Zn-substitution, and that these changes are the explanation for the lack of change in $\lambda$ between 4

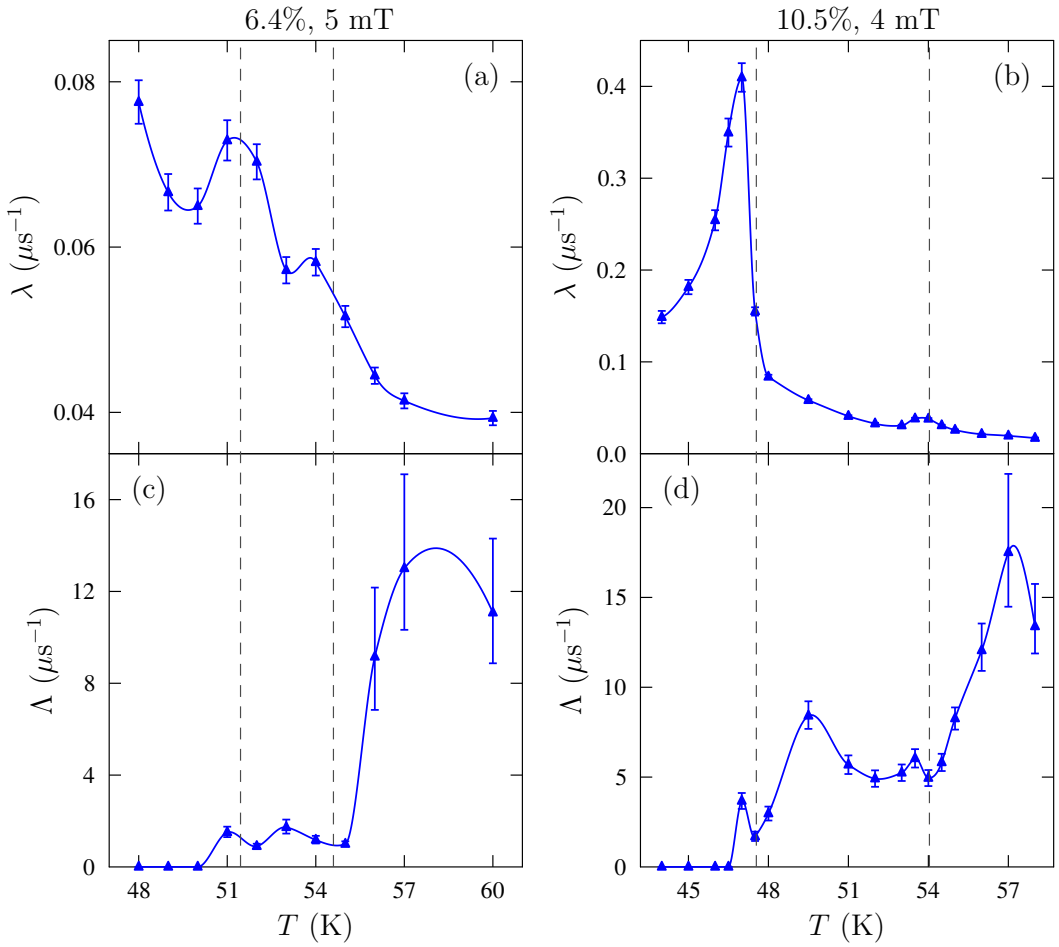


**Figure 5.4:** Relaxation rates $\lambda$ (a–b) and $\Lambda$ (c–d) extracted from LF $\mu$SR measurements of polycrystalline (a,c) 6.4% or (b,d) 10.5% Zn-substituted $Cu_2OSeO_3$. Measurements were performed under application of a weak external magnetic field such that precession of the muon spin in the local field was resolvable. Values of $T_c$, corresponding to the $T_c$ of different Zn-concentrations throughout the sample, as extracted with $\mu$SR are shown as dashed lines. The solid lines are a guide to the eye.

and 16 mT in 10.5% Zn-substituted $Cu_2OSeO_3$.

For both measured samples, the oscillatory component only appears once a significant volume fraction of the sample is above $T_c$ (above the lower identified transition temperature in both cases). This, in addition to the dramatic change in $\Lambda$ at the upper transition temperature, suggests that the source of the oscillatory component is likely associated with parts of the sample remaining magnetically ordered, whereas other parts have become magnetically disordered. One such scenario would be that muons stopping in the grains that are magnetically disordered feel a dipolar field from the local magnetically ordered grains, and precess in this field. This would explain why the amplitude of this component is not as large as one would expect. Further, the step like increase in $\Lambda$ at transition temperatures does suggest an increase in the width of the distribution of the field at the muon site at these temperatures, consistent with this model. In this scenario one would expect that the relative amplitude of the oscillatory component should change at the upper transition. Due to the very low amplitude of this component this cannot be categorically ruled out; holding the relative amplitudes fixed as a function of temperature produces good fits.

Finally, one can calculate the volume fraction of each different level of Zn-substitution in these samples by calculation $L_i/(L_1 + L_2)$. The increase in the relaxing asymmetry around $T_c$, $L_i$, occurs due to the time resolution in these measurements typically not being sufficient to observe precession at the muon site. For a polycrystalline sample, in the absence of an applied field, one would therefore expect 1/3 of the muons stopping in a particular sample to contribute to the asymmetry at $T \ll T_c$, recovering to all the muons around $T_c$. Application of an external field changes the field at the muon site, which subsequently changes the fraction away from 1/3, as seen in Fig. 3.4. It is therefore difficult, in general, to conclude much about the magnetism from these values. If however, as is the case in the Zn-substituted $Cu_2OSeO_3$ samples, we have $N$ domains with similar magnetism, but each with different values of $T_c$, we can assume that the '1/3' fraction will be the same in each domain. Therefore, the quantity $L_i/(\sum_j^N L_j)$

will give the fraction of muons stopping in each different type of domain, and hence, in this case, the volume fraction of each different level of Zn-substitution, where those with lower values of $T_c$ are those with higher levels of Zn-substitution.

Calculated from $L_i/(L_1 + L_2)$, for 6.4% Zn-substituted $Cu_2OSeO_3$ 46(3)% of the sample is the low-$T_c$ substitution (corresponding to higher Zn-substitution), whereas for 10.5% Zn-substituted $Cu_2OSeO_3$ this figure is 60.9(2)%. As already stated, for 6.4% Zn-substituted $Cu_2OSeO_3$ these measurements were not performed at a sufficiently low-$T$ to be sensitive to the lowest-$T_c$, highest Zn-substitution phase in this sample, believed to be around 15% of the sample by weight. The percentage obtained here therefore reflects the relative weights of the two identified phases. The values for both samples are in excellent agreement with x-ray and magnetometry measurements [92], and demonstrate that LF $\mu$SR can be used to accurately identify not only magnetic volume fractions, but also chemical volume fractions, as is widely done in ZF $\mu$SR.

To further probe Zn-substituted $Cu_2OSeO_3$, we performed TF $\mu$SR measurements of 6.4% Zn-substituted $Cu_2OSeO_3$ in an applied field of 18 mT. In TF $\mu$SR, rather than simply fitting the asymmetry (which ignores any positrons that are not detected in the forward/backward detectors) as has previously been done for the LF $\mu$SR, the number of counts in all detectors is fit simultaneously, with a phase offset on the signal appropriate for each detector. This means that the polarisation of the muon-spin ensemble is fitted directly. For these measurements,

$$P_x(t) = \sum_{i=1}^{2} a_i \exp\left[-(\sigma_i t)^2\right] \cos(\gamma_\mu B_i t) + a_b, \tag{5.5}$$

capturing the effect of muons stopping in an ordered field averaging $B_i$, and each component has a respective relaxation rate $\sigma_i$. No phase offset on these oscillatory components was needed to well describe the data in this case. We find that the two sites can be identified as a high field (above the applied field below $T_c$) and low field (below the applied field) site.

Whilst one would typically expect $a_i$ to be temperature independent (as it reflects the number of muons stopping in each site), this is not the case in these data, as seen in Fig. 5.5. We find that most of the muons stop in the high-field site

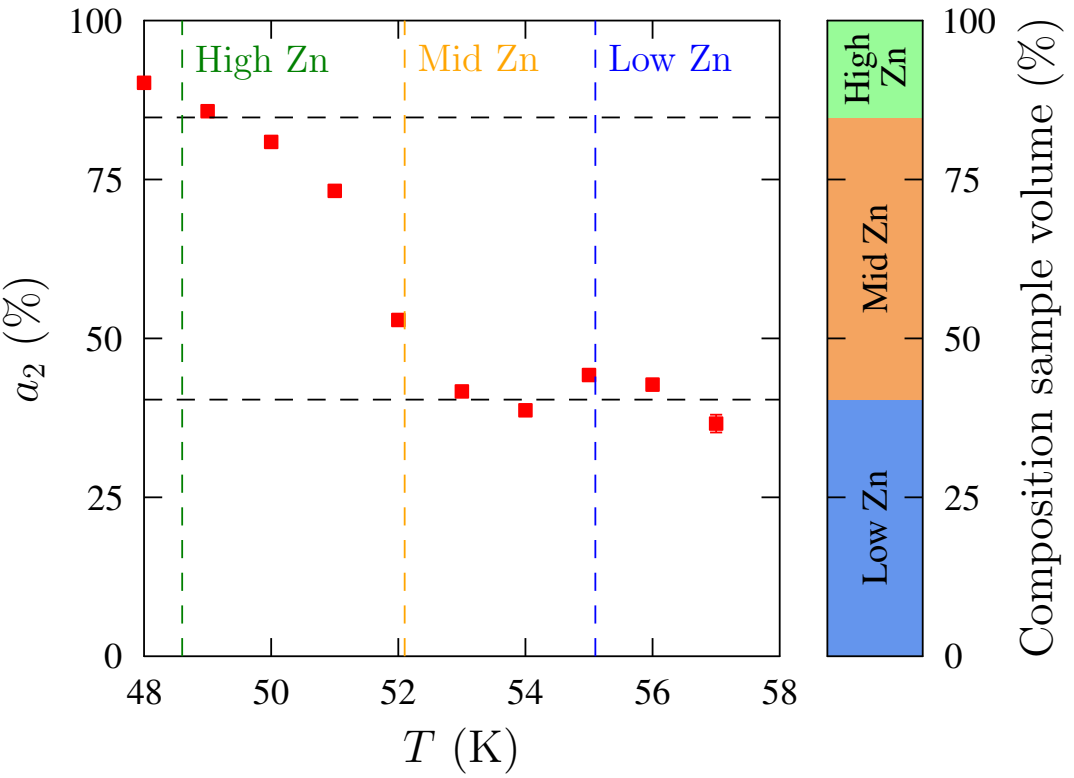


**Figure 5.5:** *Left*: Percentage amplitude $a_2$ of the second component needed to fit TF $\mu$SR data measured on 6.4% Zn-substituted $Cu_2OSeO_3$ with an applied field of 18 mT. This shows the fraction of muons stopping in site best described by the high-field component, which is identified as muons stopping in parts of the sample that are magnetically ordered. Vertical dashed lines mark the $T_c$ of the different Zn-compositions in the sample as measured by magnetometry. *Right*: Percentage of each Zn concentration in the polycrystalline sample as measured by x-ray and magnetometry methods [92]. Dashed lines on left panel mark the percentages on the right panel. Changes are seen to be most dramatic around the intersection of the vertical and horizontal dashed lines.

(denoted site 2) at low $T$, with this fraction decreasing with increasing $T$. The values cannot be accurately extracted above $T_c$, where the fields converge upon the applied field and hence cannot be unambiguously separated. When comparing the number of muons stopping in high-field site we see close resemblance to the fraction of the sample known to be each Zn-concentration (as identified by x-ray and magnetometry methods [92]). We therefore interpret the high-field site as muons stopping in grains of the sample that are magnetically ordered at that temperature, with the low-field site capturing the precession of muon-spins that stop in magnetically disordered grains, precessing in the sum of the applied field and demagnetisation field from nearby ordered grains. As $T$ is increased through the $T_c$ of one of the levels of Zn-substitution in the sample, the muons stopping in these grains transition from precessing in magnetically ordered sites (hence contributing to $a_2$), and instead sit in magnetically disordered grains. This leads to the observed fractions seen in Fig. 5.5, with the fraction of muons in the high field site falling as more of the sample becomes magnetically disordered on increasing $T$. This gives a measurement of the fraction of the sample volume occupied by each different Zn-composition that is independent to the above argument based on $L_i$.

Having understood the origin of the two components, we now turn to look at the field at the muon site $B$, and associated relaxation rate $\sigma$ (Fig. 5.6). We can first use the measurement of $\sigma_2$ (corresponding to the magnetically ordered part of the sample) as a consistency check with AC susceptibility measurements by estimating the correlation time of magnetic fluctuations in the SkL phase compared with surrounding phases. The relaxation rate $\sigma$ of the oscillating components in a static, magnetically-ordered phase can be related to the width of the distribution of magnetic fields at the muon site via $\sigma^2 = \Delta^2/2$, where $\Delta = \gamma_\mu \langle B_i^2 \rangle$. Although we know that dynamic effects dominate the width of the spectra in the SkL phase (Fig. 4.4), hence making this equation not valid, this approximation should give the correct order of magnitude for $\Delta$. Combining this with the general result derived for $\lambda$ in Chap. 3, Eqn. 3.30, one can obtain the correlation

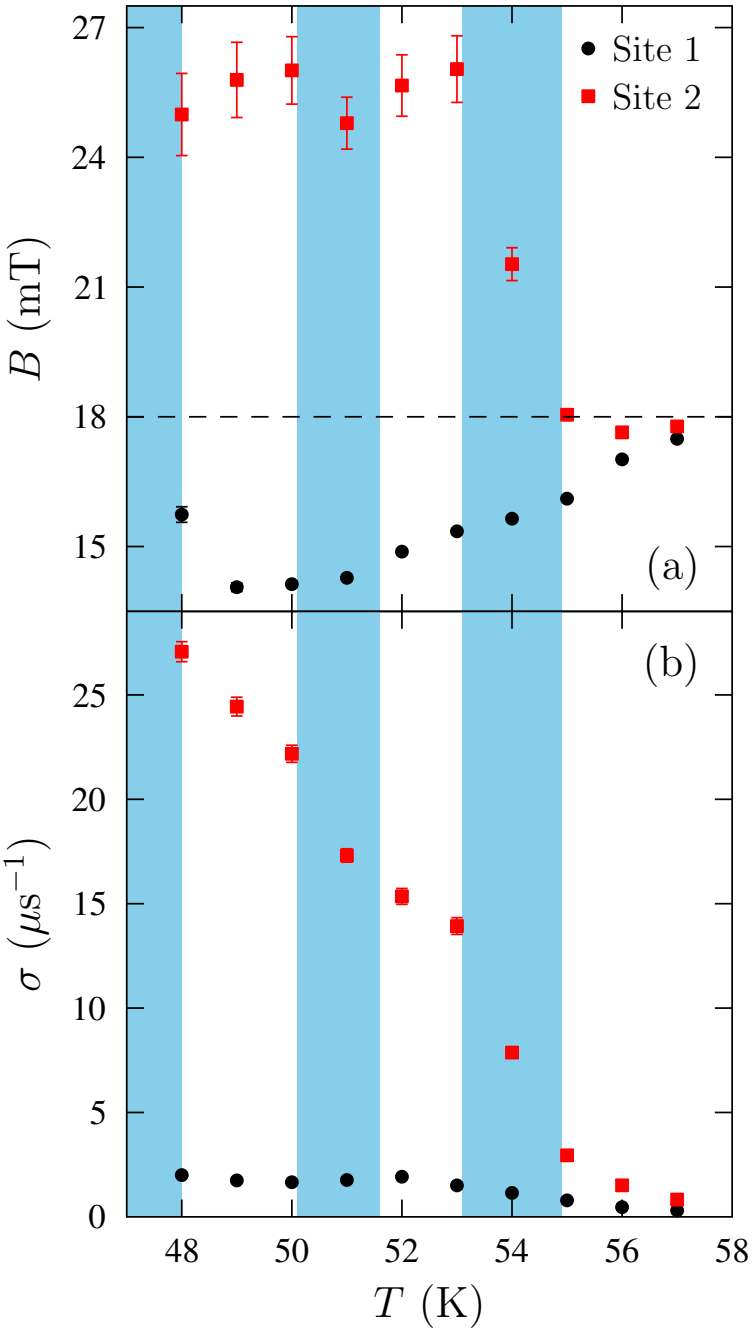


**Figure 5.6:** Fitted parameters extracted from TF $\mu$SR measurements of 6.4% Zn-substituted $Cu_2OSeO_3$ with an applied field of 18 mT. (a) The field $B_i$ of each compoenent in the fitting. Site 1 (2) correspond to muons stopping in the magnetically disordered (ordered) grains of the sample. (b) The corresponding relaxation rates $\sigma$ for each component. Temperatures at which the SkL is stabilised at this applied field according to AC susceptibility measurements are indicated in light blue.

time $\tau = 1/\nu$. In the ordered regime, but outside of the SkL, we find that the $\tau \simeq 0.1$ ns (corresponding to an energy $\Delta E = \hbar/t \simeq 10$ $\mu$eV of the magnetic fluctuations which most strongly interact with the muon-spin). This is approximately constant with $T$ (once again consistent with a picture of the grains of the sample acting independently). Inside the SkL the correlation time doubles to around $\tau \simeq 0.2$ ns ($\Delta E \simeq$ 5 $\mu$eV), possibly reflecting an increase in spin stiffness in the SkL phase compared to the surrounding magnetic phases. This is reassuringly consistent with the decrease in the real part of the magnetic susceptibility $\chi'$ observed in the SkL phase.

Considering the measured internal field $B$, we find that the magnetic field in the low-field site is below the applied field, getting closer to the applied field as $T$ increases, as one would expect from muons subject to the applied field and an ever-decreasing percentage of the sample with a significant demagnetisation field. The high-field site is relatively constant until the highest $T_c$ is reached, where it begins to collapse. This is consistent with a picture of the static magnetism of each different Zn-composition in the sample acting independently, if, as previously suggested [110], the three SkL phases occurred from the same grains of the sample, one would expect $B$ to have temperature dependence. Interestingly, this contrasts to the dynamics observed, where by 10.5% Zn-substitution the nature of $\lambda$ has changed dramatically. This suggests that, on the muon-timescale, the most dramatic changes to the SkL happen in the dynamics, not in the static magnetism. This is consistent with our previous observations on the single crystal samples.

## 5.4 Conclusion

Our measurements of polycrystalline $Cu_2OSeO_3$ show consistent results with the single-crystal experiments presented in Chap. 4, specifically an enhancement of $\lambda$ in the SkL phase. Measurements of polycrystalline Zn-substituted $Cu_2OSeO_3$ reveal multiple different magnetic environments that are best explained as different levels of Zn-substitution in different grains of the sample. Both LF and TF

$\mu$SR can accurately extract the respective weights of each of these different Zn-substitution phases, giving values consistent with x-ray and magnetometry measurements. TF $\mu$SR measurements suggest the nature of the static magnetism in the SkL phases of each different Zn-substitution level phases is relatively similar, whilst LF $\mu$SR shows more dramatic changes with Zn-substitution. This suggests that, consistent with the measurements on single crystals, on the muon-timescale dynamic changes to the SkL are far more important than changes to the static structure. This is consistent with other observations of the behaviour of the SkL in Zn-substituted $Cu_2OSeO_3$, for example the dramatic increase of the metastable lifetime of the SkL with Zn-substitution [79] is a dynamic effect.

# Chapter 6

# Skyrmion lattice dynamics in $Co_xZn_yMn_{20-x-y}$

This chapter presents muon-spin spectroscopy ($\mu$SR) measurements on materials in the $Co_xZn_yMn_{20-x-y}$ family, a particularly interesting system due to the dramatic changes to the magnetic properties that occur through varying $x$ and $y$. Known to host various different incommensurate magnetic structures, multiple topological magnetic states manifest in different compositions of $Co_xZn_yMn_{20-x-y}$, including skyrmions and merons (half-skyrmions). This chapter presents longitudinal field (LF) $\mu$SR measurements of several compositions of $Co_xZn_yMn_{20-x-y}$, allowing us to contrast the response to different magnetic states. We find that there are megahertz dynamics in materials that host topological magnetism. These dynamics correspond well to the reduction in frequency of the characteristic excitations of the skyrmion lattice (SkL), identifying the lowest frequency excitation to be $\approx$ 1–2 GHz. I believe this is the first measurement of the frequency of the skyrmion modes in $Co_xZn_yMn_{20-x-y}$. In $Co_8Zn_8Mn_4$, transverse-field (TF) $\mu$SR measurements above $T_c$ reveal a change from a system dominated by critical behaviour just above $T_c$ to paramagnetic behaviour of a metal with fluctuating moments, as evidenced by a significant Knight shift persisting to high $T$. Below $T_c$ LF $\mu$SR experiments show enhanced dynamics when the external field is one that stabilises the SkL over a wide range of temperatures (including at temperatures

where the SkL would not normally be expected to be stabilised). By stabilising a metastable SkL, we are able to further enhance these dynamics, likely due to a greater proportion of muons being sensitive to SkL effects. After discussing several scenarios, we conclude that the most likely source of these dynamics is the decay of skyrmions.

This chapter is based on work published in Ref. [16]. The samples were provided by collaborators at the University of Warwick. The $\mu$SR data were measured by myself, alongside collaborators at Durham University and ISIS Neutron and Muon Source; I have performed the subsequent analysis of the $\mu$SR data. I calculated the muon stopping sites in these materials. The overall discussion is my own.

## 6.1 Introduction

Soon after the discovery of the magnetic skyrmion, and the realisation of the potential for technological applications, the hunt for materials hosting a SkL at room-temperature began. Unlike the search for room-temperature superconductivity, the discovery came quickly in the form of $Co_xZn_yMn_{20-x-y}$ [21], which have critical temperatures $T_c > 300$ K. Contrasting many other SkL hosts (including already studied $Cu_2OSeO_3$) which often crystallise in the $P2_13$ structure [3, 18, 19, 20], $Co_xZn_yMn_{20-x-y}$ is a metallic system with the $\beta$-Mn structure (shown later in the context of muon site calculations, Fig. 6.1). Despite this difference, a familiar process leads to the stabilisation of incommensurate magnetic structures in $Co_xZn_yMn_{20-x-y}$. Specifically, the lack of inversion centre arising from the non-centrosymmetric crystal structure leads to a bulk Dzyaloshinskii–Moriya interaction, which then competes with the symmetric exchange.

The magnetic properties of $Co_xZn_yMn_{20-x-y}$ change significantly with $x$ and $y$, leading to different magnetic states in different members of the series. Certain compositions are not reported to host any topological magnetic state, however others host a SkL [21] similar to that of $Cu_2OSeO_3$. Changing the composition further can lead to modifications of this SkL. Additional frustrated magnetism

inherent to the $\beta$-Mn structure leads to a disordered SkL in $Co_7Zn_7Mn_6$, where the skyrmion tubes deform and point in various directions [112]. In $Co_8Zn_9Mn_3$ another different magnetic state is reported: the meron-antimeron lattice [113]. This is a lattice of topological magnetic excitations with winding number $N = \pm 1/2$, contrasting the SkL where $N = 1$.

Despite the high $T_c$ of $Co_xZn_yMn_{20-x-y}$, and the variety of magnetic states which can be stabilised, chemical substitutional site disorder inherent in these systems may prevent this system from being optimal for applications. Broadening, both in temperature and applied field, of the magnetic transitions due to locally different crystallographic environments throughout the sample, and dramatic effects on $T_c$ with relatively subtle changes in composition, are common in these systems [114]. In this chapter we study the $\mu$SR response of $Co_xZn_yMn_{20-x-y}$ with $(x, y) = (10, 10)$, $(8, 9)$ and $(8, 8)$, detecting megahertz dynamics that vary across the series. By studying these three materials we can consider the effect of increasing crystallographic site disorder (which mainly occurs on the 12d Wyckoff site) on the magnetism. The level of disorder increases with decreasing $y$ until, once $y \lesssim 7$, a spin glass ground state is realised [112]. Here we study the regime where the system remains magnetically ordered.

## 6.2 Experimental Details

Single crystal and polycrystalline $Cu_2OSeO_3$ samples were synthesised and characterised by Geetha Balakrishnan, Monica Ciomaga Hatnean, and Ales Štefančič at the University of Warwick, as described in Ref. [16].

LF $\mu$SR measurements were carried out at the STFC-ISIS Neutron and Muon Source, UK. Measurements on polycrystalline $Co_xZn_yMn_{20-x-y}$ were performed using the HiFi instrument at ISIS. In the case of $Co_8Zn_8Mn_4$ two different boulles were used, each of which had slightly different growth procedures. Additional TF $\mu$SR measurements on one of these polycrystalline boulles of $Co_8Zn_8Mn_4$ were performed at the Swiss Muon Source, Paul Scherrer Institut, Switzerland using the GPS instrument. Regardless of measurement orientation, unless otherwise

stated, samples were cooled in the absence of an applied field (which we refer to as zero-field cooled [ZFC]). Data analysis was carried out using the WiMDA program [68] and made use of the MINUIT algorithm [93] via the iminuit [94] Python interface for global refinement of parameters.

DFT calculations were performed to calculate the muon stopping sites in $Co_xZn_yMn_{20-x-y}$ using the plane wave, pseudopotential code, CASTEP [76] through the MuFinder application [115]. Calculations were carried out using the PBE exchange-correlation functional [95], with the experimentally obtained crystal structure relaxed with the lattice parameters held constant. Modelling the implanted muon as an ultrasoft hydrogen pseudopotential, various initial positions were used to randomly sample the crystal structure. The structure and the implanted muon were allowed to relax until the calculated forces on the atoms were all $< 5 \times 10^{-2}$ eV Å$^{-1}$ and the total energy and atomic positions converged to within $2 \times 10^{-5}$ eV per atom and $1 \times 10^{-3}$ Å, respectively.

## 6.3 Results & Discussion

### 6.3.1 Muon stopping sites

To allow comparison between different compositions of $Co_xZn_yMn_{20-x-y}$, it is important to know whether the muon-stopping sites significantly change as the composition does. The muon stopping sites in $Co_{10}Zn_{10}$, $Co_8Zn_9Mn_3$, and $Co_8Zn_8Mn_4$ were therefore calculated using DFT methods. To account for site disorder inherent for each composition [114], multiple unit cell configurations for each composition were trialled, where each atom was randomly assigned to be either Co, Zn, or Mn according to the probability of each element being at that site. This results in calculating the muon sites in many different systems with a Mn concentration in the range 0–30%. The final stopping sites were considered based on the symmetry of the parent unit cell (that is, one with multiple occupancy on each site).

The same muon stopping sites were found for all calculations, as shown in

**Table 6.1:** Calculated muon stopping sites in $Co_xZn_yMn_{20-x-y}$. Typical energies of the site are given relative to the lowest energy site. The ranges reflect the fact that the local environment of each site affects the energy. For sites 2 and 3 the energy ranges only apply for 20% Mn concentration and below, above this concentration the sites are not realised in the calculations.

| Muon site | Fractional coordinates | Typical energy range (eV) |
|---|---|---|
| 1 | (0.179, 0.571, 0.319) | 0.00–0.98 |
| 2 | (0.344, 0.398, 0.337) | 0.31–1.03 |
| 3 | (0.426, 0.568, 0.073) | 0.42–0.97 |

Fig. 6.1(a) and Tab. 6.1. As the local environment of the muon affects its energy, each site has a range of energies (depending on the atoms near the site for the particular simulated structure), complicating any conclusion as to which sites may or may not be occupied. Site 1 was always the lowest energy and most common site in each structure, suggesting it is likely always occupied, however some of the symmetrically equivalent sites (based on the parent cell) were much higher in energy, sometimes up to 1 eV, suggesting that not all symmetrically equivalent sites will be occupied due to the different combination of Co and Zn atoms in the vicinity. Sites 2 and 3 become increasingly uncommon as the Mn concentration is increased and are not realised in calculations with greater than 20% Mn concentration. All realised muon sites were found to be approximately 1.6 Å from the nearest Zn ion, suggesting this is the most important factor for determining the muon site, whereas the distance to the nearest Co and Mn ions seems random with no correlation between distance and site energy. On increasing Mn concentration the distance between the muon site and nearest Zn ion decreases, both in absolute terms and as a fraction of the lattice parameter [Fig. 6.1(b)].

From these results, we can conclude that the lowest energy muon-stopping site is unlikely to be significantly affected by the different compositions. Whilst higher-energy sites are changed, these are likely to have a lower occupancy than the lowest energy energy site, and therefore will only have a limited effect on

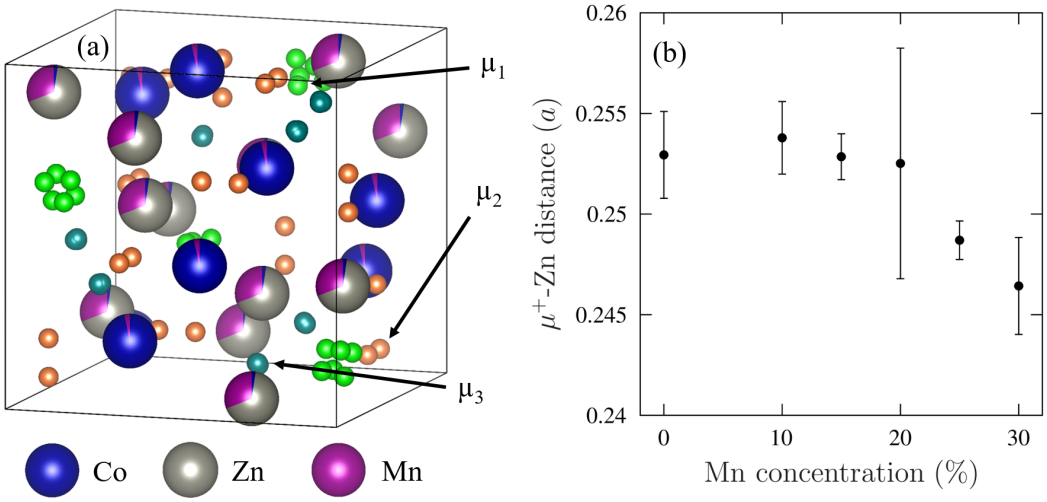


**Figure 6.1:** (a) Muon stopping sites in $Co_xZn_yMn_{20-x-y}$. All symmetrically equivalent muon stopping sites are shown, however which ones are occupied will depend on nearby ions. The unit cell shown here is that of $Co_8Zn_9Mn_3$. Image produced with VESTA [108]. (b) The distance between the muon stopping site and the nearest Zn ion (in terms of the lattice parameter $a$) as a function of Mn concentration.

the $\mu$SR spectra. We conclude that it is therefore reasonable to assume that any changes that arise in the $\mu$SR spectra of this series are due to changes in magnetic behaviour (whether that be static or dynamic), and not occurring due to changes in the muon position.

### 6.3.2 $Co_{10}Zn_{10}$

With the muon stopping sites determined, we now turn to consider the muon-response of various different compositions in the $Co_xZn_yMn_{20-x-y}$ series, starting with the parent compound, $Co_{10}Zn_{10}$. Whilst still exhibiting a helimagnetic groundstate with wavelength $\lambda = 185$ nm [21], $Co_{10}Zn_{10}$ has not been reported to stabilise a SkL. $Co_{10}Zn_{10}$ has a particularly high $T_c \simeq 460$ K; typically increasing the Mn concentration is the dominant reason that $T_c$ becomes suppressed, reflecting the reduction in strength of the exchange interaction $J$ with increasing Mn concentration [21]. This also decreases the periodicity of the helical state in the compounds, which is proportional to $J/D$, where $D$ is the strength of the DM interaction. (See Chap. 2 for more details.) By measuring the LF $\mu$SR response of $Co_{10}Zn_{10}$, we can study the effect of dynamics in the series in the absence of any topological magnetism. The measurements have been performed at applied fields that stabilise complex magnetic textures in other systems to provide the most direct comparison.

Exponential decay of the LF $\mu$SR asymmetry is seen at all measured temperatures and magnetic fields. A weak, temperature-independent relaxation is observed on the baseline with a rate consistent with Ag (see Tab. 6.2). The data are fitted to the function

$$A(t) = a_r \exp(-\lambda t) + a_b \exp(\lambda_b t). \quad (6.1)$$

As for $Cu_2OSeO_3$, the relaxing amplitude is constrained to follow Eqn. 4.2, leaving only $\lambda$ with temperature dependence. The fitted parameters can be seen in Tab. 6.2, with the resulting relaxation rate $\lambda$ shown in Fig. 6.2.

We find that measurements at two longitudinal fields have similar temperature dependence, with the overall shape of $\lambda$ reminiscent of that measured for

**Table 6.2:** Parameters obtained from fitting LF $\mu$SR measurements of $Co_{10}Zn_{10}$ at a particular applied field.

| $\mu_0 H$ (mT) | $a_b$ (%) | $a_{r0}$ (%) | $k$ | $L$ (%) | $T_c$ (K) | $\lambda_b$ ($\mu s^{-1}$) |
|---|---|---|---|---|---|---|
| 10 | 20.57(2) | 1.42(3) | 0.081(3) | 8.21(3) | 455.0(6) | 0.0027(2) |
| 18 | 20.47(3) | 1.46(7) | 0.135(6) | 8.24(8) | 460.8(3) | 0.0026(2) |

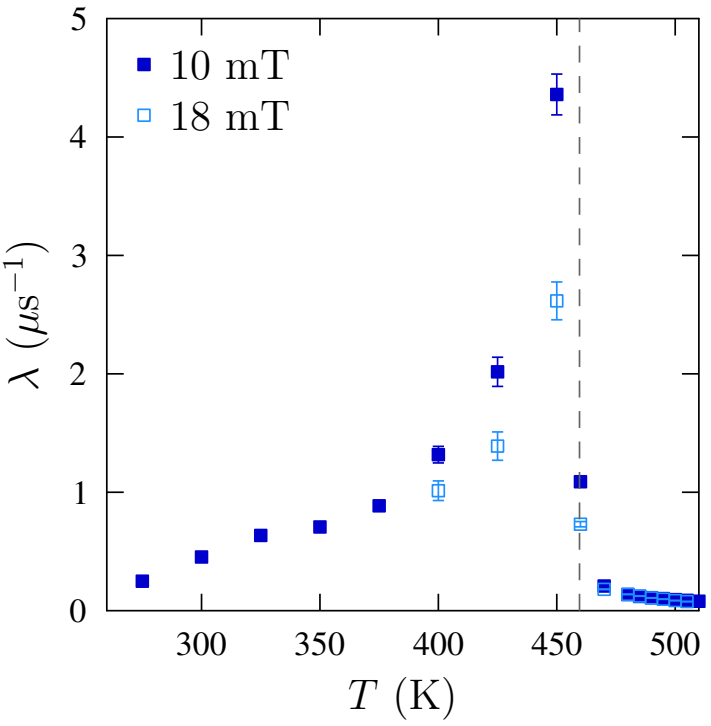


**Figure 6.2:** Extracted values of relaxation rate $\lambda$ from fitting LF $\mu$SR measurements of $Co_{10}Zn_{10}$. The dashed line indicates the average value of $T_c$ as extracted from fitting the LF $\mu$SR data.

$Cu_2OSeO_3$ at 40 mT [Fig. 4.3(a)], i.e. outside the skyrmion phase, where there is also a transition from the conical to paramagnetic phase. There is no evidence for any additional dynamics at either field, with the sharp peak likely occurring due to critical slowing down of the magnetic fluctuations as $T_c$ is approached [c.f. Fig. 4.3(b)]. Further, we find very similar fitting parameters (Tab. 6.2) at both applied fields, again suggesting no significant change in dynamics.

There are two notable differences in the field dependence of these parameters when compared to $Cu_2OSeO_3$. Firstly, in $Co_{10}Zn_{10}$ we observe a small increase in $T_c$ with $\mu_0 H$, whereas in $Cu_2OSeO_3$ we see the opposite. As we interpret the extracted $T_c$ in $Cu_2OSeO_3$ as the transition from complex, incommensurate magnetism to field-alignment, it may suggest that the nature of this transition is slightly different in $Co_{10}Zn_{10}$. Given the lack of topological magnetism (which in similar materials is stabilised in an applied field), perhaps this is unsurprising. Secondly, in contrast to $Cu_2OSeO_3$ where $k$ (sensitive to the rate of change of the relaxing amplitude, and hence static magnetism, around $T_c$) was seen to decrease with increasing applied field, here it increases, suggesting a sharper transition between the two magnetic states. This once again suggests the nature of the transition with applied field does not behave in the same way as in $Cu_2OSeO_3$.

### 6.3.3 $Co_8Zn_9Mn_3$

Next we discuss $Co_8Zn_9Mn_3$, a composition which can stabilise not only a SkL, but also a meron-antimeron spin texture. Both of these textures have been observed in thin plates [113], however in the bulk only the SkL state has been reported, with evidence consisting of magnetisation and magnetic entropy measurements [114]. In thin plate samples the region in the $B$–$T$ phase diagram stabilising topological magnetic states is dramatically enhanced in both $B$ and $T$ compared to the equivalent region in bulk materials.

We have performed LF $\mu$SR measurements of $Co_8Zn_9Mn_3$ in two applied fields: $B_{ext} = 10$ mT, which stabilises a SkL just below $T_c$ in bulk samples ($321 \lesssim T \lesssim 326$ K), and 18 mT, which gives a field-polarised magnetic

**Table 6.3:** Parameters obtained from fitting LF $\mu$SR measurements of $Co_8Zn_9Mn_3$ at a particular applied field.

| $\mu_0 H$ (mT) | $a_b$ (%) | $a_{r0}$ (%) | $k$ | $L$ (%) | $T_c$ (K) | $\lambda_b$ ($\mu s^{-1}$) |
|---|---|---|---|---|---|---|
| 10 | 21.90(2) | 1.20(3) | 0.229(4) | 8.08(4) | 341.58(9) | 0.00261(14) |
| 18 | 21.76(2) | 1.20(2) | 0.239(3) | 8.44(3) | 342.06(7) | 0.00207(14) |

state. The spectra decay exponentially at all temperatures and fields and are fitted using the same method as above, with $\lambda$ shown in Fig. 6.3 and the globally refined fitting parameters shown in Tab. 6.3. The temperature dependence of $\lambda$ is different to that found in $Co_{10}Zn_{10}$: the peak for $Co_8Zn_9Mn_3$ is significantly broadened with the peak in $\lambda$ occurring significantly below the obtained $T_c$, with similar behaviour seen at both a field that is expected to stabilise the SkL and one that is not. The relaxation rate $\lambda$ at 10 mT is very well described by the equation previously derived for the coupling to gigahertz excitations, Eqn. 4.3, derived in App. A. At 18 mT this model reproduces the correct magnitude for $\lambda$, but does not quite capture the correct shape. This suggests there are additional megahertz dynamics that contribute at this higher applied field. These fits are shown in Fig. 6.3.

In the derivation of Eqn. 4.3 we assume 3D Heisenberg scaling parameters. If we choose a different set of scaling parameters we obtain a very similar fit to the data. This likely occurs as different, physically meaningful scaling parameters do not dramatically change the overall behaviour of the reduction in frequency of the gigahertz excitation. $\mu$SR is sensitive to the drop of frequency through the muon time-window, which will be far more sensitive to the zero-temperature frequency than the exact path the reduction in frequency takes. Note that we find that the critical behaviour of both $\Delta$ and $\nu$ are required to well describe the data, and that critical behaviour of one parameter alone cannot describe them. This suggests that the model described by Eqn. 4.3 is likely the minimal set of assumptions needed to describe the observed effect.

As shown by the fits in Fig. 6.3, this model suggests that $\Delta_{T=0} \simeq 10$–$20$ mT,

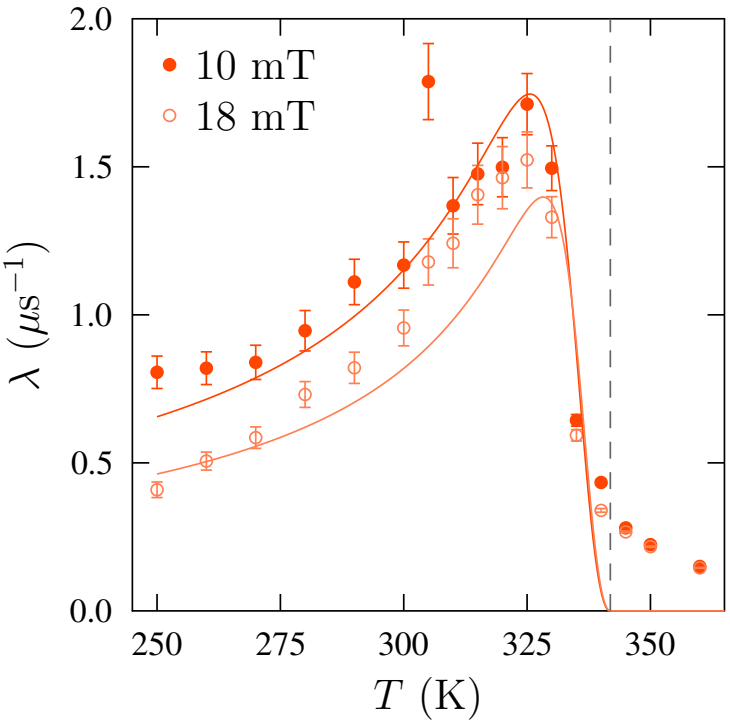


**Figure 6.3:** Extracted values of $\lambda$ from fitting LF $\mu$SR measurements of $Co_8Zn_9Mn_3$. The dashed lines indicate the average value of $T_c$ in the sample according to the relaxing amplitude. Fits are described in the main text.

and $\nu_{T=0} \simeq 1$–2 GHz. This frequency can be identified with the characteristic excitations in this regime, and is very similar to those found for other SkL systems [43]. This suggests that there are dynamics occurring over a range of applied magnetic fields with spectral weight that decreases in frequency with increasing temperature, passing through the frequency range that $\mu$SR is sensitive to just below $T_c$. Further evidence for the similarity at both measured fields comes from the fitted parameters shown in Tab. 6.3; in contrast to those observed in $Co_{10}Zn_{10}$, where the fitted parameters changed significantly between 10 mT and 18 mT, the fitted parameters from measurements of $Co_8Zn_9Mn_3$ are almost identical at both fields.

Interestingly, the fits to Eqn. 4.3 are best above $T \simeq 280$ K, spanning a far greater extent in $T$ than the reported stability region of the SkL in bulk samples. This temperature regime does align with the location in the $B$–$T$ diagram of the SkL and meron-antimeron states are reported in thin plates [113]. The wide range of fields over which we detect enhanced dynamics in these bulk samples and the contrast in the extent of the SkL in plates might therefore suggest that the decisive mechanism determining the extent of the phase diagram in the thin plate samples of $Co_8Zn_9Mn_3$ is confinement, and that dynamics associated with the SkL phase persist beyond the equilibrium SkL in these samples. This may hint at a possible source of megahertz dynamics in these systems beyond the reduction in frequency of the skyrmion modes shown above. It is this possibility which we will now discuss by studying $Co_8Zn_8Mn_4$.

### 6.3.4 $Co_8Zn_8Mn_4$

$Co_8Zn_8Mn_4$ hosts a SkL around room temperature, as shown in Fig. 6.4(a) [23], with the exact location of the SkL phase dependent on the precise level of Mn present. We have performed LF $\mu$SR measurements on two different polycrystalline samples of (nominally) $Co_8Zn_8Mn_4$. LF $\mu$SR measurements on sample 1 again show exponential relaxation. The same fitting procedure is employed as above, however there was no need to include any relaxation of the baseline in

**Table 6.4:** Parameters obtained from fitting LF $\mu$SR measurements of $Co_8Zn_8Mn_4$, sample 1, at a particular applied field.

| $\mu_0 H$ (mT) | $a_b$ (%) | $a_{r0}$ (%) | $k$ | $L$ (%) | $T_c$ (K) |
|---|---|---|---|---|---|
| 8 | 8.958(12) | 0.82(2) | 0.126(4) | 5.01(6) | 308.2(3) |
| 26 | 9.063(8) | 0.96(2) | 0.144(4) | 4.69(5) | 308.8(2) |

this case. (In the data collected on $Co_8Zn_8Mn_4$ it was not possible to accurately estimate $\alpha_{exp}$, leading to a vertical offset on the data, reflected in the low value of $a_b$. This does not affect any of the conclusions presented here.) To most clearly highlight the different behaviours observed, the relaxation rate $\lambda$ measured in an applied field of 8 mT and 26 mT is shown in Fig. 6.4(c). Additional data measured at 15 mT is visually similar to that measured at 26 mT. The fitting parameters are shown in Tab. 6.4.

At $B_{ext} = 8$ mT a SkL is not expected to be stable at any temperature. Although the peak in $\lambda$ is well below $T_c$, the overall behaviour looks typical of previous measurements that do not stabilise a SkL. The behaviour at 26 mT (which does stabilise SkL just below $T_c$) is more unusual, with a flattened, broad maximum, and enhanced values of $\lambda$ observed over a range of temperatures. The suppressed peak at $T_c$ is consistent with different grains of the sample undergoing a transition at slightly different temperatures, caused by slightly varied compositions across parts of the sample. (Mn metal has considerable vapour pressure at 1025 °C, meaning that Mn can migrate toward the surface of the melt during sample synthesis, forming a gradient in composition as observed in $Ni_2MnGa$ [116].)

We find that the enhanced relaxation rate in $Co_8Zn_8Mn_4$ is found at those fields that stabilise the SkL in the $B$–$T$ phase diagram, even at temperatures lower than those that stabilise the SkL state. It is notable that individual skyrmion formation has been reported in MnSi above $T_c$ at those fields that stabilise the SkL [117]. Both our LF $\mu$SR, and these observations in MnSi, therefore report dynamics/dynamic processes associated with the SkL outside of the equilibrium

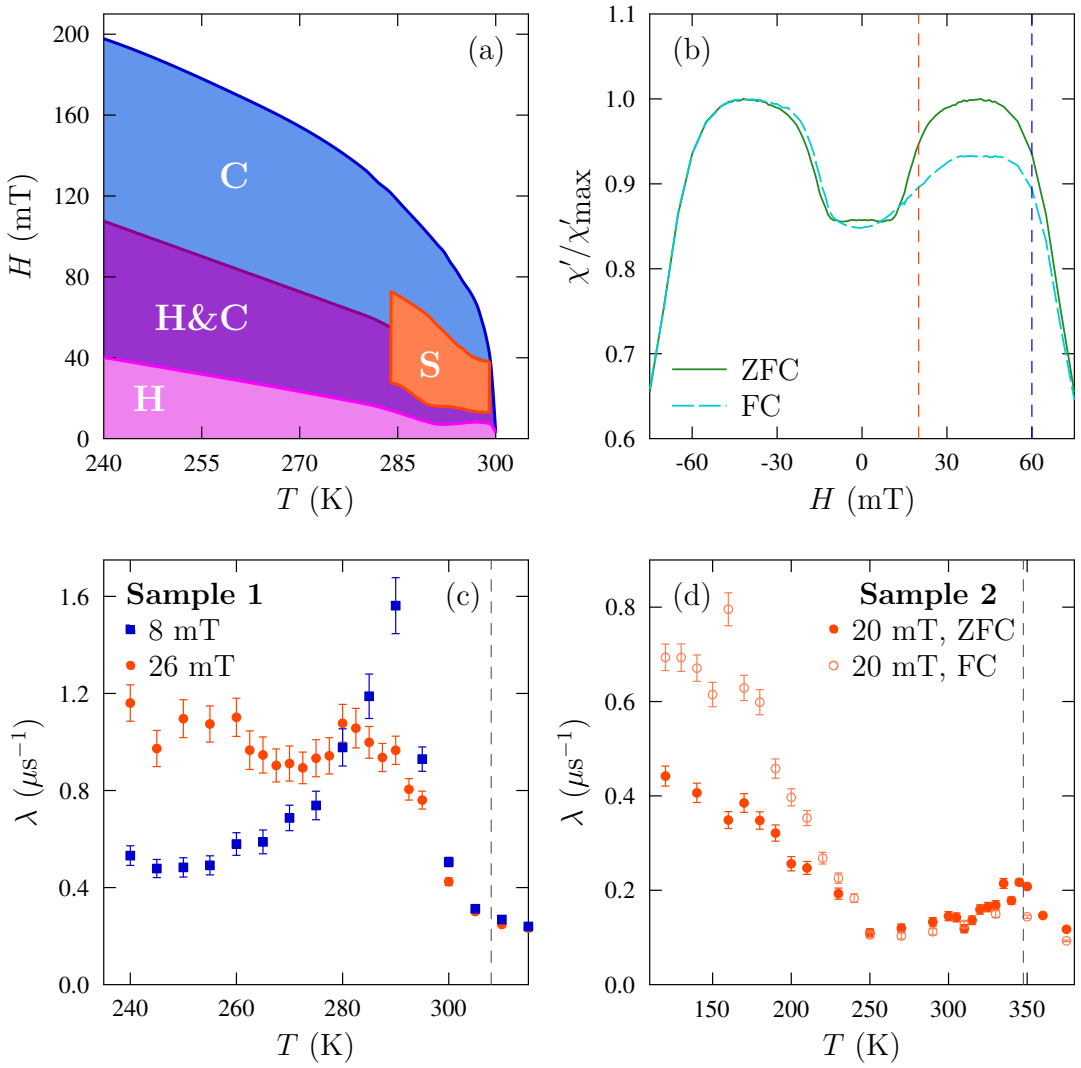


**Figure 6.4:** (a) Representative phase diagram of $Co_8Zn_8Mn_4$, showing helical (H), conical (C) and skyrmion lattice (S) phases, as well as a region of coexistence. Phase diagram reproduced from measurements in Ref. [23]. (b) AC susceptibility measurements at 250 K after cooling in zero-applied field (ZFC) and rapidly cooling in an applied field (FC) (in 15 mT) on one sample of $Co_8Zn_8Mn_4$, indicating a metastable SkL after FC. Fields measured with $\mu$SR in (d) and Fig. 6.6 are indicated with dashed lines. (c–d) Relaxation rate $\lambda$ from LF $\mu$SR measurements on two different samples, with $T_c$ indicated. In (d) different field cooling protocols are employed.

SkL phase. This suggests that the important parameter for skyrmion creation in the Hamiltonian is the applied field, with, as is the current consensus [4, 6], thermal fluctuations stabilising the SkL phase over a significant sample volume.

For further study of $Co_8Zn_8Mn_4$, again on sample 1. To probe the behaviour of $Co_8Zn_8Mn_4$ on the muon timescale, particularly above $T_c$, we have performed additional TF $\mu$SR measurements on this sample. At low $T$ there is evidence in our TF measurements for muons stopping in high-field sites and rapidly depolarising, suggesting that there is a distribution of high internal fields with significant width. The appearance of observable oscillations in the polarisation at high $T$ indicate that $T_c = 300(2)$ K. We, therefore, parametrise the polarisation of the muon-spin ensemble above $T_c$ using

$$P(t) = \sum_{i=1}^{3} a_i \exp(-\Lambda_i t) \cos(\gamma_\mu B_i t), \tag{6.2}$$

which accounts for muons stopping in three distinct magnetic field sites, $B_i$, in the proportions reflected by the amplitudes $a_i$. The muon-spin precesses with the polarisation decaying at a rate $\Lambda_i$ determined both by dynamic effects and also the width of the static magnetic field distribution at each set of muon sites. Component 3 accounts for muons that stop outside of the sample and is temperature independent with $B_3 = 15$ mT, accounting for about 10% of the muon stopping sites. The other two components show a temperature independent amplitude ($a_1 \simeq 70\%$ and $a_2 \simeq 20\%$), with $B_i$ and $\Lambda_i$ [Fig. 6.5]. Above $T_c$ the rates $\Lambda_{1,2}$ decrease rapidly with $T$ and do not follow simple power-law behaviour. By plotting as a function of $T/(T-T_c)$ [Fig. 6.5(a)], motivated by the relaxation rate of a local probe in a strongly correlated electron system [118], one can see two distinct regimes of behaviour, one between 300 K and 307 K and another above this temperature. There is also evidence for these changes in behaviour in the local field [Fig. 6.5(b)], which demonstrates a significant Knight shift, with changes in the gradient between about 303 K and 312 K. The crossover may suggest a change from a system dominated by critical behaviour just above $T_c$ to paramagnetic behaviour of a metal with fluctuating moments, as evidenced by the significant Knight shift persisting to high $T$.

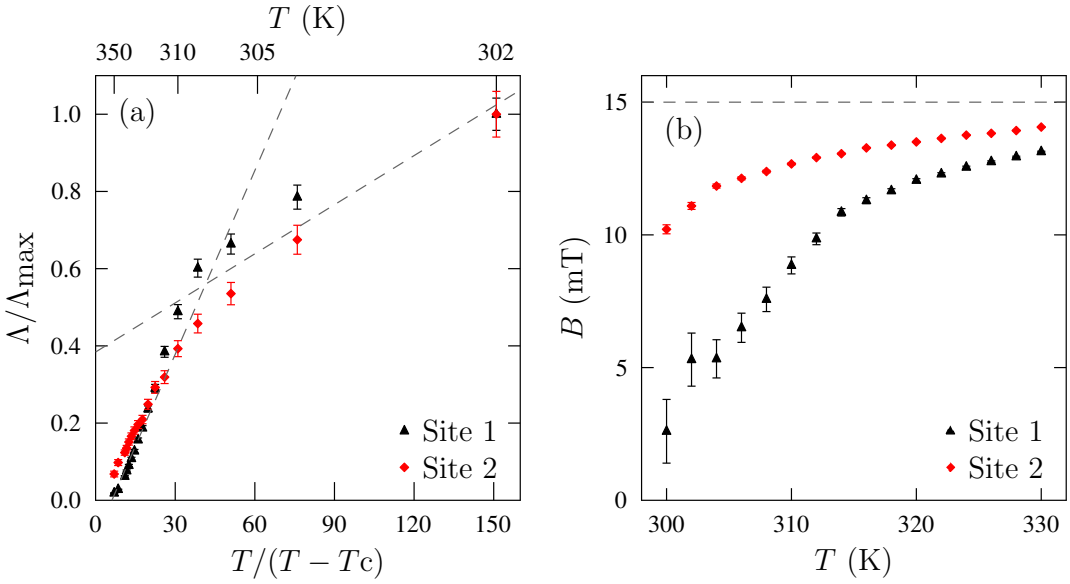


**Figure 6.5:** Scaled relaxation rates (a) and internal fields (b) for TF $\mu$SR measurements at 15 mT on $Co_8Zn_8Mn_4$. In (a) the dashed lines are a guide to the eye. The applied field is indicated with a dashed line in (b).

To further study these dynamics at fields that stabilise a SkL, it is helpful to perturb the magnetic state, either expanding or contracting the extent of the SkL phase in the $B$–$T$ diagram. This can be done through the stabilisation of metastable skyrmions. We consider the effect of a rapid field-cooled (FC) protocol in $Co_8Zn_8Mn_4$, where by rapidly cooling the sample in an applied field that stabilises the SkL at higher $T$, one can stabilise a metastable SkL over a wide range of temperature. For these measurements we used a different sample, labelled sample 2. To confirm the existence of the metastable SkL, AC susceptibility measurements were performed and are presented in Fig. 6.4(b); the suppression of $\chi'$, typical of the SkL, is seen over a wide range of fields when employing a FC protocol. LF $\mu$SR measurements were performed after both ZFC and FC protocols, with $\lambda$ shown in Fig. 6.4(d). To ensure that the effects seen are real, and not fitting artefacts, the parameters that are normally globally refined were shared between both cooling procedures. These parameters are seen in Tab. 6.5. The higher value of $T_c$ is likely obtained due to a subtly different composition of sample 2 compared to sample 1 used for these measurements. Specifically,

**Table 6.5:** Parameters obtained from fitting LF $\mu$SR measurements of $Co_8Zn_8Mn_4$, sample 2, at a particular applied field. Note that, at 20 mT, these parameters were globally refined over measurements made after both ZFC and FC protocols.

| $\mu_0 H$ (mT) | $a_b$ (%) | $a_{r0}$ (%) | $k$ | $L$ (%) | $T_c$ (K) |
|---|---|---|---|---|---|
| 20 | 12.27(2) | 1.97(2) | 0.168(3) | 5.56(2) | 347.97(11) |
| 60 | 14.19(2) | 1.66(3) | 0.20(2) | 4.47(7) | 347.3(4) |

we expect that sample 2 is Mn deficient, with the differences between samples likely occurring due to the different lengths of time at which the sample annealed during synthesis.

The data measured at $B_{ext} = 60$ mT (see Fig. 6.6) show a peak in $\lambda$, typical of those scans that do not cut through the SkL. At 20 mT, where a SkL is formed just below $T_c$, similar behaviour is seen as was found in Fig. 6.4(c), with a suppressed, flattened peak at $T_c$ for both field protocols. There is, however, an enhanced response in $\lambda$ at low $T$ for FC compared to ZFC, suggesting that the stabilisation of a metastable SkL is affecting the dynamics on the muon timescale that we observe. Although this contrasts with the results seen for $Cu_2OSeO_3$, it is consistent with the expected higher stability, and hence increased volume fraction, of the metastable SkL in $Co_8Zn_8Mn_4$ [23, 79]. This may suggest that the crystallographic site disorder allows dynamics similar to those observed in the SkL to persist to lower temperatures. In this case, stabilisation of the metastable SkL likely makes the dynamics more prominent, leading to the enhanced $\lambda$ observed.

Having observed a dynamic effect from both the equilibrium and metastable SkL, we can now consider the source of these dynamics in more detail. There are three obvious classes of dynamics that one may consider as a potential source of this enhanced relaxation: (1) dynamics of the SkL, (2) dynamics associated with the creation of skyrmions, or (3) dynamics associated with decay of skyrmions. We will discuss each of these in turn.

(1) There could be dynamics from collective motion of the SkL, occurring

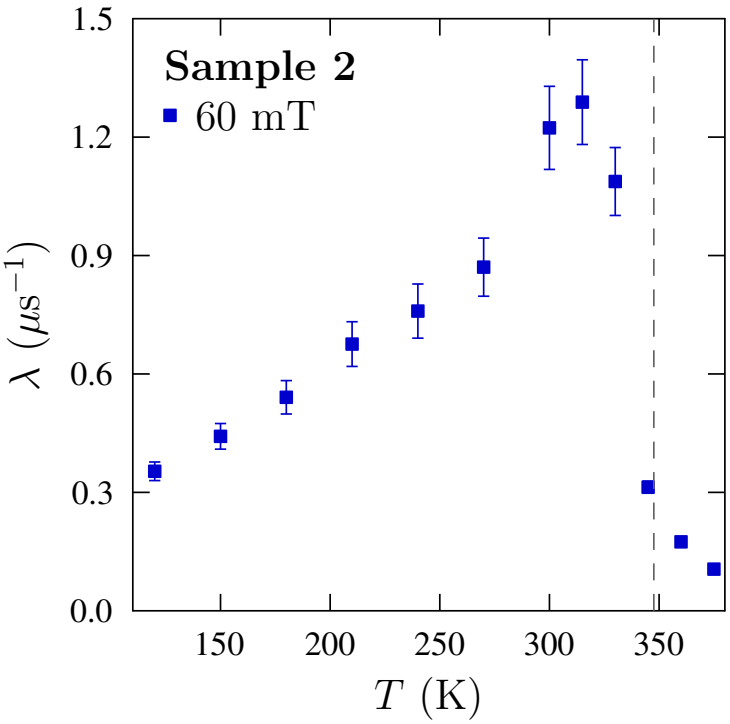


**Figure 6.6:** Relaxation rate $\lambda$ from LF $\mu$SR measurements on $Co_8Zn_8Mn_4$, sample 2, with $T_c$ indicated.

from skyrmions moving in a way that is correlated to the other skyrmions in the lattice. Given the larger effective mass of the SkL compared to individual skyrmions, one would expect these dynamics to be lower in frequency than the gigahertz excitations of an individual skyrmion, and may fall into the megahertz regime to which we are sensitive to in these measurements. For these dynamics to exist, there must be a SkL existing over a significant spatial extent. It therefore seems unlikely that these dynamics can explain the observed enhancement of $\lambda$ in $Co_8Zn_9Mn_3$ at temperatures where there is no equilibrium SkL phase.

(2) The creation of skyrmions can be a relatively slow process, as already discussed in the case of $Cu_2OSeO_3$ (Chap. 4). Reference [86] shows that, in the case of Zn-substituted $Cu_2OSeO_3$, the process of creation of the SkL takes 100s of seconds, indicating that there are likely dynamics over an exceptionally wide range of frequencies. Whilst this seems like a promising candidate for the megahertz dynamics, it seems unlikely that these dynamics will occur in the metastable SkL where, due to the non-equilibrium nature, creation of new skyrmions should be a rare occurrence, and very unlikely to occur over a significant enough volume fraction to detect with $\mu$SR. We therefore conclude that it is unlikely that the megahertz dynamics occur due to creation of skyrmions.

(3) Similar to the creation of skyrmions, the decay of skyrmions is a sufficiently slow process (taking seconds in Zn-substituted $Cu_2OSeO_3$ [86]) that one can expect dynamic effects over a wide range of frequencies, including the megahertz regime where we are sensitive. However, in contrast to creation, decay occurs in the metastable and equilibrium SkL phase (where the rate of creation equals the rate of decay).

It seems most likely that the megahertz dynamics detected with $\mu$SR are dynamics associated with the decay of individual skyrmions. We therefore have a picture of the decay of skyrmions causing fluctuations in the local field at the muon site in the megahertz regime that we then detect. These fluctuations will occur in both the metastable SkL, where there is decay of skyrmions towards zero skyrmion density, and in the equilibrium SkL, where the rate of skyrmion decay

equals the rate of skyrmion creation.

## 6.4 Conclusion

Through $\mu$SR measurements, we are able to detect a range of behaviour in $Co_xZn_yMn_{20-x-y}$ that corresponds to the dramatic differences in magnetism reported through the series. In $Co_{10}Zn_{10}$ we see relatively simple behaviour consistent with critical slowing down around a phase transition. There is no evidence for any abnormal dynamic effects, consistent with the comparatively simple magnetic phase diagram that is not reported to host any topological magnetic states. In contrast, we have shown evidence for megahertz dynamics in $Co_8Zn_9Mn_3$ that are well described by a model of the reduction in frequency near $T_c$ of the characteristic excitations of the skyrmion, finding coupling to $\simeq$ 1–2 GHz excitations. I believe this represents the first measurement of the characteristic excitation modes of the skyrmion in $Co_xZn_yMn_{20-x-y}$. The significant extent of the enhanced dynamics in the $B$–$T$ phase diagram, persisting over a much wider range than the equilibrium SkL, suggests that confinement effects are key to the stabilisation of the static structure of the SkL, and that dynamics associated with skyrmions may be far easier to stabilise. In $Co_8Zn_8Mn_4$ we have shown evidence for enhanced dynamics over a wide range of temperatures when the external field is one that stabilises the SkL. Stabilisation of a metastable SkL enhances these dynamics, likely due to a greater proportion of muons being sensitive to SkL effects. The most likely source of these dynamics seems to be the decay of skyrmions, with both lattice and creation dynamics not being able to explain the observed features.

Considering the series as a whole, we see that as crystallographic site disorder increases (i.e. as $y$ decreases), so too does the complexity of the dynamic response on the muon timescale. This suggests that this site disorder plays a role in stabilising complex excitations. This is consistent with the picture of substitution in $Cu_2OSeO_3$ leading to changes in the stability of the SkL already discussed, although it should be noted that the extent of the relevant effects in the $B$–$T$

phase diagram suggests it is easier to stabilise complex dynamics than complex statics. The effect of chemical site substitution, and the role it plays in stabilising SkL-excitations, will be further discussed in the following chapter.

# Chapter 7

# The effect of substitution in $GaV_4S_{8-y}Se_y$

This chapter presents an investigation of the influence of low-levels of chemical substitution on the magnetic ground state and Néel skyrmion lattice (SkL) state in $GaV_4S_{8-y}Se_y$, where $y = 0, 0.1, 0.2, 7.9$, and 8. Muon-spin spectroscopy ($\mu$SR) measurements on $y \leq 0.2$ materials reveal that the magnetic ground state consists of microscopically coexisting incommensurate cycloidal and ferromagnetic environments, while chemical substitution leads to the growth of localised regions of increased spin density. The magnetism is more robust to chemical substitution at the Se-rich end of the series, with relatively minor changes observed with $\mu$SR. $\mu$SR measurements of emergent low-frequency skyrmion dynamics show that the SkL exists under low-levels of substitution at both ends of the series. These dynamics show two contributions, one from the critical slowing down of the characteristic skyrmion modes of the system, as was the case for $Co_8Zn_9Mn_3$ in the previous chapter, and other megahertz dynamics that look qualitatively similar to those observed for $Cu_2OSeO_3$ in Chap. 4. These skyrmionic excitations persist to temperatures below the equilibrium SkL in substituted samples at both ends of the series, with an extended region of emergent low-frequency dynamics evident at low temperatures. This suggests the presence of skyrmion precursors over a wide range of temperatures. There appears to be additional dynamics at the

lowest measured temperatures in the most heavily substituted systems studied here, which may be the onset of glass-like dynamics that are observed at higher substitution levels (where there is no long-range magnetic order).

This chapter is based on work published in Ref. [119]. The samples were provided by collaborators at the University of Warwick. The $\mu$SR data were measured by myself, alongside collaborators at Durham University and ISIS Neutron and Muon source. The analysis of the data is my own and utilises muon site calculations performed by a collaborator, Ben Huddart (Durham University), which I subsequently used to calculate the field at the muon site for various different magnetic structures. The magnetometry measurements were performed by either myself or a collaborator at the University of Warwick, and I analysed the data. The density functional theory (DFT) calculations were proposed by myself, and carried out by Zachary Hawkhead (Durham University) with whom I jointly analysed the results. The overall discussion is my own.

## 7.1 Introduction

Of the two types of skyrmion with winding number $N = 1$ found in bulk crystals, the Néel skyrmion is by far the less common. First introduced in Chap. 2, the spins across the diameter of the Néel skyrmion form a Néel-type domain wall; it is this that distinguishes it from the Bloch skyrmion counterpart. Both types of skyrmion have a propensity for formation in a lattice when stabilised in bulk materials. To date there are two families of bulk materials that are known to form a Néel-SkL, $GaV_4S_{8-y}Se_y$ [22, 120] and $VOSe_2O_5$ [121]; it is the former family which is the subject of this chapter.

Given the low number of Néel-type SkL hosts, it is imperative to find other systems which stabilise the Néel SkL so that these exotic magnetic textures can be thoroughly studied. As previously discussed, chemical substitution, where atoms in a particular crystal structure are systematically replaced with distinct, but chemically similar, elements, is one way to achieve this. Whilst a promising avenue of research, prior to our work the study of the effects of chemical substitu-

tion in bulk skyrmion materials has previously concentrated on materials hosting Bloch SkL states, and substitution of the magnetic ions. This work extends this to the Néel SkL and chemical substitution of non-magnetic elements.

$GaV_4S_8$ and $GaV_4Se_8$ are isostructural, both being lacunar spinels [122] which crystallise in the polar rhombohedral structure $R3m$ below a structural phase transition at 42 K and 43 K respectively [123]. (The low temperature structure is shown later in the context of DFT calculations, Fig. 7.8.) Above this temperature the materials form the cubic $F\bar{4}3m$ phase, consisting of $V_4X_4$ and $GaX_4$ tetrahedra ($X$ = S, Se) arranged in the NaCl structure [124]. Below the structural phase transition, there is no centre of inversion symmetry, which leads to competition between the exchange and Dzyaloshinskii-Moriya interaction and gives rise to the complex magnetic states observed in the $B$–$T$ phase diagram. Also important (particularly in $GaV_4S_8$) is the easy-axis anisotropy, which can be interpreted as an exchange anisotropy [125], with the direction of the easy axis aligning with the direction of the rhombohedral distortion, where a single V ion distorts along one of the possible $\langle 111 \rangle$ directions in the $V_4X_4$ cluster [22, 123]. Work is ongoing to understand this distortion and the subsequent changes in the magnetism, however it is believed to be driven by mechanisms such as a cooperative Jahn-Teller distortion [126] and charge order of the three $V^{3+}$ and one $V^{4+}$ ions that make up the cluster [127]. This removes some of the degeneracy of the magnetic d-orbitals. In this thesis we restrict ourselves to studying the $GaV_4S_{8-y}Se_y$ family in the $R3m$ phase.

A Néel SkL can be found in $GaV_4S_8$ when the material is cooled to between approximately 8 K and 13 K, and an external magnetic field of between approximately 10 mT and 160 mT is applied, with the precise location of the SkL in the $B$–$T$ phase diagram dependent on the orientation of the applied field and the crystallographic axes [22]. Similarly, in $GaV_4Se_8$ the Néel SkL is formed below approximately 17 K (extending down to the lowest measured temperatures), in an external magnetic field of between approximately 20 mT and 400 mT [120] once again with precise details depending on crystal orientation. There are of-

ten limitations when studying $GaV_4S_{8-y}Se_y$ with many experimental techniques; x-ray based methods are typically unable to reach sufficiently low temperatures (the required cryostat would block the x-rays), there is significant incoherent scattering from vanadium atoms when using neutrons to probe the material, and, as Lorentz Transmission Electron Microscopy is only sensitive to the in-plane magnetic field, it cannot easily study the Néel SkL. This leads to a necessity for other experimental techniques which do not have these constraints; here we employ $\mu$SR.

We have previously studied the influence of high-levels of chemical substitution on the Néel SkL compounds $GaV_4S_8$ and $GaV_4Se_8$, by investigating $y = 2$ and 4 compositions in the $GaV_4S_{8-y}Se_y$ series [128]. These compositions do not undergo the structural phase transition on cooling [127], and hence induce a spin-glass ground state, which makes it impossible to continuously evolve the magnetic state of $GaV_4S_8$ into $GaV_4Se_8$. This lack of long-range magnetic order prevents the stabilisation of the SkL at this level of substitution. Further, we demonstrated that, in polycrystalline samples of $GaV_4Se_8$, the SkL is confined to a smaller region of the $B$–$T$ phase diagram than previously reported in single crystals.

In this chapter we will focus on the effect on the magnetism of low-levels of chemical substitution in the $GaV_4S_{8-y}Se_y$ series, predominantly by studying the $y = 0.1$ and $y = 7.9$ materials and contrasting them to the $y = 0$ ($GaV_4S_8$) and $y = 8$ ($GaV_4Se_8$) compounds. We investigate these systems through $\mu$SR, AC susceptibility and first principles calculations carried out using DFT.

## 7.2 Experimental Methods

Polycrystalline samples of $GaV_4S_{8-y}Se_y$ with $y = 0$, 0.1, 0.2, 7.9 and 8 were synthesised and characterised by Geetha Balakrishnan, Ales Štefančič and Samuel Holt at the University of Warwick as described in Ref. [128, 127, 123].

Magnetisation and AC susceptibility measurements were performed using a Quantum Design MPMS3, a Quantum Design MPMS-5S and the AC susceptibility option of a Quantum Design PPMS. For AC susceptibility measurements

an excitation field of 0.3 mT was normally applied, apart from the measurements on $GaV_4S_8$ where 0.1 mT was used. All results are normalised by the relevant excitation field.

Zero-field (ZF) and transverse-field (TF) $\mu$SR measurements were made using the general purpose surface-muon (GPS) instrument at the Swiss Muon Source (S$\mu$S), Paul Scherrer Institut, Switzerland, whilst longitudinal-field (LF) $\mu$SR measurements were made using the HiFi spectrometer at the ISIS Neutron and Muon Source, UK. Polycrystalline samples were packed into Ag foil packets and mounted in a He4 cryostat. For the GPS instrument, the sample was suspended in the muon-beam on a fork in the fly-past geometry (minimising the contribution from muons stopping outside of the sample), whereas the sample was mounted on a silver backing plate for measurements using the HiFi spectrometer. Muon data analysis was carried out using the WiMDA program [68] and made use of the MINUIT algorithm [93] via the iminuit [94] Python interface for global refinement of parameters.

First principles calculations using DFT were carried out using the CASTEP planewave, pseudopotential code [76]. The generalised gradient approximation (PBE) [95] was used in all calculations. A planewave cutoff energy of 1000 eV and a 3×3×3 Monkhorst-Pack grid [129] was used to converge the calculations to a tolerance of 0.01 eV per unit cell. An effective Hubbard $U$, $U_{\text{eff}} = U - J$, where $U$ is the bare Hubbard repulsion and $J$ is the Hund coupling, of 2.5 eV was included on the vanadium d orbitals to act as a local Coulombic repulsion. Various $U_{\text{eff}}$ were tested over the range 0.5–3.25 eV, with 2.5 eV found to be the minimum value which produced V magnetic moments that did not change upon further increasing $U_{\text{eff}}$.

We have used the muon stopping sites calculated in Ref. [128], along with the MUESR code [96] to perform simulations of magnetic field distributions at these sites for various spin structures in $GaV_4S_{8-y}Se_y$. We employed $\lambda_{\text{C}} = 17$ nm [22] when simulating the cycloidal state.

## 7.3 Results & Discussion

### 7.3.1 Magnetometry

AC magnetic susceptibility measurements of polycrystalline $GaV_4S_{8-y}Se_y$ with $y = 0,\ 0.1,\ 7.9$ and 8 are shown in Fig. 7.1(a–d). Measurements of the AC magnetic susceptibility is typically highly sensitive to phase boundaries and hence are often used to determine the phase diagram of a material. Whilst polycrystalline samples of $GaV_4S_{8-y}Se_y$ are likely to exhibit a different magnetic phase diagram to those of single crystals (whose behaviour varies depending on the alignment between applied field and crystallographic axes), our previous work has shown that the SkL can be identified unambiguously [128]. Our measurements indicate relatively small changes in the position of the phase boundaries in the substituted materials when compared to their pristine counterparts, suggesting the SkL state is still formed. In the substituted systems, the maximum susceptibility is approximately an order of magnitude greater than in the pristine systems, suggesting enhanced dynamics at low frequencies.

The magnetisation of these materials, measured in an applied field of 5 mT, is shown in Fig. 7.1(e–f). The most striking feature at the S-rich end of the series is the increase in magnetisation of the $GaV_4S_{7.9}Se_{0.1}$ compared to $GaV_4S_8$, showing that the effect of substituting Se in $GaV_4S_8$ at these levels is a small increase in magnetisation of the sample. At the Se-rich end of the series the opposite is true, with addition of S leading to a reduction in the magnetisation. The splitting between the zero-field cooled and field-cooled measurements is likely due to the alignment of magnetic domains and is a fingerprint of magnetic order.

### 7.3.2 Zero-field muon-spin spectroscopy

To further probe the magnetic states of $GaV_4S_{8-y}Se_y$ we performed $\mu$SR measurements in the ZF, LF and TF geometries; example spectra can be seen in Fig. 7.2. First we consider the measurements obtained with ZF $\mu$SR, which probes the magnetic ground state of the system. In $GaV_4S_8$, above $T_c = 12.7(3)$ K we

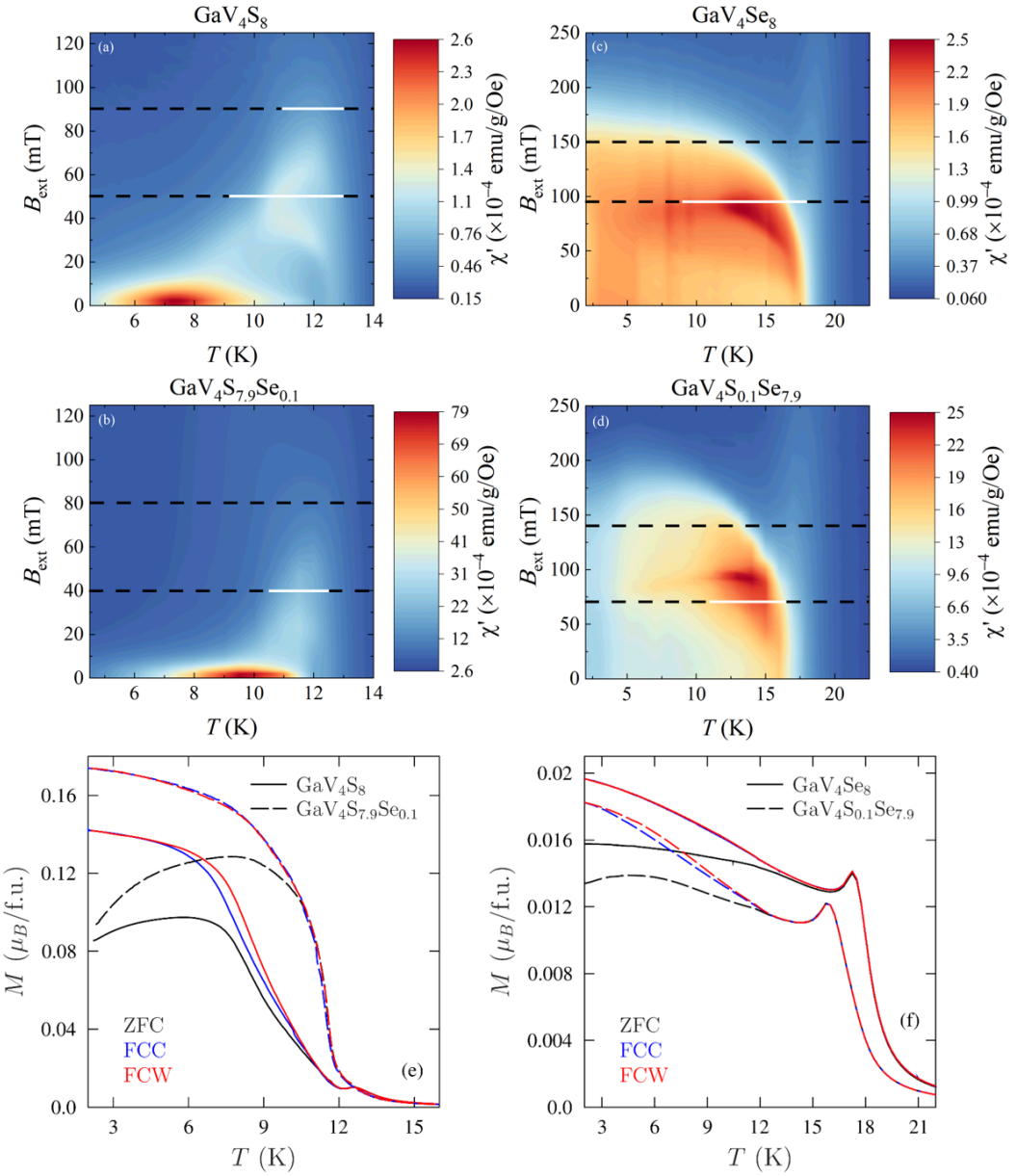


**Figure 7.1:** Real component of AC susceptibility in constant field $B_{\text{ext}}$ for (a) $y = 0$ (b) $y = 0.1$, (c) $y = 8$ and (d) $y = 7.9$. Lines indicate fields where $\mu$SR measurements were performed, with white highlighting proposed SkL regions as based on $\mu$SR measurements (see text). (e–f) Magnetisation of $GaV_4S_{8-y}Se_y$, measured in an applied field of 5 mT. Three field protocols are employed: cooling in the absence of an applied magnetic field and measuring on warming (ZFC), measuring whilst cooling in an applied field (FCC), and measuring on warming after cooling in an applied field (FCW).

find the muon-spin asymmetry $A(t)$ is parametrised by $A(t) = a_r \exp(-\lambda t) + a_b \exp(-\lambda_b t)$, typical of a paramagnet. The first term with amplitude $a_r$ reflects relaxation at rate $\lambda$ from muons that stop within the sample in the paramagnetic state, whilst the $a_b$ component captures the contributions from muons that stop outside the sample. It is often helpful to consider the Fourier transforms (FT) of $A(t)$ in the ordered phase ($T < T_c$) of a material as it reveals the spectral weight of internal magnetic fields at the muon sites. Example FTs for $GaV_4S_8$ are shown in Fig. 7.4(a–c). By comparing these FTs to the expected probability distribution of different magnetic states in the material one can identify the magnetic state.

We have performed simulations of the magnetic field at the muon-stopping sites using the MUESR code [96, 128] for the ground-state magnetic structures proposed for $GaV_4S_8$ [22, 130, 127]. Specifically, we have simulated the muon response to ferromagnetic-like (FM*) (Fig. 7.3) and incommensurate cycloidal order by calculating each of the relevant contributions to the field at the muon site, as introduced in Chap. 3. Whilst the $\boldsymbol{B}_{\text{dip}}$ and $\boldsymbol{B}_{\text{Lor}}$ terms are calculable simply from an expression for the vector spin in each different structure, $\boldsymbol{B}_{\text{dem}}$ and $\boldsymbol{B}_{\text{con}}$ need slightly more thought. In a polycrystalline sample, such as those used in this work, each crystal grain, in the absence of an externally applied field, will be made up of multiple randomly oriented magnetic domains. Hence, in this case the magnetisation of an individual grain will be approximately zero (due to multiple unaligned magnetic domains), meaning $\boldsymbol{B}_{\text{dem}}$ will be approximately zero for the zero-field simulations performed in this work. We found that $\boldsymbol{B}_{\text{con}}$ does not have a significant effect on the local field at the muon site, so in the shown simulations this contribution has been assumed to be zero. In systems such as $GaV_4S_{8-y}Se_y$ where there are multiple crystallographically distinct muon stopping sites the experimental spectra will consist of contributions from all sites with relative amplitudes reflecting the proportion of muons that stop in each site. This is further complicated when the magnetic structure of the system leads to crystallographically equivalent muon stopping sites that are magnetically distinct. Calculating the proportion of muons that stop in each site is still an

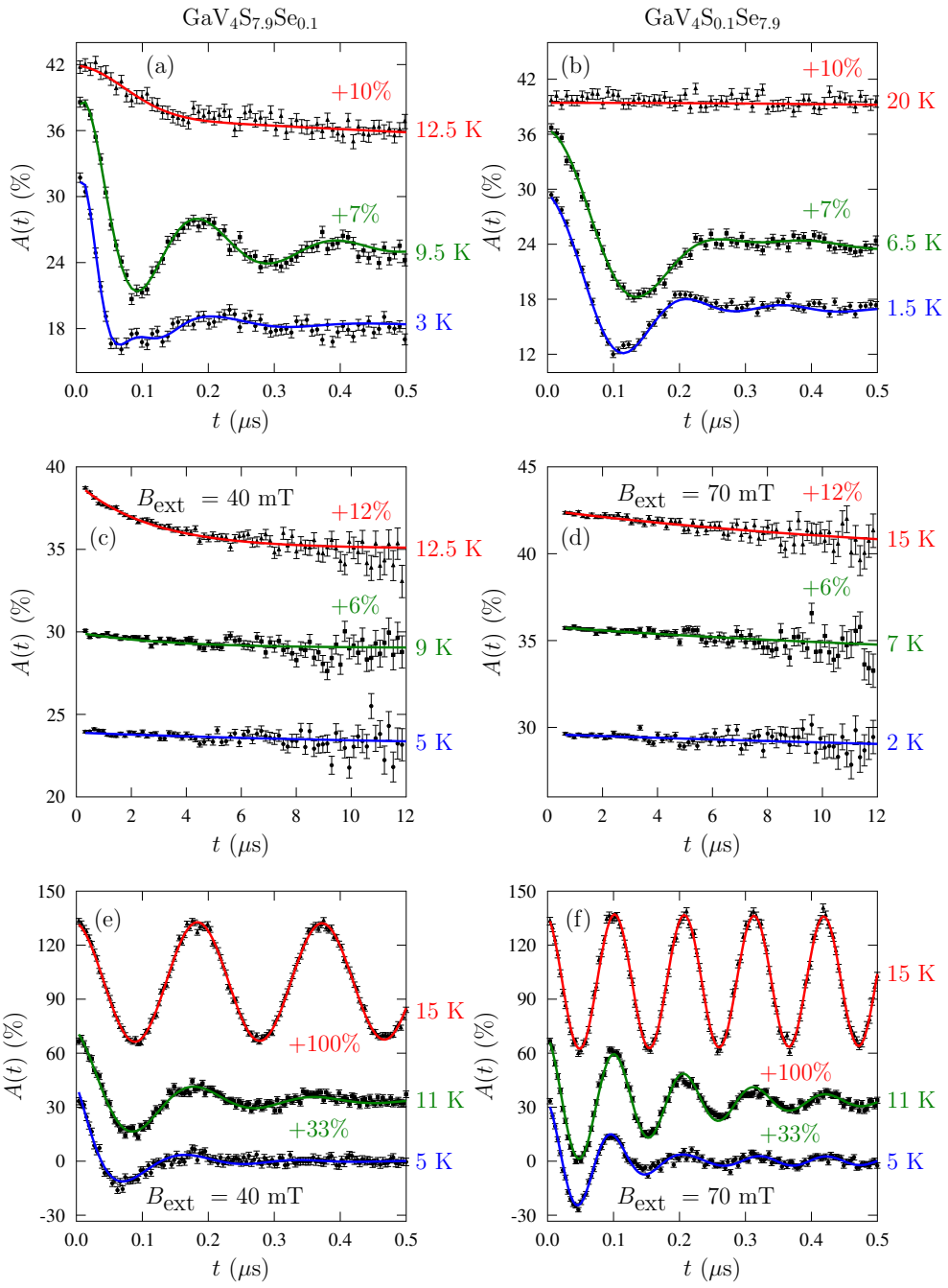


**Figure 7.2:** Example zero field (a–b), longitudinal field (c–d) and transverse field (e–f) muon spin spectroscopy measurements on $GaV_4S_{8-y}Se_y$ with $y = 0.1$ (a,c,e) and $y = 7.9$ (b,d,f). Some data is shown with an indicated vertical offset for clarity.

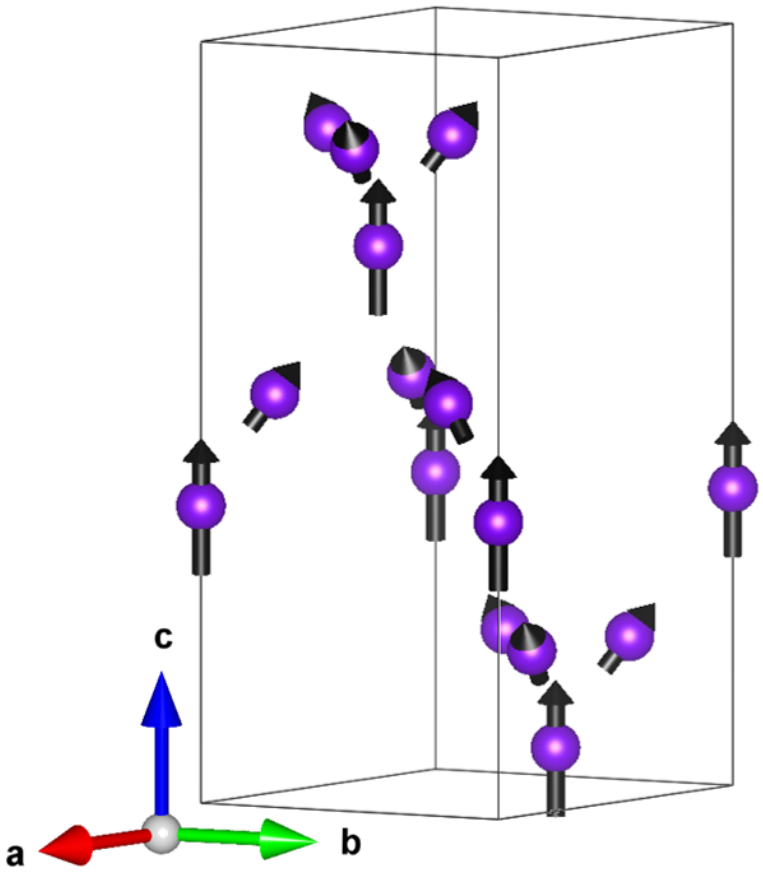


**Figure 7.3:** FM* ground state for $GaV_4S_8$, V atoms are shown. Image produced with VESTA [108].

open problem (being an instance of a multi-scale, non-equilibrium ion-stopping problem), hence for the simulations in this work it was assumed that the muons have equal probability to stop in each of the four lowest energy sites as this well reproduces the experimental results. The results of these simulations are shown in Fig. 7.4(a–c).

Our simulations show that the distribution most closely resembles the FM* state at low-temperatures, and the cycloidal state at higher temperatures. At all temperatures the spectra have features similar to those of both magnetic structures, however the data cannot be described by a simple sum of the two simulations as would be expected for spatially separated domains of FM* and cycloidal order. Our data therefore suggests a continuous evolution of the magnetic ground state from FM* to cycloidal (rather than an abrupt phase transition) where the

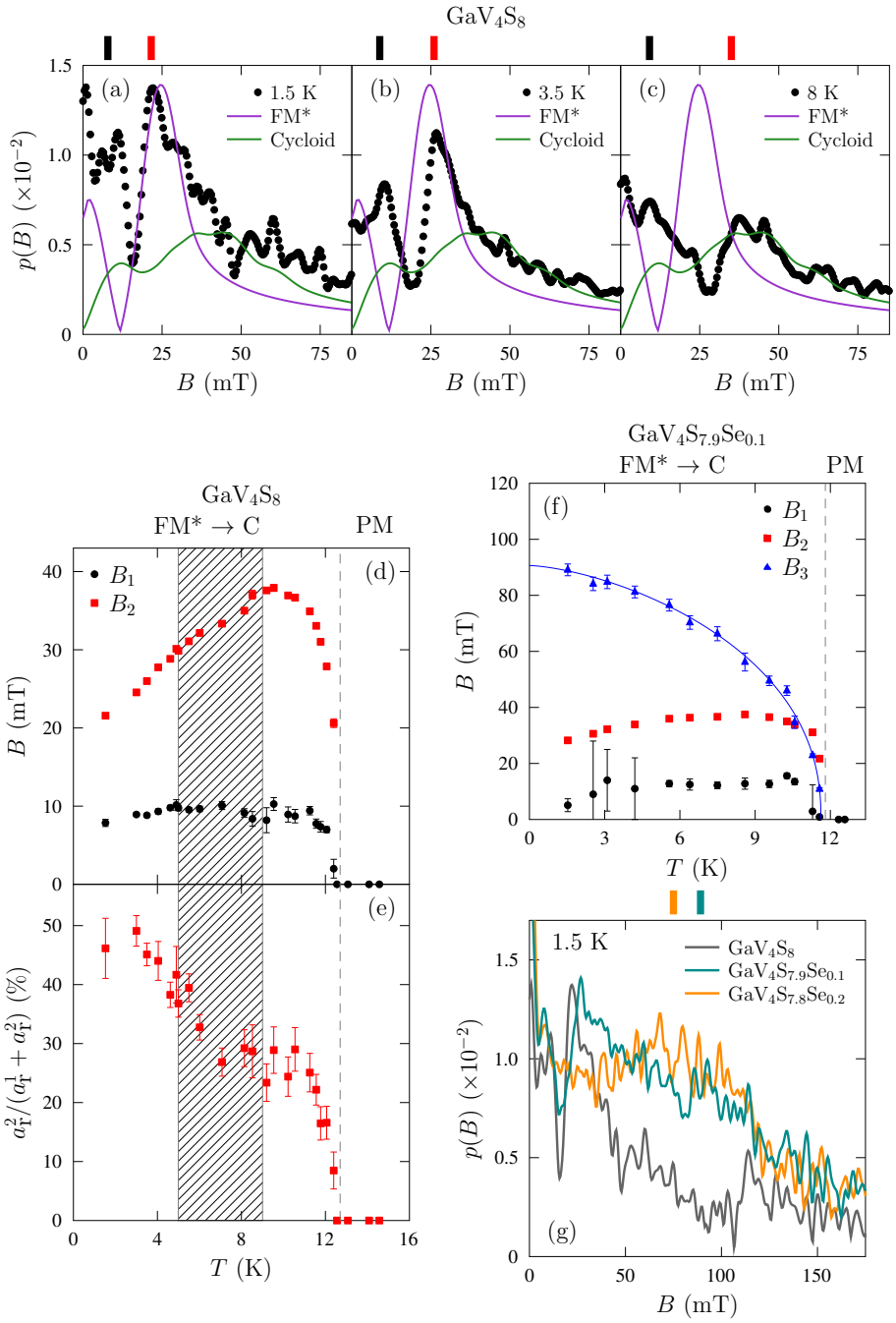


**Figure 7.4:** (a–c) Internal magnetic field distributions $p(B)$ for $GaV_4S_8$, obtained via the FTs of ZF $\mu$SR data at several temperatures, compared to simulations of the ferromagnetic-like (FM*) (Fig. 7.3) and cycloidal (C) states. Parameters from ZF $\mu$SR measurements of $GaV_4S_{8-y}Se_y$for (d–e) $y = 0$ and (f) $y = 0.1$. The extracted internal fields seen in (d) are marked in (a–c). (g) $p(B)$ for $y = 0$, $y = 0.1$ and $y = 0.2$, with the $B_3$ component marked for $y = 0.1$ and $y = 0.2$. The vertical dashed lines indicate $T_c$.

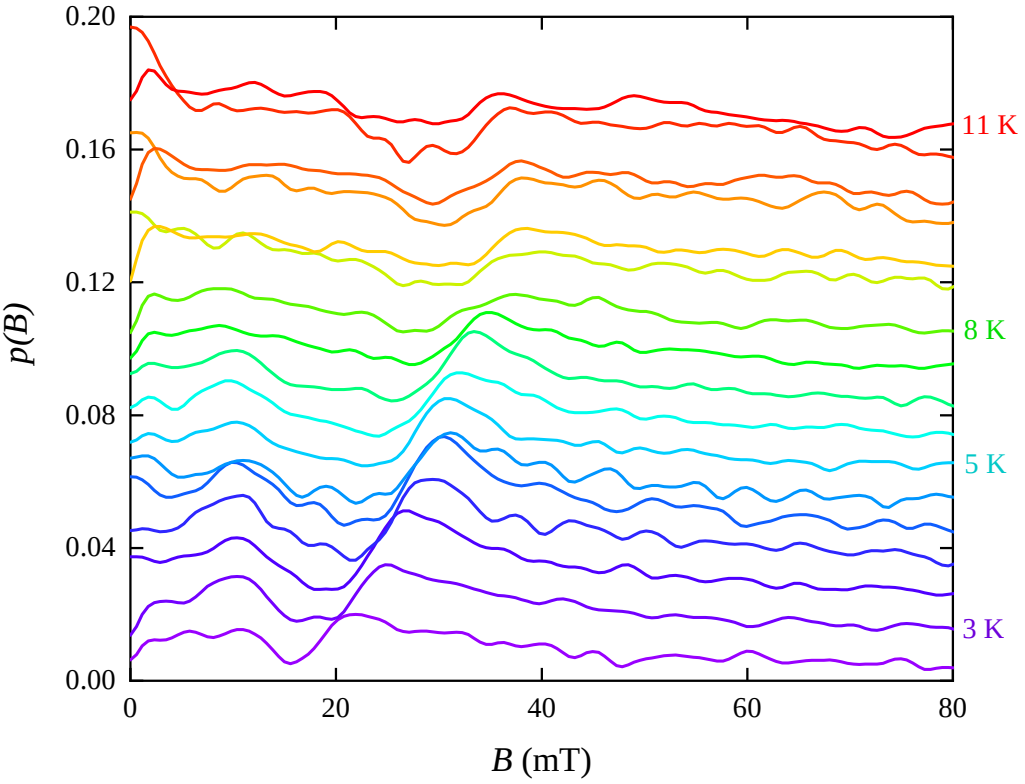


**Figure 7.5:** FT of ZF $\mu$SR measurements of $GaV_4S_8$. The continuous nature of the crossover from the FM* to cycloidal phase can be seen as the continuous changes in the observed peaks.

spins slowly transform from one structure to the other. In fact, this crossover has been suggested to occur via nucleation and growth of solitons [131, 132], with the associated cycloidal anharmonicity likely to help explain some of the discrepancies between simulation and experiment. The precise mechanism is likely to depend sensitively on the crystalline anisotropy in the system [133]. Our data, therefore, suggests FM* domains are prevalent at low $T$, with the possibility of soliton-like cycloidal domain walls growing continuously with increasing $T$ until a cycloidal-majority phase is realised. For completeness, additional Fourier transforms of the ZF $\mu$SR data measured on $GaV_4S_8$ can be seen in Fig. 7.5, highlighting the continuous transformation from the FM* to cycloidal-dominated phases.

To investigate the possibility of the spin being localised on the V cluster rather than the individual atoms in $GaV_4S_8$, the cycloidal state was simulated both as

suggested in Ref. [130], i.e. with the spin localised on the V atoms, and with the spin localised instead on the V cluster. The latter do not produce spectra consistent with the results of $\mu$SR, suggesting that the spin is indeed localised on the V atoms. This is consistent with neutron diffraction data presented in Ref. [127], and our DFT results presented below.

To extract more quantitative information on the ground state of $GaV_4S_{8-y}Se_y$ it is informative to fit the ZF $\mu$SR asymmetry with a model consisting of multiple relaxing oscillatory functions. In general, at temperatures $T < T_c$, the asymmetry $A(t)$ is fitted to

$$A(t) = \sum_{i=1}^{n} a_{ri} \exp(-\Lambda_i t) \cos(\gamma_\mu B_i t + \phi_i) + a_b \exp(-\lambda_b t), \tag{7.1}$$

where each component with amplitude $a_{ri}$, and relaxation rate $\Lambda_i$, reflects muons that stop in local field $B_i$ and precess with phase offset $\phi_i$. Each muon site contributes $a_{ri}$ to the total amplitude, proportional to the number of muons stopping in each site. The oscillatory signal decays with relaxation rate $\Lambda_i$, dependent predominantly on the width of the distribution of magnetic fields at the muon site. The baseline contribution comes both from muons stopping with their spin initially aligned parallel to the local-field, depolarising due to dynamic effects with relaxation rate $\lambda_b$, and due to muons stopping outside of the sample in the silver foil or backing plate.

ZF $\mu$SR asymmetry curves of $GaV_4S_8$ contain a temperature-independent oscillatory component with $B = 112.7(5)$ mT. As this signal does not disappear at $T_c$, as would be expected if it was coming from $GaV_4S_8$, we attribute this signal to a low-level secondary phase in the sample, most likely $V_5S_8$, an antiferromagnet with $T_N \simeq 35$ K. An antiferromagnetic fraction would only contribute to magnetisation measurements performed after field-cooling, so may account for some of the differences seen between the cooling protocols seen in Fig. 7.1(e). From the amplitude of this component we estimate this contaminant to be 6(2)% of the total sample volume. The discussion for the rest of this chapter focuses on the signal coming from muons which stop in $GaV_4S_8$.

For the ZF $\mu$SR spectra measured on $GaV_4S_8$, we require only $n = 2$ in

Eqn. 7.1 to capture the behaviour of the signal coming from $GaV_4S_8$. This indicates two magnetically distinct components with local field magnitude $B_i$. Extracted parameters [Figs. 7.4(d,e)] show that $B_1$ corresponds with the low-field peak seen in the simulations of both the FM* and cycloidal states [indicated in Figs. 7.4(a–c) with a black line], with $B_2$ corresponding to the high field peak (red line). We find that $\phi_1$ is approximately zero, whereas $\phi_2 \simeq 20°$. The unusual decrease in $B_2$ with decreasing temperature, along with a change in the fraction of muons subject to this magnetic field, reflects the continuous evolution of the magnetic state, providing further evidence for a smooth crossover between the FM* and cycloidal states. The crossover region $5 \lesssim T \lesssim 9$ K [shaded in Fig. 7.4(e)] reflects the most rapid change of spin structure which leads to the enhanced AC susceptibility response seen in Fig. 7.1(a).

For the $GaV_4S_{7.9}Se_{0.1}$ material, up to $T_c = 11.6(2)$ K ZF $\mu$SR measurements are well parametrised by Eqn. 7.1 with $n = 3$, indicating a third, magnetically-distinct muon environment not observed in $GaV_4S_8$ [Fig. 7.4(f)]. Below $T_c$, the amplitudes $a_{ri}$ are found to be temperature independent, indicating that 13(5)% of the muons stopping in the sample stop in sites with $B_1$, 32(3)% in $B_2$, and 55(4)% in $B_3$. Interestingly, the phase offsets have changed compared to $GaV_4S_8$. For $GaV_4S_{7.9}Se_{0.1}$, $\phi_1 \simeq -35°$, $\phi_2 \simeq 10°$ and $\phi_3 \simeq -70°$. The 45° offset between $\phi_1$ and $\phi_2$ is often an indication of incommensurate magnetic structures [134, 135], and may suggest the cycloidal phase dominates at all temperatures in $GaV_4S_{7.9}Se_{0.1}$. There are three mechanisms which can explain the appearance of the $B_3$ component in $GaV_4S_{7.9}Se_{0.1}$. (i) A change in spin structure. This can be ruled out as $B_1$ and $B_2$ are very similar in magnitude and $T$ evolution to $GaV_4S_8$, suggesting similar underlying behaviour. (ii) An increase in the magnetic moment $m$. The field at the muon site $B_i \propto m$. As $B_3/B_2 \simeq 3$ this would imply an increase of moment by the same factor, which can again be ruled out as there is no evidence for this in $B_1$ and $B_2$. Further, whilst there is a small increase in the magnetisation of $GaV_4S_{7.9}Se_{0.1}$ compared to $GaV_4S_8$ [Fig. 7.1(e)], this increase alone is not sufficient to explain the ratio $B_3/B_2 \simeq 3$. (iii) A change

in distance $r$ between the spin density and the muon. As $B_i \propto 1/r^3$, even a modest change in spin density could lead to dramatic changes in $B_i$. We therefore suggest that the most likely explanation of the appearance of the $B_3$ component is an increase in spin density near the muon sites such that these regions of high magnetic field condense around the substituent. This is supported by the FT of $A(t)$ for $GaV_4S_{7.9}Se_{0.1}$ and $GaV_4S_{7.8}Se_{0.2}$ [Fig. 7.4(g)] which show that the signature FM* peak around 25 mT is further suppressed upon increased substitution, with spectral weight shifting to the broad, high-field peak not present in $GaV_4S_8$. As the $B_3$ component becomes more pronounced with increased Se substitution this suggests the increase in spin density is not caused by muon implantation during the measurements.

In $GaV_4S_{7.9}Se_{0.1}$ the $B_3$ field is observed to follow a power law dependency as

$$B = B_0 \left(1 - (T/T_c)^{3/2}\right)^{\beta}, \tag{7.2}$$

where $B_0$ is the zero-temperature field value, $\beta = 0.436(11)$ is the critical exponent near $T_c$ and the power 3/2 is due to 3D gapless magnons near zero-temperature. Whilst this value of $\beta$ is slightly higher than one would expect for a typical Heisenberg or Ising-type magnet [14], it is likely that Heisenberg-like behaviour probably well describes this system, as the temperature dependence of this component is likely to have contributing factors beyond simple critical scaling.

The extracted values of $\Lambda_i$ when fitting Eqn. 7.1 to ZF $\mu$SR measurements of $GaV_4S_8$ and $GaV_4S_{7.9}Se_{0.1}$ are shown in Fig. 7.6. The upper-temperature boundary of the crossover regime (where, on decreasing temperature, cycloidal order gives way to FM* order), is marked by a peak in both $\Lambda_1$ and $\Lambda_2$. No such peak is observed in the data measured on $GaV_4S_{7.9}Se_{0.1}$. This may suggest that the FM* order does not appear, and that cycloidal order dominates down to the lowest temperatures, consistent with the 45° phase offset observed in these data. Alternatively, it is possible that the peak in $\chi'$ observed in the AC susceptibility measurements may also indicate the crossover regime in these materials. Whilst, in $GaV_4S_8$, this peak matches that observed in $\Lambda_1$ and $\Lambda_2$, occurring around

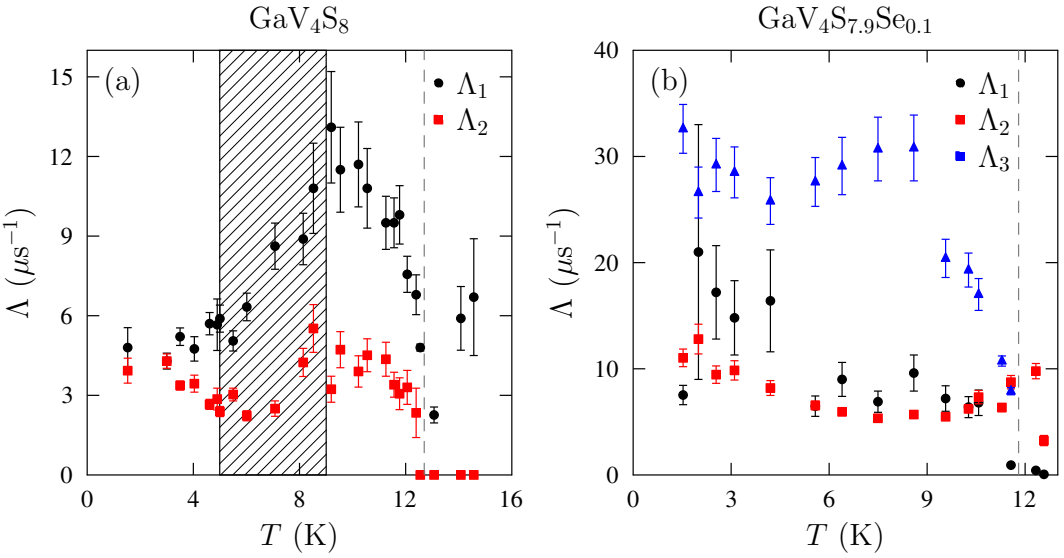


**Figure 7.6:** Zero field muon spin spectroscopy relaxation rates $\Lambda$ as a function of temperature for (a) $GaV_4S_8$, (b) $GaV_4S_{7.9}Se_{0.1}$. Relaxation rates correspond to the same term as the fields shown in Fig. 7.4. The vertical dashed lines indicate $T_c$.

7 K, in $GaV_4S_{7.9}Se_{0.1}$ this peak occurs at the higher temperature of around 10 K, persisting up to just below $T_c$. If, instead, the peak in $\chi'$ is interpreted as temperatures at which there is competition between phases, this peak may correspond to the competition between paramagnetism and long-range magnetic order; a broadening in temperature of a magnetic transition is a common consequence of chemical substitution. Further work to investigate the nature of this transition would be beneficial.

The Se-rich end of the series shows more conventional magnetic behaviour, with $\mu$SR measurements of $GaV_4Se_8$ suggesting $T_c = 17.5(5)$ K with FT spectra consistent with simulations of a cycloidal spin structure. These measurements can once again be fitted with Eqn. 7.1 with $n = 2$, the extracted parameters can be seen in Fig. 7.7. For $GaV_4Se_8$, 85(2)% of the muons are found to stop in the site where the field is $B_1$ (with $\phi_1$ approximately zero), with the remaining 15(2)% in the $B_2$ site ($\phi_2 \simeq -70°$). Measurements of $GaV_4S_{0.1}Se_{7.9}$ show similar average fields, but the fitting also requires an additional relaxing component and larger

relaxation rates, indicating a broadening of the local magnetic-field distribution. For $GaV_4S_{0.1}Se_{7.9}$ 68(3)% of the muons are found to stop in the site with field $B_1$ ($\phi_1 \simeq -70°$), with 25(3)% in the $B_2$ site ($\phi_2 \simeq -90°$). The remaining 5.8(5)% of the muons stop in sites which lead to a purely relaxing component.

The oscillatory relaxation rates are presented in Fig. 7.7 and show very similar behaviour between the compounds, suggesting that the magnetism is more robust to chemical substitution at this end of the series. The extracted internal fields demonstrate power law behaviour, see Eqn. 7.2. With $\beta$ and $T_c$ used as shared fitting parameters between the two fields in each sample, values of $\beta = 0.40(3)$ and $T_c = 17.4(2)$ K were obtained for $GaV_4Se_8$, whilst, for $GaV_4S_{0.1}Se_{7.9}$, $\beta = 0.48(2)$ and $T_c = 16.1(2)$ K. The fact that both fields in each sample have the same power law dependency shows that they arise from the same magnetic order, with just a scale factor due to different muon site positions in the crystal lattice. Again, relatively modest changes in $\beta$ suggest the nature of the magnetism at the Se-rich end of the series is not dramatically affected by this level of chemical substitution.

### 7.3.3 Density functional theory

To further understand the effect of substitution in $GaV_4S_{8-y}Se_y$ we performed first principles calculations using DFT, comparing the pristine materials to substitution of $y = 1$ or $y = 7$ (which are not measured here) by replacing the atoms on one S or Se site with the relevant substituent. This allows us to simulate the effect of low-levels of substitution. Whilst the DFT calculations presented here are on the $y = 1$ and $y = 7$ materials, in reality these materials do not form the rhombohedral phase [127, 123], and hence these calculations are not of a physically realised system. DFT calculations of lower substitution levels are unfeasibly expensive. We avoid this issue by imposing the symmetry of the experimentally realised crystal structure of the $y = 0.1$ or $y = 7.9$ materials on a unit cell containing a substitution. This therefore allows investigation of the effects on the spin density of substitution in the crystal structure this substituent realises for

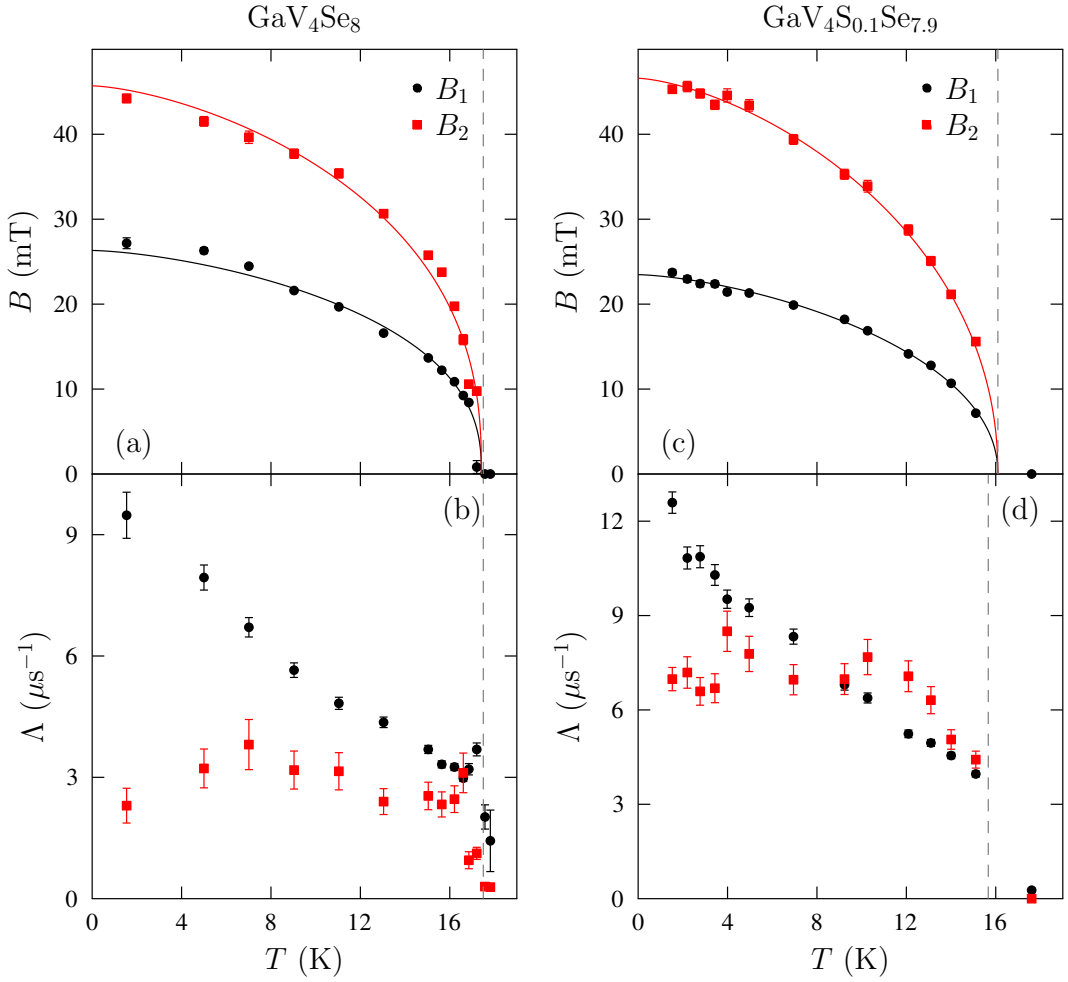


**Figure 7.7:** Zero field muon spin spectroscopy internal fields $B_i$ and relaxation rates $\Lambda_i$ as a function of temperature for (a–b) $GaV_4Se_8$ and (c–d) $GaV_4S_{0.1}Se_{7.9}$. Fits in (a) and (c) are as detailed in the text. The vertical dashed lines indicate $T_c$.

low-levels of substitution. The calculations should therefore be interpreted as indicating the effect of the substitution local to the substituents.

Our calculations indicate an almost ferromagnetic distribution of spin density (as observed in experiment) for all systems, however the moments obtained are consistently larger. The magnetic moment is found to be localised on the V atoms, consistent with the results of our calculations of the field at the muon site.

To study the effect of substitution, we compare the spin density in electron bands that dominate the contribution to the magnetism (i.e. those occupied in only one spin channel), with the difference between $y = 0$ and $y = 1$ for the $S_3$ site shown in Fig. 7.8. Regardless of the site chosen for substitution, more dramatic changes in spin density are seen at the S end of the series than at the Se end. Whilst most of the change in spin density retains the expected d-orbital character, some site substitutions result in an increase in spin density within the V tetrahedral cluster. Since there are muon-stopping sites around the cluster, this provides an explanation for the observed large magnetic field $B_3$. The change in spin density may also lead to altered exchange pathways, which upon increased substitution could lead to the glass-like magnetic ground state seen for $y = 2$ and $y = 4$ [128] where multiple different exchange pathways (depending on the local substitution level) cannot be simultaneously satisfied.

It is worth noting that the results presented here do not seem to depend heavily on the value of $U_{\text{eff}}$ once the magnetic moment has saturated. Previous work has demonstrated that different values of $U_{\text{eff}}$ can all lead to similar band structure results in these materials [136, 137].

### 7.3.4 Muon-spin spectroscopy in an applied field

We next explore the SkL state that appears in an applied field, through TF and LF $\mu$SR. Samples were cooled in zero applied magnetic field, and the measurements were made in field (as indicated in Fig. 7.1) on warming. As discussed in Chap. 3, TF $\mu$SR measurements are mainly sensitive to static disorder along

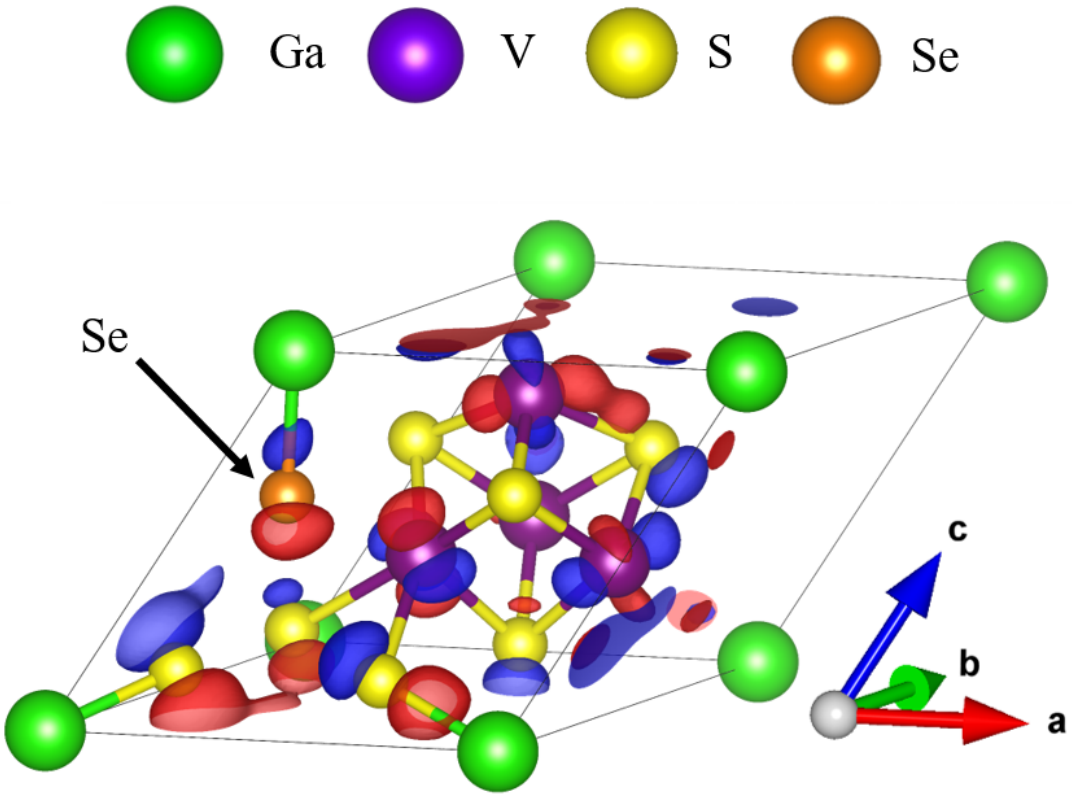


**Figure 7.8:** Difference in spin density between $y = 0$ and $y = 1$ for Se substitution on the $S_3$ site from DFT. Image produced with VESTA [108].

with the component of dynamic fluctuations of the local field parallel to the applied field, while LF $\mu$SR measurements are sensitive to dynamics in those local fields perpendicular to the applied field. The SkL orientation, determined predominantly by the crystalline anisotropy, will be randomised in a polycrystalline sample like ours, even under application of an external magnetic field, and hence the two techniques are expected to be sensitive to the same dynamic field correlations.

We will consider the TF $\mu$SR data first. In all cases an external field was applied that was expected to stabilise a SkL phase, as indicated by the lowest-field line on each panel of Fig. 7.1. This corresponds to 50 mT for $GaV_4S_8$, 40 mT for $GaV_4S_{7.9}Se_{0.1}$, 95 mT for $GaV_4Se_8$, and 70 mT for $GaV_4S_{0.1}Se_{7.9}$. In a TF $\mu$SR experiment, rather than simply fitting the asymmetry (which ignores any positrons that are not detected in the forward/backward detectors), the number of counts in all detectors is fit simultaneously, with a phase offset on the signal appropriate for each detector. This means that the polarisation of the muon-spin ensemble is fitted directly. For these measurements, $P_x(t) = \sum_{i=1}^{n} a_i \exp(-\Lambda_i t) \cos(\gamma_\mu B_i t + \phi_i) + a_\mathrm{b}$, where the number of components $n$ will depend on the material being measured. At the S-rich end of the series we find $n = 2$, whereas at the Se-rich end $n = 3$ is the most appropriate. In all cases, the amplitudes of each component (reflecting the number of muons stopping in a particular class of stopping site) and phases were found to be temperature independent.

For $GaV_4S_8$, 32(1)% of the muons were found to stop in the site with field $B_1$ ($\phi_1 \simeq -20°$) and the remaining 68(2)% stop in the $B_2$ site ($\phi_2 \simeq 10°$). The origin of these phase offsets can be understood by considering the polycrystalline nature of the samples studied here. A distribution of angles between the internal and applied field will be present at the muon sites, giving rise to a distribution of net magnitudes of the internal field experienced by the muons. This distribution may not be symmetric, resulting in a phase shift when fit with a single damped cosine. Similarly, for $GaV_4S_{7.9}Se_{0.1}$, 33(1)% of the muons stop in the site with field

$B_1$ ($\phi \simeq -45°$) and the remaining 67(2)% stop in the $B_2$ site ($\phi \simeq 20°$). Despite the almost identical percentage of muons stopping in each site when compared to $GaV_4S_8$, the significant change in phases does suggest different behaviour. For $GaV_4Se_8$, 80.9(9)% of the muons stop in the $B_1$ site, 10.6(9)% stop in the $B_2$ site, and the remaining 8.5(2)% stop in the Ag foil (and hence precess at a frequency corresponding to the applied field). Both $\phi_1$ and $\phi_2$ were found to be approximately zero. For $GaV_4S_{0.1}Se_{7.9}$, 61(3)% of the muons stopping in the $B_1$ site, 33 (3)% stopping in the $B_2$ site, and the remaining 6.5(4)% stopping in the Ag foil.

In all cases, the fields $B_i$ are the most physically revealing on the nature of the magnetism in these systems. The temperature dependence of $B_i$ will be discussed alongside the LF $\mu$SR measurements below. For completeness, the transverse field relaxation rates $\Lambda_i$ are shown in Fig. 7.9. $\Lambda$ is very sensitive to subtle changes in the magnetism of a system, being proportional to both the width of the distribution of magnetic fields at the muon site, and dynamic fluctuations. As can be seen from Fig. 7.9, in these measurements the effect of substitution does not significantly change the magnetism at each end of the series, although a slight increase in $\Lambda$ upon substitution is observed. This suggests either an increase in magnetic disorder at the muon site (leading to a wider distribution of fields at the site), or an increase in the dynamic response on the muon timescale.

LF $\mu$SR measurements were performed on the materials at a minimum of two different applied magnetic fields, one which is expected to stabilise the SkL at certain temperatures, and one that is not expected to do so. The fields measured are marked on Fig. 7.10, where the results are presented. In all the measurements presented here, the LF $\mu$SR data are well described by $A(t) = a_r \exp(-\lambda t) + a_b$ over the entire temperature range, consistent with dynamic relaxation. The baseline asymmetry $a_b$ was found to be independent of temperature, and the relaxing asymmetry $a_r$ was constrained to follow Eqn. 4.2, as is common throughout this thesis. Sensitive to the dynamic response on the muon timescale, $\lambda$ is typically presented alongside $B_i$ from TF $\mu$SR measurements, which shows the good agree-

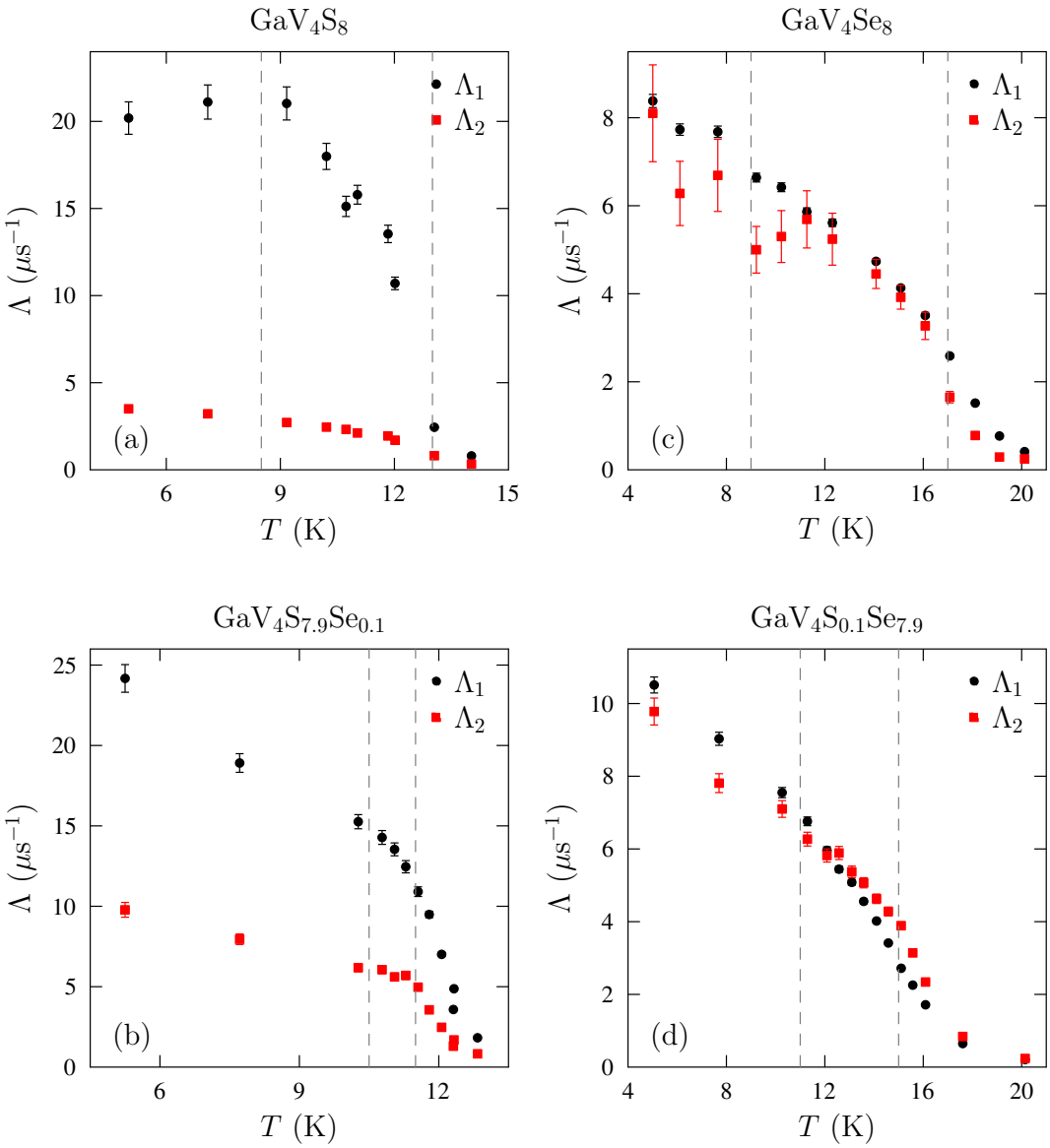


**Figure 7.9:** Transverse relaxation rate $\Lambda$ for (a) $GaV_4S_8$, (b) $GaV_4S_{7.9}Se_{0.1}$, (c) $GaV_4Se_8$, and (d) $GaV_4S_{0.1}Se_{7.9}$. Dashed lines match those on Fig. 7.10 and indicate the region over which the skyrmion phase is thought to exist throughout the entire sample.

ment between these two different techniques.

We start by considering the S-rich end of the series, with results shown primarily in Fig. 7.10. In $GaV_4S_8$ a peak in $B_1$ is seen at $9 \lesssim T \lesssim 12$ K [Fig. 7.10(a)], coinciding with the presence of the SkL. This is consistent with TF $\mu$SR of the SkL in materials such as $Cu_2OSeO_3$ [98], where an additional high-field shoulder is a signature of the SkL. LF $\mu$SR measurements performed in an applied field of 50 mT and 90 mT cut through the SkL state in at least some crystal orientations [22], as well as showing effects in our magnetometry measurements [Fig. 7.1], while measurements made at 180 mT do not. The relaxation rates extracted from these data [Fig. 7.10(b)] show that the effect of the dynamics in the SkL state is a significant enhancement in relaxation rate $\lambda$ below $T_c$ leading to a large, broadened peak, centred at temperatures within the SkL state. This is also consistent with LF measurements of the SkL in $Cu_2OSeO_3$ and $Co_xZn_yMn_{20-x-y}$, as discussed in previous chapters. Intriguingly, at 50 mT, there is clear evidence for a shoulder just below 9 K that bares a striking resemblance to that seen in LF $\mu$SR measurements of single crystalline $Cu_2OSeO_3$. Fitting parameters can be found in Tab. 7.1.

To attempt to understand the source of the additional megahertz dynamics in the SkL we once again apply a model describing the coupling of skyrmion modes to the muon-spin, as previously used for $Co_8Zn_9Mn_3$, and derived in App. A. This model is shown in Fig. 7.10(b), where above $T_c$ critical behaviour typical of a 3D Heisenberg magnet has been assumed, as for $Cu_2OSeO_3$. This model is seen to well describe the measured $\lambda$ from LF $\mu$SR measurements of $GaV_4S_8$ when cutting through the SkL phase at temperatures around $T_c$, although it cannot adequately describe the enhanced shoulder observed at lower $T$. This suggests we observe contributions from two different dynamic effects on the megahertz timescale, (1) the reduction in frequency of SkL modes (consistent with the results for $Co_8Zn_9Mn_3$) which dominate just below $T_c$, and (2) additional megahertz dynamics leading to the observed shoulder (consistent with the results for $Cu_2OSeO_3$ and $Co_8Zn_8Mn_4$) which dominate at lower $T$. It seems most likely that

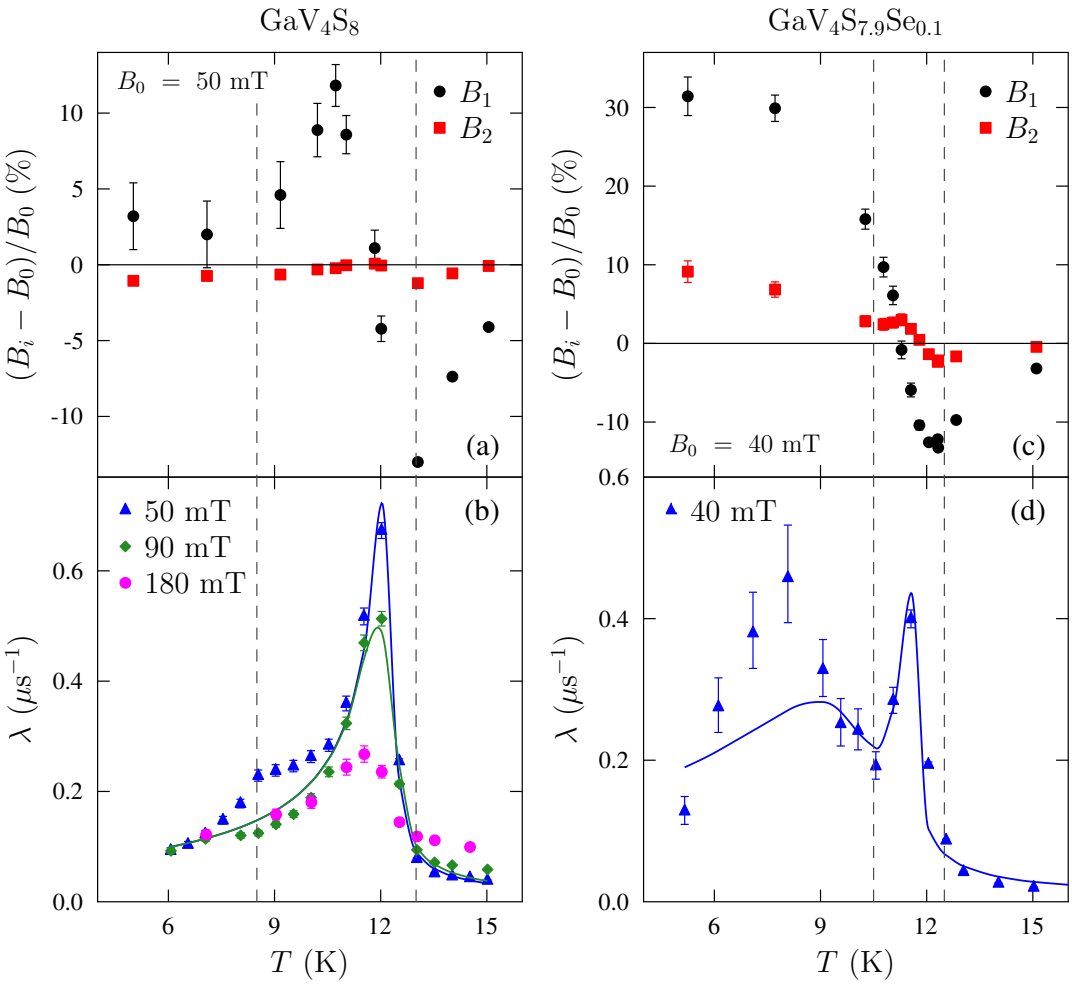


**Figure 7.10:** Results from $\mu$SR measurements of $GaV_4S_{8-y}Se_y$. Parameters from TF measurements on (a) $y = 0$, and (c) $y = 0.1$; and LF measurements on (b) $y = 0$, and (d) $y = 0.1$. Dashed lines are suggested boundaries for the SkL. Fits in (b), and (d) are based on a model describing coupling to the reduction in frequency of skyrmion modes, as detailed in the text.

**Table 7.1:** Parameters refined by simultaneously fitting all LF $\mu$SR data at a particular applied field for $GaV_4S_{8-y}Se_y$. Parameters marked with (*) were held fixed, as discussed in the main text.

| $y$ | $\mu_0 H_{\text{ext}}$ (mT) | $a_{\text{b}}$ (%) | $a_{\text{r0}}$ (%) | $k$ | $L$ (%) | $T_{\text{c}}$ (K) |
|---|---|---|---|---|---|---|
| 0 | 50 | 17.02(3) | 1.73(2) | 2.40(5) | 3.99(2) | 11.743(13) |
| | 90 | 18.62(3) | 2.23(3) | 1.78(7) | 1.92(2) | 11.45(3) |
| | 180 | 20.26(6) | 1.91(5) | 1.9(4) | 0.45(3) | 11.0(2) |
| 0.1 | 40 | 20.36(4) | 0.82(3) | 3.08(5) | 8.24(3) | 11.703(7) |
| | 80 | 23.93(4) | 0.87(3) | 1.55(5) | 4.81(4) | 11.16(2) |
| 7.8 | 57.5 | 25.20(7) | 0.90(5) | 0.48(2) | 2.67(5) | 10.64(10) |
| | 115 | 26.5(2) | 0.9(2) | 0.33(4) | 1.60(13) | 8.3(4) |
| 7.9 | 70 | 26.2(3) | 1.3(3) | 0.43(3) | 1.15(4) | 12.3(2) |
| | 140 | 25.3(6) | 3.0(6) | 0.43(8) | 0.43(3) | 10.3(5) |
| 8 | 95 | 23.5 (*) | 3.801(10) | 0.43(2) | 0.81(2) | 14.28(14) |
| | 150 | 24.0 (*) | 3.944(12) | 0.45(6) | 0.44(3) | 14.9(3) |

the dynamics that lead to the shoulder are the same source as those that lead to the same feature in $Cu_2OSeO_3$, and therefore demonstrate the need for further study to investigate the source of these dynamics. This is perhaps a surprising result, as on the megahertz timescale the Néel skyrmions in $GaV_4S_8$ appear very similar to measurements on Bloch skyrmions in other materials. From the model of the reduction in frequency of skyrmion modes, we find the zero-temperature skyrmion excitation mode frequency is 16.1(5) GHz, consistent with the 3–17 GHz range observed in Bloch skyrmion materials [43] and in good agreement with the 17–19 GHz range of frequencies measured in single crystals of $GaV_4S_8$ [138]. We also find $\Delta_0 = 23.9(3)$ mT, which is a similar width to the features in the ZF $\mu$SR spectra (for example, in Fig. 7.4).

The behaviour of $GaV_4Se_8$ is similar to that of $GaV_4S_8$ with a peak observed in the TF $\mu$SR component $B_2$ [Fig. 7.11(a)]. LF $\mu$SR measurements on $GaV_4Se_8$ in an applied field of 95 mT, [Fig. 7.10(b)] also show a significantly enhanced relaxation rate in the SkL state (and peak below $T_c$) when compared to the temperature scan with an applied field of 150 mT, where the SkL state is not stabilised. This confirms the suggestion in Ref. [128] that the SkL in polycrystalline samples is confined to a smaller region of the phase diagram than in single crystal samples. The behaviour at 95 mT is well described by the reduction in frequency of skyrmion modes, and we find a frequency of 7.9(5) GHz for the zero-temperature excitation mode, again consistent with other skyrmion materials. The corresponding $\Delta_0 = 5.7(2)$ mT. (Note that when fitting the LF $\mu$SR data measured on $GaV_4Se_8$ it was required to hold the baseline constant at a best estimate to obtain a stable fit. This leads to a potential vertical offset on $\lambda$ that is constant with temperature, so the absolute values could be slightly different to those shown here. To account for this, a vertical offset was added to the fits to the model of the reduction in frequency of skyrmion modes; a different choice of baseline gives the same results from this model.)

We will next consider the effects of low-levels of substitution at both ends of the series. TF $\mu$SR measurements of $GaV_4S_{7.9}Se_{0.1}$ were performed in an applied

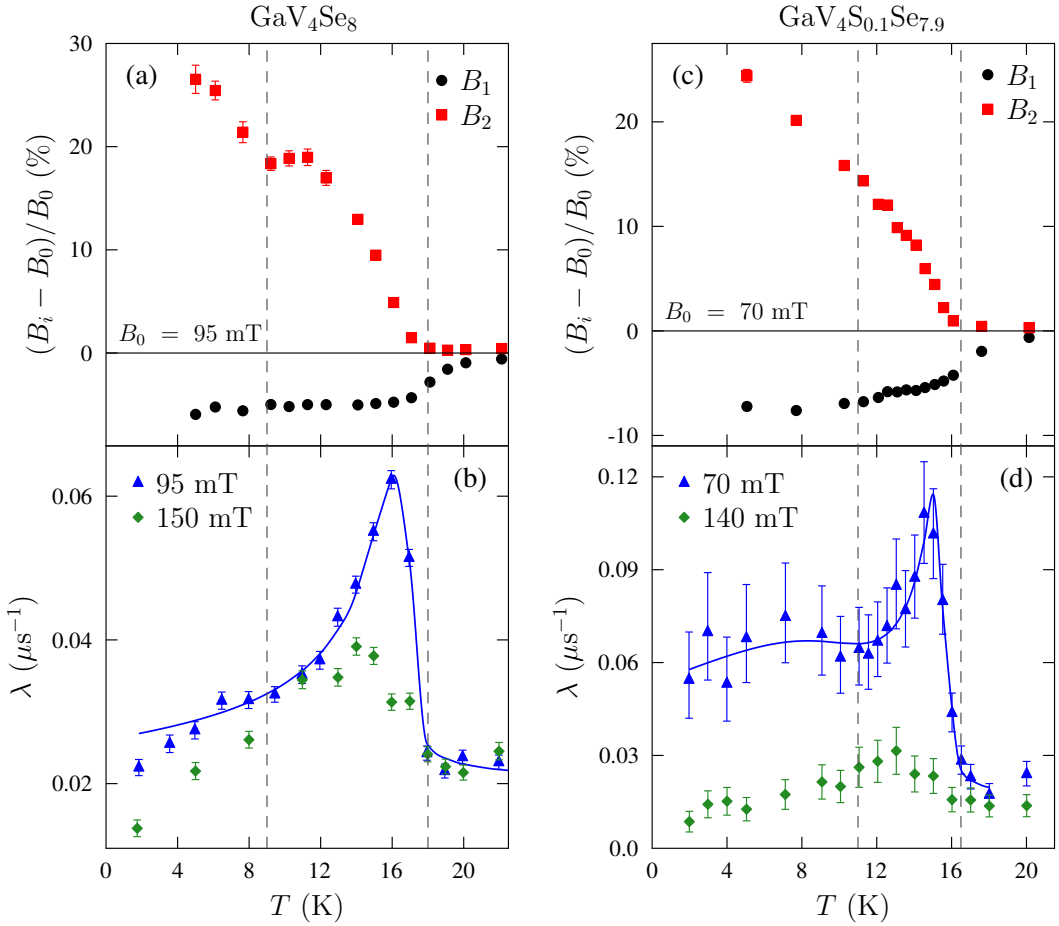


**Figure 7.11:** Results from $\mu$SR measurements of $GaV_4S_{8-y}Se_y$. Parameters from TF measurements on (a) $y = 8$, and (b) $y = 7.9$; and LF measurements for (b) $y = 8$, and (d) $y = 7.9$. Dashed lines are suggested boundaries for the SkL. Fits in (b), and (d) are based on a model describing coupling to the reduction in frequency of skyrmion modes, as detailed in the text.

field of 40 mT, where an enhanced AC susceptibility response [Fig. 7.1(b)] is consistent with a SkL state existing. Unlike the $GaV_4S_8$ case, no unambiguous signature of the SkL state is observed in the internal magnetic field. In fact, the field $B_1$ is significantly larger for $GaV_4S_{7.9}Se_{0.1}$ compared to $GaV_4S_8$, consistent with both the additional, larger internal field component observed in our ZF $\mu$SR measurements, and the increased magnetisation. This implies that any peak in internal field arising in the presence of the SkL state will be masked by these large fields. The variation in $B_2$ is similar between the samples, suggesting the underlying behaviour is similar. LF $\mu$SR measurements (performed in the same applied field as TF measurements) on the $GaV_4S_{7.9}Se_{0.1}$ material [Fig. 7.10(d)] also show significant changes when compared to $GaV_4S_8$. The behaviour around $T_c$ is similar between the two materials, exhibiting a peak that is well described by the reduction in frequency of the skyrmion modes, however, there is also an enhancement in $\lambda$ at lower $T$. At 80 mT, where AC susceptibility suggests little change in the response, consistent with the lack of a SkL, a peak around $T_c$ is observed, as shown in Fig. 7.12, however the most remarkable feature is the increase of $\lambda$ as $T$ is decreased right down to the lowest measured temperatures. In contrast to the measurements at fields that stabilise the SkL, $\lambda$ grows continuously with decreasing $T$. We will discuss the potential origins of these low $T$ enhancements later.

At the Se-rich end of the series, TF $\mu$SR measurements for $GaV_4S_{0.1}Se_{7.9}$ in an applied field of 70 mT, where an enhanced AC susceptibility response consistent with a SkL is seen just below $T_c$, were performed. Fits of these data are shown in Fig. 7.11(c). Although the overall trends in behaviour are similar to those for $GaV_4Se_8$, there is again no resolvable peak in internal field in the SkL region. However, LF $\mu$SR measurements [Fig. 7.11(d)] show that there is a clear enhanced response in $\lambda$ at 70 mT compared to 140 mT, consistent with the realisation of the SkL state at 70 mT. In addition, we again observe a separate enhancement in the low-temperature relaxation rate, similar to the behaviour observed in $GaV_4S_{7.9}Se_{0.1}$, with a broad peak in the relaxation rate centred around

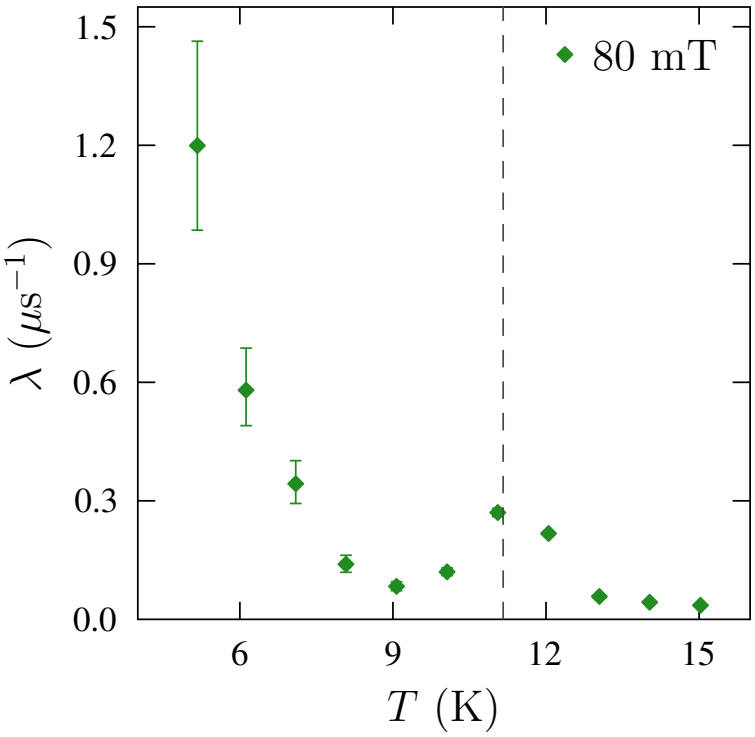


**Figure 7.12:** Additional LF $\mu$SR measurements of $GaV_4S_{8-y}Se_y$ with $y = 0.1$. Dashed line is the extracted value of $T_c$ according the the $\mu$SR measurements.

$T = 8$ K.

The second, lower temperature peak in $\lambda$ that appears upon substitution preferentially at fields at which the SkL is stabilised suggests that there are dynamics associated with the SkL extending down to lower temperatures. We propose that these dynamics occur due to skyrmion precursors (as seen in $Cu_2OSeO_3$ [139]) that are stabilised by the substituents at both ends of the series. This is consistent with the picture we have for $Co_xZn_yMn_{20-x-y}$, where we concluded that the chemical substitution increased the stability of the SkL. Note that if the dynamics were associated with the cycloidal phase one would expect a peak in $\lambda$ at all applied fields that stabilise the cycloidal phase; that is not observed here. The stabilisation of the skyrmion precursors, either due to increased formation caused by pinning, or to longer lifetimes of metastable states, leads to dynamics detectable with $\mu$SR that are not observed in the pristine materials. Both of these effects are plausible consequences of the increased substitutional disorder introduced in these systems. The dynamics likely arise from a reduced frequency SkL mode due to the $\approx 300$ substituents per skyrmion present in the substituted systems, making the skyrmions less rigid, and hence lowering their characteristic frequencies.

To model this second relaxation channel for the muon in the lightly substituted materials, we have assumed that this second relaxation rate also follows the same Redfield formula (Eqn. A.1) and scaling laws (Eqn. A.2 and Eqn. A.3). In the case where there are two coexisting frequencies in the muon response window, the observed muon relaxation rate, occurring due to fluctuations at all muon sites, is expected to be dominated by the larger of the two frequencies; we model the scenario as such. We note that the appearance of the second peak cannot be due a variance in the coupling of different muon sites to the internal fields, as this only affects $\Delta$, rather than $\nu_0$, and thus cannot significantly shift the position of the $\lambda$ peak in temperature. Fits for this two-mode model for $\lambda$ are shown in Figs. 7.10(d) and 7.11(d). We find that this model well describes both the behaviour around $T_c$ in both materials, and the low-$T$ behaviour of $GaV_4S_{0.1}Se_{7.9}$. The model misses

some of the behaviour of $GaV_4S_{7.9}Se_{0.1}$, however we have already established that at the S-end of the series there are megahertz dynamics that affect the behaviour; it is likely these dynamics that change the behaviour observed. At both ends of the series we find that the low-$T$ mode has no significant change in the width of the local field, however for $GaV_4S_{7.9}Se_{0.1}$ the frequency of this mode is approximately 25% of the high-$T$ frequency, and for $GaV_4S_{0.1}Se_{7.9}$ it is about 2%.

LF $\mu$SR measurements of $GaV_4S_{0.2}Se_{7.8}$ were also performed, with results shown in Fig. 7.13. Whilst there is no clear evidence for SkL-related dynamics, we observe an increase of $\lambda$ with decreasing $T$ at both measured applied fields. The behaviour is very similar to that observed for $GaV_4S_{7.9}Se_{0.1}$ when not stabilising a SkL. It is possible these dynamics are associated with an increase in magnetic disorder, that with sufficient substitution will lead to the spin-glass state observed in the middle of the series [128, 127, 123]. This fact that this effect is seen at lower substitution levels at the S-end, and more dramatically (with a greater value of $\lambda$) is consistent with the conclusion of the ZF $\mu$SR measurements that the magnetism at the S-end of the series is more dramatically perturbed by substitution.

## 7.4 Conclusion

In conclusion, these results show that magnetic order is preserved for low-levels of substitution in $GaV_4S_{8-y}Se_y$, at both ends of the series, in contrast to higher levels where spin glass-like behaviour is observed [128, 127, 123]. On the Se-rich end of the series, the presence of S simply leads to an increase in the width of the local magnetic field distribution, which is enough to prevent observation of the effect of the SkL in our TF $\mu$SR measurements. On the S-rich end of the series, where the ZF ordered state is formed from competing FM* and C order, substitution has a more dramatic effect, creating regions in the sample which have increased spin density, leading to the observation of high magnetic fields with $\mu$SR. These regions are shown to exist in our DFT calculations of $GaV_4S_{8-y}Se_y$with $y = 1$ or $y = 9$. These changes in spin density are likely to lead to changes in exchange coupling constants, which, in the highly-substituted

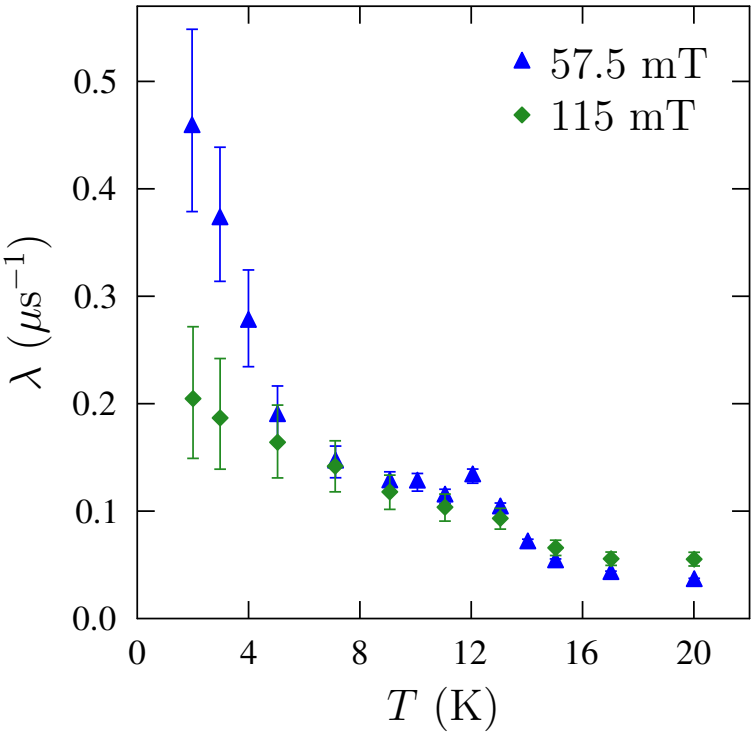


**Figure 7.13:** Additional LF $\mu$SR measurements of $GaV_4S_{8-y}Se_y$ with $y = 7.8$.

limit, will lead to the observed spin-glass behaviour.

Despite a lack of evidence for the SkL in the local field measured with TF $\mu$SR, there are clear dynamic effects, with signatures in both AC susceptibility and LF $\mu$SR measurements. At both ends of the series LF $\mu$SR provides evidence of enhanced dynamics typical of those observed in Néel SkL states. The shape in the $B$–$T$ phase diagrams of these regions is reminiscent of the SkL regions in the unsubstituted materials. We therefore conclude that a dynamically fluctuating SkL is realised in these materials with low-levels of chemical substitution. We have shown further that the zero-temperature frequency of the Néel SkL excitation modes appear to be similar to those for a Bloch SkL.

Another effect of increased substitution in $GaV_4S_{8-y}Se_y$ is the existence of a significant dynamic response, detected with LF $\mu$SR, at low-$T$. We attribute this to the increased stability of skyrmion precursors at temperatures below the equilibrium skyrmion lattice. As these states only exist at fields at which the SkL is stabilised, it is clear that the applied field plays a crucial role in allowing

the formation of skyrmions, whereas temperature simply provides the thermal fluctuations required to stabilise the lattice. Upon increased substitution we see dynamics effects which signal the onset of magnetic disorder that will eventually lead to a spin-glass ground state.

# Chapter 8

# Energy-gap driven properties in $Cr_{1/3}MS_2$

This chapter presents a theoretical and experimental investigation into the helimagnets $Cr_{1/3}MS_2$ ($M$ = Nb or Ta), which have attracted renewed attention due to the discovery of a chiral soltion lattice (CSL) stabilised in an applied magnetic field. We focus on the unusual low-temperature electronic and magnetic behaviour of the materials, which originates from previous reports of an unusual temperature-dependence of the muon-spin precession frequency in transverse field (TF) muon-spin spectroscopy ($\mu$SR) measurements, and in Seebeck and Hall coefficients. In addition to these previously reported experimental findings, we present AC susceptibility and longitudinal-field (LF) $\mu$SR measurements that show similarly unexpected behaviour below $T \simeq 50$ K in both materials. These experimental observations hitherto lacked a unifying explanation. Our electronic structure calculations demonstrate that $Cr_{1/3}MS_2$ ($M$ = Nb or Ta) are half-metals whose low-temperature electronic and magnetic behaviour can be explained by the presence of a gap-like feature (width in range 40–100 meV) in the density of states of one spin channel. Our magnetometry measurements confirm the existence of this gap. Dynamic spin fluctuations driven by excitations across this gap are seen over a wide range of frequencies (0.1 Hz to MHz) with AC susceptibility and $\mu$SR measurements. We show further how effects due to the CSL

in $Cr_{1/3}NbS_2$, as detected with $\mu$SR, dominate over the gap-driven magnetism when the CSL is stabilised as the majority phase.

This chapter is based on work currently under peer review. A preprint of the work is available [140]. The samples were provided by collaborators at the University of Warwick. The density functional theory calculations were proposed by myself, and carried out predominantly by a collaborator, Zachary Hawkhead (Durham University); the interpretation of the results of these calculations and subsequent BOLTZTRAP calculations was done jointly between myself and Zachary Hawkhead. The magnetometry measurements were performed and analysed by myself. The $\mu$SR data were measured by myself, alongside collaborators at Durham University and ISIS Neutron and Muon Source. The analysis of the $\mu$SR data is my own, and uses muon site calculations I performed. The overall discussion is my own.

## 8.1 Introduction

Transition metal dichalcogenides ($MX_2$, $M$ = transition metal and $X$ = chalcogen) have long been the subject of much research effort [141], the reduced dimensionality [142] of these semiconductors leads to a suite of exciting electrical, optical and mechanical properties [143, 144, 145]. $Cr_{1/3}MS_2$, $M$ = Nb or Ta is based on the same structure as superconducting $NbS_2$, but with Cr atoms intercalated between $M$ layers (shown later in the context of muon stopping sites, Fig. 8.5). The intercalation removes the inversion symmetry, leading to a noncentrosymmetric structure which can host a Dzyaloshinksii-Moriya (DM) interaction. These materials have attracted attention as rare examples of 2D materials with helical magnetic ordering, thought to occur due to the competition between exchange, the DM interaction and spin-orbit coupling (SOC) [146, 147]. Application of a magnetic field perpendicular to the $c$ axis causes the helical ground state to transform to the chiral soliton lattice (CSL) [148, 149], consisting of domain-wall-like 360° magnetic kinks separated by regions of ferromagnetic ordering, with a field along a different direction tilting the CSL [45, 150]. The

existence of the CSL in $Cr_{1/3}NbS_2$ is well established [148], but has only recently been reported in $Cr_{1/3}TaS_2$ [149]. As discussed in Chap. 2, these magnetic solitons are reduced-dimensional analogues of skyrmions [6], both of which are topological spin structures. As in the case of skyrmions, there are many potential technological applications of magnetic solitons [148].

There have been multiple reports of unusual low-temperature transport and magnetic properties in $Cr_{1/3}NbS_2$, including a sizeable change in the thermal conductivity and Seebeck coefficient around $T = 40$ K [151], and a rapid increase in the Hall coefficient below 50 K [152], all suggesting modifications to the electronic behaviour. Additionally, muon-spin rotation ($\mu$SR) identifies an increase in oscillation frequency below 50 K [153], suggesting a different local magnetic-field distribution. The above observations have led to contrasting explanations, including a change in the dominant transport mechanism due to spin-orbit-coupling-induced alterations of the electronic structure [151], or an increased helical length at low $T$ due to a decrease in the magnitude of the DM interaction [153]. Such explanations do not account for all of the observations, and whilst an increase in the helical length below 90 K is observed in lamellae of $Cr_{1/3}NbS_2$ [154], this is not found in bulk [155].

In this chapter we explain the low-temperature behaviour of $Cr_{1/3}MS_2$ ($M$ = Nb or Ta) using electronic structure calculations supported by AC susceptibility and LF $\mu$SR measurements. We find that the presence of an energy-gap-like feature in the density of states can account for the observed phenomena over a wide range of energy scales.

## 8.2 Computational Details

In addition to the work presented here, there are a number of additional electronic structure calculations of $Cr_{1/3}MS_2$ ($M$ = Nb or Ta) that were carried out for this project that are beyond the scope of this thesis. Details of the calculations relevant to this thesis are provided here. Full details of all calculations can be found in Ref. [140].

The electronic structure of $Cr_{1/3}MS_2$ ($M$ = Nb or Ta) was determined using the CASTEP implementation of spin-polarised density functional theory (DFT) [76]. The lattice parameters used were $a = b = 5.76$ Å, $c = 11.84$ Å and $a = b = 5.74$ Å, $c = 11.90$ Å for $Cr_{1/3}NbS_2$ and $Cr_{1/3}TaS_2$ respectively, close to our experimentally measured values. Exchange and correlation interactions were treated under the generalised gradient approximation (GGA), using the PBE functional [95]. Ultrasoft pseudopotentials were used to approximate electrons in the atomic core. The total energy was found using a self-consistent field (SCF) calculation with a tolerance of $10^{-5}$ eV/atom. Calculations were performed with a plane wave basis cut off of 1400 eV and Monkhorst-Pack SCF $k$-point sampling of 15×15×15 [129], leading to convergence better than 0.01 eV per unit cell. $Cr_{1/3}MS_2$ ($M$ = Nb or Ta) have long period helimagnetic groundstates at low temperature [151, 147] such that the local arrangement of magnetic moments is approximately ferromagnetic. We use spin-polarised DFT to realise a ferromagnetic configuration with a Cr magnetic moment of approximately $3\mu_B$, satisfying the necessary condition for half-metals to have integer spin [156]. This moment matches that found experimentally. Spectral calculations were performed to generate band structures and densities of states (DOS) for $Cr_{1/3}MS_2$. When calculating the densities of states a 25×25×25 $k$-point grid was used for $Cr_{1/3}NbS_2$, and 15×15×15 for $Cr_{1/3}TaS_2$.

The Seebeck coefficients for $Cr_{1/3}NbS_2$ and $Cr_{1/3}TaS_2$ were calculated using the BOLTZTRAP code [157], a program which calculates the semi-classical transport coefficients. The BOLTZTRAP calculations are initialised using the electronic structure calculations described above. Transport properties depend on the temperature of the sample and any applied bias, which has the effect of shifting the Fermi energy. We calculated the Seebeck coefficient in both materials over a temperature range of 1–300 K and chemical potential spanning 1.36 meV with 0.14 meV spacing centred around the Fermi level calculated from DFT. To reduce the effects of noise at low temperatures, we used 100 lattice points per $k$-point and 200 lattice points per $k$-point for $Cr_{1/3}NbS_2$ and $Cr_{1/3}TaS_2$ to account for their relative $k$-point densities. We find that the Seebeck coefficient is highly

sensitive to the choice of chemical potential. In order to best match the experimental Seebeck coefficient in $Cr_{1/3}NbS_2$ the value of Fermi energy was taken as approximately $-18$ meV with respect to the Fermi energy predicted by DFT. This is within the uncertainty of our calculations. Due to the practicalities of measuring the Seebeck coefficient, it is difficult to ensure that the measurement is taken at precisely zero bias, this is also reflected in the choice of Fermi energy. In $Cr_{1/3}TaS_2$ it is expected that the Seebeck coefficient behaves similarly to that of $Cr_{1/3}NbS_2$ so a value of approximately $-6$ meV with respect to the DFT Fermi energy was chosen. Similarly, the Hall coefficient was calculated using the BOLTZTRAP code.

## 8.3 Experimental Details

Polycrystalline samples of $Cr_{1/3}MS_2$ ($M$ = Nb or Ta) were synthesised as described in Ref. [140]. To characterise the bulk magnetic properties of the polycrystalline samples, magnetisation and AC magnetic susceptibility measurements were performed using a Quantum Design MPMS. Measurements were performed after cooling in zero applied magnetic field from above the transition temperature. For AC measurements, in addition to the indicated DC magnetic field, a time-varying magnetic field of amplitude 0.3 mT was applied, with frequencies ranging between 0.2 and 149 Hz.

LF $\mu$SR measurements were made using the HIFI spectrometer at the ISIS Neutron and Muon Source, UK. Samples were packed into Ag foil packets and mounted on a silver backing plate and placed in either in a He-4 cryostat or CCR. Measurements were performed on warming in an applied magnetic field after cooling in zero applied field. Data analysis was carried out using the WiMDA analysis program [68].

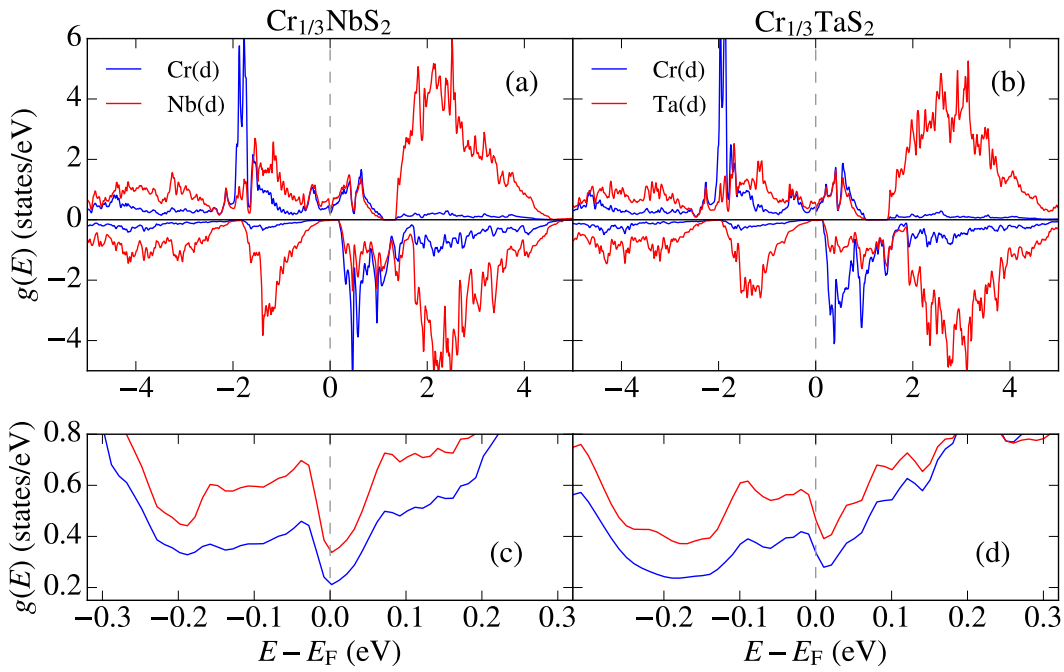


**Figure 8.1:** (a,b) Contributions from transition metal $d$-orbitals to the densities of states in $Cr_{1/3}MS_2$ ($M$ = Nb or Ta). (c,d) Regions around the Fermi level showing the pseudogap. Spin-up(down) densities are positive (negative).

## 8.4 Results & Discussion

### 8.4.1 Density functional theory

The DOS of $Cr_{1/3}MS_2$ ($M$ = Nb or Ta) according to DFT calculations is shown in Fig. 8.1. In both materials there is splitting of the spin-up and spin-down bands with ferromagnetic moments on the Cr ions. The largest contribution to the DOS at the Fermi level comes from the spin-up channel, with little contribution from spin-down. The lack of spin-down density around the Fermi level, which, in addition to the integer spin per unit cell [156], suggests both materials are half-metallic [158]. (Previously $Cr_{1/3}NbS_2$ has been reported as a low carrier concentration metal or heavily doped semiconductor [151].) In both materials, there is a reduction to almost zero in the spin-up channel of the DOS at the Fermi level over a width of approximately $\Delta E$ = 80–90 meV. This reduction has previously been observed in $Cr_{1/3}NbS_2$ and was termed a pseudogap [151], but the influence of this feature was not investigated. The previous observation, plus the tendency of DFT to underestimate the size of a gap [159], gives confidence that this pseudogap is a real feature of the DOS. Additional electronic structure calculations (see Ref. [140]) performed with the inclusion of SOC have no resolvable impact on the pseudogap.

To understand the low-temperature transport properties in $Cr_{1/3}MS_2$ we calculate the Seebeck coefficient $S_{\mu\nu}$ from DFT using the BOLTZTRAP code [157]. The Seebeck coefficient, a measure of the voltage induced across a material that has a temperature gradient, indicates whether the material has electron- or hole-dominated transport, thus changes in $S_{\mu\nu}$ indicate changes in the concentration and/or type of free carriers in the system. Figure 8.2(a–b) shows $S = \mathrm{Tr}\,(S_{\mu\nu})\,/3$, with a characteristic maximum reflecting the presence of the pseudogap. This prediction of $S$ for $Cr_{1/3}NbS_2$ qualitatively matches the measurements in the low-temperature regime [151]. Around $T_c$ the computed behaviour deviates from experiment due to the onset of the magnetic transition, which is not captured in our model. The gap found in DFT is slightly larger than the measured gap (see

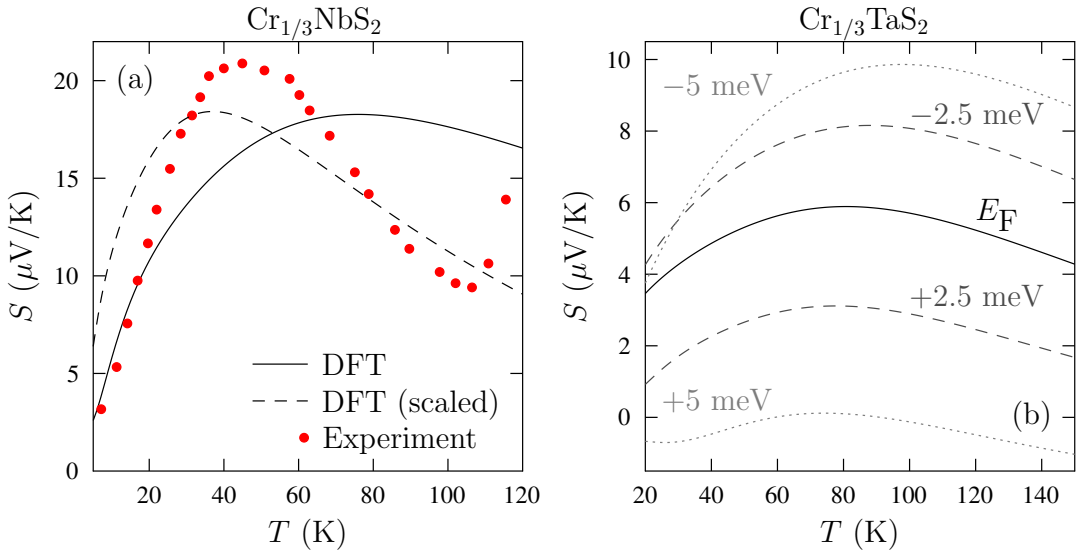


**Figure 8.2:** Seebeck coefficient $S = \mathrm{Tr}\,(S_{\mu\nu})\,/3$ for (a) $Cr_{1/3}NbS_2$ and (b) $Cr_{1/3}TaS_2$. In (a) $S$ is compared to experiment [151], and is also shown with temperatures scaled according to the gap size (see text). In (b) the range of the possible values of the Seebeck coefficient due to uncertainty in the Fermi energy is shown.

below), causing the features in $S$ to occur at higher $T$ than found experimentally. To better compare to the experimental values, we can adjust the energy scale in the calculation to that of the measured gap [$T \to T\Delta E_{\mathrm{exp}}/\Delta E_{\mathrm{DFT}}$, Fig. 8.2(a)], which then provides a better agreement with the experimental peak position. We find similar behaviour of $S$ for $Cr_{1/3}TaS_2$ [Fig 8.2(b)], as expected from the similar electronic structures. Our DFT calculations can also reproduce the observed rapid increase in Hall coefficient on decreasing $T$ in $Cr_{1/3}NbS_2$ below 50 K [152], as seen in Fig. 8.3.

The magnetic moment $m$ can be estimated from the difference in the DOS in the spin-up and spin-down channels. We find, for both materials, $d$-orbitals contribute most significantly to $m$, with around 95% of the total moment coming from the Cr $d$-orbitals. We find good agreement between the saturation moment of our calculations and that found experimentally. The $T$ dependence, $m(T)$, caused by thermally-activated changes in band occupation (but excluding critical

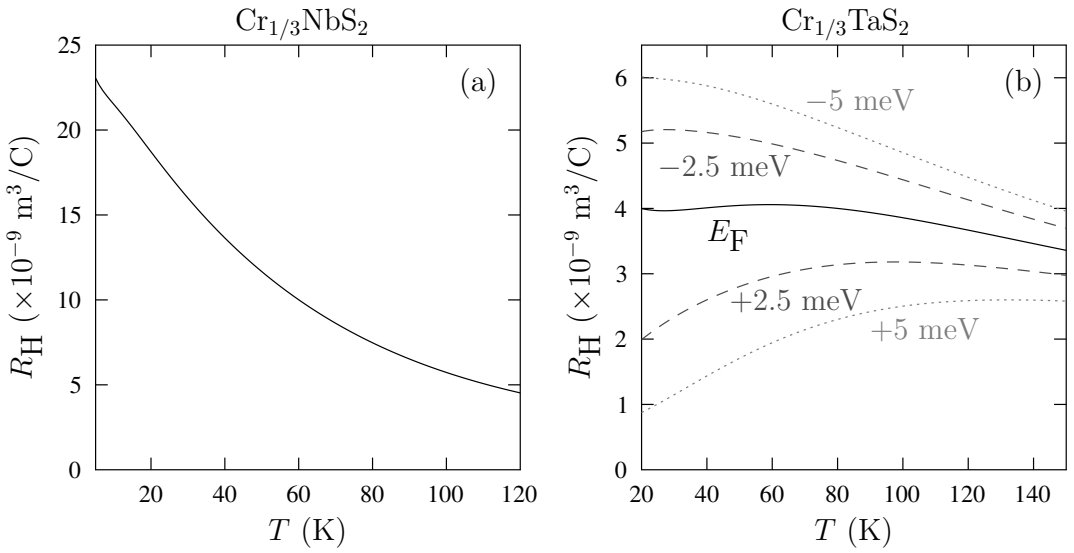


**Figure 8.3:** Calculated Hall coefficient $R_H$ for (a) $Cr_{1/3}NbS_2$ and (b) $Cr_{1/3}TaS_2$. In (b) the range of possible values of $R_H$ due to uncertainty in the Fermi Energy is shown.

behaviour due to the phase transition at $T_c$ [151, 160]) is given by the difference in number of electrons in the up and down spin channels. This is predicted by integrating the DOS weighted by the Fermi-Dirac distribution $f_{FD}(E,T)$ at a given temperature,

$$m(T) = N^{\uparrow} - N^{\downarrow} = \mu_B \int_{-\infty}^{\infty} \left[g^{\uparrow}(E) - g^{\downarrow}(E)\right] f_{FD}(E,T)\, dE, \tag{8.1}$$

where $g^{\uparrow(\downarrow)}(E)$ are the spin-up (spin-down) components of the partial DOS. The change in $m(T)$ (compared to $T = 0$) is shown in Fig. 8.4(a–b). As $T$ is increased, electrons start to populate excited states, leading to a steady increase in $m(T)$, with the change being dominated by the $M$ = Nb or Ta $d$-orbitals, despite their small overall contribution to the total moment.

Although these changes in $m(T)$ are likely too small to be detected by a bulk measurement of the magnetisation, $\mu$SR, a local probe sensitive to the magnitude of the internal field at the muon site, can detect such small changes. Reference [153] reports an increase in the local field at the muon site at low $T$ [inset of Fig. 8.4(c)]. We calculated the muon stopping site in these materials using DFT methods [115], following the approach for materials in the $GaV_4S_{8-y}Se_y$

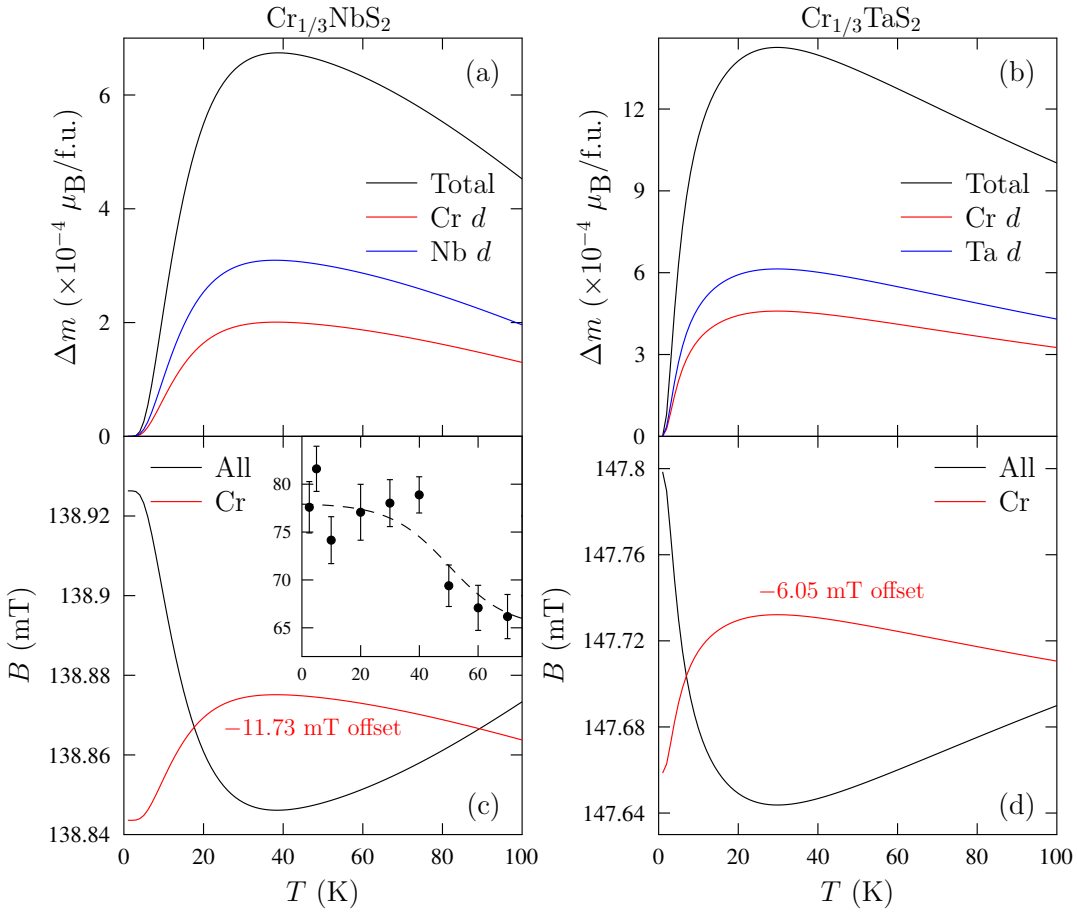


**Figure 8.4:** (a–b) Temperature evolution of the change in $m$ for $Cr_{1/3}NbS_2$ (a) and $Cr_{1/3}TaS_2$ (b). (Total change, and change in Cr and $M$ $d$-orbitals is shown.) (c–d) Effect on the field at the muon-site in (c) $Cr_{1/3}NbS_2$ and (d) $Cr_{1/3}TaS_2$. The field from the Cr moment alone is shown with a vertical offset. Inset: measured field at the muon-site [153] (same axes as (c), dashed line is a guide to the eye).

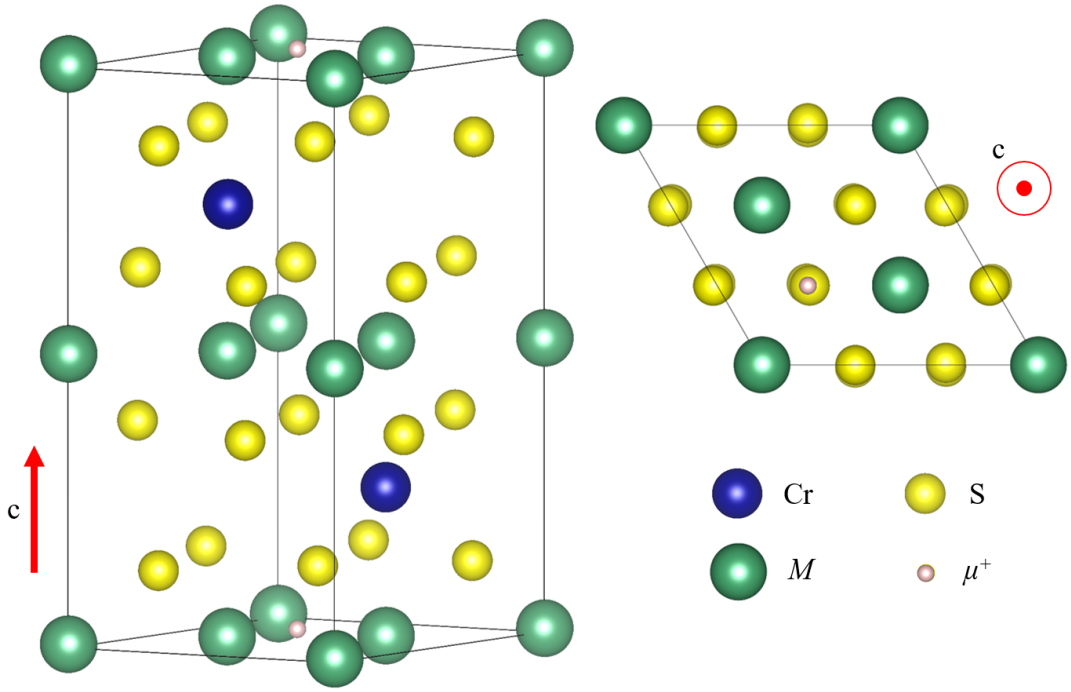


**Figure 8.5:** The muon site found using DFT methods in $Cr_{1/3}MS_2$ ($M$ = Nb or Ta). Image produced with VESTA [108].

family [128]. Whilst muon sites have previously been reported for $Cr_{1/3}NbS_2$ in Ref. [153], they are unphysically close to atoms, and only one frequency is observed with ZF $\mu$SR, despite two muon sites being found. Our calculations find a single muon site in both materials, sat at the centre of the triangle of $M$ atoms, as shown in Fig. 8.5. Note that although the number of Cr atoms intercalated between the $M$ layers varies throughout the crystal, all possible unit cells give the same muon sites with very similar energies. Note also that in the absence of Cr (i.e. in $MS_2$) there is a possible second muon site in the layer where the Cr sits; unit cells without Cr within the sample measured in Ref. [153] may explain the two muon sites detected.

The measured field can be compared to predictions using our stopping sites to calculate the expected $T$-dependent dipole field at the muon site due to our predicted $m(T)$ [Fig. 8.4(a–b)], calculated using the MUESR code [96]. As the incommensurate nature of the spin on the $M$ and S atoms was unknown (contrasting the helical evolution of the Cr moments), the calculations were performed using

the dipolar field component only of a ferromagnetic configuration for all atoms. This will closely approximate the dipolar field for the long-period helimagnet known to exist in $Cr_{1/3}NbS_2$, where the Lorentz field (due to the contribution of spins far from the muon) should be zero. (Note that including the Lorentz field merely shifts the field at the muon site up or down in magnitude, so would not affect the conclusions drawn here.) In these calculations there was assumed to be no hyperfine interaction and negligible demagnetisation effects.

The field at the muon site is highly sensitive to both the amount of Cr intercalated in the material, and to the precise location of the spin density with respect to the muon, neither of which are easy to accurately estimate. Therefore, our calculation of the absolute magnitude of the field at the muon site, as well as the size of the increase with temperature, does not quantitatively match experiment. There are three main reasons for the quantitative disagreement: (1) the hyperfine interaction is not captured by this model. As this contribution generally points collinear to the dipolar field, inclusion of this term would increase the magnitude of the effect, more closely matching experiment. (2) The model takes the spin density according to DFT and creates a localised moment at the centre of the nucleus. In reality, as we know from the half-metallic property of the material, the spin will be somewhat delocalised over the unit cell. (3) The atom and muon positions are not perfectly known. Allowing the atom and muon positions to move up to 0.15 Å from their high symmetry positions (within the error of the muon site, and less than 10% of atom separation) can double the maximum difference in internal field as a function of temperature, and change the zero-temperature field by 40 mT, over 25% of the value found. This highlights the sensitivity of the muon to very small changes in the unit cell, as expected, as the internal field is inversely proportional to the cube of the distance between the moment and muon. Hence it is not surprising that the changing internal field with temperature is only captured qualitatively.

Despite these limitations, we predict the same trend in $Cr_{1/3}NbS_2$ as found Ref. [153] [Fig. 8.4(c)], with a sharp increase in the field at the muon-site at low

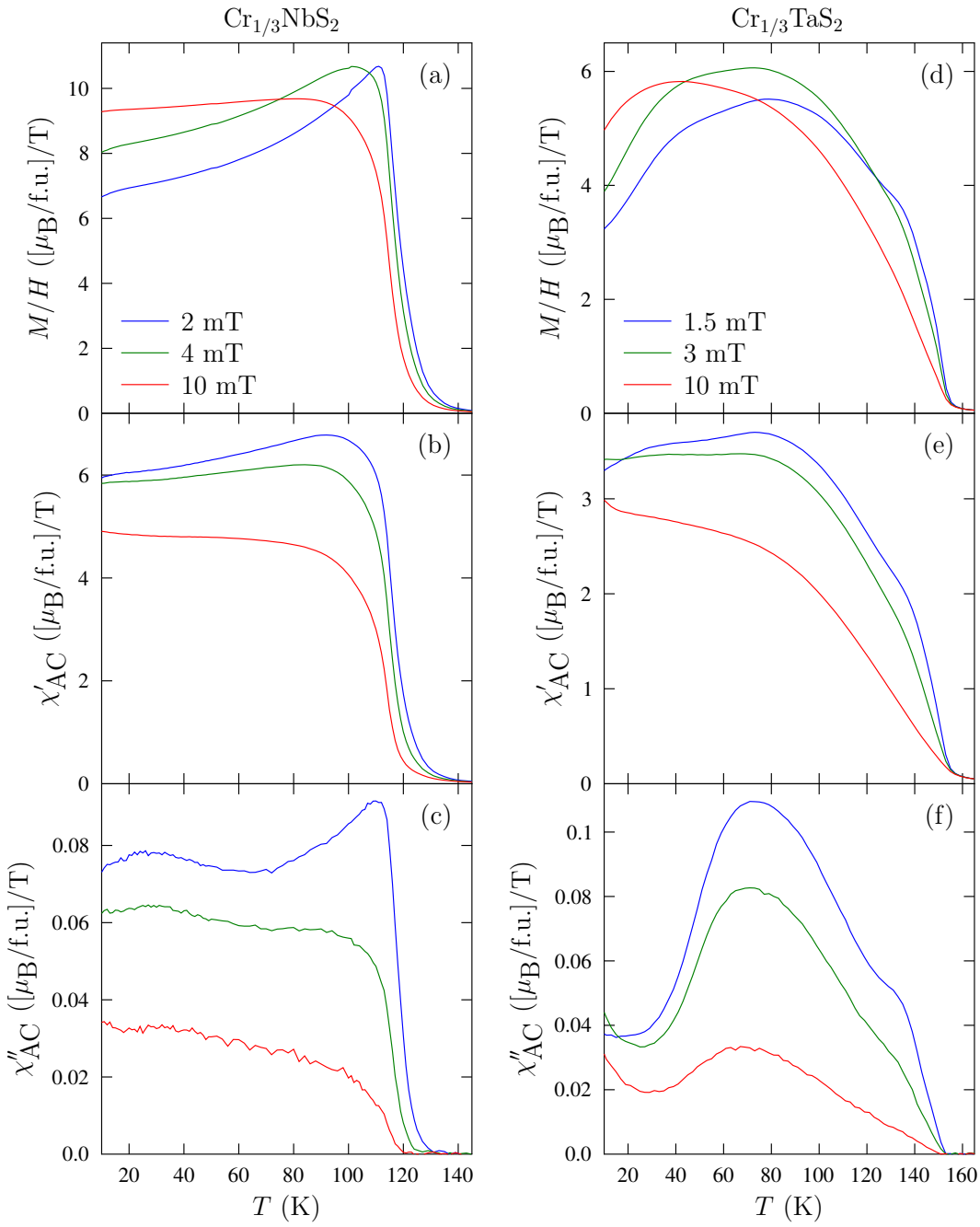


**Figure 8.6:** Magnetisation (a,d) and AC susceptibility (b–c, e–f) measurements of $Cr_{1/3}NbS_2$ (a–c) and $Cr_{1/3}TaS_2$ (d–f) at constant applied field. Measurements are performed after cooling in zero applied magnetic field. Magnetisation measurements are shown normalised by the applied magnetic field. AC susceptibility measurements were performed in an external DC magnetic field, with an oscillating AC field of magnitude 0.3 mT and frequency 79 Hz.

$T$. It is notable that the moment of all elements must be considered to obtain this effect; considering the moments on the Cr atoms alone does not reproduce the trend. As the moment on the Nb atoms (less than 5% of the total moment of the unit cell) must be included to get the shown effect we know that the spin throughout the unit cell is important, emphasising point (2) above. Our calculations also suggest significant shifts in $B$ at the muon site compared to the applied field. This is consistent with the $B$ field extracted from LF $\mu$SR at all measured fields as seen later.

Our first-principles electronic structure calculations therefore explain the published observations of unusual low-temperature electronic and magnetic properties. The existence of the pseudogap, and thermally activated transitions across this gap, are key to these findings. As the previously published work has all focused on static, average properties of the system, in the next section we will discuss experimental measurements of the dynamic magnetism that occurs due to the pseudogap.

### 8.4.2 Magnetometry

To confirm the influence of the pseudogap on the magnetism, we performed magnetisation and AC susceptibility measurements on polycrystalline samples of $Cr_{1/3}MS_2$ ($M$ = Nb or Ta). The critical temperature $T_c$ of each material matches previous reports [147], although the field required to induce the forced-ferromagnetic state is lower for both materials [161], implying a smaller DM interaction (likely due to different levels of Cr intercalation affecting the bonding and charge transfer between the $M$ ions, and hence the magnetic properties). Despite these differences, single-crystal samples of $Cr_{1/3}NbS_2$ prepared in the same way as our samples show a CSL in Lorentz transmission electron microscopy measurements [162].

Magnetisation and AC susceptibility measurements of $Cr_{1/3}MS_2$ ($M$ = Nb or Ta) can be seen in Figs. 8.6 and 8.7. Using the approach of Ref. [161], we can construct magnetic phase diagrams for the two materials (Fig. 8.8). Ref. [149]

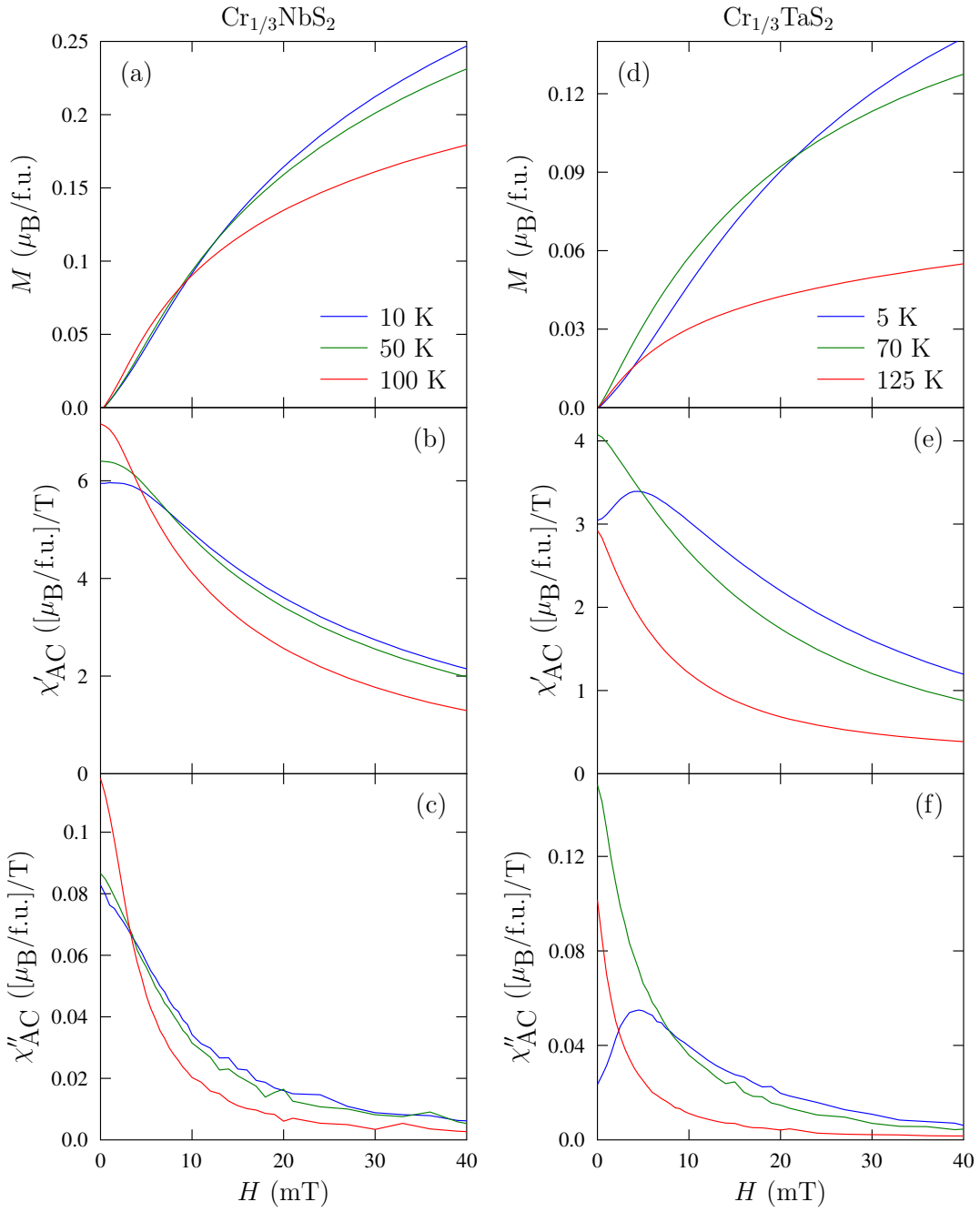


**Figure 8.7:** Magnetisation (a,d) and AC susceptibility (b–c, e–f) measurements of $Cr_{1/3}NbS_2$ (a–c) and $Cr_{1/3}TaS_2$ (d–f) at constant temperature. Measurements are performed after cooling in zero applied magnetic field. AC susceptibility measurements were performed in an external DC magnetic field, with an oscillating AC field of magnitude 0.3 mT and frequency 79 Hz.

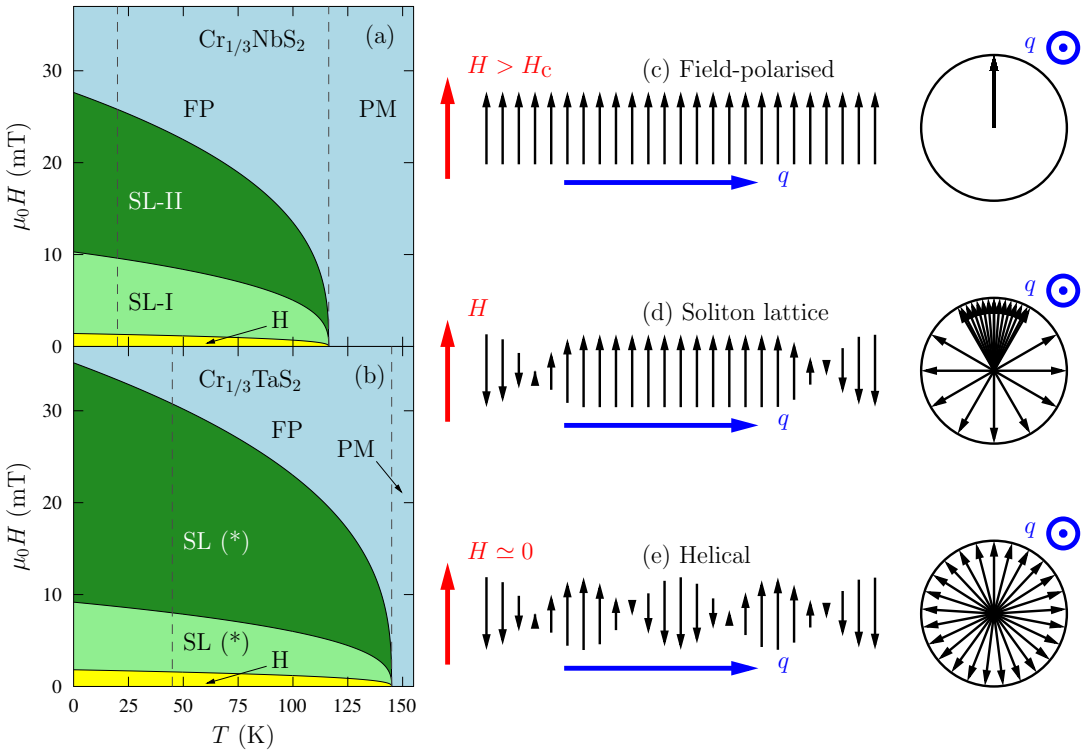


**Figure 8.8:** Phase diagram of (a) $Cr_{1/3}NbS_2$ and (b) $Cr_{1/3}TaS_2$ from magnetisation measurements. Indicated phases are helical (H), SL-I/II (soliton lattice, with the spacing between solitons greater in II than I), field-polarised (FP), and paramagnetic (PM). Sketches are shown in (c–e). There has been a preliminary report of the existence of a CSL in $Cr_{1/3}TaS_2$, however it does report the two phases we observe [149]; we therefore denote this phase SL (*). Dashed lines indicate the low-temperature feature $T^*$ and $T_c$.

reports a CSL in $Cr_{1/3}TaS_2$, however it does not report the two distinct phases we observe.

Both $Cr_{1/3}NbS_2$ and $Cr_{1/3}TaS_2$ exhibit three regimes of behaviour: (i) $T \lesssim T^*$, (ii) $T^* \lesssim T < T_c$, and (iii) $T > T_c$, where the low-temperature crossover $T^* \simeq 20$ K for $Cr_{1/3}NbS_2$, and $T^* \simeq 45$ K for $Cr_{1/3}TaS_2$. In region (iii) the materials are paramagnetic, transitioning to long-range order when the samples are cooled into region (ii). On cooling to region (i), changes are seen most clearly in the phase lag $\phi$ between the applied time-varying magnetic field and the AC susceptibility response. This suggests dissipative processes [52] determined by

fluctuations across the pseudogap. $Cr_{1/3}NbS_2$ shows a peak in $\phi$ around $T^*$, whereas $Cr_{1/3}TaS_2$ exhibits an decrease in this quantity. For $Cr_{1/3}NbS_2$ the behaviour is well described by a Gaussian peak with a vertical offset, whereas a sigmoid function with a vertical offset is most appropriate for $Cr_{1/3}TaS_2$. Both functions allow the extraction of a characteristic temperature $T^*$ (the peak location of the Gaussian, or the inflection point of the sigmoid). Fig. 8.9(b,d) shows that $T^*$ follows an Arrhenius law, with the gradient giving an activation energy $E_a$ consistent with the pseudogap $\Delta E$ = 80–90 meV identified in the spin-up DOS. [In $Cr_{1/3}NbS_2$ the gap is slightly smaller than identified via DFT, and this is the value used to rescale $S$ in Fig. 8.2(a).] The observed dynamics are therefore consistent with moment fluctuations caused by temperature driven transitions across the gap.

### 8.4.3 Muon-spin spectroscopy

To further probe dynamic fluctuations around the pseudogap, we performed LF $\mu$SR measurements on $Cr_{1/3}MS_2$ ($M$ = Nb or Ta), which are sensitive predominantly to megahertz dynamics (i.e. much higher frequencies than the $<$ 150 Hz dynamics probed with AC susceptibility). Both materials show changes in the initial asymmetry $A_0$ near $T_c$ for all applied fields, indicating the magnetic transition. Example spectra are shown in Fig. 8.10.

We first look at $Cr_{1/3}NbS_2$. A small applied field will decouple the nuclear contribution to the spectra leaving us sensitive to electronic fluctuations. An example spectrum for $T < T_c$ is shown in Fig. 8.11, where $\mu_0 H_{ext}$ = 2 mT. A reduction in $A_0$ is observed at low $T$ [Fig. 8.11(a)]. Extrapolating the Arrhenius behaviour seen with AC susceptibility to frequencies appropriate for $\mu$SR ($\gamma_\mu B_{ext}$), gap driven effects should be observed around $T^*$ = 35 K (marked as a dashed line in Fig. 8.11); it is below $T^*$ where changes in $A_0$ are observed. A reduction in $A_0$ indicates a larger proportion of the muons stopping in sites where there is a component of the magnetic field perpendicular to the initial muon-spin, causing precession too rapid to be observed in the experiment. This suggests an

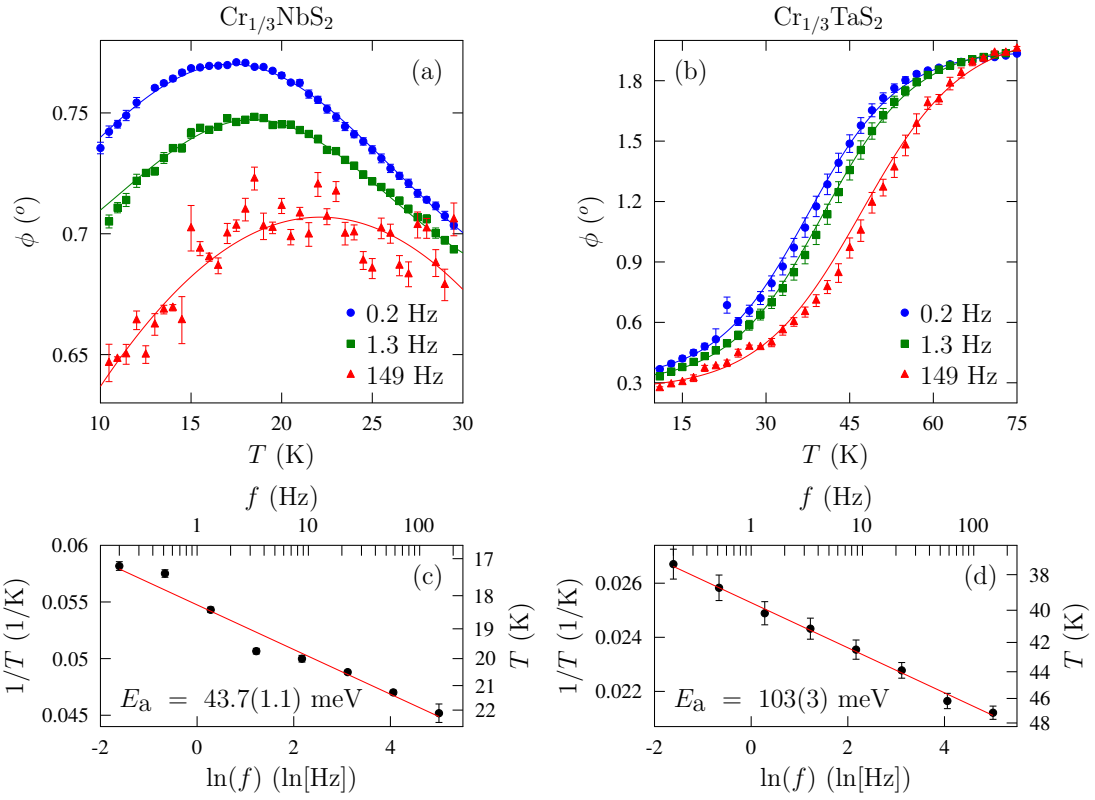


**Figure 8.9:** (a–b) Example measurements of the phase lag $\phi$ of AC susceptibility measurements on $Cr_{1/3}MS_2$ ($M$ = Nb or Ta). Solid lines are fits to the data as described in the text. The central position of these fits is shown in (c–d). Fitting these data gives the activation energies $E_a$ indicated.

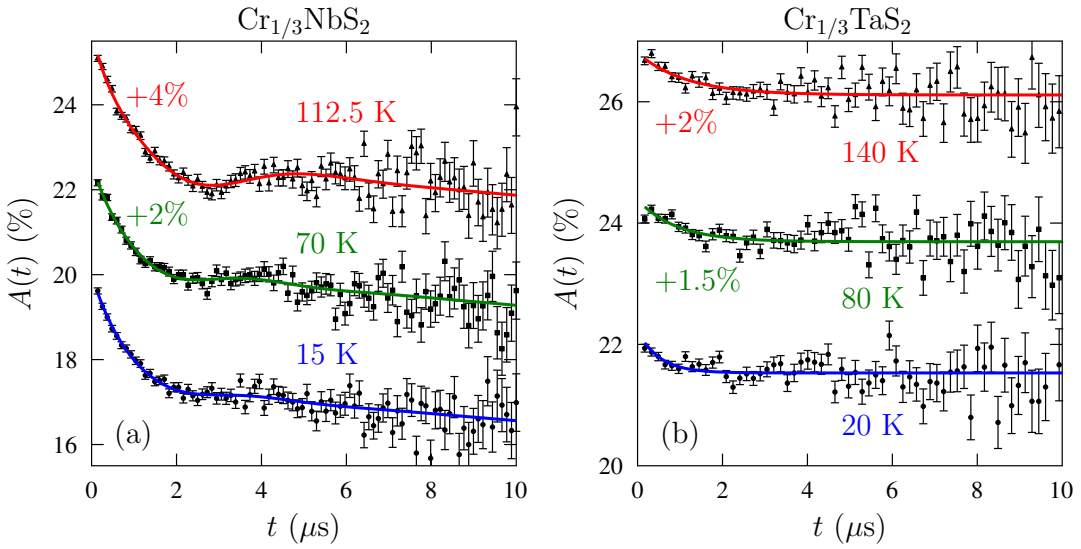


**Figure 8.10:** Example measurements and fits of the muon-spin relaxation asymmetry spectra of $Cr_{1/3}MS_2$ ($M$ = Nb or Ta). Some data is shown with an indicated vertical offset.

increase in the internal field at low $T$, as seen with ZF $\mu$SR [153] in Fig. 8.4(e). As the external field is increased, this increased internal field becomes less important, which is reflected in the reduced resolution of this effect in $A_0$.

The LF $\mu$SR spectra measured on $Cr_{1/3}NbS_2$ at all applied fields were fitted with

$$A(t) = a_1 \exp\left(-\sigma^2 t^2\right) \cos\left(\gamma_\mu B t\right) + a_2 \exp\left(-\lambda t\right) + a_\mathrm{b} \exp\left(-\lambda_\mathrm{b} t\right), \tag{8.2}$$

where the first term accounts for muons in sites where the average internal field is not parallel to the initial muon-spin, leading to precession in the effective LF field $B$, the second term accounts for muons in a purely longitudinal average magnetic field, leading to relaxation from dynamic fluctuations, and the third term accounts for muons that stop outside the sample and weakly relax due to the presence of Ag nuclear moments. This model should only be applicable below $T_\mathrm{c}$, however we find it describes the data well over the entire temperature range since it also approximates the expected LF Kubo-Toyabe behaviour above $T_\mathrm{c}$ that occurs due to relaxation from disordered electronic moments. As typical, the two regimes are separated by a peak in $\lambda$ around $T_\mathrm{c}$. We find at each field, $\lambda_\mathrm{b}$ and $\sigma$

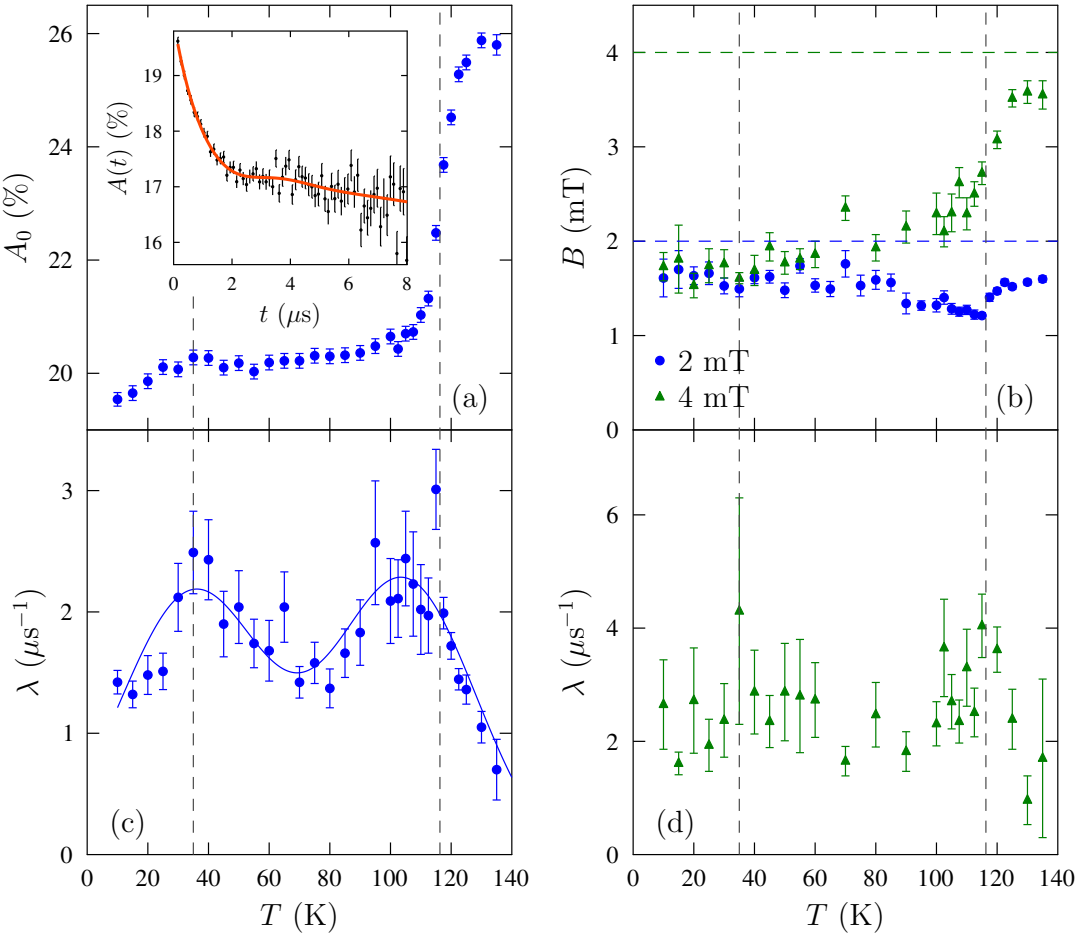


**Figure 8.11:** LF $\mu$SR results for $Cr_{1/3}NbS_2$. The initial asymmetry is shown in (a). The inset shows an example of the spectra and fit for 2 mT and 15 K. Fitted parameters using the model presented in the text are shown in (b–d). The solid blue line in (c) is a guide to the eye. Dashed lines indicate $T_c$ (high $T$) and $T^*$ (low $T$, extrapolated from AC susceptibility).

are $T$-independent, therefore we fix them to $\lambda_b = 0.005\ \mu s^{-1}$ and $\sigma = 0.28$, 0.55, 0.52 $\mu s^{-1}$ for 2, 4, 10 mT respectively. The $T$-independence of $\sigma \propto \langle (B - \langle B \rangle)^2 \rangle$ suggests the distribution of magnetic fields at the muon site does not significantly change. Fitted parameters extracted from the 2 mT measurements are shown in Fig. 8.11(b–d).

The main result from our $\mu$SR is that the observed megahertz dynamics are consistent with the pseudogap-driven magnetism. As shown in Fig. 8.11(c), there is a clear peak in $\lambda$ at $T^*$. This occurs due to the same dynamic fluctuations of the moment size as are responsible for the behaviour observed in AC susceptibility measurements. As $T$ is increased the fluctuation rate $\nu$ increases in frequency, passing through the muon time-window. Since we expect the relaxation rate to evolve via $\lambda \propto \nu / \left(\nu^2 + \gamma_\mu^2 B_{ext}^2\right)$, where $\gamma_\mu = 2\pi \times 135.5\ \mathrm{MHzT}^{-1}$ is the gyromagnetic ratio of the muon, this leads to a peak in $\lambda$ around $T^*$ corresponding to $\nu(T^*) = \gamma_\mu B_{ext}$, as predicted from the Arrhenius behaviour of the AC susceptibility.

We have additionally performed LF $\mu$SR measurements in applied field of 4 mT (where we expect a significant volume fraction of the sample in the CSL state), and 10 mT (where the solitons in the CSL have large separations, accounting for a lower volume fraction of the sample). Measurements at these fields were found to be well described by the same model as at 2 mT, with results seen in Figs. 8.12 and 8.13. At 10 mT, where the effect of CSL is minimal, the behaviour of all fitted parameters was found to be very similar to 2 mT, however more dramatic changes are observed at 4 mT. Most notably, the dynamic changes at $T^*$ observed through $\lambda$ are not seen at 4 mT [Fig. 8.11(d)], but are recovered at 10 mT. It is possible that since the topologically-protected CSL has a large energy barrier preventing changes to the static structure, the more robust magnetism in this phase might prevent the effects of energy-gap driven magnetism being measurable. Other differences are seen in the effective local field $B$ [Fig. 8.11(b)], which at 2 mT remains fairly constant at slightly less than the applied external field (with a deviation at $T_c$). However, at 4 mT there is a sizeable reduction

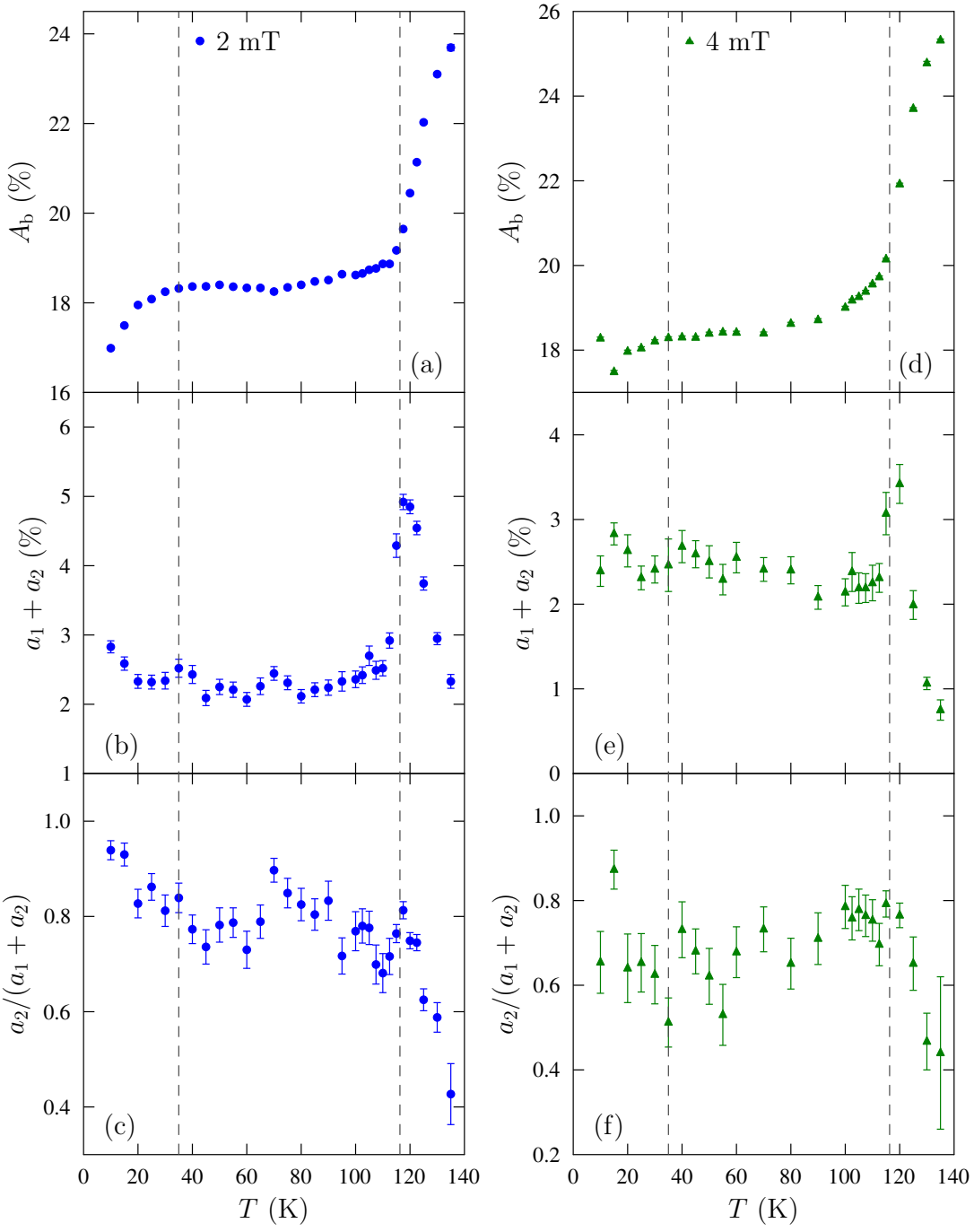


**Figure 8.12:** Parameters extracted through fitting LF $\mu$SR asymmetry spectra of $Cr_{1/3}NbS_2$ collected at 2 and 4 mT. Dashed lines indicate $T_c$ (high $T$) and $T^*$, extrapolated from AC susceptibility data (low $T$).

compared to the applied field, with $B$ decreasing continuously with decreasing temperature, perhaps suggesting a continuous evolution in the size of the static field at the muon site in the CSL. Below $T_c$ at 10 mT, where the CSL is expected to occur with reduced volume fraction, $B$ is approximately constant at a value significantly reduced compared to the applied field.

LF $\mu$SR measurements of $Cr_{1/3}TaS_2$ were performed in an applied field of 1.5 mT, however as can be seen in Fig. 8.10 much of the asymmetry is relaxed out too rapidly to be seen on with the time resolution available at ISIS, suggesting a much higher field at the muon site than in $Cr_{1/3}NbS_2$. As this is not observed in our muon-site field calculations, this suggests delocalised electrons leading to magnetism that is not well described by a classical model, consistent with the results of DFT calculations (see Ref. [140]), and the assertion of the importance of this in the muon-site field calculations. Whilst there are subtle hints in the data that the same model as used for $Cr_{1/3}NbS_2$ may be appropriate to fit these data, it could not be fitted reliably, so $A(t) = a\exp(-\lambda t) + a_b$ was used. The fits have a temperature independent relaxing asymmetry $a$, with $a = 0.69(2)$ %. Although $a$ would normally be temperature dependent, changing dramatically at $T_c$, due to the rapid depolarisation of the muon-spin this effect cannot be decoupled from $a_b$. The temperature dependence of $\lambda$ and $a_b$ can be seen in Fig. 8.14. Changes in $\lambda$ are seen around $T_c$, although oddly there is no peak. As for $Cr_{1/3}NbS_2$, low-$T$ changes concentrated in the region below $T^*$ can be seen, with an enhancement/peak in $\lambda$ (suggesting dynamic changes), and a subtle change in the rate of change of $a_b$ with $T$ (suggesting static changes). This suggests similar underlying magnetic behaviour.

## 8.5 Conclusion

In conclusion, the results of electronic structure calculations explain the low-$T$ properties of half-metallic $Cr_{1/3}MS_2$ ($M$ = Nb or Ta); all published low-$T$ observations can be explained by considering electrons transitioning across the small pseudogap in the spin-up channel. These effects do not require the inclu-

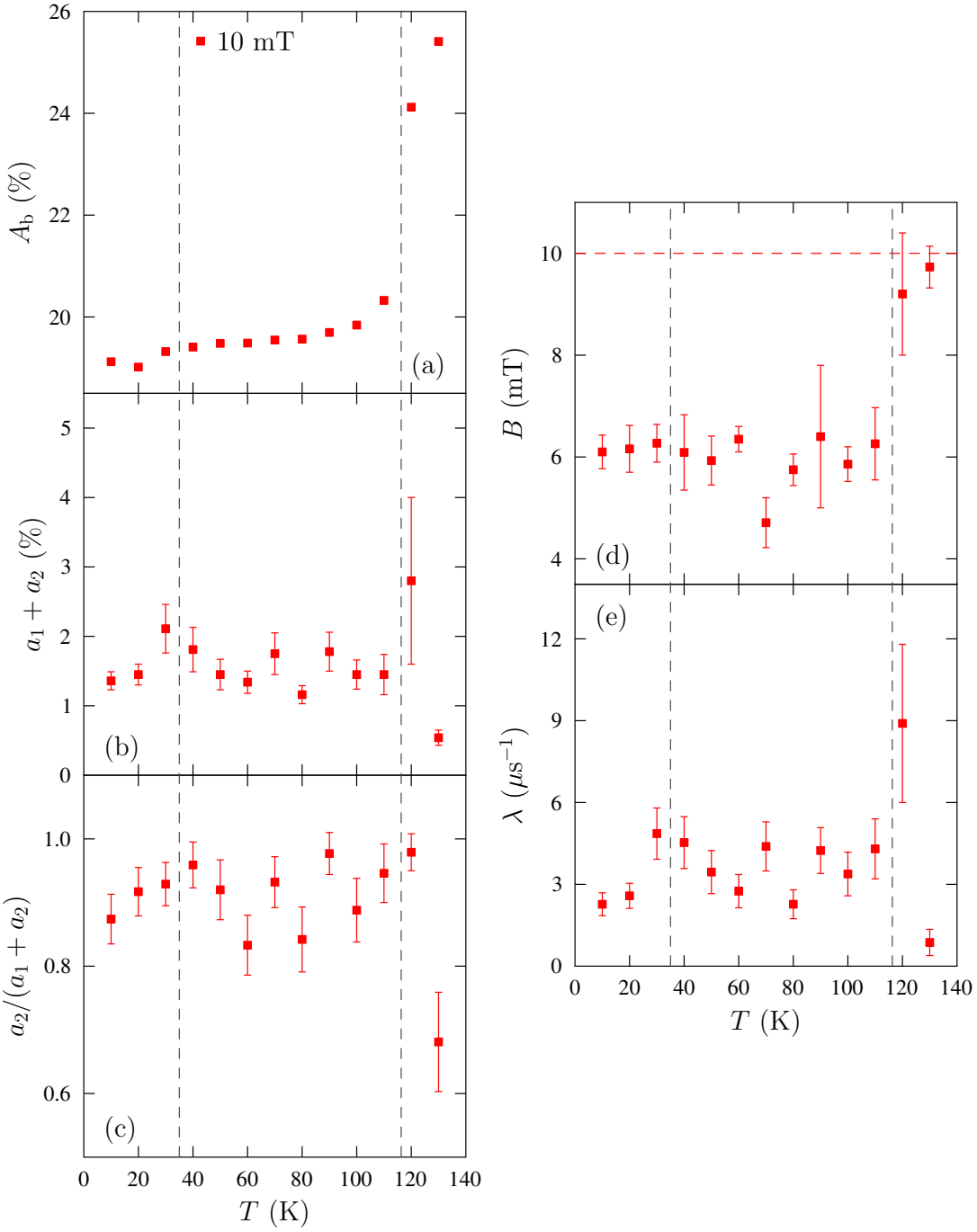


**Figure 8.13:** Parameters extracted through fitting LF $\mu$SR asymmetry spectra of $Cr_{1/3}NbS_2$ collected at 10 mT. Dashed lines indicate $T_c$ (high $T$) and $T^*$, extrapolated from AC susceptibility data (low $T$).

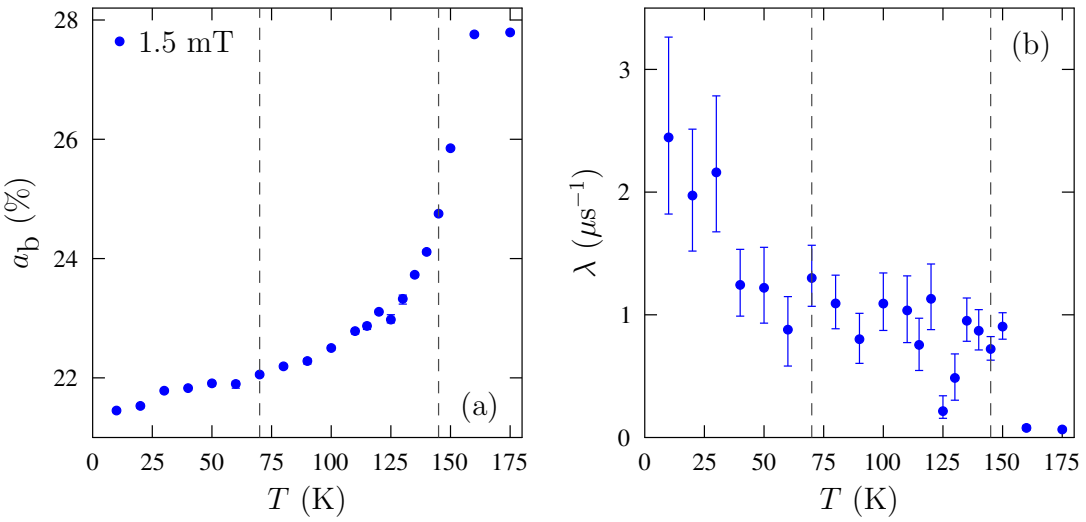


**Figure 8.14:** Parameters extracted through fitting LF $\mu$SR asymmetry spectra of $Cr_{1/3}TaS_2$ in a 1.5 mT external field, as detailed in the text. $T_c$, and $T^*$ (extrapolated from AC susceptibility data) are indicated with dashed lines.

sion of SOC in the calculation, and do not imply a change of DM interaction, or a change in the helical length, as previously suggested. We have measured the pseudogap using AC susceptibility, finding good agreement with DFT, while our measurements reveal dynamic transitions across the gap occur over a wide range of fluctuation frequencies (0.1 Hz to MHz). In $Cr_{1/3}NbS_2$, $\mu$SR suggests that the CSL masks the low-$T$ effects. The similar electronic and magnetic behaviour of $Cr_{1/3}MS_2$ ($M$ = Nb or Ta) is consistent with the realisation of a CSL in $Cr_{1/3}TaS_2$, a recent report [149] has provided the first direct evidence of this. Our work demonstrates that, even in materials where topological magnetism leads to desirable properties for applications, the magnetic properties cannot be considered in isolation, and a thorough understanding of the electronic structure is essential.

# Chapter 9

# Conclusions and further work

The results presented in this thesis demonstrate that muon-spin spectroscopy ($\mu$SR) is a very helpful tool in the study of materials hosting topological magnetic states. Unique insights into the static magnetic configuration, dynamic behaviour, and electronic structure have all been demonstrated with the $\mu$SR technique. A particular strength of the technique is the frequency range to which $\mu$SR is most sensitive; for the work in this thesis we are typically probing the megahertz regime. This is a frequency range that is difficult to access with other techniques (Chap. 3) where comparatively little is known about the topological magnetic states (Chap. 2). By applying $\mu$SR to many different systems, we have observed some behaviour that seems to be consistent across the materials, whilst others are material-specific. This allows insight into behaviours we can associate with the topological magnetic states, and can therefore expect to observe in other, as-yet unstudied materials.

More specifically, we have studied the behaviour of materials hosting both a Bloch skyrmion lattice (SkL), $Cu_2OSeO_3$ and $Co_xZn_yMn_{20-x-y}$, and those hosting a Néel SkL, $GaV_4S_{8-y}Se_y$. We find a dynamic response that is remarkably consistent; when performing a temperature scan at an applied field sufficient to cut through the SkL phase we observe a greatly enhanced dynamic response compared to surrounding phases, demonstrating that the SkL is highly dynamic on time muon-timescale, typically in the megahertz regime. (It is worth noting that

we are not restricted to studying the megahertz regime with $\mu$SR, that just happens to be the most appropriate dynamic range for $\mu$SR in these systems.) In the case of $Co_xZn_yMn_{20-x-y}$ (Chap. 6) and $GaV_4S_{8-y}Se_y$ (Chap. 7) we see that the dynamic response of the SkL can at least partially be explained by the reduction in frequency of the characteristic gigahertz single skyrmion modes, as derived in App. A. This does not tell the whole story through, with other contributions to the dynamic response unique to the SkL evident, especially in $Cu_2OSeO_3$ (Chap. 4). By studying the SkL phase out-of-equilibrium, both as a metastable skyrmion lattice stabilised after rapid field cooling, and through application of an electric-field to multiferroic $Cu_2OSeO_3$, we show that these additional dynamics are most likely associated with the decay of skyrmions.

This thesis demonstrates that a particular strength of the $\mu$SR technique is the application to materials which have some degree of chemical substitution. The most comprehensive example of this is the study of $GaV_4S_{8-y}Se_y$ in Chap. 7. We find that magnetic order is preserved for low-levels of substitution, at both ends of the series, in contrast to higher levels where spin glass-like behaviour is observed [128, 127, 123]. We are able to see dramatic differences in the behaviour at each end of the series; at the S end of the series substitution creates regions in the sample which have increased spin density, leading to the observation of high magnetic fields with $\mu$SR. Contrastingly, the magnetism at the Se end of the sample was demonstrated to be more robust to substitution effects. Density functional theory (DFT) calculations of these materials were able to confirm these effects. The enhanced dynamic response of the SkL is preserved under low-levels of substitution at both ends of the series, and we conclude that a dynamically fluctuating SkL is realised in these materials with characteristic excitations similar to those in Bloch skyrmion systems. Perhaps most interestingly, at low temperature in the slightly-substituted systems an enhanced dynamic response suggests the stabilisation of skyrmion precursors. This forms a consistent picture with the results of Chap. 6 on $Co_xZn_yMn_{20-x-y}$, where as crystallographic site disorder increases, so too does the complexity of the dynamic response on the muon

timescale. Taking these results together, it suggests that in multiple systems crystallographic site disorder plays a role in stabilising complex excitations, and possibly the SkL itself.

Another substituted material to which $\mu$SR was applied was polycrystalline Zn-substituted $Cu_2OSeO_3$ (Chap. 5). This work demonstrates the strength of $\mu$SR in these systems alongside other experimental techniques, in this case magnetometry and x-ray diffraction. This holistic view of the system was able to reveal multiple different magnetic environments that are best explained as different levels of Zn-substitution in different grains of the sample, explaining the previously reported splitting of the SkL phase in the $B$–$T$ phase diagram [110]. $\mu$SR was able to extract the relative weights of the different Zn-substitution phases in each sample, giving values consistent with other measurement techniques. We also reveal that, consistent with the measurements on single crystals, on the muon-timescale dynamic changes to the SkL are far more important than changes to the static structure. This is consistent with other dynamic behaviours of the SkL in Zn-substituted $Cu_2OSeO_3$, for example the dramatic increase of the metastable lifetime of the SkL with Zn-substitution [79], and once again demonstrates the importance of crystallographic site disorder on the stability of the SkL.

The ability to probe spin excitations with $\mu$SR was once again utilised for the study of chiral soliton lattice (CSL) hosts $Cr_{1/3}NbS_2$ and $Cr_{1/3}TaS_2$, in Chap. 8. We identify a small pseudogap in these materials through magnetometry and DFT, demonstrating that this feature provides an explanation of the low-$T$ transport and magnetic properties in this system, with all published experimental observations able to be explained by considering electrons transitioning across the small pseudogap in the spin-up channel. Having measured the pseudogap in both materials using AC susceptibility, finding good agreement with DFT, $\mu$SR is able to probe excitations across this gap at megahertz frequencies. We find consistent behaviour over a large dynamic range. In $Cr_{1/3}NbS_2$, $\mu$SR suggests that the CSL masks these low-$T$ effects.

The unifying question for the work presented in this thesis was whether $\mu$SR

was a useful tool for the study of materials hosting topological magnetic states. The answer is a resounding yes, with myriad insights into a wide range of behaviours that are uniquely accessible with $\mu$SR. The results in this thesis pose a few unresolved questions which further research would be beneficial. The most significant one is the source of the megahertz dynamics observed in many SkL hosting systems. Whilst we provide strong evidence for the origin being associated with the decay of the skyrmion, to the author's knowledge there are no theoretical studies that demonstrate these effects, nor are there direct experimental measurements of these phenomena. Both of these approaches would be beneficial. Understanding these dynamics is essential if skyrmions are to be used technologically.

Another area in which further work would be advantageous is in the study of the $GaV_4S_{8-y}Se_y$ series, and in $Cr_{1/3}TaS_2$. In both cases, $\mu$SR (and other techniques presented in this thesis) suggests that currently unidentified topological magnetic states may exist. In the case of $GaV_4S_{8-y}Se_y$ we see evidence for low-temperature skyrmionic precursors in substituted systems. In $Cr_{1/3}TaS_2$ our work finds no significant difference between the electronic and magnetic behaviour of $Cr_{1/3}NbS_2$. There have been recent initial reports of a CSL in $Cr_{1/3}TaS_2$ [149], however they do not report the splitting of this phase in two, as this work shows. $\mu$SR is not a $q$-resolved probe, and cannot image these states in real-space, therefore other techniques (such as small angle diffraction experiments, Lorentz Transmission Electron Microscopy, or x-ray holography) can be beneficially applied to these systems to further investigate these potentially new states.

Despite these unresolved areas of research, we have seen that $\mu$SR is a very useful tool for the study of materials hosting topological magnetic states. This thesis demonstrates a body of work that has advanced the application of $\mu$SR in these areas, and revealed new insights into the materials studied. It is the hope of the author that this work can be built upon by other researchers to continue to advance the study of topological magnetic states, and the $\mu$SR technique.

# Appendix A

# Muon coupling to skyrmion modes

Throughout this thesis, a regularly employed model is one of coupling between the characteristic excitations of individual skyrmions to the muon-spin, which leads to relaxation of the muon-spin polarisation. Specifically, we consider the reduction in frequency of the skyrmion modes as the temperature increases towards the critical temperature $T_{\mathrm{c}}$. The main idea behind this model is that excitations around $\gamma_{\mu}B_{\mathrm{ext}}$ most strongly relax the muon-spin polarisation, and therefore, despite the characteristic excitations of the skyrmion typically being in the gigahertz regime, as $T_{\mathrm{c}}$ is approached, critical behaviour will lead to contributions over a wide range of frequencies.

In a longitudinal field (LF) muon-spin relaxation ($\mu$SR) experiment spin-polarised positive muons are implanted in a sample in the presence of an external magnetic field $B_{\mathrm{ext}}$ parallel to the initial muon-spin direction. Implanted muons interact with the local magnetic field at the muon site, which is a sum of the external and internal fields. In the fast-fluctuation regime, typical for an ordered magnet, exponential decay of the muon-spin polarisation is often observed with a relaxation rate

$$\lambda \;=\; \frac{2\Delta^2\nu}{\omega_0^2+\nu^2}, \tag{A.1}$$

where $\nu$ is the characteristic frequency of fluctuations of the local field $B$, with

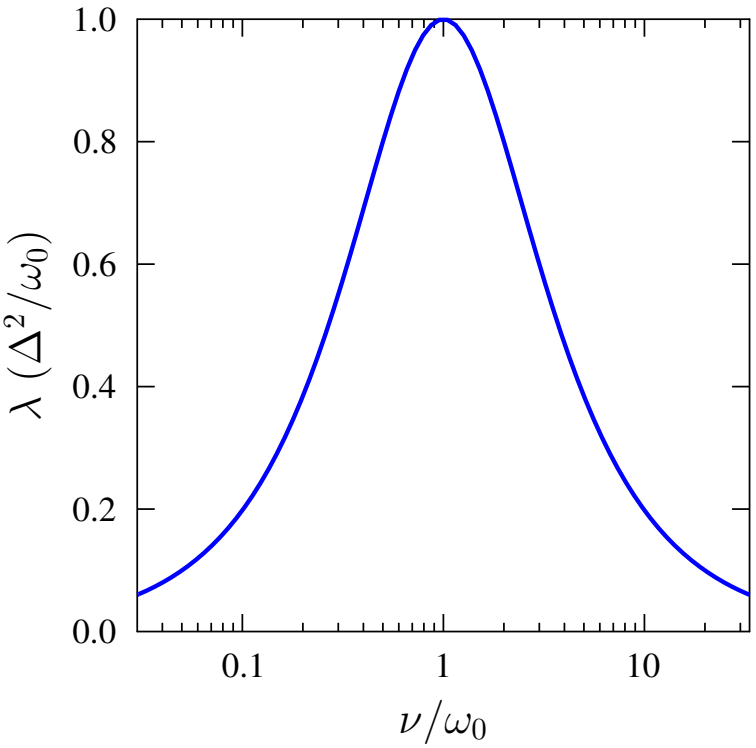


**Figure A.1:** The muon-spin polarisation relaxation rate $\lambda$ (normalised by the amplitude of magnetic fluctuations $\Delta$) as a function of the fluctuation frequency according to Eqn. A.1. The muon-spin polarisation is most effectively relaxed by fluctuations at a frequency near $\omega_0 = \gamma_\mu B_{\text{ext}}$.

corresponding amplitude $\Delta = \gamma_\mu \sqrt{\langle B^2 \rangle}$. The precession frequency of the muon is given by $\omega_0 = \gamma_\mu B_{\text{ext}}$, where the gyromagnetic ratio of the muon is $\gamma_\mu = 2\pi \times 135.5$ MHz T$^{-1}$. The fluctuations themselves can be described by a spectral density $J(\omega)$, which represents the Fourier transform of the autocorrelation function of the magnetic field at the muon site(s). In cases where $J(\omega)$ is broad in frequency, the muon spin polarisation will be most effectively relaxed by the part of the spectral density at frequencies close to $\omega_0 = \gamma_\mu B_{\text{ext}}$, which typically lies in the megahertz regime for values of $B_{\text{ext}}$ applied in the measurements presented in this thesis. This is most clearly seen in Fig. A.1, which shows the relaxation rate $\lambda$ (normalised by a constant $\Delta$) as a function of the frequency of fluctuations.

To understand the dynamic response of the SkL, we model the response on

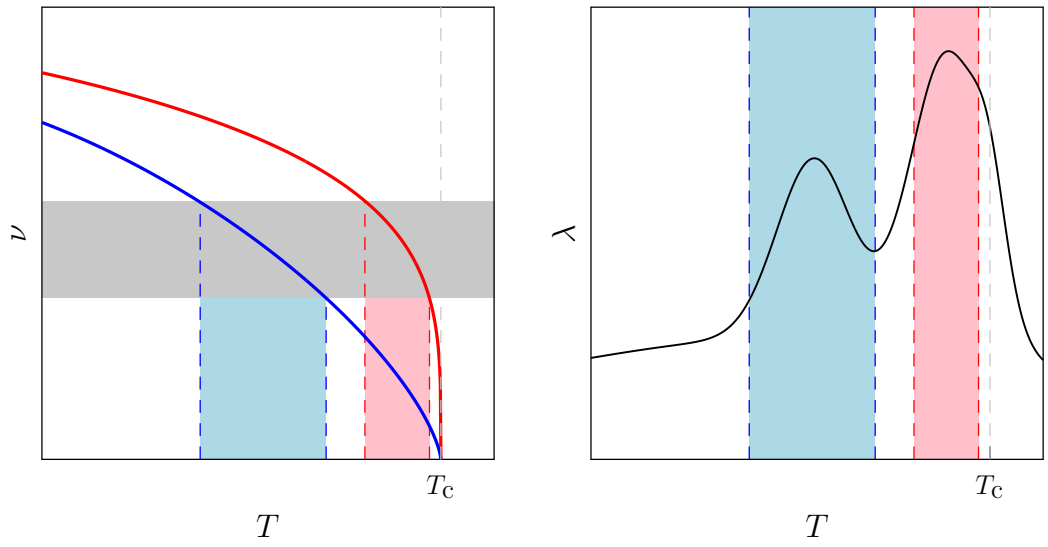


**Figure A.2:** A diagrammatic representation of the mechanism leading to the peaks in $\lambda$ according to the model discussed in this section. (a) Frequency $\nu$ of modes undergoing softening on increasing temperature. Two different modes are shown, showing how these would separately contribute to $\lambda$. The region of frequencies over which there is a significant $\mu$SR response (centred on $\gamma_\mu B_{\text{ext}}$) is shown in grey. (b) Resultant peaks in $\lambda$ from modes within the muon response window.

the muon timescale of skyrmion excitation modes with frequency $\nu$ (such as the low-frequency rotational and breathing modes in the SkL plane [43]) that soften (decreasing in frequency) as $T$ increases towards $T_c$ [163, 164]. As these modes cross through the frequency window where $\mu$SR is sensitive the relaxation rate increases. We can see this diagrammatically in Fig. A.2, where different modes contribute to $\lambda$ at different temperatures.

To model the temperature dependence of $\lambda$ according to Eqn. A.1, we apply power-law behaviour, assuming $\Delta$ and $\nu$ follow universal scaling laws. The scaling law for the divergence in $\nu$ at $T_c$ is

$$\nu = \nu_0 \left(1 - \frac{T}{T_c}\right)^{\zeta z}, \tag{A.2}$$

where $\nu_0$ is the zero-temperature autocorrelation frequency, $\zeta$ is the correlation-length critical exponent, and $z$ is the dynamical critical exponent. The scaling

law for the internal field distribution width, which we assume is proportional to the mean internal field magnitude $B$, is

$$\Delta = \Delta_0 \left(1 - (T/T_c)^{\alpha}\right)^{\beta}, \tag{A.3}$$

for $T \leq T_c$. Whenever we apply this model in this thesis, we use typical values of the critical exponents for the 3D Heisenberg universality class, $\alpha = 3/2$, $\beta = 0.365$ [14, 165], $\zeta = 0.7048$ [166], and $z = 2.035$ [102]. This gives, $\nu = \nu_0 \left(1 - T/T_c\right)^{1.43}$ and $\Delta = \Delta_0 \left(1 - (T/T_c)^{3/2}\right)^{0.365}$. Substituting these into Eqn. A.1 in turn gives

$$\lambda = \frac{2\Delta_0^2 \nu_0 \left[1 - (T/T_c)^{3/2}\right]^{0.73} \left(1 - T/T_c\right)^{1.43}}{\gamma_\mu^2 B_{\text{ext}}^2 + \nu_0^2 \left(1 - T/T_c\right)^{2.86}}. \tag{A.4}$$

It is this equation which we regularly employ throughout the thesis.

# Bibliography


[1] M. Z. Hasan and C. L. Kane, Colloquium: topological insulators, Reviews of Modern Physics **82**, 3045 (2010).

[2] X.-L. Qi and S.-C. Zhang, Topological insulators and superconductors, Reviews of Modern Physics **83**, 1057 (2011).

[3] S. Mühlbauer, B. Binz, F. Jonietz, C. Pfleiderer, A. Rosch, A. Neubauer, R. Georgii, and P. Böni, Skyrmion lattice in a chiral magnet, Science **323**, 915–919 (2009).

[4] K. Everschor-Sitte, J. Masell, R. M. Reeve, and M. Kläui, Perspective: Magnetic skyrmions – Overview of recent progress in an active research field, Journal of Applied Physics **124**, 240901 (2018).

[5] Y. Cao, Z. Huang, Y. Yin, H. Xie, B. Liu, W. Wang, C. Zhu, D. Mandrus, L. Wang, and W. Huang, Overview and advances in a layered chiral helimagnet $Cr_{1/3}NbS_2$, Materials Today Advances **7**, 100080 (2020).

[6] T. Lancaster, Skyrmions in magnetic materials, Contemporary Physics **60**, 246–261 (2019).

[7] A. Altland and B. D. Simons, *Condensed Matter Field Theory* (Cambridge University Press, Cambridge, 2010).

[8] A. Fert, V. Cros, and J. Sampaio, Skyrmions on the track, Nature Nanotechnology **8**, 152–156 (2013).

[9] G. Finocchio, F. Büttner, R. Tomasello, M. Carpentieri, and M. Kläui, Magnetic skyrmions: from fundamental to applications, Journal of Physics D: Applied Physics **49**, 423001 (2016).

[10] A. Fert, N. Reyren, and V. Cros, Magnetic skyrmions: advances in physics and potential applications, Nature Reviews Materials **2**, 1–15 (2017).

[11] S. Li, W. Kang, X. Zhang, T. Nie, Y. Zhou, K. L. Wang, and W. Zhao, Magnetic skyrmions for unconventional computing, Materials Horizons **8**, 854–868 (2021).

[12] S. J. Blundell, R. De Renzi, T. Lancaster, and F. L. Pratt, *Muon Spectroscopy: An Introduction* (Oxford University Press, Oxford, 2021).

[13] S. Blundell, Spin-polarized muons in condensed matter physics, Contemporary Physics **40**, 175–192 (1999).

[14] S. J. Blundell, *Magnetism in Condensed Matter* (Oxford University Press, Oxford, 2003).

[15] T. Moriya, Anisotropic superexchange interaction and weak ferromagnetism, Physical Review **120**, 91 (1960).

[16] T. J. Hicken, M. N. Wilson, K. J. A. Franke, B. M. Huddart, Z. Hawkhead, M. Gomilšek, S. J. Clark, F. L. Pratt, A. Štefančič, A. E. Hall, *et al.*, Megahertz dynamics in skyrmion systems probed with muon-spin relaxation, Physical Review B **103**, 024428 (2021).

[17] C. Back, V. Cros, H. Ebert, K. Everschor-Sitte, A. Fert, M. Garst, T. Ma, S. Mankovsky, T. Monchesky, M. Mostovoy, *et al.*, The 2020 skyrmionics roadmap, Journal of Physics D: Applied Physics **53**, 363001 (2020).

[18] W. Münzer, A. Neubauer, T. Adams, S. Mühlbauer, C. Franz, F. Jonietz, R. Georgii, P. Böni, B. Pedersen, M. Schmidt, *et al.*, Skyrmion lattice in the doped semiconductor $Fe_{1-x}Co_xSi$, Physical Review B **81**, 041203(R) (2010).

[19] H. Wilhelm, M. Baenitz, M. Schmidt, U. K. Rößler, A. A. Leonov, and A. N. Bogdanov, Precursor phenomena at the magnetic ordering of the cubic helimagnet FeGe, Physical Review Letters **107**, 127203 (2011).

[20] S. Seki, X. Z. Yu, S. Ishiwata, and Y. Tokura, Observation of skyrmions in a multiferroic material, Science **336**, 198–201 (2012).

[21] Y. Tokunaga, X. Z. Yu, J. S. White, H. M. Rønnow, D. Morikawa, Y. Taguchi, and Y. Tokura, A new class of chiral materials hosting magnetic skyrmions beyond room temperature, Nature Communications **6**, 1–7 (2015).

[22] I. Kézsmárki, S. Bordács, P. Milde, E. Neuber, L. M. Eng, J. S. White, H. M. Rønnow, C. D. Dewhurst, M. Mochizuki, K. Yanai, *et al.*, Néel-type skyrmion lattice with confined orientation in the polar magnetic semiconductor $GaV_4S_8$, Nature Materials **14**, 1116–1122 (2015).

[23] K. Karube, J. S. White, N. Reynolds, J. L. Gavilano, H. Oike, A. Kikkawa, F. Kagawa, Y. Tokunaga, H. M. Rønnow, Y. Tokura, *et al.*, Robust metastable skyrmions and their triangular–square lattice structural transition in a high-temperature chiral magnet, Nature Materials **15**, 1237–1242 (2016).

[24] Z. Hou, W. Ren, B. Ding, G. Xu, Y. Wang, B. Yang, Q. Zhang, Y. Zhang, E. Liu, F. Xu, *et al.*, Observation of various and spontaneous magnetic skyrmionic bubbles at room temperature in a frustrated kagome magnet with uniaxial magnetic anisotropy, Advanced Materials **29**, 1701144 (2017).

[25] S. Bordács, A. Butykai, B. G. Szigeti, J. S. White, R. Cubitt, A. O. Leonov, S. Widmann, D. Ehlers, H.-A. K. von Nidda, V. Tsurkan, *et al.*, Equilibrium skyrmion lattice ground state in a polar easy-plane magnet, Scientific Reports **7**, 1–11 (2017).

[26] T. Kurumaji, T. Nakajima, M. Hirschberger, A. Kikkawa, Y. Yamasaki, H. Sagayama, H. Nakao, Y. Taguchi, T. Arima, and Y. Tokura, Skyrmion

lattice with a giant topological hall effect in a frustrated triangular-lattice magnet, Science **365**, 914–918 (2019).

[27] M. Hirschberger, T. Nakajima, S. Gao, L. Peng, A. Kikkawa, T. Kurumaji, M. Kriener, Y. Yamasaki, H. Sagayama, H. Nakao, *et al.*, Skyrmion phase and competing magnetic orders on a breathing kagomé lattice, Nature Communications **10**, 1–9 (2019).

[28] H. C. Wu, P. J. Sun, D. J. Hsieh, H. J. Chen, D. C. Kakarla, L. Z. Deng, C. W. Chu, and H. D. Yang, Observation of skyrmion-like magnetism in magnetic Weyl semimetal $Co_3Sn_2S_2$, Materials Today Physics **12**, 100189 (2020).

[29] N. D. Khanh, T. Nakajima, X. Yu, S. Gao, K. Shibata, M. Hirschberger, Y. Yamasaki, H. Sagayama, H. Nakao, L. Peng, *et al.*, Nanometric square skyrmion lattice in a centrosymmetric tetragonal magnet, Nature Nanotechnology , 1–6 (2020).

[30] P. D. de Réotier, A. Maisuradze, A. Yaouanc, B. Roessli, A. Amato, D. Andreica, and G. Lapertot, Determination of the zero-field magnetic structure of the helimagnet MnSi at low temperature, Physical Review B **93**, 144419 (2016).

[31] N. Nagaosa and Y. Tokura, Topological properties and dynamics of magnetic skyrmions, Nature Nanotechnology **8**, 899–911 (2013).

[32] P. Milde, D. Köhler, J. Seidel, L. Eng, A. Bauer, A. Chacon, J. Kindervater, S. Mühlbauer, C. Pfleiderer, S. Buhrandt, *et al.*, Unwinding of a skyrmion lattice by magnetic monopoles, Science **340**, 1076–1080 (2013).

[33] H. S. Park, X. Yu, S. Aizawa, T. Tanigaki, T. Akashi, Y. Takahashi, T. Matsuda, N. Kanazawa, Y. Onose, D. Shindo, *et al.*, Observation of the magnetic flux and three-dimensional structure of skyrmion lattices by electron holography, Nature Nanotechnology **9**, 337–342 (2014).

[34] S. Seki, M. Garst, J. Waizner, R. Takagi, N. D. Khanh, Y. Okamura, K. Kondou, F. Kagawa, Y. Otani, and Y. Tokura, Propagation dynamics of spin excitations along skyrmion strings, Nature Communications **11**, 1–7 (2020).

[35] P. G. De Gennes and J. Matricon, Collective modes of vortex lines in superconductors of the second kind, Reviews of Modern Physics **36**, 45 (1964).

[36] G. Derrick, Comments on nonlinear wave equations as models for elementary particles, Journal of Mathematical Physics **5**, 1252–1254 (1964).

[37] Y. Tokura and N. Kanazawa, Magnetic skyrmion materials, Chemical Reviews **121**, 2857–2897 (2020).

[38] X. Yu, Y. Onose, N. Kanazawa, J. H. Park, J. Han, Y. Matsui, N. Nagaosa, and Y. Tokura, Real-space observation of a two-dimensional skyrmion crystal, Nature **465**, 901–904 (2010).

[39] F. Büttner, C. Moutafis, M. Schneider, B. Krüger, C. Günther, J. Geilhufe, C. v. K. Schmising, J. Mohanty, B. Pfau, S. Schaffert, *et al.*, Dynamics and inertia of skyrmionic spin structures, Nature Physics **11**, 225–228 (2015).

[40] V. Ukleev, Y. Yamasaki, D. Morikawa, N. Kanazawa, Y. Okamura, H. Nakao, Y. Tokura, and T.-h. Arima, Coherent resonant soft x-ray scattering study of magnetic textures in FeGe, Quantum Beam Science **2**, 3 (2018).

[41] M. Langner, S. Roy, S. Mishra, J. Lee, X. Shi, M. Hossain, Y.-D. Chuang, S. Seki, Y. Tokura, S. Kevan, *et al.*, Coupled skyrmion sublattices in $Cu_2OSeO_3$, Physical Review Letters **112**, 167202 (2014).

[42] Y. Yamasaki, D. Morikawa, T. Honda, H. Nakao, Y. Murakami, N. Kanazawa, M. Kawasaki, T. Arima, and Y. Tokura, Dynamical process of skyrmion-helical magnetic transformation of the chiral-lattice magnet FeGe probed by small-angle resonant soft x-ray scattering, Physical Review B **92**, 220421 (2015).

[43] M. Garst, J. Waizner, and D. Grundler, Collective spin excitations of helices and magnetic skyrmions: review and perspectives of magnonics in non-centrosymmetric magnets, Journal of Physics D: Applied Physics **50**, 293002 (2017).

[44] Y. Onose, Y. Okamura, S. Seki, S. Ishiwata, and Y. Tokura, Observation of magnetic excitations of skyrmion crystal in a helimagnetic insulator $Cu_2OSeO_3$, Physical Review Letters **109**, 037603 (2012).

[45] J. I. Yonemura, Y. Shimamoto, T. Kida, D. Yoshizawa, Y. Kousaka, S. Nishihara, F. J. T. Goncalves, J. Akimitsu, K. Inoue, M. Hagiwara, *et al.*, Magnetic solitons and magnetic phase diagram of the hexagonal chiral crystal $CrN_3S_6$ in oblique magnetic fields, Physical Review B **96**, 184423 (2017).

[46] V. F. Hess, Über beobachtungen der durchdringenden strahlung bei sieben freiballonfahrten, Phys. Z. **13**, 1084 (1912).

[47] M. Conversi, E. Pancini, and O. Piccioni, On the decay process of positive and negative mesons, Phys. Rev. **68**, 232 (1945).

[48] M. Conversi, E. Pancini, and O. Piccioni, On the disintegration of negative mesons, Phys. Rev. **71**, 209 (1947).

[49] J. Beringer, J. F. Arguin, R. M. Barnett, K. Copic, O. Dahl, D. E. Groom, C. J. Lin, J. Lys, H. Murayama, C. G. Wohl, *et al.*, Review of particle physics, Physical Review D-Particles, Fields, Gravitation and Cosmology **86**, 010001 (2012).

[50] R. L. Garwin, L. M. Lederman, and M. Weinrich, Observations of the failure of conservation of parity and charge conjugation in meson decays: the magnetic moment of the free muon, Phys. Rev. **105**, 1415 (1957).

[51] P. D. De Reotier and A. Yaouanc, Muon spin rotation and relaxation in magnetic materials, Journal of Physics: Condensed Matter **9**, 9113 (1997).

[52] C. V. Topping and S. J. Blundell, AC susceptibility as a probe of low-frequency magnetic dynamics, Journal of Physics: Condensed Matter **31**, 013001 (2018).

[53] T. Lancaster, *Muon-spin relaxation and its application to magnetic systems of differing dimensionality*, Ph.D. thesis, University of Oxford (2004).

[54] R. P. Feynman, *The Feynman Lectures on Physics* (Basic Books, New York, 1965).

[55] E. Roduner and H. Fischer, Muonium substituted organic free radicals in liquids. Theory and analysis of $\mu$SR spectra, Chemical Physics **54**, 261–276 (1981).

[56] R. Kubo and T. Toyabe, *Magnetic resonance and relaxation* (North Holland, Amsterdam, 1967).

[57] R. S. Hayano, Y. J. Uemura, J. Imazato, N. Nishida, T. Yamazaki, and R. Kubo, Zero-and low-field spin relaxation studied by positive muons, Physical Review B **20**, 850 (1979).

[58] Wolfram Research, Inc., Mathematica, Version 12.3.1 (2021).

[59] K. F. Riley, M. P. Hosbon, and S. J. Bence, *Mathematical Methods for Physics and Engineering*, 3rd ed. (Cambridge University Press, Cambridge, 2006).

[60] K. W. Kehr, G. Honig, and D. Richter, Stochastic theory of spin depolarization of muons diffusing in the presence of traps, Zeitschrift für Physik B Condensed Matter **32**, 49–58 (1978).

[61] A. Keren, Generalization of the Abragam relaxation function to a longitudinal field, Physical Review B **50**, 10039 (1994).

[62] R. C. Williams, W. J. A. Blackmore, S. P. M. Curley, M. R. Lees, S. M. Birnbaum, J. Singleton, B. M. Huddart, T. J. Hicken, T. Lancaster, S. J.

Blundell, *et al.*, Near-ideal molecule-based Haldane spin chain, Physical Review Research **2**, 013082 (2020).

[63] F. D. M. Haldane, Continuum dynamics of the 1-D Heisenberg antiferromagnet: Identification with the $O(3)$ nonlinear sigma model, Physics Letters A **93**, 464–468 (1983).

[64] F. D. M. Haldane, Nonlinear field theory of large-spin Heisenberg antiferromagnets: semiclassically quantized solitons of the one-dimensional easy-axis Néel state, Physical Review Letters **50**, 1153 (1983).

[65] T. Sakai and M. Takahashi, Effect of the Haldane gap on quasi-one-dimensional systems, Physical Review B **42**, 4537 (1990).

[66] K. Wierschem and P. Sengupta, Characterizing the Haldane phase in quasi-one-dimensional spin-1 Heisenberg antiferromagnets, Modern Physics Letters B **28**, 1430017 (2014).

[67] K. Wierschem and P. Sengupta, Quenching the haldane gap in spin-1 Heisenberg antiferromagnets, Physical Review Letters **112**, 247203 (2014).

[68] F. L. Pratt, WiMDA: a muon data analysis program for the Windows PC, Physica B: Condensed Matter **289**, 710–714 (2000).

[69] T. Lancaster, S. J. Blundell, M. L. Brooks, P. J. Baker, F. L. Pratt, J. L. Manson, C. P. Landee, and C. Baines, Magnetic order in the quasi-one-dimensional spin-1/2 molecular chain compound copper pyrazine dinitrate, Physical Review B **73**, 020410 (2006).

[70] S. Capponi, M. Dupont, A. W. Sandvik, and P. Sengupta, NMR relaxation in the spin-1 Heisenberg chain, Physical Review B **100**, 094411 (2019).

[71] T. Lancaster, F. Xiao, B. Huddart, R. Williams, F. Pratt, S. Blundell, S. Clark, R. Scheuermann, T. Goko, S. Ward, *et al.*, Quantum magnetism in molecular spin ladders probed with muon-spin spectroscopy, New Journal of Physics **20**, 103002 (2018).

[72] M. Buchner, K. Höfler, B. Henne, V. Ney, and A. Ney, Tutorial: Basic principles, limits of detection, and pitfalls of highly sensitive SQUID magnetometry for nanomagnetism and spintronics, Journal of Applied Physics **124**, 161101 (2018).

[73] S. Clark, *Complex structures in tetrahedrally bonded semiconductors*, Ph.D. thesis, University of Edinburgh (1994).

[74] P. Hohenberg and W. Kohn, Inhomogeneous electron gas, Phys. Rev **136**, B864 (1964).

[75] W. Kohn and L. J. Sham, Self-consistent equations including exchange and correlation effects, Physical Review **140**, A1133 (1965).

[76] S. J. Clark, M. D. Segall, C. J. Pickard, P. J. Hasnip, M. J. Probert, K. Refson, and M. C. Payne, First principles methods using CASTEP, Zeitschrift für Kristallographie - Crystalline Materials **220**, 567–570 (2005).

[77] H. Effenberger and F. Pertlik, The crystal structures of the copper (II) oxoselenites $Cu_2O(SeO_3)$ (cubic and monoclinic) and $Cu_4O(SeO_3)_3$ (monoclinic and triclinic), Chemical Monthly **117**, 887–896 (1986).

[78] J. S. White, I. Levatić, A. A. Omrani, N. Egetenmeyer, K. Prša, I. Živković, J. L. Gavilano, J. Kohlbrecher, M. Bartkowiak, H. Berger, *et al.*, Electric field control of the skyrmion lattice in $Cu_2OSeO_3$, Journal of Physics: Condensed Matter **24**, 432201 (2012).

[79] M. T. Birch, R. Takagi, S. Seki, M. N. Wilson, F. Kagawa, A. Štefančič, G. Balakrishnan, R. Fan, P. Steadman, C. J. Ottley, M. Crisanti, R. Cubitt, T. Lancaster, Y. Tokura, and P. D. Hatton, Increased lifetime of metastable skyrmions by controlled doping, Physical Review B **100**, 014425 (2019).

[80] K. D. Chandrasekhar, H. C. Wu, C. L. Huang, and H. D. Yang, Effects of Jahn–Teller distortion on the skyrmion stability of $(Cu_{1-x}Ni_x)_2OSeO_3$, Journal of Materials Chemistry C **4**, 5270–5274 (2016).

[81] J.-W. G. Bos, C. V. Colin, and T. T. M. Palstra, Magnetoelectric coupling in the cubic ferrimagnet $Cu_2OSeO_3$, Physical Review B **78**, 094416 (2008).

[82] M. Belesi, T. Philippe, I. Rousochatzakis, H. Wu, H. Berger, S. Granville, I. Shvets, and J.-P. Ansermet, Magnetic properties of the magnetoelectric compound $Cu_2OSeO_3$: Magnetization and 77Se NMR study, in *Journal of Physics: Conference Series*, Vol. 303 (IOP Publishing, 2011) p. 012069.

[83] A. Maisuradze, Z. Guguchia, B. Graneli, H. M. Rønnow, H. Berger, and H. Keller, $\mu$SR investigation of magnetism and magnetoelectric coupling in $Cu_2OSeO_3$, Physical Review B **84**, 064433 (2011).

[84] F. Qian, L. J. Bannenberg, H. Wilhelm, G. Chaboussant, L. M. Debeer-Schmitt, M. P. Schmidt, A. Aqeel, T. T. M. Palstra, E. Brück, A. J. E. Lefering, *et al.*, New magnetic phase of the chiral skyrmion material $Cu_2OSeO_3$, Science Advances **4**, eaat7323 (2018).

[85] M. Halder, A. Chacon, A. Bauer, W. Simeth, S. Mühlbauer, H. Berger, L. Heinen, M. Garst, A. Rosch, and C. Pfleiderer, Thermodynamic evidence of a second skyrmion lattice phase and tilted conical phase in $Cu_2OSeO_3$, Physical Review B **98**, 144429 (2018).

[86] M. N. Wilson, M. Crisanti, C. Barker, A. Štefančič, J. S. White, M. T. Birch, G. Balakrishnan, R. Cubitt, and P. D. Hatton, Measuring the formation energy barrier of skyrmions in zinc-substituted $Cu_2OSeO_3$, Physical Review B **99**, 174421 (2019).

[87] T. Schwarze, J. Waizner, M. Garst, A. Bauer, I. Stasinopoulos, H. Berger, C. Pfleiderer, and D. Grundler, Universal helimagnon and skyrmion excitations in metallic, semiconducting and insulating chiral magnets, Nature Materials **14**, 478–483 (2015).

[88] V. P. Gnezdilov, K. V. Lamonova, Y. G. Pashkevich, P. Lemmens, H. Berger, F. Bussy, and S. L. Gnatchenko, Magnetoelectricity in the ferri-

magnetic $Cu_2OSeO_3$: symmetry analysis and Raman scattering study, Low Temperature Physics **36**, 550–557 (2010).

[89] K. H. Miller, X. S. Xu, H. Berger, E. S. Knowles, D. J. Arenas, M. W. Meisel, and D. B. Tanner, Magnetodielectric coupling of infrared phonons in single-crystal $Cu_2OSeO_3$, Physical Review B **82**, 144107 (2010).

[90] M. Ozerov, J. Romhanyi, M. Belesi, H. Berger, J.-P. Ansermet, J. vandenBrink, J. Wosnitza, S. A. Zvyagin, and I. Rousochatzakis, Establishing the fundamental magnetic interactions in the chiral skyrmionic Mott insulator $Cu_2OSeO_3$ by terahertz electron spin resonance, Physical Review Letters **113**, 157205 (2014).

[91] J. Romhányi, J. vandenBrink, and I. Rousochatzakis, Entangled tetrahedron ground state and excitations of the magnetoelectric skyrmion material $Cu_2OSeO_3$, Physical Review B **90**, 140404(R) (2014).

[92] A. Štefančič, S. H. Moody, T. J. Hicken, M. T. Birch, G. Balakrishnan, S. A. Barnett, M. Crisanti, J. S. O. Evans, S. J. R. Holt, K. J. A. Franke, *et al.*, Origin of skyrmion lattice phase splitting in Zn-substituted $Cu_2OSeO_3$, Physical Review Materials **2**, 111402 (2018).

[93] F. James and M. Roos, Minuit: a system for function minimization and analysis of the parameter errors and corrections, Computer Physiscs Commununications **10**, 343–367 (1975).

[94] iminuit team, iminuit – a python interface to minuit, `https://github.com/scikit-hep/iminuit` (Accessed: 14-01-2021).

[95] J. P. Perdew, K. Burke, and M. Ernzerhof, Generalized gradient approximation made simple, Physical Review Letters **77**, 3865–3868 (1996).

[96] P. Bonfà, I. J. Onuorah, and R. De Renzi, Introduction and a quick look at MUESR, the Magnetic structure and mUon Embedding Site Refinement suite, in *Proceedings of the 14th International Conference on Muon Spin Rotation, Relaxation and Resonance (μSR2017)* (2018) p. 011052.

[97] S. Seki, S. Ishiwata, and Y. Tokura, Magnetoelectric nature of skyrmions in a chiral magnetic insulator $Cu_2OSeO_3$, Physical Review B **86**, 060403(R) (2012).

[98] T. Lancaster, R. C. Williams, I. O. Thomas, F. Xiao, F. L. Pratt, S. J. Blundell, J. C. Loudon, T. Hesjedal, S. J. Clark, P. D. Hatton, *et al.*, Transverse field muon-spin rotation signature of the skyrmion-lattice phase in $Cu_2OSeO_3$, Physical Review B **91**, 224408 (2015).

[99] S. L. Zhang, G. van der Laan, and T. Hesjedal, Direct experimental determination of spiral spin structures via the dichroism extinction effect in resonant elastic soft x-ray scattering, Physical Review B **96**, 094401 (2017).

[100] F. L. Pratt, P. J. Baker, S. J. Blundell, T. Lancaster, M. A. Green, and M. Kurmoo, Chiral-like critical behavior in the antiferromagnet cobalt glycerolate, Physical Review Letters **99**, 017202 (2007).

[101] A. Pelissetto and E. Vicari, Critical phenomena and renormalization-group theory, Physics Reports **368**, 549–727 (2002).

[102] E. Pospelov, V. Prudnikov, P. Prudnikov, and A. Lyakh, Non-equilibrium critical behavior of the 3D classical Heisenberg model, in *Journal of Physics: Conference Series*, Vol. 1163 (IOP Publishing, 2019) p. 012020.

[103] I. Živković, J. S. White, H. M. Rønnow, K. Prša, and H. Berger, Critical scaling in the cubic helimagnet $Cu_2OSeO_3$, Physical Review B **89**, 060401(R) (2014).

[104] M. N. Wilson, M. T. Birch, A. Štefančič, A. C. Twitchett-Harrison, G. Balakrishnan, T. J. Hicken, R. Fan, P. Steadman, and P. D. Hatton, Stability and metastability of skyrmions in thin lamellae of $Cu_2OSeO_3$, Physical Review Research **2**, 013096 (2020).

[105] J. Miltat, S. Rohart, and A. Thiaville, Brownian motion of magnetic domain walls and skyrmions, and their diffusion constants, Physical Review B **97**, 214426 (2018).

[106] M. Weißenhofer and U. Nowak, Diffusion of skyrmions: the role of topology and anisotropy, New Journal of Physics **22**, 103059 (2020).

[107] T. Reimann, A. Bauer, C. Pfleiderer, P. Böni, P. Trtik, A. Tremsin, M. Schulz, and S. Mühlbauer, Neutron diffractive imaging of the skyrmion lattice nucleation in MnSi, Physical Review B **97**, 020406(R) (2018).

[108] K. Momma and F. Izumi, VESTA 3 for three-dimensional visualization of crystal, volumetric and morphology data, Journal of applied crystallography **44**, 1272–1276 (2011).

[109] A. Yaouanc and P. D. De Reotier, *Muon spin rotation, relaxation, and resonance: applications to condensed matter* (Oxford University Press, Oxford, 2011).

[110] H. C. Wu, T. Y. Wei, K. D. Chandrasekhar, T. Y. Chen, H. Berger, and H. D. Yang, Unexpected observation of splitting of skyrmion phase in Zn doped $Cu_2OSeO_3$, Scientific Reports **5**, 1–9 (2015).

[111] R. H. Heffner, J. E. Sonier, D. E. MacLaughlin, G. J. Nieuwenhuys, G. Ehlers, F. Mezei, S.-W. Cheong, J. S. Gardner, and H. Röder, Observation of two time scales in the ferromagnetic manganite $La_{1-x}Ca_xMnO_3$, $x \simeq 0.3$, Physical Review Letters **85**, 3285 (2000).

[112] K. Karube, J. S. White, D. Morikawa, C. D. Dewhurst, R. Cubitt, A. Kikkawa, X. Yu, Y. Tokunaga, T.-h. Arima, H. M. Rønnow, *et al.*, Disordered skyrmion phase stabilized by magnetic frustration in a chiral magnet, Science Advances **4**, eaar7043 (2018).

[113] X. Z. Yu, W. Koshibae, Y. Tokunaga, K. Shibata, Y. Taguchi, N. Nagaosa, and Y. Tokura, Transformation between meron and skyrmion topological spin textures in a chiral magnet, Nature **564**, 95–98 (2018).

[114] J. D. Bocarsly, C. Heikes, C. M. Brown, S. D. Wilson, and R. Seshadri, Deciphering structural and magnetic disorder in the chiral skyrmion host

materials $Co_xZn_yMn_z$ ($x+y+z=20$), Physical Review Materials **3**, 014402 (2019).

[115] B. M. Huddart, *Muon stopping sites in magnetic systems from density functional theory*, Ph.D. thesis, Durham University (2020).

[116] D. L. Schlagel, Y. L. Wu, W. Zhang, and T. A. Lograsso, Chemical segregation during bulk single crystal preparation of Ni–Mn–Ga ferromagnetic shape memory alloys, Journal of Alloys and Compounds **312**, 77–85 (2000).

[117] J. Kindervater, I. Stasinopoulos, A. Bauer, F. X. Haslbeck, F. Rucker, A. Chacon, S. Mühlbauer, C. Franz, M. Garst, D. Grundler, *et al.*, Weak crystallization of fluctuating skyrmion textures in MnSi, Physical Review X **9**, 041059 (2019).

[118] R. S. Hayano, Y. J. Uemura, J. Imazato, N. Nishida, T. Yamazaki, H. Yasuoka, and Y. Ishikawa, Observation of the $T/(T-T_c)$ divergence of the $\mu^+$ spin-lattice relaxation rate in MnSi near $T_c$, Physical Review Letters **41**, 1743 (1978).

[119] T. J. Hicken, S. J. R. Holt, K. J. A. Franke, Z. Hawkhead, A. Štefančič, M. N. Wilson, M. Gomilšek, B. M. Huddart, S. J. Clark, M. R. Lees, *et al.*, Magnetism and Néel skyrmion dynamics in $GaV_4S_{8-y}Se_y$, Physical Review Research **2**, 032001(R) (2020).

[120] Y. Fujima, N. Abe, Y. Tokunaga, and T. Arima, Thermodynamically stable skyrmion lattice at low temperatures in a bulk crystal of lacunar spinel $GaV_4Se_8$, Physical Review B **95**, 180410 (2017).

[121] T. Kurumaji, T. Nakajima, V. Ukleev, A. Feoktystov, T.-h. Arima, K. Kakurai, and Y. Tokura, Néel-type skyrmion lattice in the tetragonal polar magnet $VOSe_2O_5$, Physical Review Letters **119**, 237201 (2017).

[122] D. Brasen, J. M. Vandenberg, M. Robbins, R. H. Willens, W. A. Reed, R. C. Sherwood, and X. J. Pinder, Magnetic and crystallographic properties of

spinels of the type $A_xB_2S_4$ where A = Al, Ga, and B = Mo, V, Cr, Journal of Solid State Chemistry **13**, 298–303 (1975).

[123] S. J. R. Holt, A. Štefančič, C. Ritter, A. E. Hall, M. R. Lees, and G. Balakrishnan, Structure and magnetism of the skyrmion hosting family $GaV_4S_{8-y}Se_y$ with low levels of substitutions between $0 \leq y \leq 0.5$ and $7.5 \leq y \leq 8$, Physical Review Materials **4**, 114413 (2020).

[124] R. Pocha, D. Johrendt, and R. Pöttgen, Electronic and structural instabilities in $GaV_4S_8$ and $GaMo_4S_8$, Chemistry of Materials **12**, 2882–2887 (2000).

[125] D. Ehlers, I. Stasinopoulos, I. Kézsmárki, T. Fehér, V. Tsurkan, H. K. von Nidda, D. Grundler, and A. Loidl, Exchange anisotropy in the skyrmion host $GaV_4S_8$, Journal of Physics: Condensed Matter **29**, 065803 (2016).

[126] Z. Wang, E. Ruff, M. Schmidt, V. Tsurkan, I. Kézsmárki, P. Lunkenheimer, and A. Loidl, Polar dynamics at the Jahn-Teller transition in ferroelectric $GaV_4S_8$, Physical Review Letters **115**, 207601 (2015).

[127] A. Štefančič, S. J. Holt, M. R. Lees, C. Ritter, M. J. Gutmann, T. Lancaster, and G. Balakrishnan, Establishing magneto-structural relationships in the solid solutions of the skyrmion hosting family of materials: $GaV_4S_{8-y}Se_y$, Scientific Reports **10**, 9813 (2020).

[128] K. J. A. Franke, B. M. Huddart, T. J. Hicken, F. Xiao, S. J. Blundell, F. L. Pratt, M. Crisanti, J. A. T. Barker, S. J. Clark, A. Štefančič, *et al.*, Magnetic phases of skyrmion-hosting $GaV_4S_{8-y}Se_y$ ($y = 0$, 2, 4, 8) probed with muon spectroscopy, Physical Review B **98**, 054428 (2018).

[129] H. J. Monkhorst and J. D. Pack, Special points for Brillouin-zone integrations, Physical Review B **13**, 5188–5192 (1976).

[130] E. Ruff, S. Widmann, P. Lunkenheimer, V. Tsurkan, S. Bordács, I. Kézsmárki, and A. Loidl, Multiferroicity and skyrmions carrying electric polarization in $GaV_4S_8$, Science Advances **1**, e1500916 (2015).

[131] J. S. White, A. Butykai, R. Cubitt, D. Honecker, C. D. Dewhurst, L. F. Kiss, V. Tsurkan, and S. Bordács, Direct evidence for cycloidal modulations in the thermal-fluctuation-stabilized spin spiral and skyrmion states of $GaV_4S_8$, Physical Review B **97**, 020401(R) (2018).

[132] E. M. Clements, R. Das, G. Pokharel, M. H. Phan, A. D. Christianson, D. Mandrus, J. C. Prestigiacomo, M. S. Osofsky, and H. Srikanth, Robust cycloid crossover driven by anisotropy in the skyrmion host $GaV_4S_8$, Physical Review B **101**, 094425 (2020).

[133] Y. A. Izyumov, Modulated, or long-periodic, magnetic structures of crystals, Soviet Physics Uspekhi **27**, 845 (1984).

[134] J. Major, J. Mundy, M. Schmolz, A. Seeger, K.-P. Döring, K. Fürderer, M. Gladisch, D. Herlach, and G. Majer, Zero-field muon spin rotation in monocrystalline chromium, Hyperfine Interactions **31**, 259–264 (1986).

[135] A. Amato, Heavy-fermion systems studied by $\mu$SR technique, Reviews of Modern Physics **69**, 1119 (1997).

[136] H. Müller, W. Kockelmann, and D. Johrendt, The magnetic structure and electronic ground states of mott insulators $GaV_4S_8$ and $GaV_4Se_8$, Chemistry of Materials **18**, 2174–2180 (2006).

[137] J. T. Zhang, J. L. Wang, X. Q. Yang, W. S. Xia, X. M. Lu, and J. S. Zhu, Magnetic properties and spin-driven ferroelectricity in multiferroic skyrmion host $GaV_4S_8$, Physical Review B **95**, 085136 (2017).

[138] D. Ehlers, I. Stasinopoulos, V. Tsurkan, H. A. Krugvon Nidda, T. Fehér, A. Leonov, I. Kézsmárki, D. Grundler, and A. Loidl, Skyrmion dynamics under uniaxial anisotropy, Physical Review B **94**, 014406 (2016).

[139] L. J. Bannenberg, H. Wilhelm, R. Cubitt, A. Labh, M. P. Schmidt, E. Lelièvre-Berna, C. Pappas, M. Mostovoy, and A. O. Leonov, Multiple low-temperature skyrmionic states in a bulk chiral magnet, Quantum Materials **4**, 1–8 (2019).

[140] T. J. Hicken, Z. Hawkhead, M. N. Wilson, B. M. Huddart, A. E. Hall, G. Balakrishnan, F. L. Pratt, S. J. Clark, and T. Lancaster, Energy-gap driven low-temperature magnetic and transport properties in $Cr_{1/3}MS_2$ ($M$ = Nb or Ta), arXiv:2105.01393 (2021).

[141] R. G. Dickinson and L. Pauling, The crystal structure of molybdenite, Journal of the American Chemical Society **45**, 1466–1471 (1923).

[142] S. Manzeli, D. Ovchinnikov, D. Pasquier, O. V. Yazyev, and A. Kis, 2d transition metal dichalcogenides, Nature Reviews Materials **2**, 1–15 (2017).

[143] J. A. Wilson and A. D. Yoffe, The transition metal dichalcogenides discussion and interpretation of the observed optical, electrical and structural properties, Advances in Physics **18**, 193–335 (1969).

[144] Q. H. Wang, K. Kalantar-Zadeh, A. Kis, J. N. Coleman, and M. S. Strano, Electronics and optoelectronics of two-dimensional transition metal dichalcogenides, Nature Nanotechnology **7**, 699–712 (2012).

[145] W. Choi, N. Choudhary, G. H. Han, J. Park, D. Akinwande, and Y. H. Lee, Recent development of two-dimensional transition metal dichalcogenides and their applications, Materials Today **20**, 116–130 (2017).

[146] T. Moriya and T. Miyadai, Evidence for the helical spin structure due to antisymmetric exchange interaction in $Cr_{1/3}NbS_2$, Solid State Communications **42**, 209–212 (1982).

[147] Y. Kousaka, T. Ogura, J. Zhang, P. Miao, S. Lee, S. Torii, T. Kamiyama, J. Campo, K. Inoue, and J. Akimitsu, Long periodic helimagnetic ordering in $CrM_3S_6$ ($M$=Nb and Ta), in *Journal of Physics: Conference Series*, Vol. 746 (IOP Publishing, 2016) p. 012061.

[148] Y. Togawa, T. Koyama, K. Takayanagi, S. Mori, Y. Kousaka, J. Akimitsu, S. Nishihara, K. Inoue, A. Ovchinnikov, and J.-i. Kishine, Chiral magnetic soliton lattice on a chiral helimagnet, Physical Review Letters **108**, 107202 (2012).

[149] C. Zhang, J. Zhang, C. Liu, S. Zhang, Y. Yuan, P. Li, Y. Wen, Z. Jiang, B. Zhou, Y. Lei, *et al.*, Chiral helimagnetism and one-dimensional magnetic solitons in a Cr-intercalated transition metal dichalcogenide, Advanced Materials , 2101131 (2021).

[150] D. A. Mayoh, J. Bouaziz, A. E. Hall, J. B. Staunton, M. R. Lees, and G. Balakrishnan, submitted (2021).

[151] N. J. Ghimire, M. A. McGuire, D. S. Parker, B. Sipos, S. Tang, J.-Q. Yan, B. C. Sales, and D. Mandrus, Magnetic phase transition in single crystals of the chiral helimagnet $Cr_{1/3}NbS_2$, Physical Review B **87**, 104403 (2013).

[152] A. C. Bornstein, B. J. Chapman, N. J. Ghimire, D. G. Mandrus, D. S. Parker, and M. Lee, Out-of-plane spin-orientation dependent magnetotransport properties in the anisotropic helimagnet $Cr_{1/3}NbS_2$, Physical Review B **91**, 184401 (2015).

[153] D. Braam, C. Gomez, S. Tezok, E. V. L. de Mello, L. Li, D. Mandrus, H.-Y. Kee, and J. E. Sonier, Magnetic properties of the helimagnet $Cr_{1/3}NbS_2$ observed by $\mu$SR, Physical Review B **91**, 144407 (2015).

[154] Y. Togawa, J. Kishine, P. A. Nosov, T. Koyama, G. W. Paterson, S. McVitie, Y. Kousaka, J. Akimitsu, M. Ogata, and A. S. Ovchinnikov, Anomalous temperature behavior of the chiral spin helix in $CrN_3S_6$ thin lamellae, Physical Review Letters **122**, 017204 (2019).

[155] E. B. Borisenko, V. A. Berezin, N. N. Kolesnikov, V. K. Gartman, D. V. Matveev, and O. F. Shakhlevich, Structural and magnetic ordering of $CrNb_3S_6$ single crystals grown by gas transport method, Physics of the Solid State **59**, 1310–1313 (2017).

[156] J. M. D. Coey and S. Sanvito, Magnetic semiconductors and half-metals, Journal of Physics D: Applied Physics **37**, 988 (2004).

[157] G. K. Madsen and D. J. Singh, BoltzTraP. a code for calculating band-structure dependent quantities, Computer Physics Communications **175**, 67–71 (2006).

[158] J. M. D. Coey and M. Venkatesan, Half-metallic ferromagnetism: Example of $CrO_2$, Journal of Applied Physics **91**, 8345–8350 (2002).

[159] J. P. Perdew, Density functional theory and the band gap problem, International Journal of Quantum Chemistry **28**, 497–523 (1985).

[160] M. Mito, H. Ohsumi, T. Shishidou, F. Kuroda, M. Weinert, K. Tsuruta, Y. Kotani, T. Nakamura, Y. Togawa, J. Kishine, *et al.*, Observation of orbital angular momentum in the chiral magnet $CrNb_3S_6$ by soft x-ray magnetic circular dichroism, Physical Review B **99**, 174439 (2019).

[161] H. Han, L. Zhang, D. Sapkota, N. Hao, L. Ling, H. Du, L. Pi, C. Zhang, D. G. Mandrus, and Y. Zhang, Tricritical point and phase diagram based on critical scaling in the monoaxial chiral helimagnet $Cr_{1/3}NbS_2$, Physical Review B **96**, 094439 (2017).

[162] A. E. Hall *et al.*, in preparation .

[163] S. Seki, Y. Okamura, K. Shibata, R. Takagi, N. D. Khanh, F. Kagawa, T. Arima, and Y. Tokura, Stabilization of magnetic skyrmions by uniaxial tensile strain, Physical Review B **96**, 220404(R) (2017).

[164] R. Tomasello, A. Giordano, S. Chiappini, R. Zivieri, G. Siracusano, V. Puliafito, I. Medlej, A. La Corte, B. Azzerboni, M. Carpentieri, *et al.*, Micromagnetic understanding of the skyrmion hall angle current dependence in perpendicularly magnetized ferromagnets, Physical Review B **98**, 224418 (2018).

[165] R. Pełka, D. Pinkowicz, B. Sieklucka, and M. Fitta, Molecular realizations of 3D Heisenberg magnet: Critical scaling, Journal of Alloys and Compounds **765**, 520–526 (2018).

[166] M. Troyer, M. Imada, and K. Ueda, Critical exponents of the quantum phase transition in a planar antiferromagnet, Journal of the Physical Society of Japan **66**, 2957–2960 (1997).